

UNCLASSIFIED

AD NUMBER

AD759065

LIMITATION CHANGES

TO:

Approved for public release; distribution is unlimited.

FROM:

Distribution authorized to U.S. Gov't. agencies and their contractors; Critical Technology; DEC 1972. Other requests shall be referred to Army Assistant Chief of Staff for Intelligence, Attn: ACSI-FE, Washington, DC. This document contains export-controlled technical data.

AUTHORITY

MICOM per DTIC form 55

THIS PAGE IS UNCLASSIFIED

AD-759 065

ELECTRON DENSITY BEHAVIOR IN THE WAKE
OF SPHERES FLOWN AT 14,500 FEET/SECOND

D. Heckman, et al

Defense Research Establishment

Prepared for:

Advanced Research Projects Agency

December 1972

DISTRIBUTED BY:



National Technical Information Service
U. S. DEPARTMENT OF COMMERCE
5285 Port Royal Road, Springfield Va. 22151

**BEST
AVAILABLE COPY**

**MISSING PAGE
NUMBERS ARE BLANK
AND WERE NOT
FILMED**

DREV R-680/72
PROJ. 95-51-10

NON CLASSIFIÉ
UNCLASSIFIED

AD 759065

ELECTRON DENSITY BEHAVIOR IN THE WAKE OF SPHERES FLOWN AT 14,500 FEET/SECOND

D. Heckman, L. Sevigny, A. Fitchett, A. Emond and P. Doyon



Reproduced by
NATIONAL TECHNICAL
INFORMATION SERVICE
U.S. Department of Commerce
Springfield, VA 22151

D D C
REF ID: A651162
MAY 1 1973
B

CENTRE DE RECHERCHES POUR LA DEFENSE
DEFENCE RESEARCH ESTABLISHMENT
VALCARTIER

DEFENCE RESEARCH BOARD

CONSEIL DE RECHERCHES POUR LA DÉFENSE

Québec, Canada



December/décembre 1972

188

ELECTRON DENSITY BEHAVIOR IN THE WAKE OF SPHERES
FLOWN AT 14,500 FEET/SECOND

by

D. Heckman, L. Sévigny, A. Fitchett, A. Emond and P. Doyon

This document is subject to special export controls and each transmittal to foreign governments or foreign nationals, other than Canada and U.S., may be made only with prior approval of both the Canadian Department of National Defence and the U.S. Army Assistant Chief of Staff for Intelligence, Attn: ACSI-FE, Washington, D.C.

This research was sponsored jointly by

The Defence Research Establishment
Valcartier
P.O. Box 880
Courcelette, Quebec, Canada
Under Project D-95-51-10

The Advanced Research Projects
Agency
ARPA Order 133
Monitored by the U.S. Army
Missile Command,
Redstone Arsenal, Alabama
35809
Contract DA-H01-69-C-0921

CENTRE DE RECHERCHES POUR LA DEFENSE
DEFENCE RESEARCH ESTABLISHMENT
VALCARTIER
Tel: (418) 844-4271

RESUME

On a déduit, à partir de mesures de phase réalisées à l'aide d'un interféromètre micro-onde à deux faisceaux fonctionnant dans la bande χ_s , l'amplitude et la largeur des distributions radiales présupposées de forme gaussienne, de la densité électronique dans le sillage d'une sphère hypersonique projetée à 14,500 pied/seconde dans une atmosphère d'azote ou d'air à diverses pressions. Les résultats obtenus portent sur la région du proche sillage et montrent que la densité électronique passe de 10^{11} électrons/centimètre³, près du projectile, à 10^9 électrons/centimètre³ à une distance de quelques centaines de diamètre de projectile de la sphère. Notre étude révèle, par ailleurs, qu'il est possible de reproduire les mesures de la densité électronique, et ce dans les conditions normales d'opération du tunnel balistique 5 du Centre de recherches pour la défense, Valcartier (CRDV). En raison de la dissimilitude des conditions expérimentales, il nous a été impossible de comparer nos résultats avec ceux d'autres laboratoires. Toutefois, la tendance générale de nos résultats semble en accord avec celle observée ailleurs.

ABSTRACT

The amplitudes and widths of the assumed gaussian distributions of electron density in the wakes of hypersonic spheres flown at 14,500 feet/second in atmospheres of air and nitrogen at various pressures have been derived from phase shift measurements with a dual channel interferometer, operating at χ_s -band. The data apply to the near wake extending from just behind the spherical projectile out to several hundreds of body diameters, and cover a band of electron number densities from $10^{11}/\text{centimeter}^3$ to less than $10^9/\text{centimeter}^3$. A conclusion of major importance is that it is possible to obtain reproducible electron density measurements under the normal operating conditions in the Defence Research Establishment, Valcartier (DREV) Range 5. No data from other laboratories were found at sufficiently similar conditions to permit an exact comparison with the present results. However, the general trend of the data seems to follow that observed elsewhere.

TABLE OF CONTENTS

RESUME/ABSTRACT	
1.0 INTRODUCTION	1
2.0 INTERFEROMETER EQUIPMENT	2
3.0 ANALYSIS	3
3.1 Determination of Transmission Arm Phase Shifts	3
3.2 Characteristics of Wake Electron Density Distribution	6
4.0 PRESENTATION OF THE RESULTS	8
4.1 Interferometer Firing Report	8
4.2 Interferometer SIN ϕ Displays	8
4.3 Data Reduction	8
5.0 RESULTS IN AIR ATMOSPHERES	10
5.1 'Dirty Rounds' and 'Clean Rounds'	10
5.2 Electron Density on the Wake Axis and Electron Wake Radii for Air Atmospheres by Simultaneous Solutions	10
5.3 Electron Density on the Axis in Air Wakes deduced with a Prescribed Electron Wake Radius	11
5.4 Interferometer Signals with Clean and Dirty Rounds	12
6.0 RESULTS IN NITROGEN ATMOSPHERES	13
6.1 Electron Density on the Wake Axis and Electron Wake Radii for Nitrogen Atmospheres by Simultaneous Solutions	13
6.2 Electron Density on the Axis in Nitrogen Wakes deduced with a Prescribed Wake Radius	14
7.0 WAKE RADII	15
7.1 Wake Radii in Nitrogen Wakes	15
7.2 Average Wake Radius	15
8.0 DISCUSSION	16
9.0 CONCLUSIONS	17
REFERENCES	19
TABLE I to V	

UNCLASSIFIED

iii

- | | | |
|-------------|---|----|
| APPENDIX A. | Interferometer Firing Reports and SIN ϕ Displays.
Air Atmospheres | 71 |
| APPENDIX B. | Electron Densities on the Axis and Electron
Density Radii from Simultaneous Solutions.
Air Atmospheres | |
| APPENDIX C. | Electron Densities on the Axis Computed with a
Prescribed Electron Density Radius.
Air Atmospheres | |
| APPENDIX D. | Interferometer Firing Reports and SIN ϕ Displays.
Nitrogen Atmospheres | |
| APPENDIX E. | Electron Densities on the Axis and Electron
Density Radii from Simultaneous Solutions.
Nitrogen Atmospheres | |
| APPENDIX F. | Electron Densities on the Axis Computed with a
Prescribed Electron Density Radius.
Nitrogen Atmospheres | |

1.0 INTRODUCTION

Since 1965, DREV has been engaged in a program to experimentally determine the behavior of the turbulent wakes generated by hypersonic projectiles (References 1-5). The list of wake variables on which spatially-resolved measurements have been obtained includes velocity, mass density, temperature, and charge density.

The behavior of electron density in the wake is of particular experimental and theoretical interest as regards the modeling of the scattering of microwave radiation from wakes. The major effort at DREV has been concerned with the use of Langmuir (fine wire) electron probes and with larger continuum electrostatic ion probes. As part of the supporting (or control) experimentation, measurements have also been made of the average electron density behavior in the wake using a dual channel X_S-band microwave interferometer equipment. These microwave interferometric measurements present an estimate of the electron density integrated along the path of the microwave beam across the wake, in contrast to the spatially-resolved measurements made by a small probe. However, the equipment at DREV has a dual channel capability, and if one assumes, for example, that the distribution of electron density across the wake is gaussian, the output signals of the dual channel interferometer can be analyzed so as to yield the amplitude and width parameters of the distribution (References 6, 7).

The present document concentrates on two different aspects of the turbulent wake program.

The first of these deals with results obtained concerning the amplitude and width of the electron density distribution in the wake of hypersonic spheres, as deduced from the dual channel interferometer. A modest amount of data is presented on results obtained in air wakes at 10 torr and in nitrogen wakes at 7.6 torr and 20 torr. In all cases, the projectiles employed were 2.7 inch diameter hollow titanium spheres, and the velocity was about 14,500 feet/second.

The second aspect is of equal or greater interest to those who may wish to consider the use of some of the DREV probe measurements of charge density. With one exception, there is not presented in the reporting of this program equivalent evidence of the reproducibility of the chemistry in the wakes of hypersonic projectiles flown in the DREV ranges. The reproducibility of the wake chemistry is a measure of the control of the constituents of the range atmosphere (including water vapour) and of the cleanliness of this atmosphere. For the present program, the mass density, temperature and velocity measurements are believed to be insensitive to any variations in the atmospheric composition normally encountered in the ranges. However, this may not be true in the case of the levels of charged particle density in the wake.

UNCLASSIFIED

2

2.0 INTERFEROMETER EQUIPMENT

In a microwave interferometer, a common microwave source is used to feed two distinct microwave channels or arms, a 'reference' arm and a 'transmission' arm, in such a way that the phase difference between the signal at the output of the transmission arm and the signal at the output of the reference arm can be compared (Figure 1). In the absence of any dissimilarity in the dielectric media in the two arms, this difference in phase depends only on the difference in the number of wavelengths between the lengths of the two arms. Now, if in addition, a medium of different dielectric constant is inserted somewhere in the transmission arm, an additional shift in the phase difference between the two arms will be detected. The microwave interferometer works on this principle (Reference 6). Normally, in the operation of an interferometer, the difference in phase due to path length difference between the two arms is adjusted to some desired value before a measurement. During the measurement, the behavior of additional phase shift resulting from the introduction of some perturbation in the transmission arm is detected and recorded as a function of time. In the case where the perturbation is due to an ionized plasma, it is possible to utilize the observed phase shift to infer the charge density levels in the plasma, provided these fall within certain limits.

Figure 2 is a schematic representation of the dual channel interferometer system installed on Range 5. The microwave transmitter source is operated in the X_s-band at 9.60 GHz ($\lambda = 3.1227$ cm). The choice of frequency was dictated by the desire to have sensitivity to electron densities in the range from 10^{11} to 10^9 electrons/centimeter³ while retaining as much resolution as possible. The transmitter source is a Varian V-58 0.5 watt reflex klystron, with phase-lock frequency stabilization provided by a Microwave Specialities MOS-1 Stabilizer operating through the reflector circuit and the Hewlett Packard Model 416 B power supply unit. A high-directivity (-40 db) top-wall coupler is used to divide the transmission path from the reference path; the two arms are then directed their separate ways. The reference arm is led underneath the range tank. The transmission arm is divided into two channels; these are oriented so as to provide for illumination via conical antennae of the region in the center of the range, approximately 3/4 inch above and below the centerline. Before the division of the main transmission arm into two channels, a Hewlett Packard 8735 A PIN modulator with large dynamic range is inserted into the transmission channel. The transmitted signal is normally gated off with this modulator for short periods during a recording to provide a continuous absolute determination of the dc baseline level (Reference 7).

The projectile is launched along the range centerline and the ionized wake behind the projectile fills the region illuminated by the transmitter horns and scanned by the receiver horns. A double lens focussing system (Figure 3) is interposed between the transmitting and receiving antennae to increase the resolution of the system. With this lens system, one obtains a beam width of approximately 2 inches or 0.74 of the diameter of a 2.7 inch diameter sphere based on the -3 db contours of

the channel beam (Figure 4). The depth of field over which the beam remains at constant width (to within + 10%) is about 12 inches or about 5 diameters (Reference 8). Based on the schlieren wake width, this appears to be adequate for measurements on 2.7 inch diameter sphere wakes to at least 400 diameters behind the projectile.

The microwave energy beams transmitted across the lens system are directed through the receiver antennae and onto the entry ports of various hybrid mixers. A sample of reference signal power is directed to the other entry port of each mixer. The reference signal power level is roughly 100 times the transmitted arm signal level. The mixed reference and transmitted signals are impressed on MA-611 low noise crystal detectors incorporating IN-23G crystals. The crystals are driven into the middle of their linear response regions by the large reference signal levels. The crystals operate into low noise 10 kilohm video loads. These video loads comprise part of the input networks of Tektronix Type 'O' operational amplifier plug-ins; these units also permit subtraction of the large dc component due to the reference signal, before further amplification of 100 times.

The signals are recorded on polaroid films via the intermittency of Tektronix Type 555 and 550 oscilloscopes. The signals represent nominally $\text{SIN}\Delta\phi$ or $\text{COS}\Delta\phi$ where $\Delta\phi(t)$ is the phase shift induced by the presence of the ionized wake in the transmission arm. Sweep speeds and sensitivities are supplied in various combinations to permit an optimum recording of the signals (Table I).

This section is only intended to present an outline of the functioning of the interferometer system. Further details are given in a report dealing specifically with the actual equipment (Reference 7).

3.0 ANALYSIS

3.1 Determination of Transmission Arm Phase Shifts

As indicated previously, the detector crystals are biased by means of the reference signal to the appropriate current level for operation as linear detectors. Under these conditions, the detector current is proportional to the field strength in the guide.

$$\wedge I_d \sim K_d \Delta V_q$$

The voltage at the output of the hybrid mixer and incident upon the detector consists of the vector sum of the reference arm signal and the transmission arm signal

$$\vec{V} = \vec{V}_r + \vec{V}_s$$

UNCLASSIFIED

4

In operation, the reference signal \vec{V}_r , is made at least 1 order of magnitude greater than the transmission arm signal \vec{V}_s . The situation is represented in Figure 5.

Let A represent $|\vec{V}_s|$ and B represent $|\vec{V}_r|$ and let ϕ be the phase angle between \vec{V}_r and \vec{V}_s . Then the resultant field at the detector has the magnitude

$$\begin{aligned} |\vec{V}| &= ((B+A \cos\phi)^2 + (A \sin\phi)^2)^{\frac{1}{2}} \\ &\approx B + A \cos\phi. \end{aligned}$$

Suppose further, that in the absence of any plasma (or electrons) in the transmission arm, we align \vec{V}_r and \vec{V}_s so that $\phi_0 = 0$. Then let the phase shift due to the introduction of a plasma in the transmission arm be

$$\begin{aligned} |\vec{V}|_{\Delta\phi} &= B + A \cos\Delta\phi \\ |\vec{V}|_{\phi_0=0} &= B + A_0. \end{aligned} \quad (\text{COSINE})$$

In the last equation we have distinguished between the amplitude A_0 of the reference arm signal \vec{V}_s in the absence of a plasma ($\Delta\phi=0$) and the amplitude A in the presence of plasma and phase shift (non-zero $\Delta\phi$). (At high electron density levels and high pressures the signal transmitted across the plasma may undergo attenuation as well as phase shift so that $A \leq A_0$. However, for the conditions encountered in the present experiment, $A = A_0$).

The difference in voltage due to the addition of the phase shift is consequently

$$\Delta|\vec{V}|_{\Delta\phi_c} = A \cos\Delta\phi - A_0 \quad (\text{COSINE})$$

and the change in diode current

$$\Delta I_{d\Delta\phi_c} = K_d (A \cos\Delta\phi - A_0). \quad (\text{COSINE})$$

For low pressure weakly ionized plasmas such as encountered in the present work, $A = A_0$ and

$$\Delta I_{d\Delta\phi_c} = K_d A_0 (\cos\Delta\phi - 1) \quad (\text{COSINE})$$

We shall refer to this particular type of detection as COSINE detection (Figure 6a).

If instead of choosing $\phi = 0$ we had chosen $\phi_0 = \frac{\pi}{2}$ we would have had

$$\begin{aligned} |\vec{V}|_{\Delta\phi} &= B + A \cos(\frac{\pi}{2} + \Delta\phi) \\ |\vec{V}|_{\phi_0=\frac{\pi}{2}} &= B \end{aligned} \quad (\text{SINE})$$

and

$$\Delta|\vec{V}|_{\Delta\phi_s} = -A \sin\Delta\phi \quad (\text{SINE})$$

and

$$\Delta I_{d\Delta\phi_s} = -K_d A \sin\Delta\phi \quad (\text{SINE})$$

For low pressure weakly ionized plasmas, we replace A by A_o

$$\Delta I_{d\Delta\phi_s} = -K_d A_o \sin\Delta\phi \quad (\text{SINE})$$

which will be referred to as SINE detection (Figure 6b).

An important point becomes obvious by comparing the small phase shift case for the two types of detection:

$$\text{COSINE: } \Delta I_{d\Delta\phi_c} = -K_d A_o \frac{\Delta\phi^2}{2}$$

$$\text{SINE: } \Delta I_{d\Delta\phi_s} = -K_d A_o \Delta\phi.$$

Obviously for small phase shift it is better to operate with SINE detection.

(It should be obvious that the negative signs here can easily be altered to plus signs by the introduction of 180 degree phase changes and are not important to this discussion).

For situations where high electron density levels are encountered or where attenuation as well as phase shift occur in the transmission arm, both SINE and COSINE detection are required. Each detector arm is so arranged as to incorporate both types of detection simultaneously so that we have for the i^{th} channel

$$\Delta I(i)_{d\Delta\phi_c} = K_d(i,c) A(i) \cos\Delta\phi(i) - K_d(i,c) A_o(i)$$

$$\Delta I(i)_{d\Delta\phi_s} = K_d(i,s) A(i) \sin\Delta\phi(i),$$

where i refers to channel 1 or channel 2.

The two measurements ($i = 1, 2$) enable us to solve for the two unknowns $A(i)$ and $\Delta\phi(i)$.

In the method of recording on the DREV Range 5 interferometer, the signals are recorded from oscilloscopes using Polaroid cameras. The deflection sensitivities of the oscilloscopes are established prior to the firing by chopping the energy in the transmission arm and calibrating the sensitivity setting in terms of the amplitude A_0 of the electric field in the transmission arm in the absence of any plasma. The calibration is done in the COSINE arms after ensuring $\phi_0 = 0$ and in the SINE arms by removing $\frac{\pi}{2}$ radians from the value of $\phi_0 = \frac{\pi}{2}$ in these arms during the calibration period. Essentially the oscilloscopes are adjusted so that a deflection on the oscilloscope screen of 5, 10, 20 or 40 centimeters represents the amplitude A_0 . The procedure is fully described in Reference 7.

3.2 Characteristics of Wake Electron Density Distribution

According to analyses which may be found in standard texts (Reference 6), the phase shift, arising along the path of a plane wave when an electron density function $n(x)$ is introduced instead of free space, is given by

$$\begin{aligned}\Delta\phi &= \int_{\text{path}} \left(1 - \left(1 - \frac{n(x)}{n_c}\right)^{\frac{1}{2}}\right) \frac{2\pi}{\lambda} dx \\ &\approx \frac{\pi}{\lambda} \frac{1}{n_c} \int n(x) dx,\end{aligned}$$

provided that $\frac{n(x)}{n_c}$ is always less than unity. The so-called critical electron density n_c , is given by

$$n_c = \frac{\epsilon_0 m \omega^2}{e^2}$$

where x is the distance along the path of the beam
 ω is the microwave angular frequency
 ϵ_0 is the permittivity of free space
 m is the electron mass
 e is the electron charge

Substituting

$$\begin{aligned}\Delta\phi &= \frac{e^2}{2\epsilon_0 mc\omega} \int_{\text{path}} n(x) dx \\ &= \frac{1}{\omega} \frac{2\pi}{118.4} \int_{\text{path}} n(x) dx\end{aligned}$$

where x is measured in centimeters and $n(x)$ in centimeter⁻³.

For purposes of estimating electron density in the more or less cylindrical wake, we are interested in assuming that the appropriate distribution is gaussian. In cylindrical coordinates

$$n(r) = n_0 e^{-r^2/R^2}, \quad 0 \leq r < \infty.$$

Then, assuming a microwave beam passes through this distribution at a distance y from the center (Figure 7), we have

$$n(x) = n_0 e^{-y^2/R^2} e^{-x^2/R^2}$$

and

$$\int n(x) dx = \sqrt{\pi} n_0 R e^{-y^2/R^2}.$$

Suppose now that we have two focussed microwave beams looking at a cylindrical plasma (as is the case with the DREV Range 5 interferometer system) and also that the plasma has a gaussian distribution of electron charge $n(r) = n_0 e^{-r^2/R^2}$. Then if one beam traverses the cylinder at an offset distance from the axis of y_1 and the second beam traverses at an offset distance y_2 , then the two phase shifts occurring in the beams will be respectively

$$\Delta\phi_1 = K \sqrt{\pi} n_0 R e^{-y_1^2/R^2}$$

$$\text{and } \Delta\phi_2 = K \sqrt{\pi} n_0 R e^{-y_2^2/R^2},$$

$$\text{where } K = \frac{1}{\omega} \frac{2\pi}{118.4}.$$

The two parameters of the gaussian distribution of electron density n_0 and R , may be determined by solving these two equations in terms of the measured phase changes $\Delta\phi_1$ and $\Delta\phi_2$ and the known offset distances y_1 and y_2 .

Consequently

$$R^2 = (y_2^2 - y_1^2) \log_e (\Delta\phi_1 / \Delta\phi_2)$$

determines R , and subsequently

$$n_0 = \frac{\Delta\phi_j}{KR \sqrt{\pi}} e^{-y_j^2/R^2}$$

for $j = 1$ or 2 .

UNCLASSIFIED

8

Insofar as a gaussian distribution is appropriate for describing the electron density in the wake, a two-channel interferometer thus offers the possibility of determining the amplitude on the wake axis, n_0 , as well as the radius R, at the 1/e height of the distribution.

4.0 PRESENTATION OF THE RESULTS

4.1 Interferometer Firing Report

An example of a firing report for the interferometer equipment on a typical round in Range 5 is shown in Figure 9. There is one possible source of confusion in the firing report, but the explanation is rather simple. At the walls of the range, the geometrically uppermost waveguide and antenna horns carry Channel 1 (CH1), while the lower ones carry Channel 2 (CH2). In the center of the range at the location where the projectile wakes are formed, Channel 1 is now the lowermost beam, while Channel 2 is the upper beam, because of the action of the microwave lens system. Thus when the position of the projectile is high (as in Figure 8), the distance from the wake axis to the upper beam (CH2) is less than the distance to the lower beam (CH1).

4.2 Interferometer $\text{SIN}\phi$ Displays

Figure 9 shows polaroid recordings of the signals detected on Channel 1 and 2 of the interferometer on a typical observation of the wake of a 2.7 inch diameter sphere flown at 14,600 feet/second in an air atmosphere at 10 torr. Since the phase shifts along the path of the microwave beams were relatively small on these measurements, only the $\text{SIN}\Delta\phi$ or $\text{SIN}\phi$ (for short) displays were recorded. As previously described in Table I, various combinations of sensitivity and sweep speed were employed. The 5 centimeter, 0.2 millisecond/centimeter recording was used to capture the beginning of the signal. The 10 centimeter and 20 centimeter, 0.5 millisecond/centimeter recordings captured most of the remaining portion of the signal, while the 20 centimeter, 1 millisecond/centimeter recording captured the rest. Observations were thus possible to about 600 diameters of axial distance, although the separation of the horns and the growth of the wake were such that the technique of solving for the amplitude and width of the assumed electron density distribution could not give equally good results over the whole range of axial distance.

The firing report and $\text{SIN}\phi$ displays obtained from observations on a small number of 2.7 inch diameter spheres flown in air and nitrogen atmospheres are given in 'ppendix A.

4.3 Data Reduction

The signals recorded on the polaroids were digitized by superposing a rectangular grid (minimum dimension of one mm) over the polaroids and by reading the amplitude of the signals to be nearest possible decimal

of a millimeter. The periods in the signal during which the beams were gated off by the PIN modulator provided an absolute zero reference level against which both the nominal zero signal level (before the passage of the projectile) and the actual signal amplitude could be measured. The two channels were read in synchronization with the aid of the gating markers. The amplitudes were corrected for the reduction factor of 0.9 of the Polaroid cameras, and the phase shifts were calculated from the arc SIN functions. These phase shifts were then corrected to obtain the true phase shift by adding or subtracting, as required, the phase shift corresponding to any finite difference between the nominal zero signal level and the absolute reference level determined by gating off the beams.

The procedures were programed for the digital computer. The tables of data representing the digitized amplitudes of the simultaneous signals on both interferometer channels were read into the computer, along with constants representing the maximum possible signal amplitude, the sweep speed, the zero level corrections, the point in time corresponding to the beginning of the signal, the position of the beams with respect to the wake axis, and the speed of the projectile. The computer consequently calculated values of the wake electron density radius R and the amplitude n_0 of electron density on the wake axis as a function of X/D , the axial distance behind the projectile. This was done for the digitized data on each of the polaroids that were selected for analysis. Subsequently the results were plotted by the data plotter.

The electron density on the wake axis, n_0 , thus obtained is shown for a typical round in Figure 10a. Here the circles are from the 5 centimeter, 0.2 millisecond/centimeter polaroid, the diamonds from the 20 centimeter, 0.5 millisecond/centimeter polaroid, and the small squares from the 20 centimeter, 1 millisecond/centimeter recording. The results obtained from the same information recorded at different gains do not coincide, as one would expect.

In order to compare data obtained from several rounds, the mean curve shown in Figure 10b was estimated from the data points in Figure 10a. In this way the results of several rounds could be compared side by side.

The radius of the electron density distribution corresponding to Figure 10 is shown in Figure 11. Figure 11a shows the actual data points from the various polaroids. Examination of the equation defining R^2 from the known position of the beams and the relative phase shifts detected in the two channels shows that the equation is very nonlinear. When y_2 is not greatly different from y_1 , the phase shifts $\Delta\phi_1$ and $\Delta\phi_2$ tend to become equal at some axial distance behind the projectile. Fluctuations in one or both of these quantities can cause the formula to indicate a negative numerical value for R^2 . When this happens, the solution is rejected and the computer proceeds to the next pair of points. However, fluctuations in the opposite sense are accepted. Thus when attempting to define a mean curve (Figure 11b) from the data points in Figure 11a, there is strong justification for ignoring large positive excursions of the estimated wake radius.

Appendix B contains Figures similar to Figures 10 and 11 corresponding to all the data shown in Appendix A.

5.0 RESULTS IN AIR ATMOSPHERES

5.1 'Dirty Rounds' and 'Clean Rounds'

A considerable amount of interferometer data was amassed on the firings in 10 torr air for the Langmuir probe experiment (Reference 9). Among the rounds considered suitable for analysis were the following: Rounds 50, 54, 55, 59, 60, 72, 91, 93, 94, 95, 97, 98, 99 and 100. The criterion of this selection was based firstly on the availability of the polaroid recordings of the signals and secondly on the smoothly decaying behavior exhibited by the signals. Additional information on the quality of the data was available from the signals recorded with the X_S-band scattering experiment. Of the above fourteen rounds it was suspected that Round 50 was very slightly dirty while Rounds 94, 95 and 99 were considered to be slightly dirty. The adjective 'dirty' is a colloquial term which implies that there seems to be an excess of signal beyond the amplitude of the signals normally observed, and that there are possibly fluctuations or bumps superposed on the generally smooth decay of the signal amplitude observed with the interferometer as the axial distance behind the projectile increases. Of course abnormally large signals imply an excess of ionization, and this is usually attributed to dirt or impurities in the range atmosphere. A dirty range atmosphere is often blamed for what has come to be called a 'dirty round', although similar effects are observed if the projectile is damaged or accompanied down the range by broken and ablating pieces of the plastic sabot. The opposite of a 'dirty round' is a 'clean round'

On all the Langmuir probe rounds described above, the range was pumped for about four to five hours down to a pressure of from 50 to 80 microns. Then dry bottled nitrogen was introduced to bring the pressure up to 0.3 torr for the operation of scrubbing the probes. When scrubbing was completed, the range pressure was raised quickly to 10 torr by adding dry bottled air, and the round was fired. Since the flight tank of Range 5 is usually coated with a film or a deposit of material composed of sabot debris, projectile debris, bumper plate debris and fiberglass, the dry bottled gases were introduced into the range through a diffuser system which employed vacuum cleaner bags (Figure 12). The bags containing the diffuser system were frequently cleaned. This system worked well provided the bags were not exploded when the gases were introduced into the range. Unfortunately it took a considerable number of rounds before it was discovered that 'dirty rounds' were correlated with burst diffuser bags, and limitations were imposed on the speed with which bottled gas could be introduced into the range.

5.2 Electron Density on the Wake Axis and Electron Wake Radii for Air Atmospheres by Simultaneous Solutions

The results obtained by solving the equations outlined in Section 3.2 for the two parameters of the assumed gaussian distribution of electron density, the amplitude on the axis n_0 and the radius R, are available in Appendix B for most of the rounds listed in the previous section.

In two cases, Rounds 59 and 100, the projectile passed almost exactly between the two microwave beams, one channel of information was consequently redundant, and the equations could not be solved.

The various results are represented by the mean curves shown for the electron density in Figure 13a and for the radius in Figure 13b. In the case of the electron density on the wake axis, the spread on the data is of the order of a factor of five if one includes Round 50 and about a factor of four if Round 50 is excluded. The rather large spread observed on the electron density radius (Figure 13b), is disappointing but perhaps understandable, given the sensitivity of R^2 to variations in the ratio of the phase shifts in the two interferometer channels.

Nevertheless, these results did lead to a further improvement in our ability to rate or evaluate the quality of the various rounds. Since the electron density for Rounds 59 and 100 could not be computed in the normal fashion by the equations in Section 3.2, it was decided to prescribe the radius in the case of these two rounds and to compute the electron density on the wake axis for this given radius.

5.3 Electron Density on the Axis in Air Wakes deduced with a Prescribed Electron Wake Radius

As described at the end of the previous section, because of the indeterminacy of the general equations for n_0 and R/D in the case of two rounds, it was decided to compute the electron density with a prescribed radius.

The prescribed radius was taken as

$$r_n/D = 0.5 + 0.25 \log_{10}(X/D)$$

which fits the data in Figure 13b for Rounds 95, 97, 98 and 99 and seems to represent a reasonable average. This equation probably does not represent the actual wake radius at axial distances greater than about 200-300 diameters (Reference 10), so some caution should be exercised in any employment of the electron density data derived by using 'c.

With the use of a prescribed electron density radius and the assumptions of a gaussian electron density distribution, the data of both channels of the interferometer will give independent estimates of the electron density on the axis of the wake. Figure 14 presents prescribed radius electron density estimates for Channel 1 and 2 for the data presented in Figures 8-9. The new estimates are considerably smoother than those presented earlier in Figure 10a, and it is now easier to obtain a mean curve approximating the results.

The prescribed radius technique has been applied separately to the Channel 1 and 2 signals obtained on all the firings at 10 torr in air for the Langmuir probe experiment in order to obtain estimates of the electron density behavior on the wake axis. These estimates are given in Appendix C. The mean curves are plotted in Figure 15 for the apparently 'clean rounds' and in Figure 16 for the 'dirty rounds'.

The 'clean rounds' shown plotted in Figure 15 (Channel 1 results in Figure 15a and Channel 2 results in Figure 15b) comprise data from Rounds 54, 55, 59, 91, 93, 97, 98 and 100. (Round 100 does have a small anomaly which suggests a tiny fragment). If the mean prescribed radius electron density n_0 curves are compared, the overall spread is less than a factor of 2 (Figure 15). This proves beyond question that it is possible to obtain reproducible electron density measurements on Range 5.

Figure 16 plots the mean electron density data from the remaining Rounds, 50, 60, 72, 94, 95 and 99 which are now collectively classified as being 'slightly dirty', along with the data of Round 97, shown for comparison. Generally, the electron density for the slightly dirty rounds tends to decay away more slowly, such as in Rounds 95 and 99. Rounds 60 and 94 display rather prominent bumps in their electron density decay curves. Prior to the obtaining of the data in Figures 15 and 16, Round 60 had been considered as a clean round.

The data for the Langmuir rounds are also compared in Table II. Here the results obtained on Rounds 97 and 98 have been used as a standard. The percentage by which the ionization levels obtained on other rounds are greater or less than those observed with the standard rounds are tabulated in these cases where the levels were shifted by a constant factor. Otherwise a remark is given to explain any peculiarities which may have been present.

It is worth pointing out that even in the calculation of the electron density on the wake axis using a prescribed electron density radius, it is still assumed that the electron density distribution in the wake is gaussian. From Figure 15 and Table II, it is evident that with this assumption it has been possible to collapse data from several rounds into a fairly narrow band.

5.4 Interferometer Signals with Clean and Dirty Rounds

Reproductions of the polaroid recording of the interferometer signals on various rounds have been grouped together on the basis of the classification into the clean and dirty categories given in Table II. The results are shown in Figure 17. To aid in comparing various signals, the distance of the microwave beams from the wake axis are listed in Table III for most of the rounds.

Figures 17a and 17b show the interferometer signals for a number of clean rounds in 10 torr air atmospheres. An attempt has been made to give an example of the signals recorded at a sweep of 0.5 millisecond/centimeter and a maximum amplitude of 10 centimeters and 2' centimeters in each case. In the case of Rounds 59 and 91, one of the records was missing in each case, so the results were grouped together. In general, the interferometer signals from clean rounds are characterized by a smooth monotonically decaying behavior.

Figure 17c compares rounds which are slightly dirty. Round 72 was only very slightly dirty, exhibiting a level of ionization 25% above normal (Table III); the high gain signal shows a slightly higher level of fluctuation than in the case of Rounds 97 and 98. Rounds 94 and 95 were slightly dirty and show considerably larger fluctuations and somewhat higher signal levels than Round 72. The location of the beams with respect to the wake axis was very similar in the case of Rounds 72 and 95 (Table III).

Figure 17d gives an indication of the range of variation that can be expected in the behavior of the interferometer signals. Round 92 could be classified as being 'very dirty' or even 'filthy dirty' depending mainly on one's sentiments. Round 94 exhibits about twice the signal level exhibited by the clean rounds in Figures 17a and 17b. This can be seen by comparing Round 94 with Round 100. Round 100 exhibits about the same ionization levels as the standard clean rounds (Rounds 97 and 98), but is here recorded at twice the gain employed to record Round 94. The recordings from Round 100 are shown at these high gains to emphasize the little spike on the signal in Channel 2 at about 1.3 milliseconds after the passage of the projectile. This is probably the effect of a small fragment following in the wake of the projectile. As indicated in Figure 15b and Table III, it has not really affected the mean level of ionization in the wake on this particular round.

6.0 RESULTS IN NITROGEN ATMOSPHERES

6.1 Electron Density on the Wake Axis and Electron Wake Radii for Nitrogen Atmospheres by Simultaneous Solutions

Results similar to those shown in Figure 13 for the case of spheres flown in 10 torr air have been obtained by exploiting the equations in Section 3.2 to simultaneously predict the electron density on the wake axis and the wake radius of the electron density distribution for firings in nitrogen atmospheres. Unfortunately in only a minority of these rounds was the operation of the equipment 'au point'; insufficient isolation between the reference and the transmission arms caused a shifting in the signal reference levels during the measurement period and consequently the number of rounds suitable for analysis was small. The firing reports and polaroid recordings for nitrogen rounds are given in Appendix D, while the results for the two parameters of the assumed gaussian distribution of electron density in the wake are available in Appendix E.

The mean curves passed through the electron density results and the wake radii estimates are collected together in Figure 18 for the rounds in nitrogen at 7.6 torr and in Figure 19 for the rounds in nitrogen at 20 torr.

The electron density curves at 7.6 torr follow each other closely (Figure 18a). In the case of the electron density radius, the result of Round 65 seems anomalously large. On the other hand the electron density curves at 20 torr do not group very well, but the electron density radii are well clustered.

6.2 Electron Density on the Axis in Nitrogen Wakes deduced with a Prescribed Wake Radius

Calculations were also made of the electron density on the wake axis by prescribing a wake radius

$$r_n/D = 0.5 + 0.25 \log_{10} (X/D)$$

and using the measured phase shift in each channel to make independent estimates. These results are given in Appendix F.

Figure 20 shows data for five firings in nitrogen at 7.6 torr, Rounds 62, 65, 66, 68 and 75. The data for these rounds cluster within a factor of two, except for the result of Channel 1 in Round 66, which diverges from the others at axial distances greater than 60 or 70 diameters. Table IV gives a comparison of the data at 7.6 torr in nitrogen similar to that in Table II. (Table V tabulates the location of the beams with respect to the wake axis for these rounds). With the possible exception of Round 66, the results in Figure 20 and Table IV indicate that the listed rounds can be considered as clean. Figure 22 presents interferometer signals for clean rounds in nitrogen at 7.6 torr similar to the presentation of Figure 17.

Unfortunately, the ionization data for sphere firings in nitrogen at 20 torr indicate that Round 69 was dirty. The interferometer signals from Rounds 67, 69 and 71 for firings in nitrogen at 20 torr are shown in Figure 23.

Finally, calculations of the electron density level on the wake axis obtained using the prescribed radius are shown in Figure 24 for a solitary sphere launching in nitrogen at 1.5 torr.

7.0 WAKE RADII

7.1 Wake Radii in Nitrogen Wakes

The wake electron radii estimated from the dual channel microwave interferometer technique via the analysis in Section 3.2 are of considerable interest, particularly in the case of the results at 7.6 torr and 20 torr in nitrogen. For these two pressures Sévigny, Heckman and Caron (Reference 10) have estimated the radii for the ion density distributions in the wake.

Figure 25 shows the mean wake radius deduced for sphere wakes in nitrogen at 7.6 torr obtained by averaging over the data of Rounds 65, 66, 68 and 75. Similar data is shown in Figure 26 for sphere firings at 20 torr, obtained from the data of Rounds 67, 69 and 71. The data at 7.6 and 20 torr follow each other until $X/D = 100$, after which the wake radius at the lower pressure seems to grow more quickly. This apparent result is felt to be mainly the result of a limited amount of data. A reminder of the nonlinearity of the expression used to deduce the wake radius is also in order.

7.2 Average Wake Radius

An examination was made of all the data contained in Appendices B and E to discover those rounds where the wake radius parameter exhibited little scatter and consequently, was well defined. Rounds 72, 95 and 99 were among the rounds at 10 torr air where little scatter was evident. In nitrogen, Rounds 74, 66 and 69 also exhibited little scatter. The curious fact is that except for Round 74, all these rounds were classified as slightly dirty. Of course Round 74, obtained in nitrogen at 1.5 torr, was flown at laminar conditions, so that the wake radius should have been well defined on this round.

Figure 27 shows the mean electron wake radii defined by averaging over the result of Rounds 66, 68, 72, 74 and 75. In view of the nonlinearity of the equation defining the wake radius (Section 3.2), an investigation was made to determine the effect on the mean electron wake radius of discarding individual data points corresponding to wake radii estimates exceeding predetermined values. Over the region where data were obtained, the results were not changed much if data corresponding to values exceeding 3 diameters were excluded (Figure 28).

One final point concerns the prescribed wake radius

$$\tau_n/D = 0.5 + 0.25 \log_{10} (X/D)$$

used to analyze the interferometer data at several points during the foregoing analysis. Figure 27 indicates that the actual mean wake radius departs from this value, particularly at axial distance greater than

100 diameters. Accordingly, caution should be used in employing the data on the electron density on the axis in Figures 12, 20, 21 and 24 obtained by applying the above prescribed radius to the measured interferometer phase shifts. Undoubtedly, the use of a radius more closely approximating the data in Figure 27 would improve these estimates of electron density.

8.0 DISCUSSION

In order to make any ordered conclusions from the foregoing results, it is appropriate to return to the fundamental character of the measuring instrument. The interferometer makes an integrated measurement. With a dual channel version of this instrument, an attempt has been made to go a little further: By assuming the form of the electron distribution in the wake, the two measurements from the two channels have been used to derive the amplitude and width parameters of the distribution.

Using this technique, estimates are obtained of the behavior of the electron density on the wake axis which are spread by the order of a factor of four (Figure 13). This seems like quite a large spread. One can evaluate it qualitatively by comparison with the factor of two obtained when one restricts the data to clean rounds and specifies the radius of the electron density distributions (Figure 15). Since a factor of two in the reproducibility of electron density measurements is considered very good, one can argue that the factor of four achieved with the dual channel interferometer indicates that the technique gives an acceptable measurement of electron density behavior in the wake.

Support for the above view is available in the literature. Hayami and Primich (Reference 11) have reported on earlier attempts to obtain contour maps of the electron density distribution in the near wakes of ablating spheres by measuring the phase shifts across a fence of about six focussed interferometers and subsequently unfolding the distribution by inverting the Abel integral. According to these authors, "a problem with this inversion technique is that relative errors in the measured inputs of the multiple beams of the order of 10%, which would be considered excellent for an integrated electron density measurement from one beam, can generate regions of apparent negative electron densities and other anomalies in a contour plot". Apparently, it is not an easy task to derive information concerning the distribution of electron density in the wake from the integrated measurements of an interferometer.

No electron density data obtained by other laboratories at similar range conditions were found in the literature, and so no exact comparisons with the present data were possible beyond those previously published (Reference 7). The general decay behavior of the electron density with axial distance in the wake observed at 15,000 feet/second seems to follow that observed with different velocities elsewhere.

The electron density radius derived from the dual channel interferometer technique is subject to considerable scatter. The equation used to solve for the radius is nonlinear, so that it is not possible to obtain an unbiased wake radius by averaging the data.

The results obtained from the interferometer by specifying the radius of the electron density distribution and then using the measured phase shifts and the assumed gaussian distribution to determine an electron density on the wake axis are of considerable importance. In the first place it becomes possible to distinguish the clean rounds from the not-so-clean. In the second place these results show that it is possible to obtain reproducible electron density measurements under the normal operating conditions in the DREV Range 5.

9.0 CONCLUSIONS

The amplitudes and widths of the assumed gaussian distributions of electron density in the wakes of hypersonic spheres flown at 14,500 feet/second in atmospheres of air and nitrogen at various pressures have been derived from phase shift measurements with a dual channel interferometer operating at X_S-band. The data apply to the near wake extending from just behind the spherical projectile out to several hundreds of body diameters, and cover a band of electron number densities from $10^{11}/\text{centimeter}^3$ to less than $10^9/\text{centimeter}^3$. A conclusion of major importance is that it is possible to obtain reproducible electron density measurements under the normal operating conditions in the DREV Range 5. No data from other laboratories were found at sufficiently similar conditions to permit an exact comparison with the present results. However, the general trend of the data seems to follow that observed elsewhere.

REFERENCES

1. Lahaye, C., Léger, E.G., Dufresne, M., Doyle, H. and Boucher, P., "The Sequential Spark Technique: A Tool for Wake Velocity Studies in Ballistic Ranges", ICIASF'71, 71-C-33 AES, pp. 33-48, June 1971.
2. Ellington, D., Park, K.R. and Desjardins, P., "Hypersonic Wake Studies using Cooled-film Anemometer Techniques", ICIASF'71, 71-C-33 AES, pp. 45-59, June 1971.
3. Heckman, D., Emond, A., Fitchett, A. and Sévigny, L., "Mean and Fluctuating Charge Density Measurements in Turbulent Hypersonic Sphere Wakes", ICIASF'71, 71-C-33 AES, pp. 68-79, June 1971.
4. Dionne, J.G.G. and Tardif, L., "An Application of the Electron Beam Fluorescence Probe in Hyperballistic Range Wake Studies", ICIASF'71, 71-C-33 AES, pp. 80-86, June 1971.
5. Heckman, D., Tardif, L. and Lahaye, C., "Experimental Study of Turbulent Wakes in the CARDE Free-Flight Ranges", Proceedings of the Symposium on Turbulence of Fluids and Plasmas, Vol. 18, Polytechnic Press of the Polytechnic Institute of Brooklyn, N.Y., 1968.
6. Heald, M. And Wharton, C., "Plasma Diagnostics with Microwaves", John Wiley and Sons, 1965.
7. Gagne, N., Fitchett, A. and Heckman, D., " X_s -Band Microwave Interferometer for Study of Hypersonic Turbulent Wakes on Range 5", DREV Report R 660 (to be published).
8. Fitchett, A., "Resolution of the Microwave Lens System used in an X_s -Band Interferometer", DREV TN 1998/72 (Unclassified).
9. Heckman, D., Sévigny, L. and Emond, A., "Absolute Electron Density Measurements in Turbulent Hypersonic Sphere Wakes with Langmuir Probes", DREV Report (to be published) (Unclassified).
10. Sévigny, L., Heckman, D. and Caron, P., "Ion Density Measurements in the Wake of a Hypersonic Sphere", DREV Report R 670, (to be published) (Unclassified).
11. Hayami, R.A. and Primich, R.I., "Wake Electron Density Measurements behind Hypersonic Spheres and Cones", AGARD Conference Proceedings, CP 19, "Fluid Physics of Hypersonic Wakes", May 1967.

TABLE I
RECORDING PARAMETERS FOR INTERFEROMETER DATA

<u>Camera</u>	<u>Sweep</u> (ms/cm)	<u>90° Deflection</u>
1	0.2	5 cm
2	0.5	10 cm
3	0.5	20 cm
4	1.0	20 cm
* 5	0.5	40 cm

* Occasionally

TABLE II

COMPARISON FOR VARIOUS LANGMUIR PROBE ROUNDS OF THE LEVELS OF ELECTRON DENSITY ON THE WAKE AXIS AS CALCULATED WITH A PRESCRIBED RADIUS*

(Rounds 97 and 98 taken as standard)

A. Clean Rounds

Round	Channel 1 Estimate	Channel 2 Estimate	Remark
54	+ 10%	- 10%	
55	+ 20%	- 10%	
59	+ 0%	+ 0%	
91	+ 20%	+ 0%	
93	+ 5%	+ 15%	
97	+ 0%	+ 0%	
98	+ 0%	+ 0%	
100	+ 0%	+ 0%	(Tiny fragment present)

B. Dirty Rounds

Round	Channel 1 Estimate	Channel 2 Estimate	Remark
50	+ 35%	+ 40%	
60			Exhibits bump. Conclude round dirty
72	+ 25%	+ 25%	
94			Exhibits bump. Previously classified as dirty.
95			At small X/D, about same level as other rounds. However, ionization decays relatively slowly.
99			

* Radius defined by $r_n/D = 0.5 + 0.25 \log_{10} (X/D)$

TABLE IIIDISTANCE OF THE MICROWAVE BEAMS FROM THE WAKE AXIS
FOR VARIOUS ROUNDS AT 10 TORR AIR

Round	Channel 1 (in)	Channel 2 (in)	Difference (in)
50	1.0	0.6	0.4
54	1.7	0.1	1.6
55	2.2	0.6	1.6
59	0.8	0.8	0.0
60	1.5	0.2	1.3
72	1.4	0.2	1.2
91	1.9	0.3	1.6
93	0.4	1.3	0.9
94	0.5	1.1	0.6
95	2.0	0.4	1.6
97	0.9	0.7	0.2
98	1.1	0.5	0.6
99	1.9	0.3	1.6
100	0.8	0.8	0.0

UNCLASSIFIED

22

TABLE IV

COMPARISON FOR VARIOUS SPHERE FIRINGS IN NITROGEN AT 7.6 TORR
OF THE LEVEL OF ELECTRON DENSITY ON THE WAKE AXIS
AS CALCULATED WITH A PRESCRIBED RADIUS*

(Round 62 taken as standard)

Round	Channel 1 Estimate	Channel 2 Estimate	Remark
62	0	0	
65	0	+ 25%	
66	0**	- 5%	** 0% only until 70 diameters
68	0	- 15%	
75	+ 20%	- 15%	

* Radius defined by $r_n/D = 0.5 + 0.25 \log_{10} (X/D)$

TABLE V

DISTANCE OF THE MICROWAVE BEAMS FROM THE WAKE AXIS
FOR VARIOUS ROUNDS AT 7.6 TORR NITROGEN

Round	Channel 1 (in)	Channel 2 (in)	Difference (in)
62	0.9	1.1	0.2
65	0.0	1.6	1.6
66	3.2	1.6	1.6
68	1.6	0.0	1.6
75	2.1	0.5	1.6

UNCLASSIFIED

23

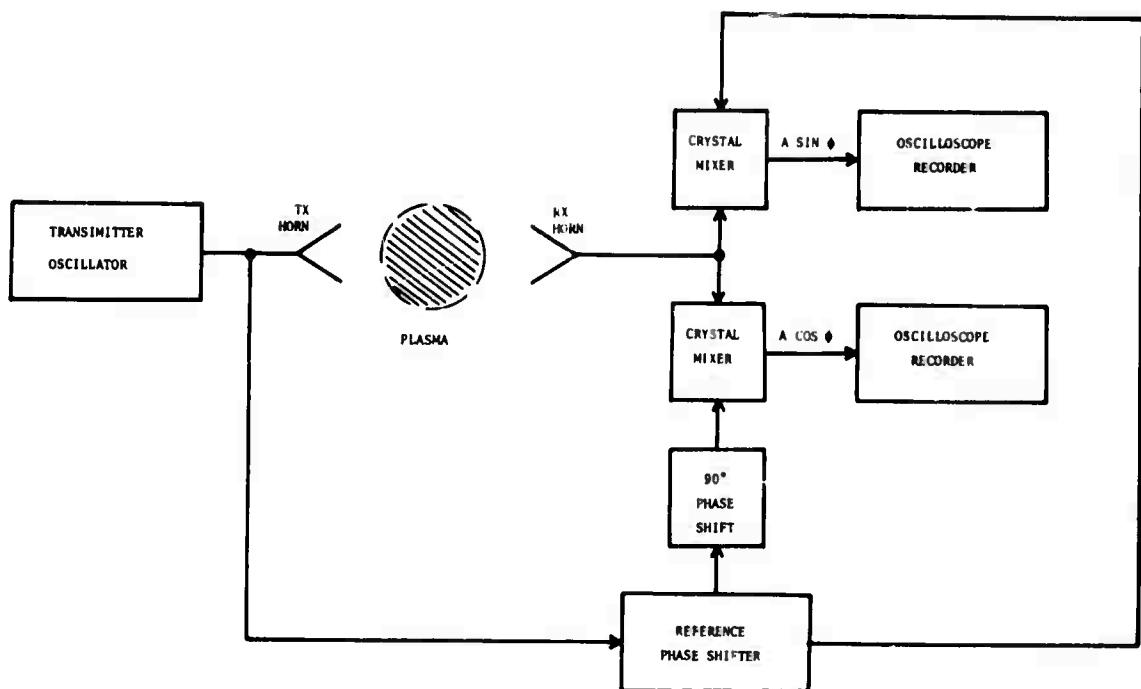


FIGURE 1 - Block diagram of microwave interferometer

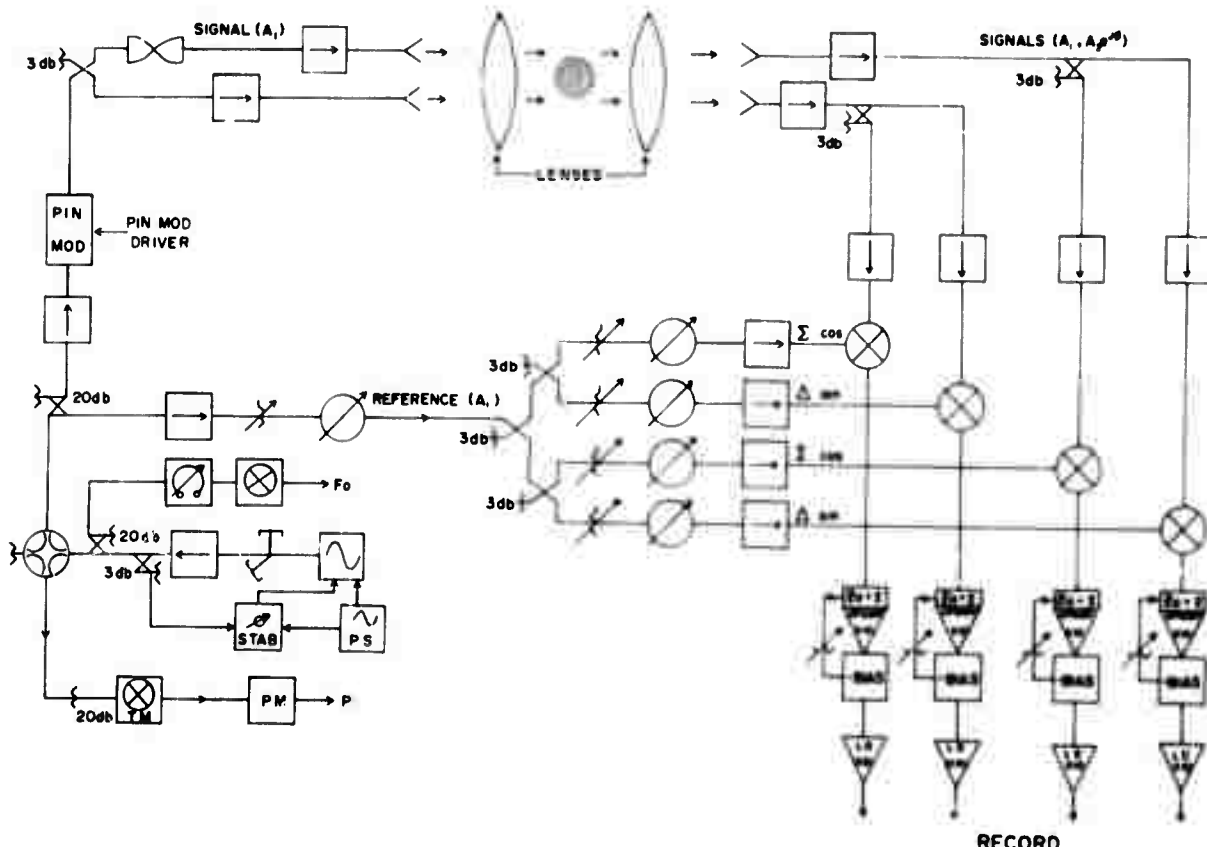


FIGURE 2 - Circuit diagram of dual channel SINE-COSINE X-band
interferometer on Range 5

UNCLASSIFIED

24

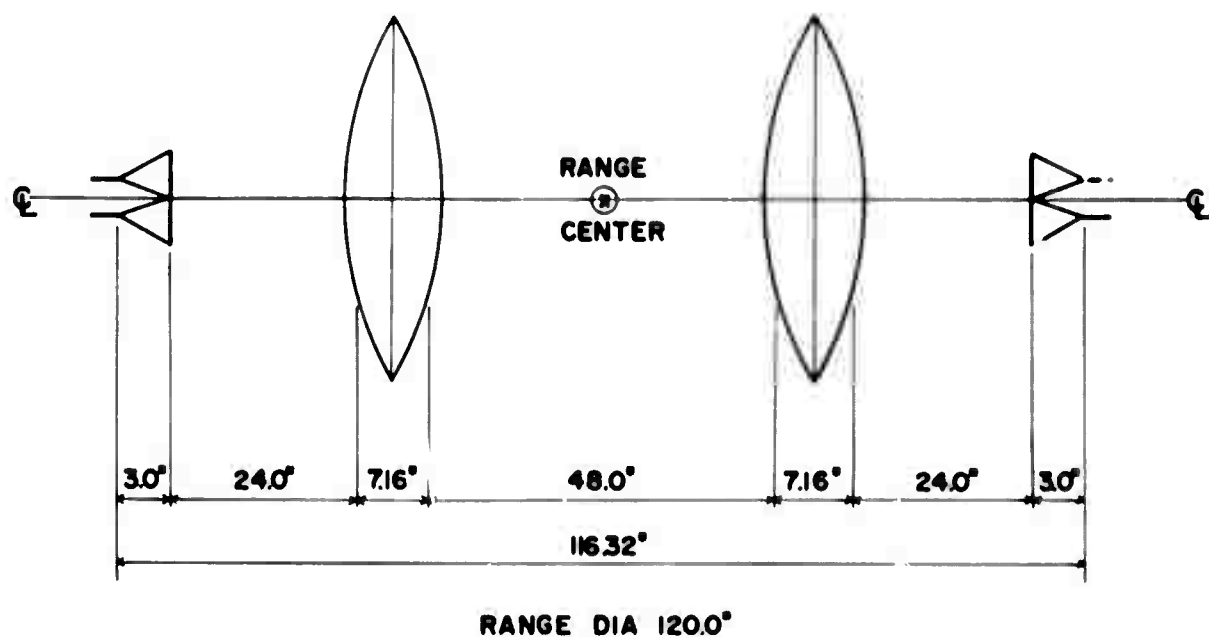


FIGURE 3 - Double focussing lens system for Range 5 interferometer

(a) Schematic layout of interferometer station

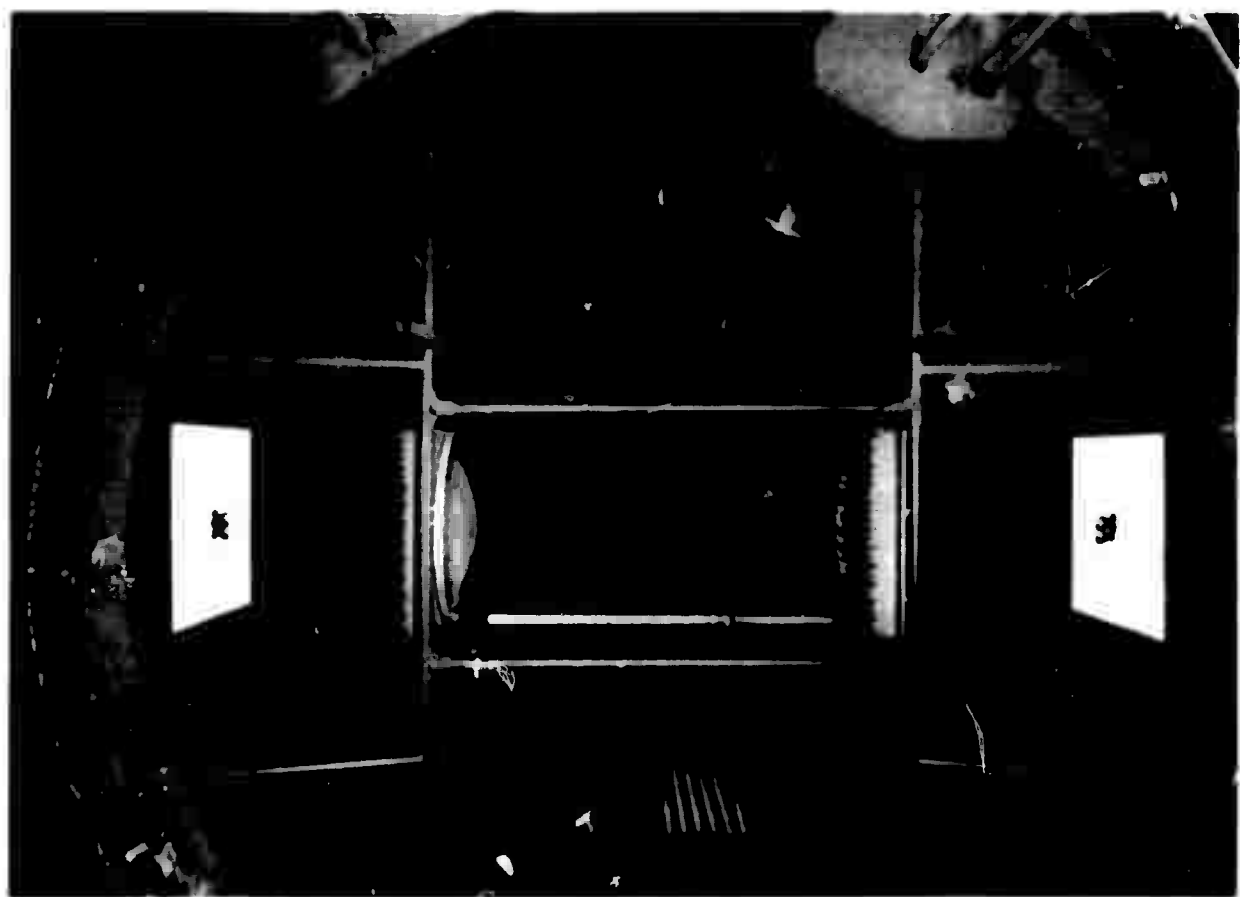


FIGURE 3 (b) - Actual station

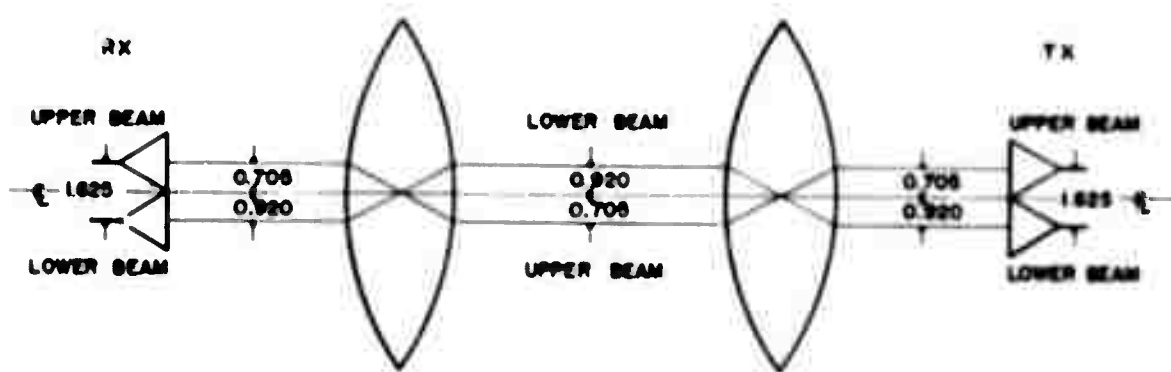


FIGURE 3 (c) - Illustration of effect of lens system on position of beams

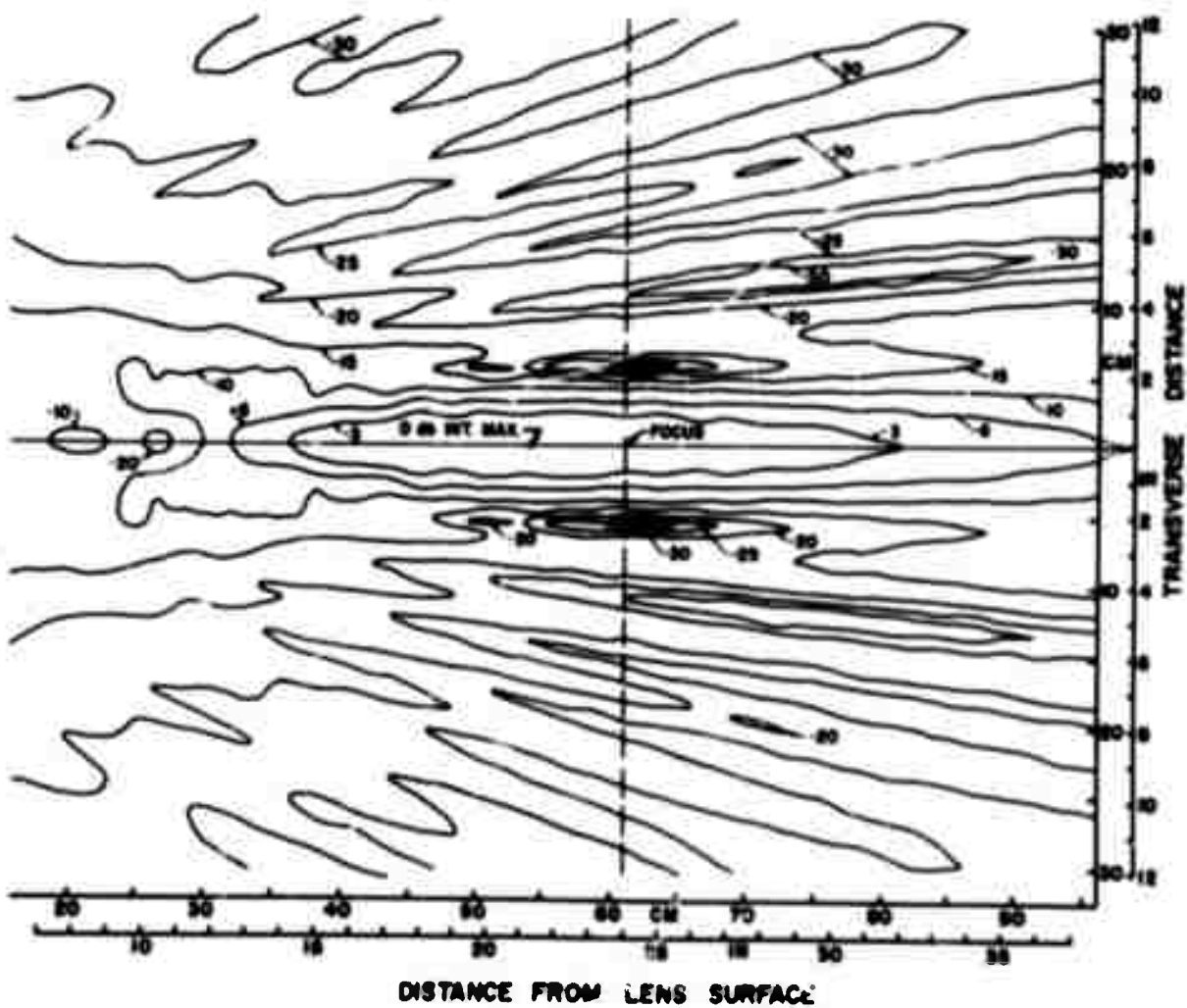


FIGURE 4 - Intensity distributions in the center of lens system
(Reference 8)

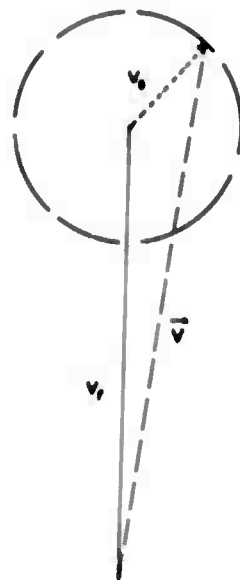
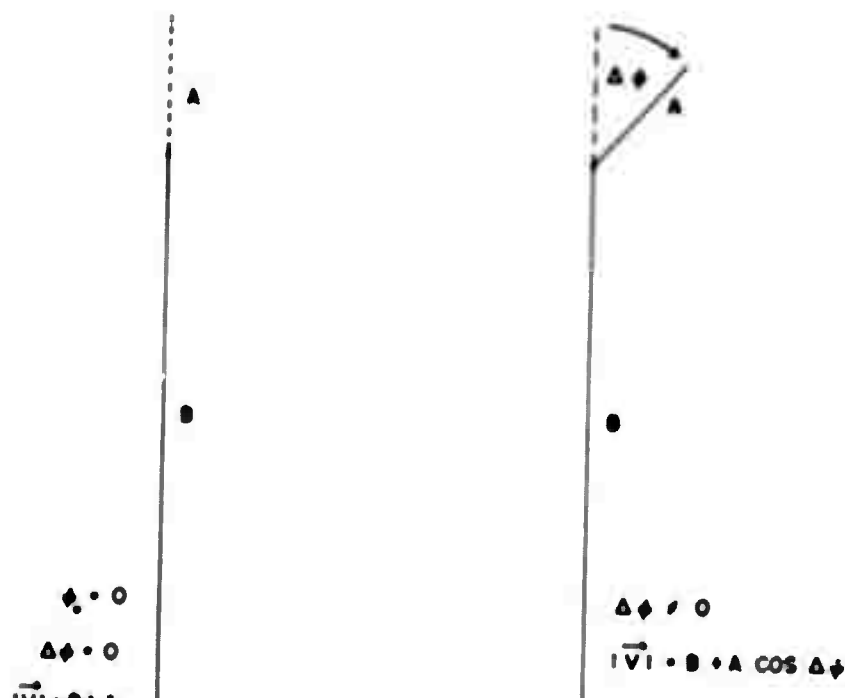


FIGURE 5 - Relative magnitudes of reference and signal vectors



COSINE DETECTION

$$\Delta |V|_{\Delta \phi C} = A (\cos \Delta \phi - 1)$$

$$\Delta I_{\Delta \phi C} = K_0 (\cos \Delta \phi - 1)$$

FIGURE 6 (a) - Cosine Detection

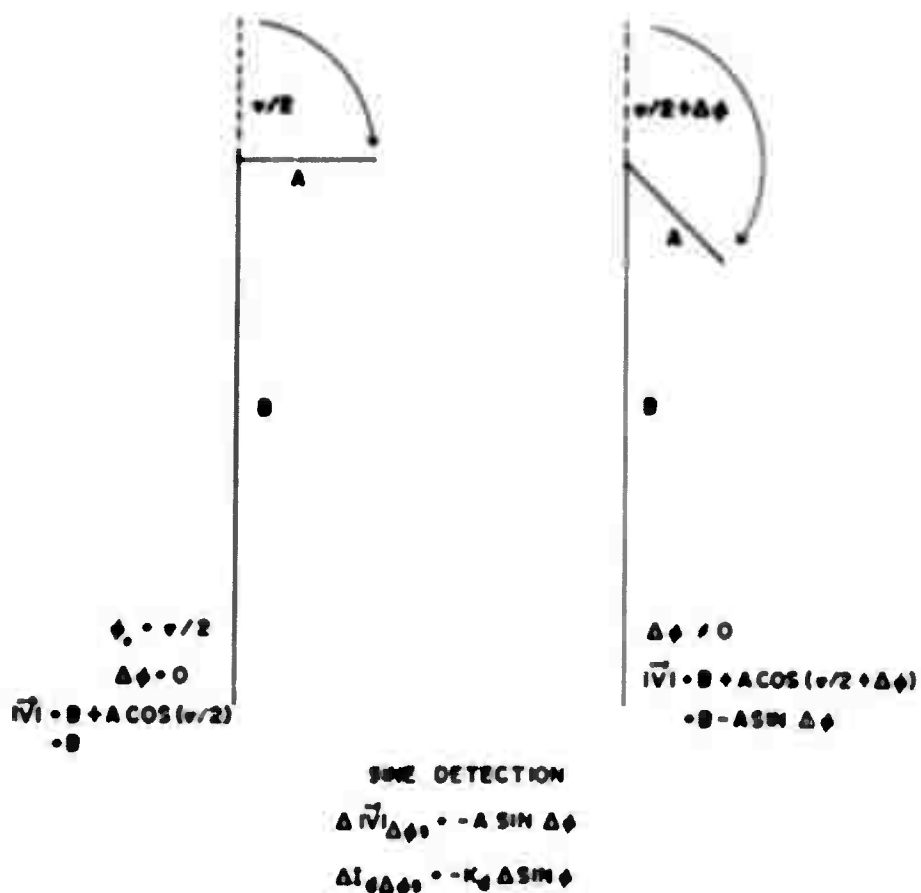


FIGURE 6 (b) - Sine Detection

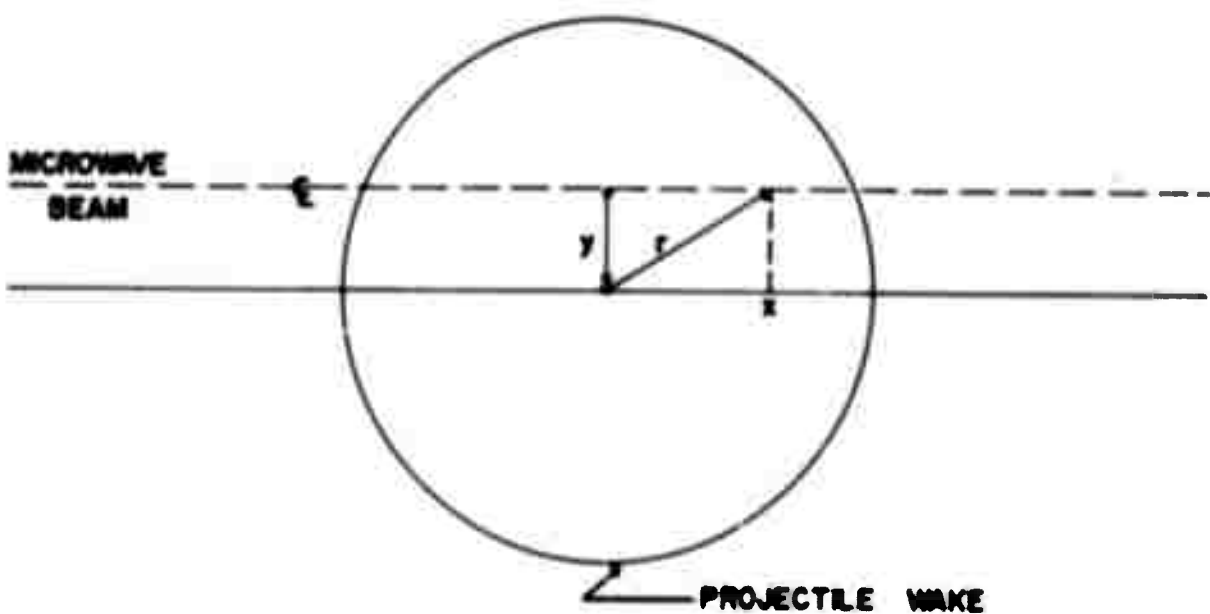


FIGURE 7 - Position of microwave beams relative to position of the wake

UNCLASSIFIED

28

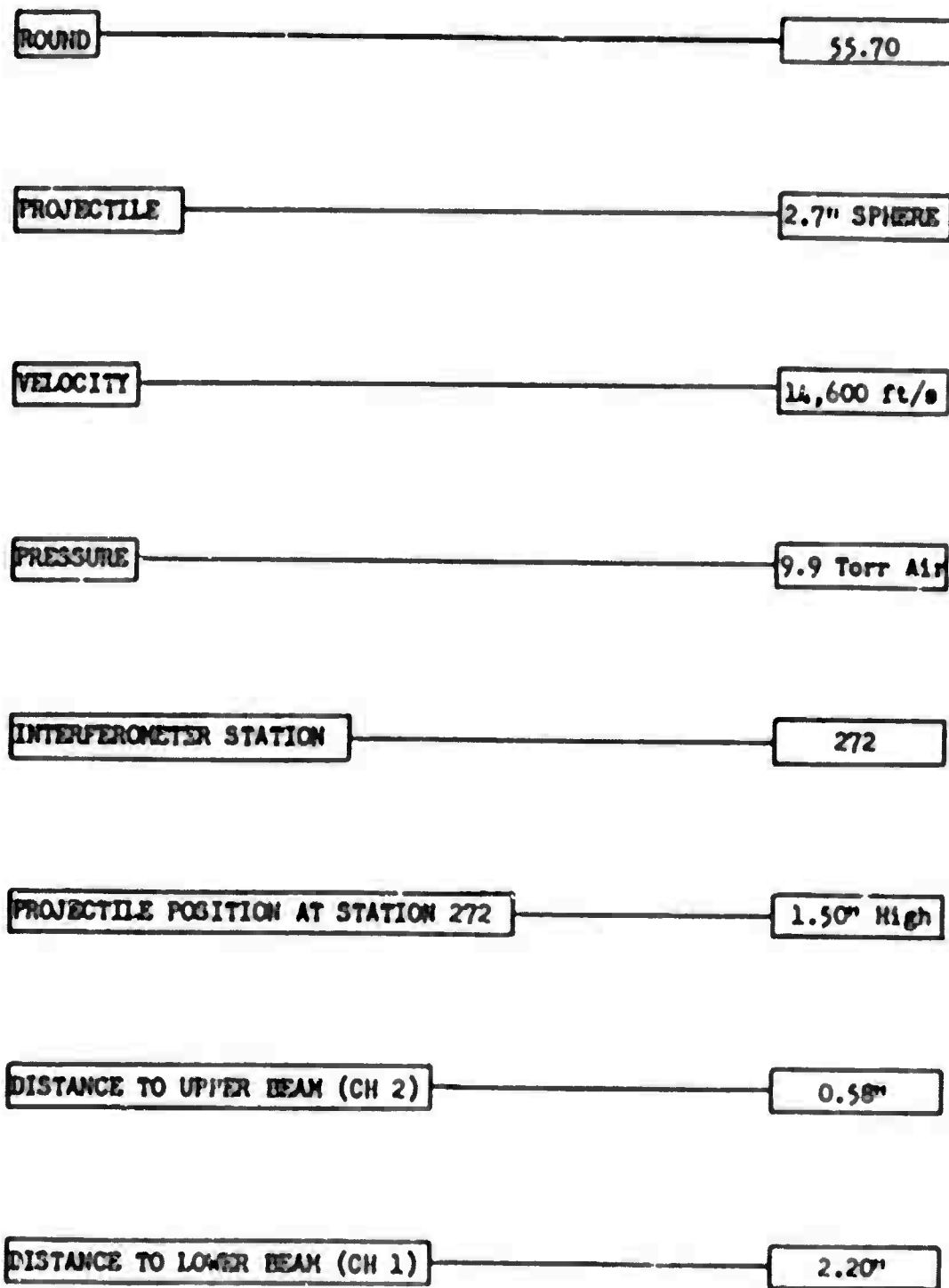
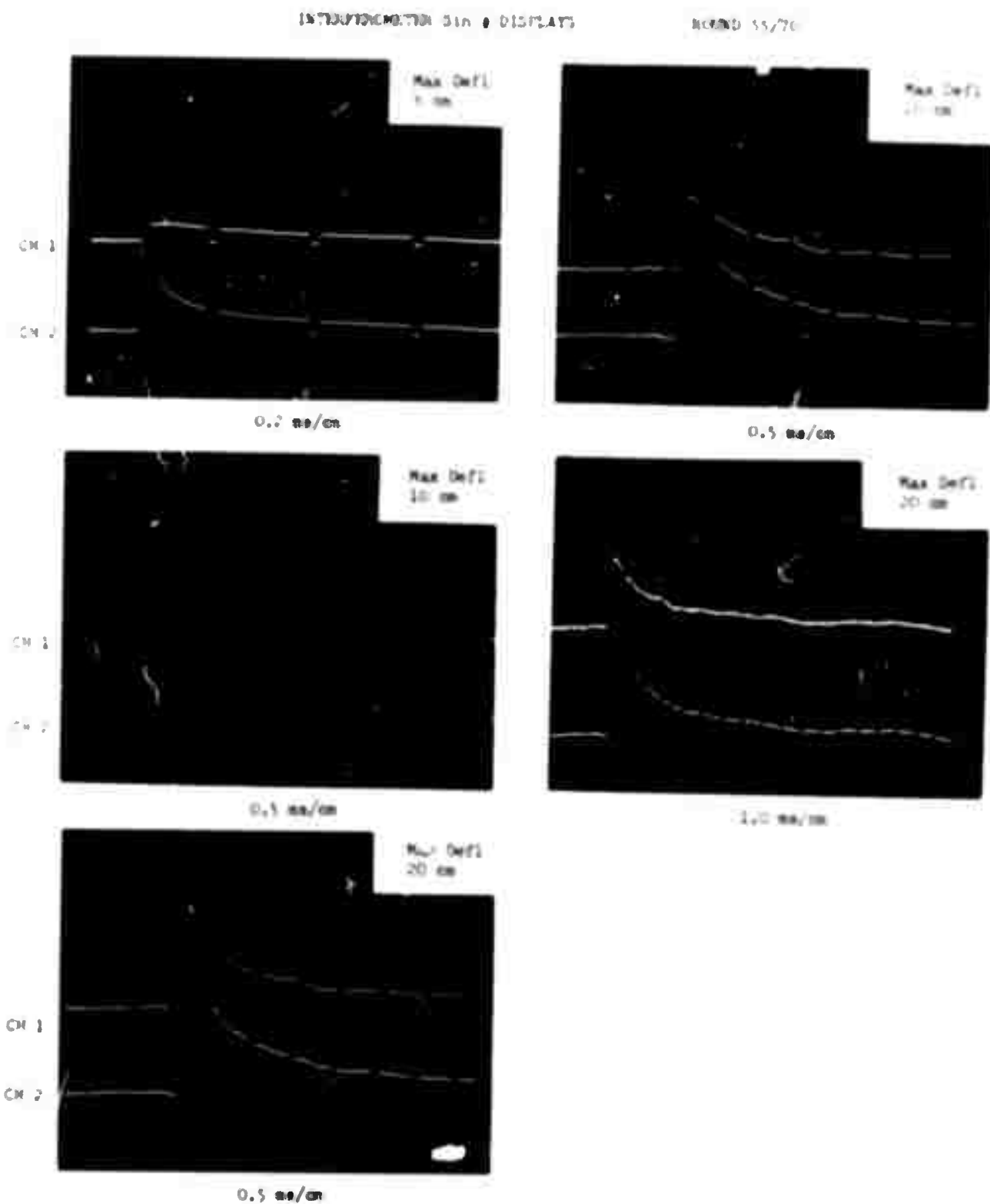
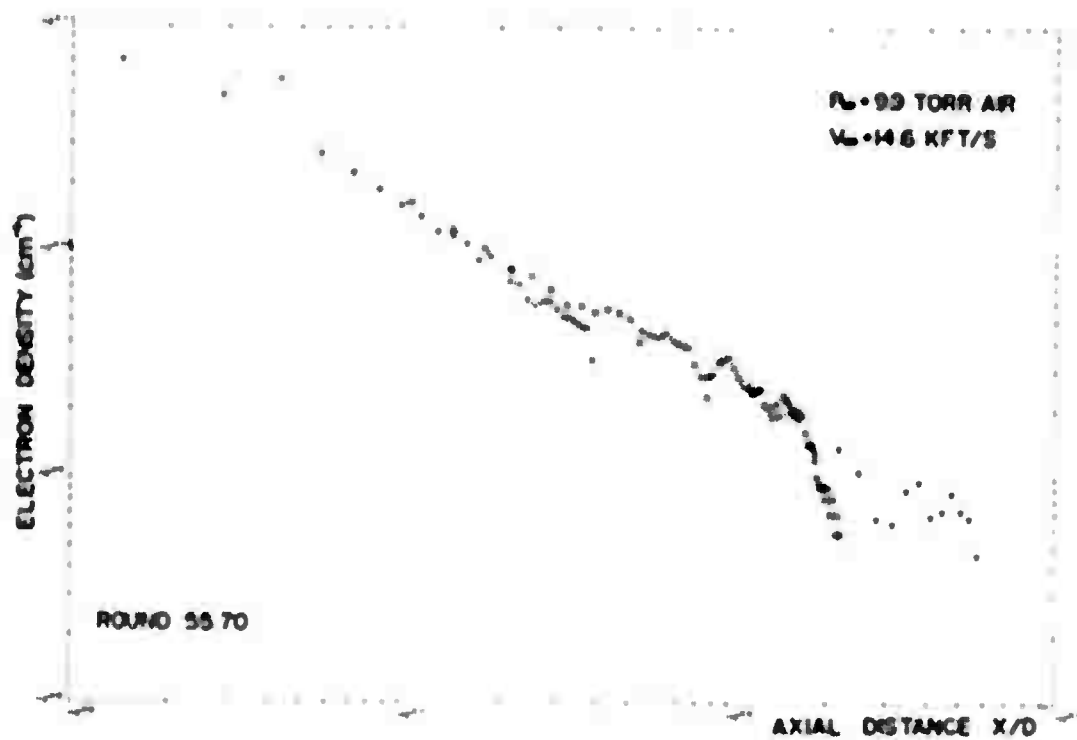


FIGURE 8 - Typical interferometer firing report

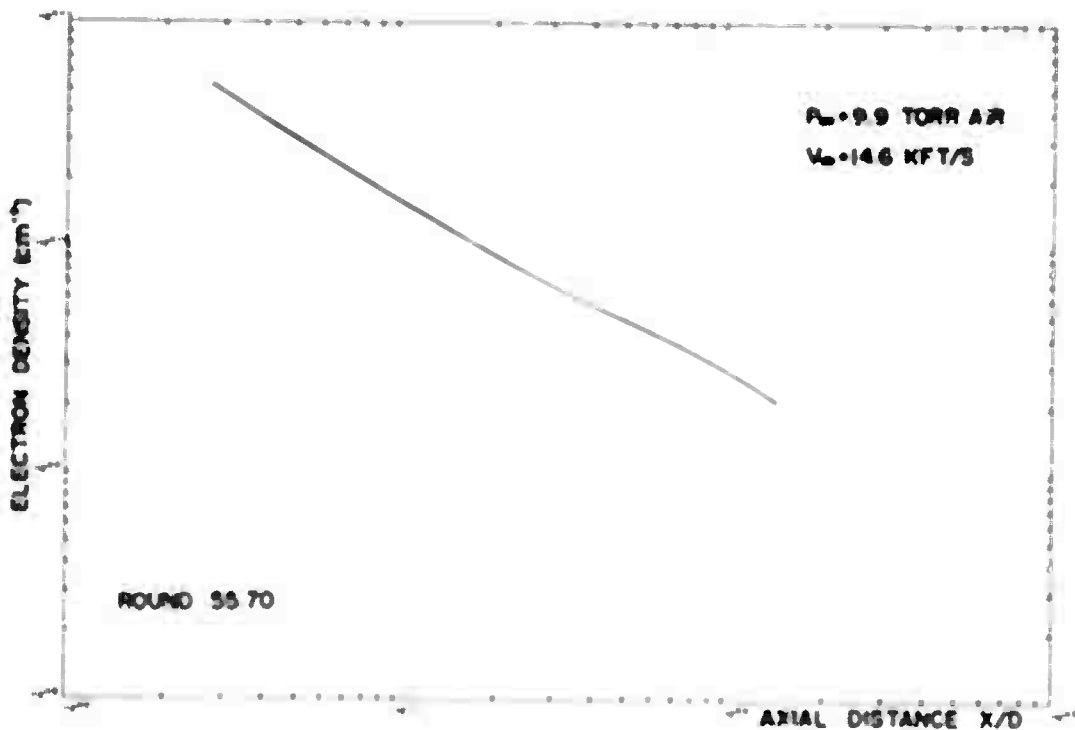
FIGURE 9 - Typical Interferometer SIN_I displays

UNCLASSIFIED

30



(a) Electron density on the wake axis

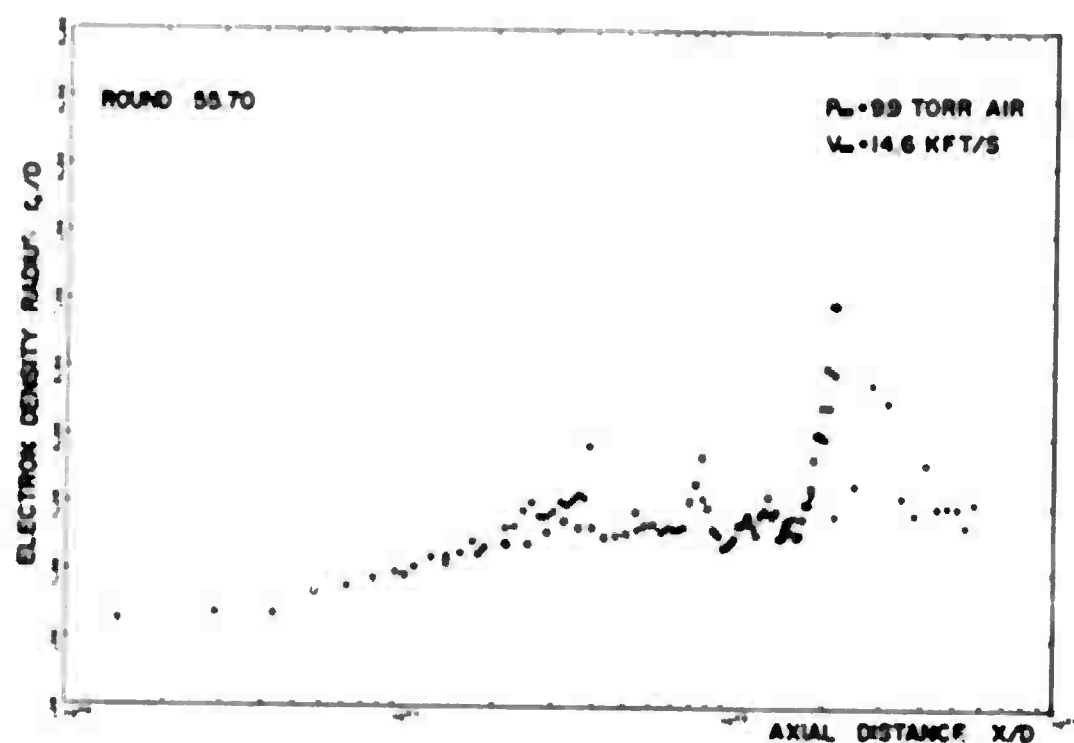


(b) Smoothed curve of electron density on the wake axis

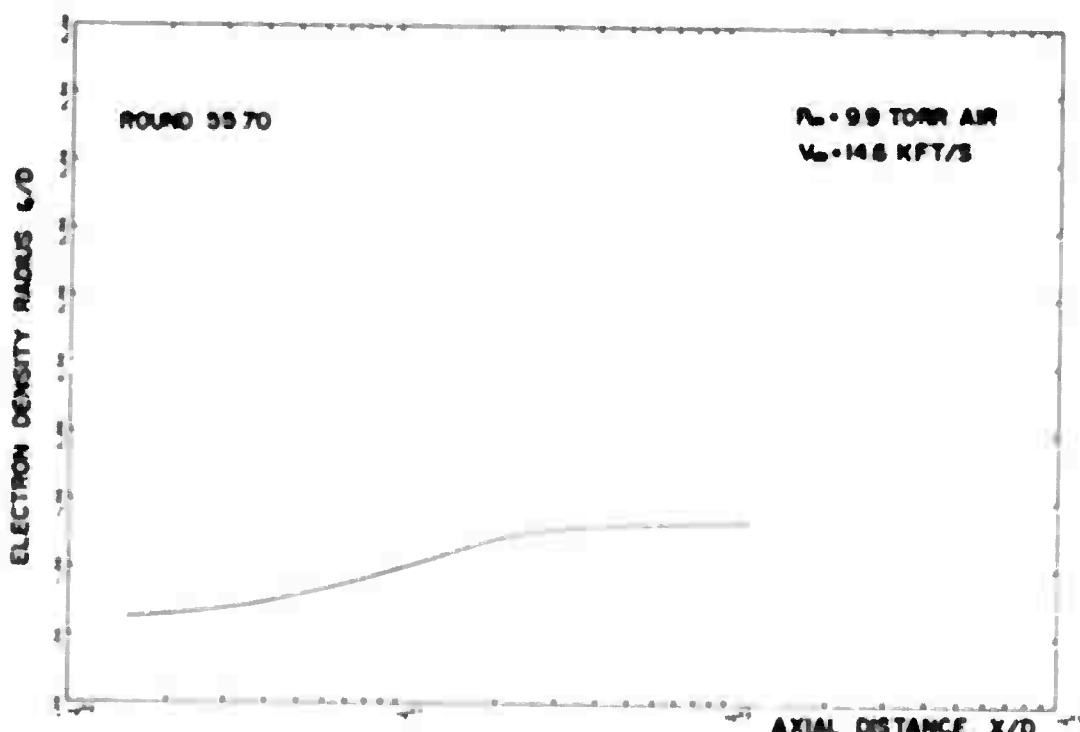
FIGURE 10 - Typical electron density results from simultaneous solutions of dual channel interferometer data

UNCLASSIFIED

31



(a) Electron density radius r_N/D

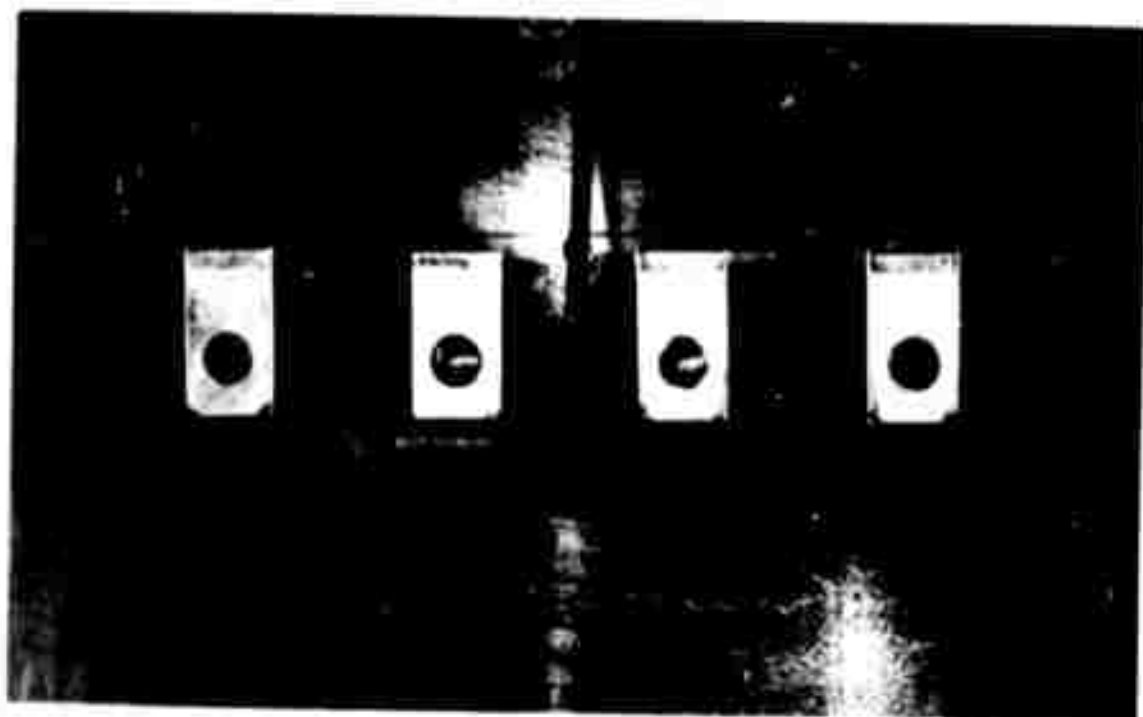


(b) Smoothed electron density radius

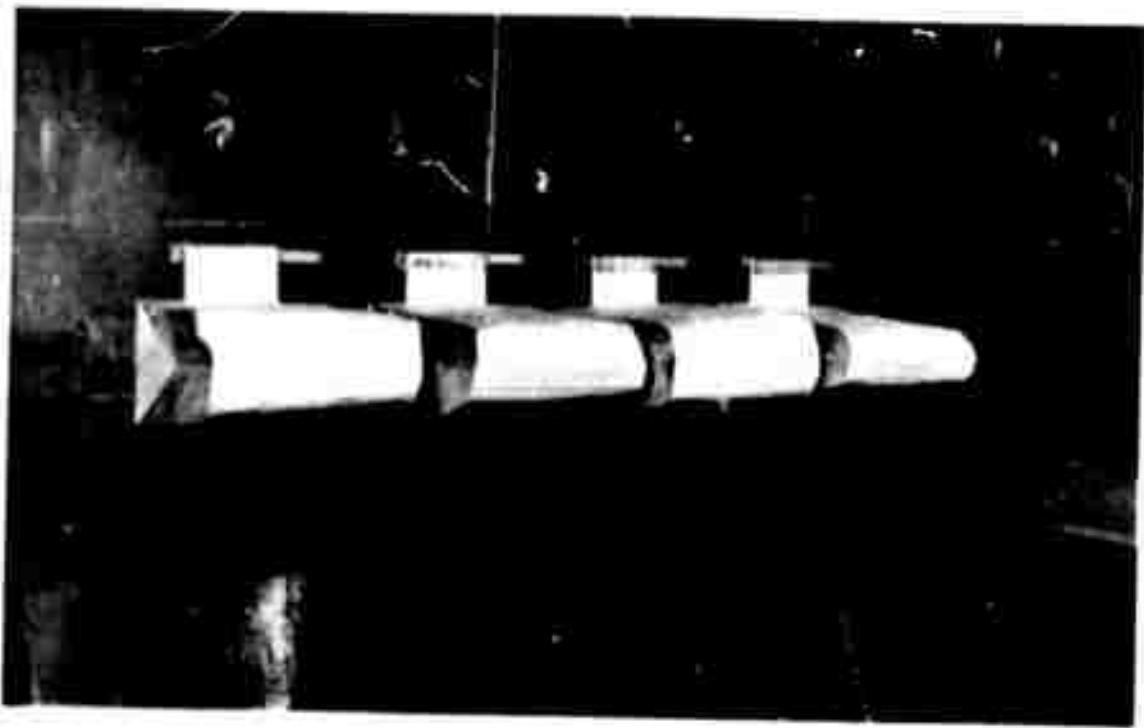
FIGURE 11 - Typical radius data from simultaneous solutions of dual channel interferometer data

UNCLASSIFIED

32

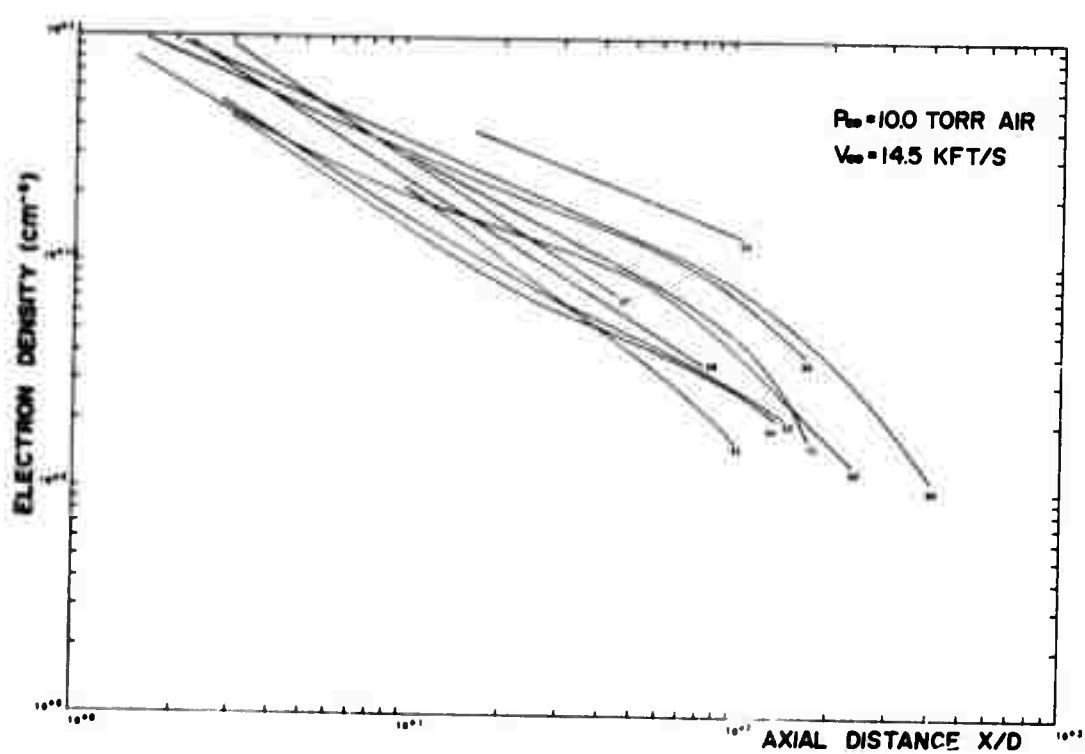


(a) Without vacuum cleaner bags

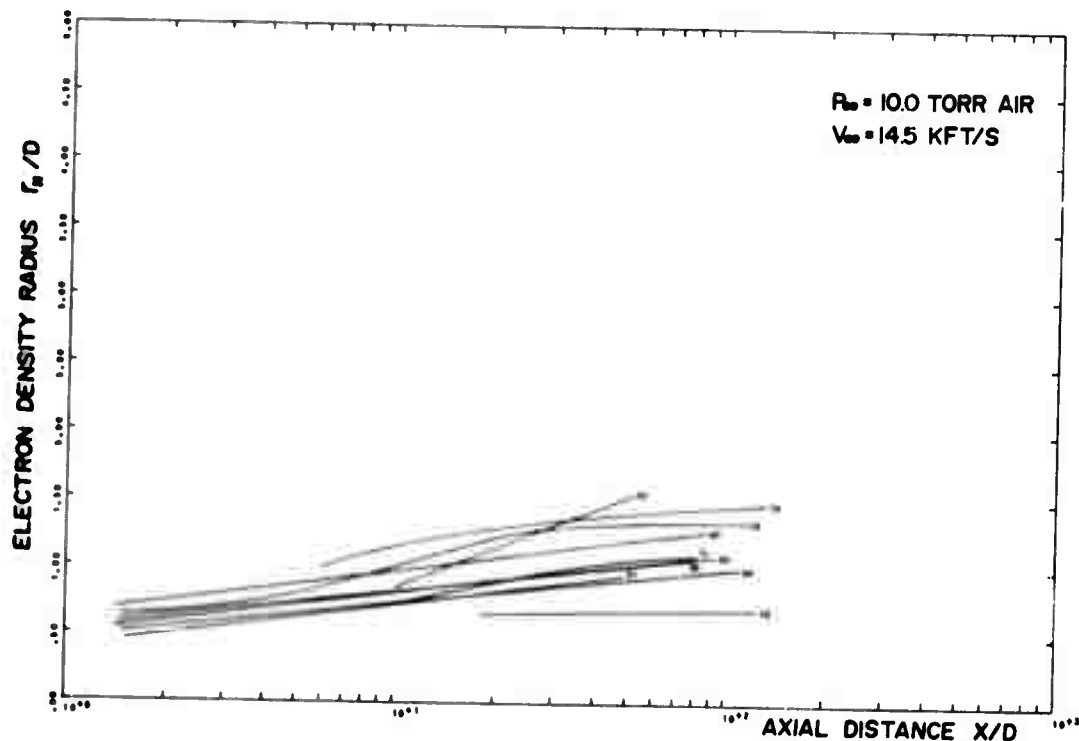


(b) With vacuum cleaner bags

FIGURE 12 - Diffuser system for the introduction of bottled air into Range 5



(a) Electron density on the wake axis

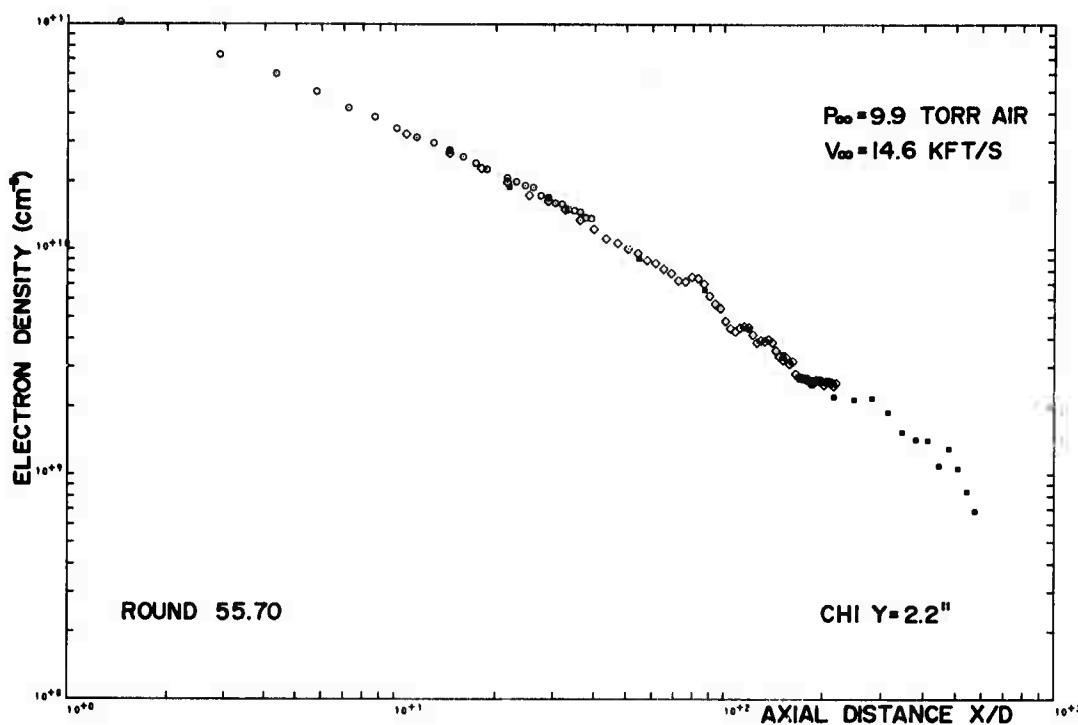


(b) Electron density radius

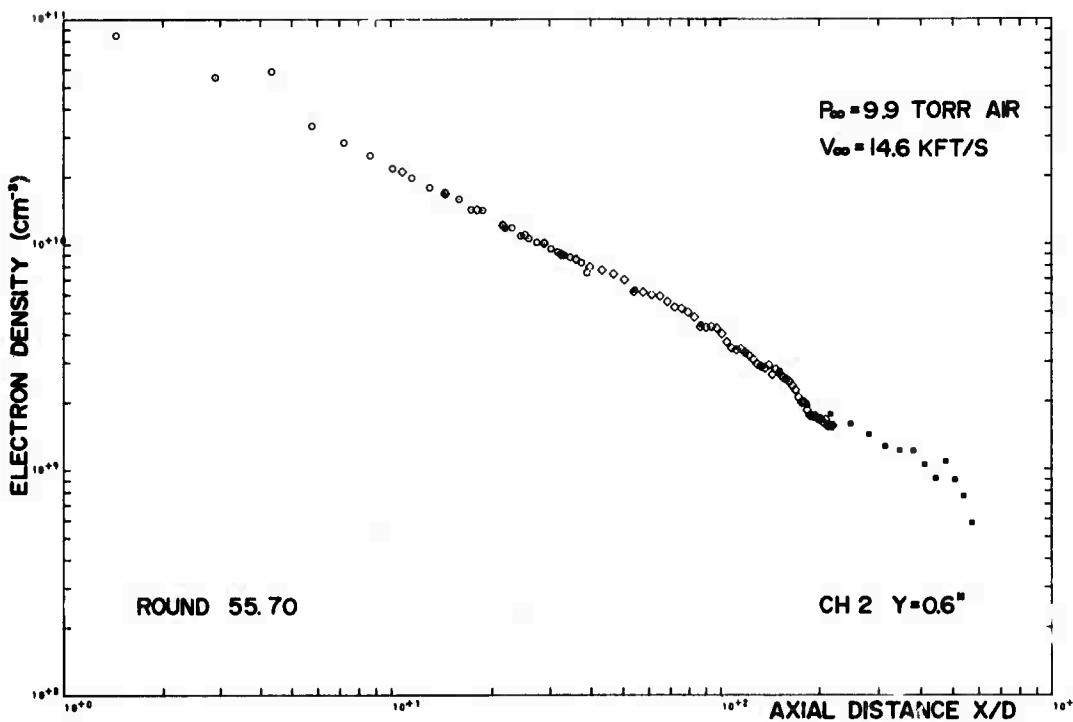
FIGURE 13 - Comparison of electron density and radius data obtained by simultaneous solutions on a number of 10 torr air rounds

UNCLASSIFIED

34

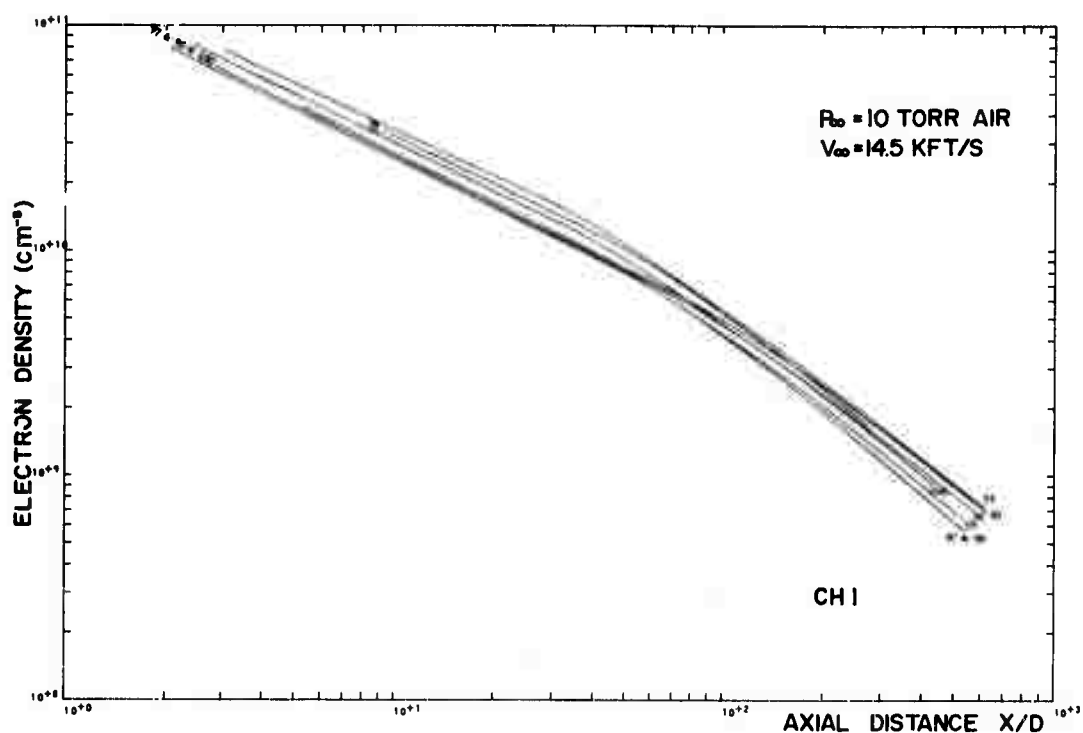


(a) From phase shift measured on interferometer Channel 1

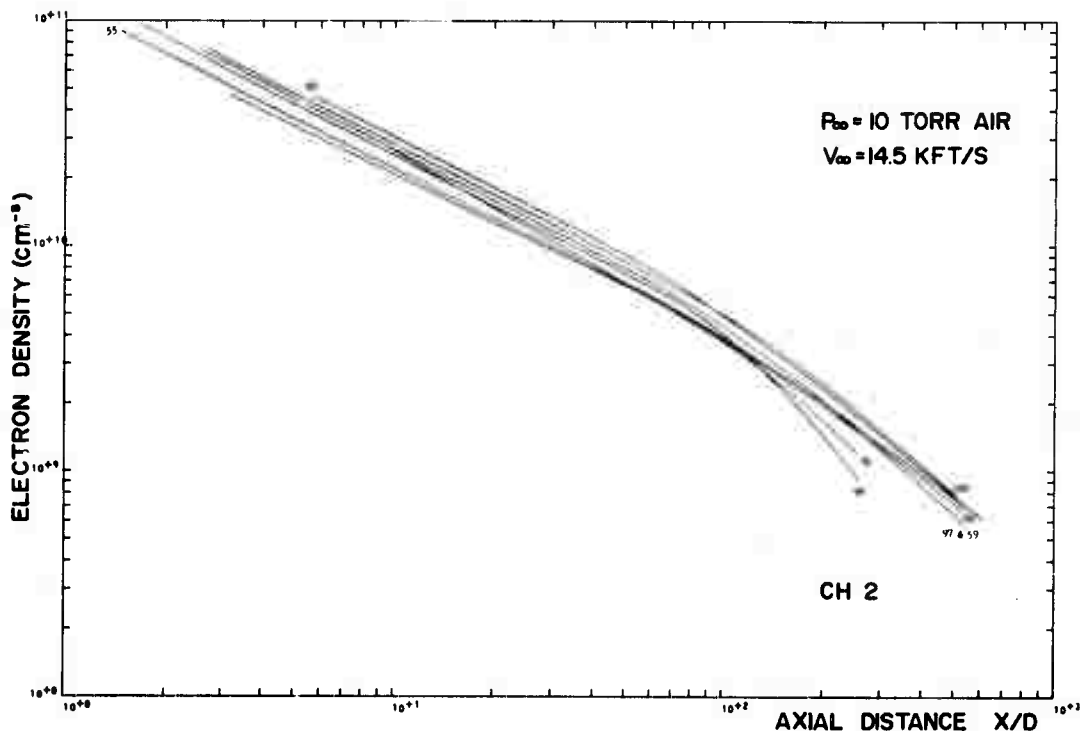


(b) From phase shift measured on interferometer Channel 2

FIGURE 14 - Typical electron density on the wake axis obtained by assuming a gaussian distribution and specifying the wake radius



(a) Channel 1 data

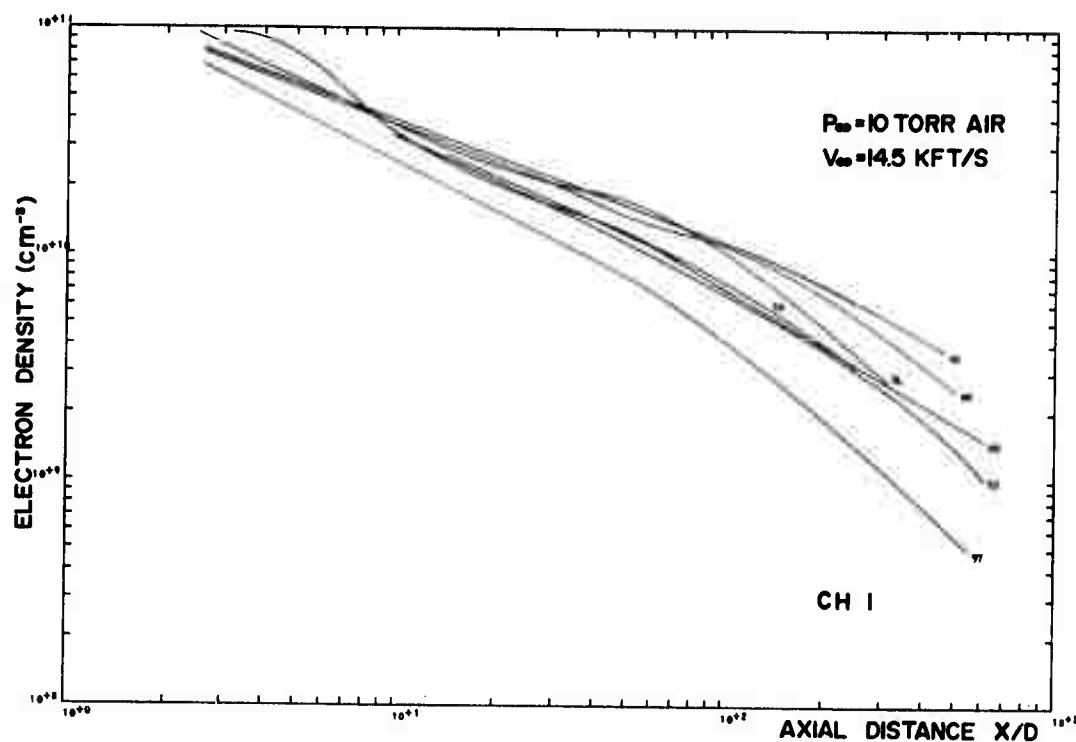


(b) Channel 2 data

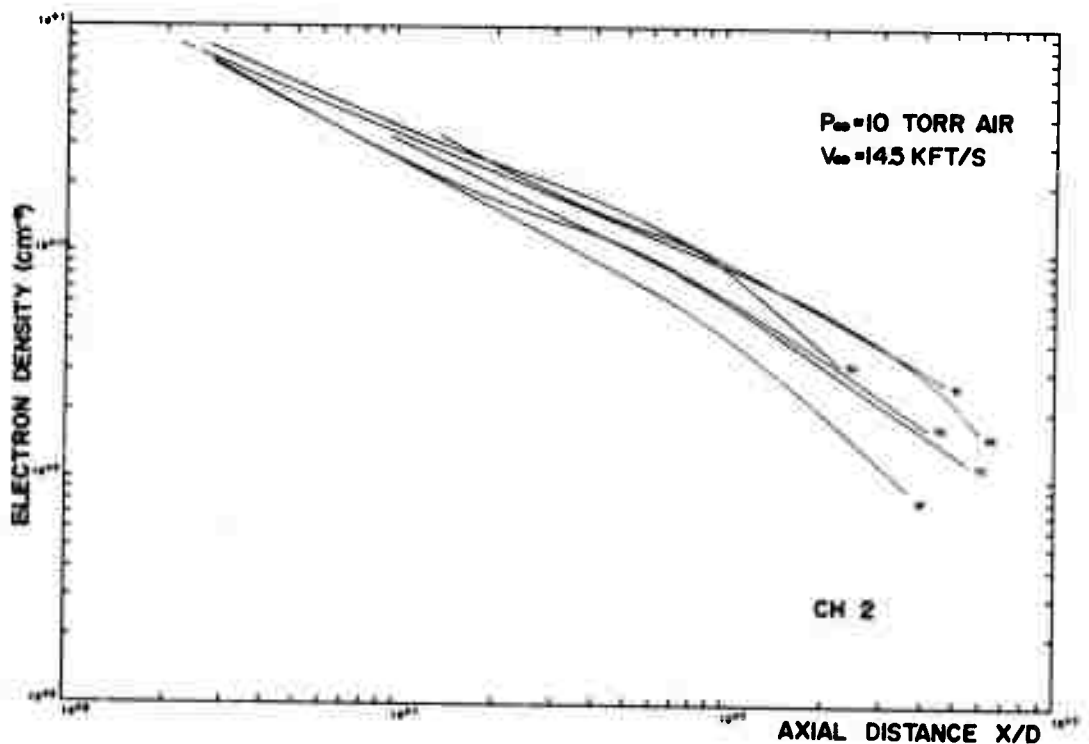
FIGURE 15 - Comparison of electron density estimates on the wake axis obtained by specifying the wake radius on CLEAN 10 torr air rounds

UNCLASSIFIED

36



(a) Channel 1 data



(b) Channel 2 data

FIGURE 16 - Comparison of electron density estimates on the wake axis obtained by specifying the wake radius on SLIGHTLY DIRTY 10 torr air rounds. A clean round (97) is shown for comparison.

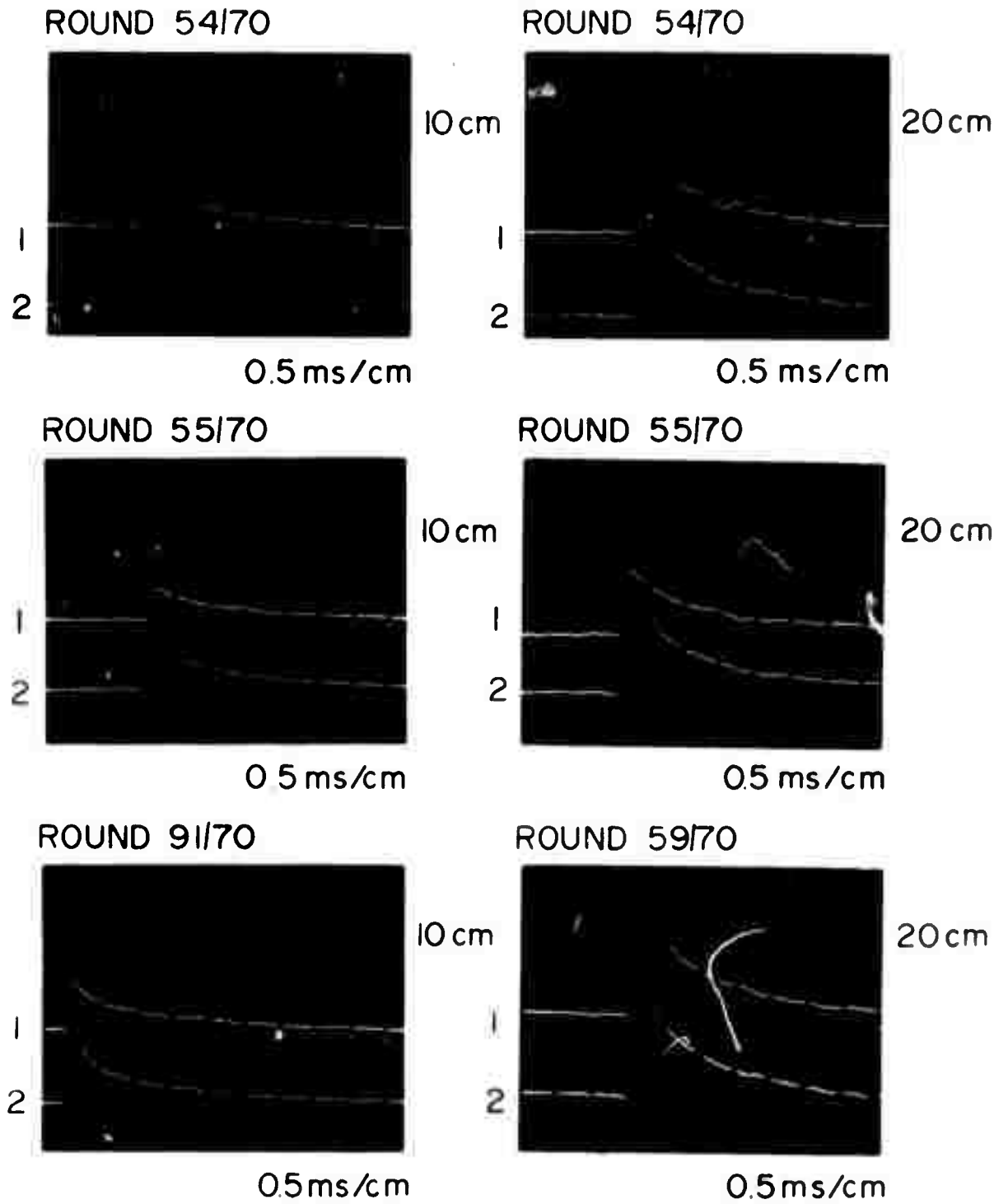


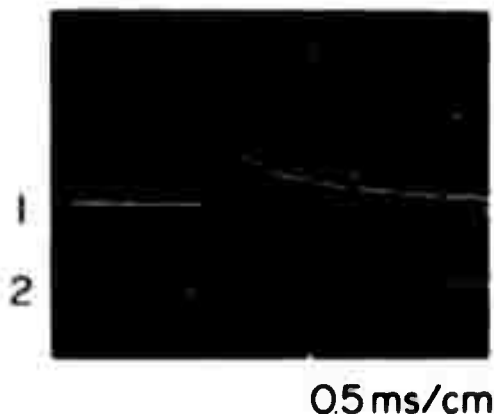
FIGURE 17 - Typical dual channel interferometer signals

(a) Clean 10 torr air rounds

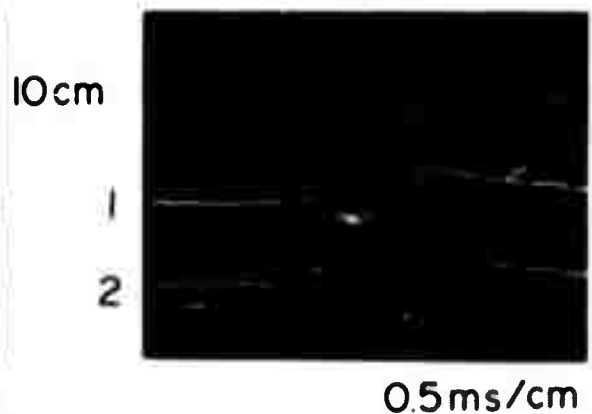
UNCLASSIFIED

38

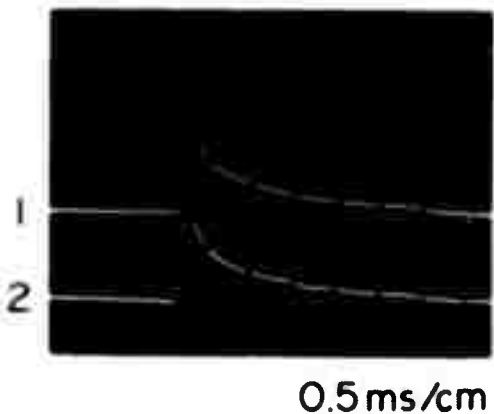
ROUND 93/70



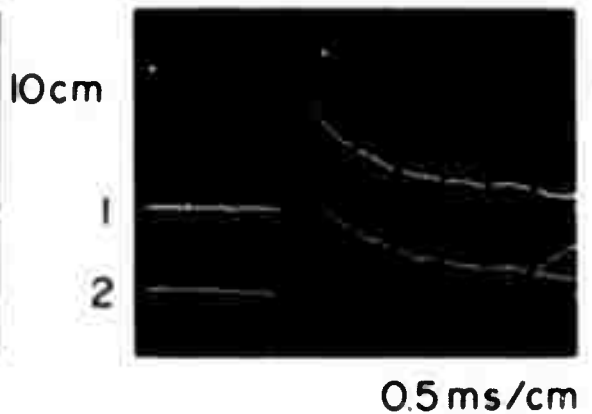
ROUND 93/70



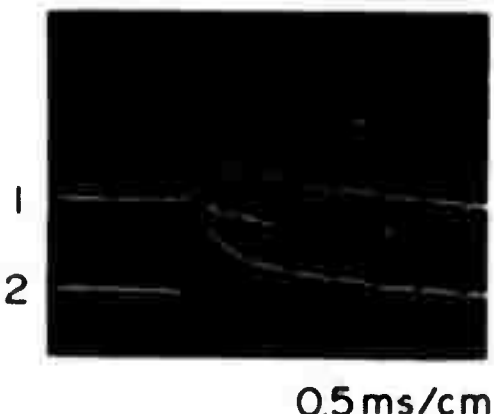
ROUND 97/70



ROUND 97/70



ROUND 98/70



ROUND 98/70

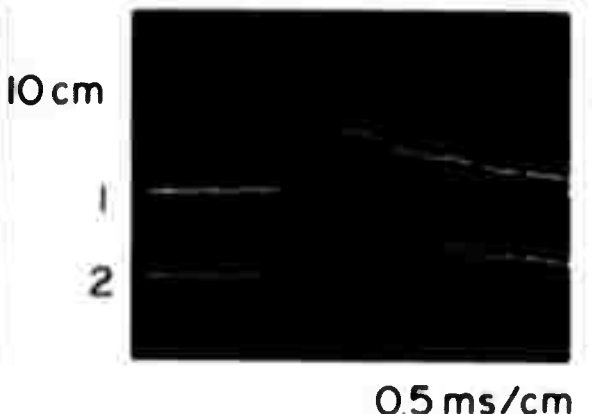


FIGURE 17 - Typical dual channel interferometer signals

(b) Clean 10 torr air rounds

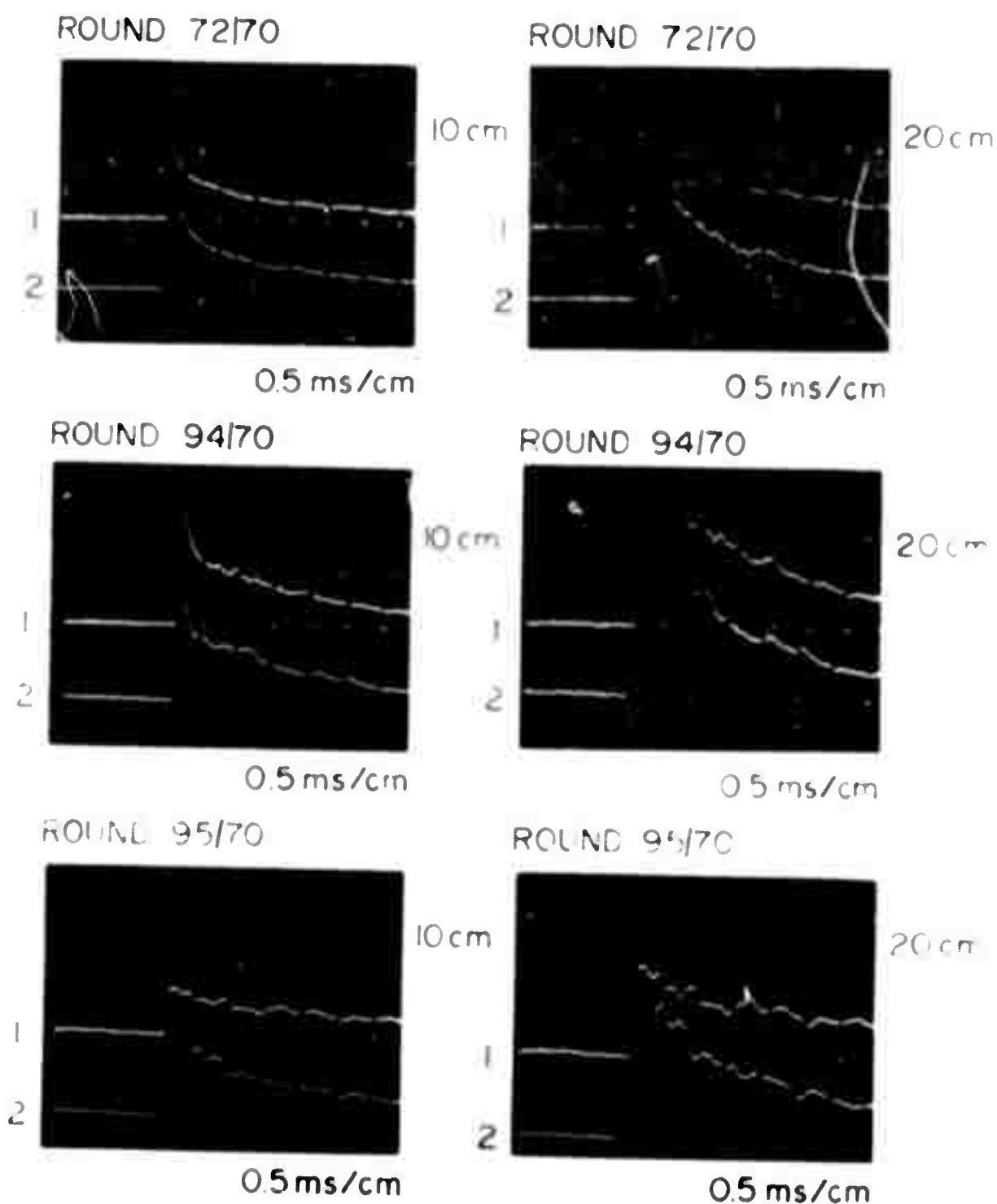


FIGURE 17 - Typical dual channel interferometer signals
(c) Very slightly dirty 10 torr air rounds

UNCLASSIFIED

10

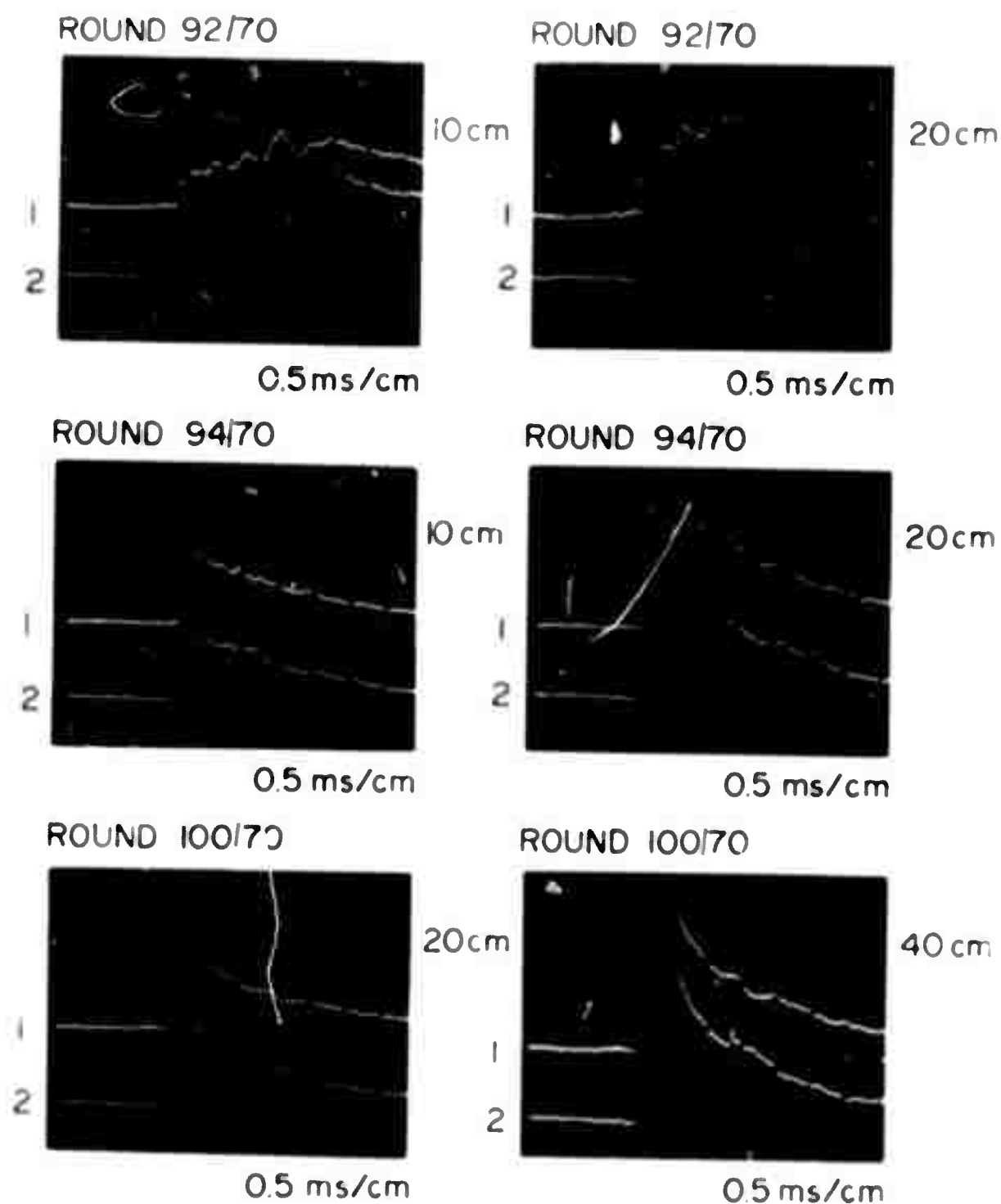


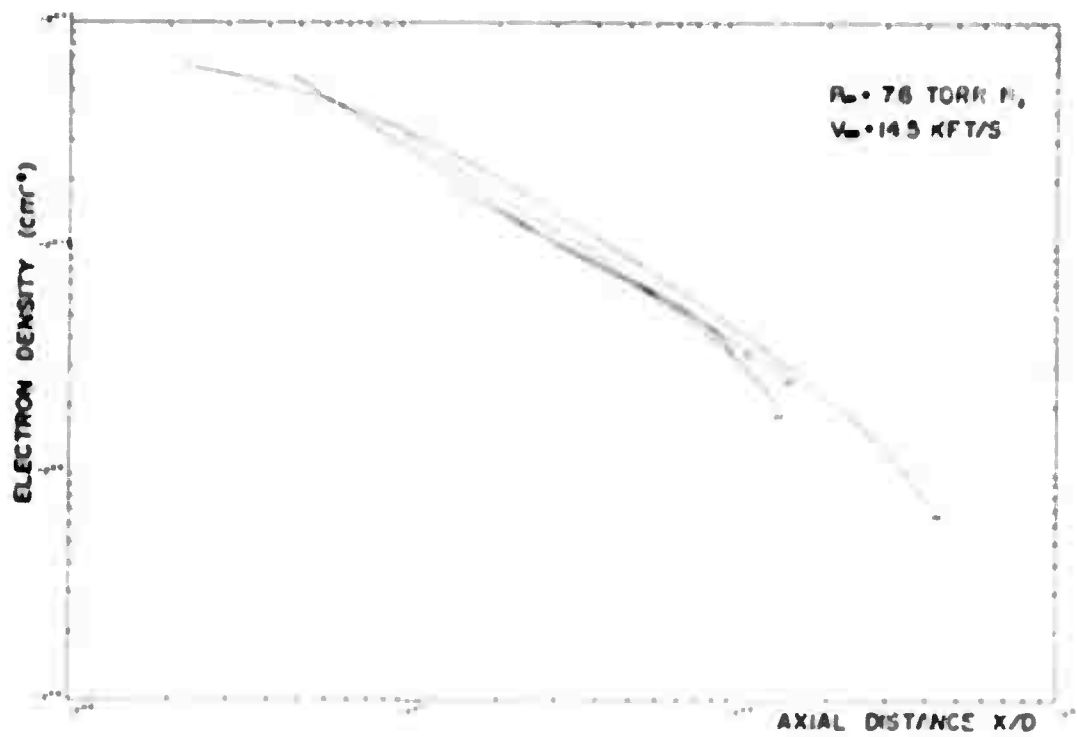
FIGURE 17 - Typical dual channel interferometer signals

(d) Various degrees of dirtiness

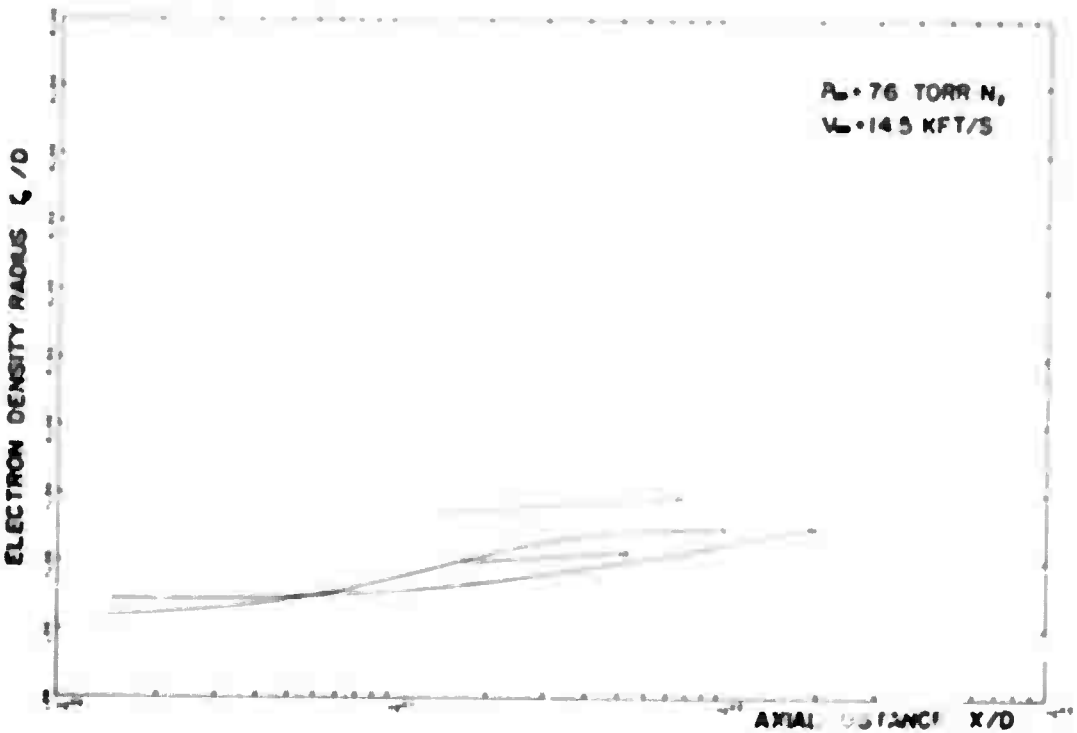
Round 92 is very dirty

Round 94 has about twice the normal level of ionization

Round 100 is clean except for the tiny fragment at 1.3 ms



(a) Electron density on the wake axis

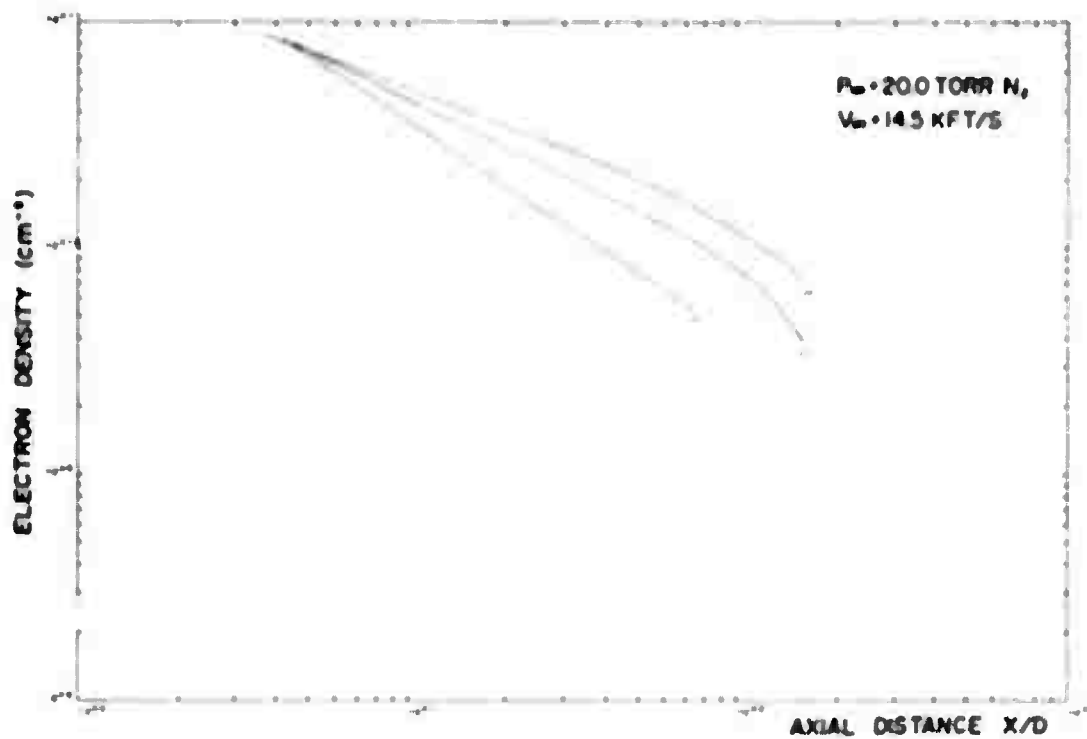


(b) Electron density radius

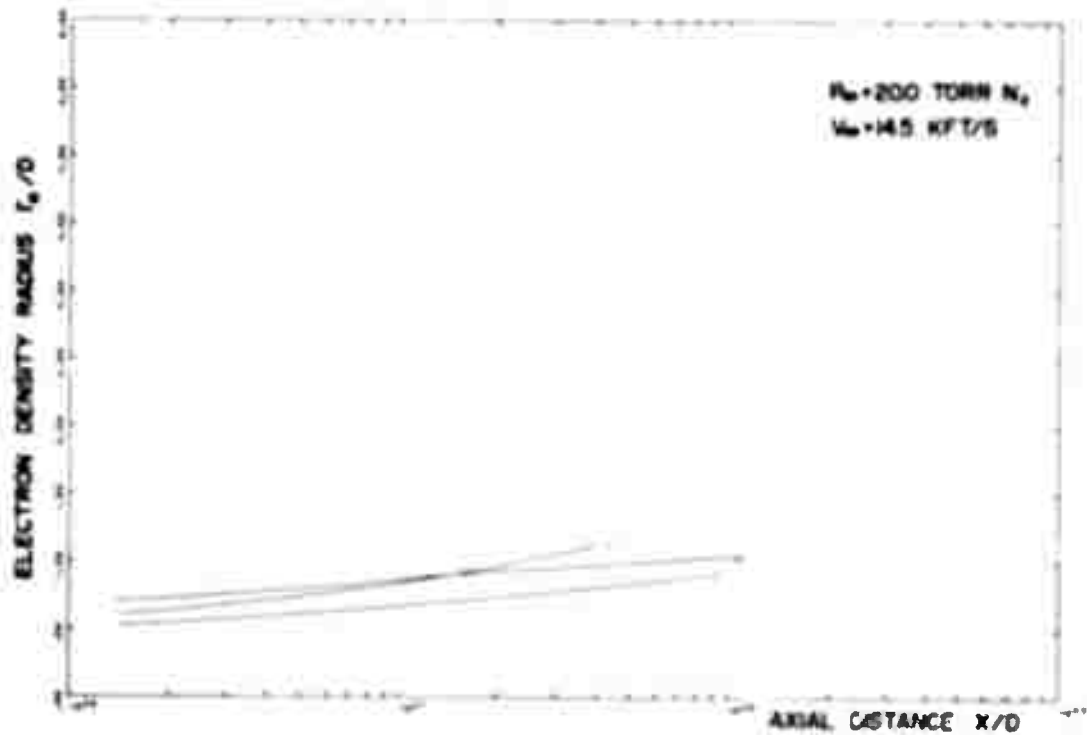
FIGURE 18 - Comparison of electron density and radius data obtained by simultaneous solutions on a number of 7.6 torr N_2 rounds

UNCLASSIFIED

42



(a) Electron density on the wake axis



(b) Electron density radius

FIGURE 19 - Comparison of electron density and radius data obtained by simultaneous solutions on a number of 20 torr N_2 rounds

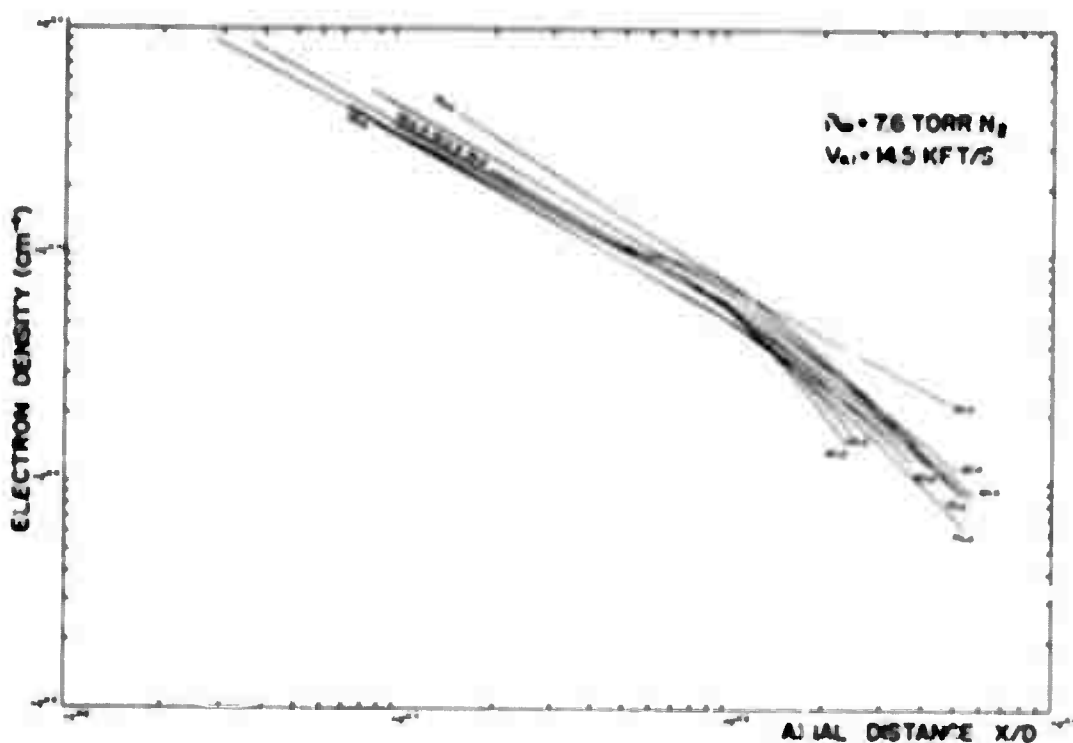


FIGURE 20 - Comparison of electron density estimates on the wake axis obtained by specifying the wake radius on 7.6 torr N_2 rounds

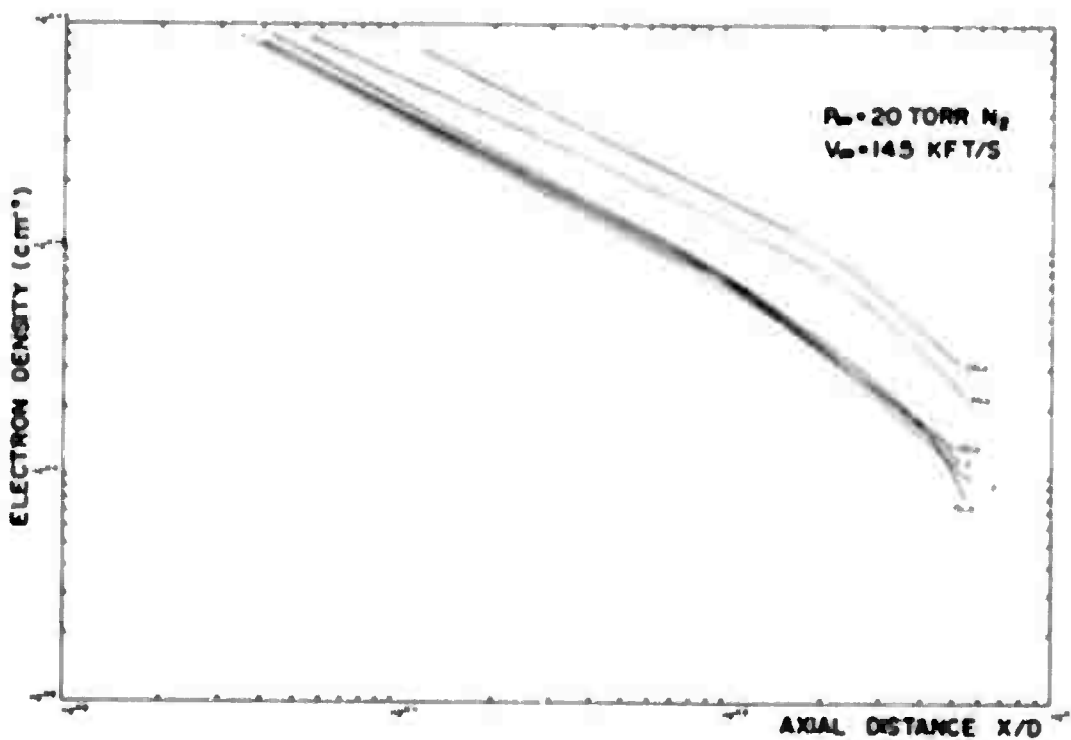


FIGURE 21 - Comparison of electron density estimates on the wake axis obtained by specifying the wake radius on 20 torr N_2 rounds. Obviously Round 69 is slightly dirty.

UNCLASSIFIED

44

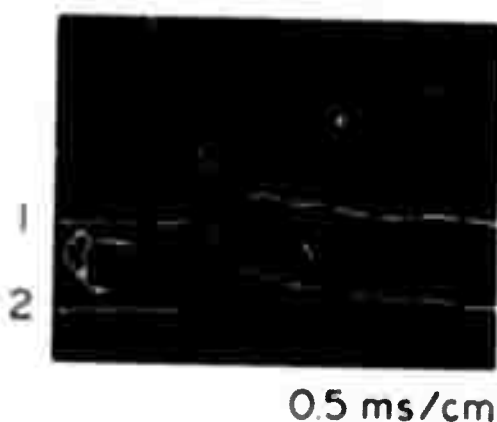
ROUND 65/70



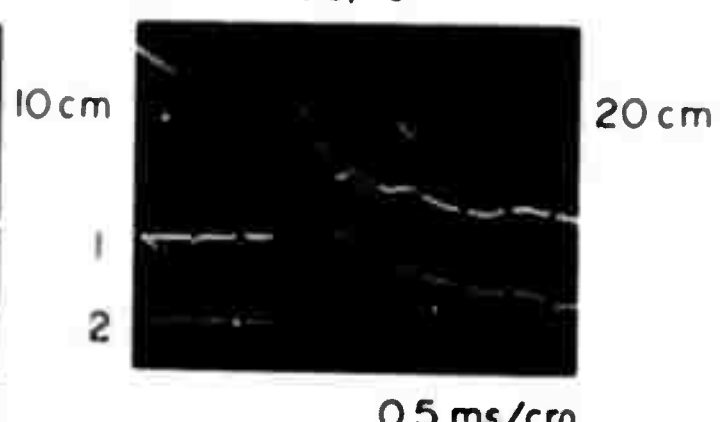
ROUND 65/70



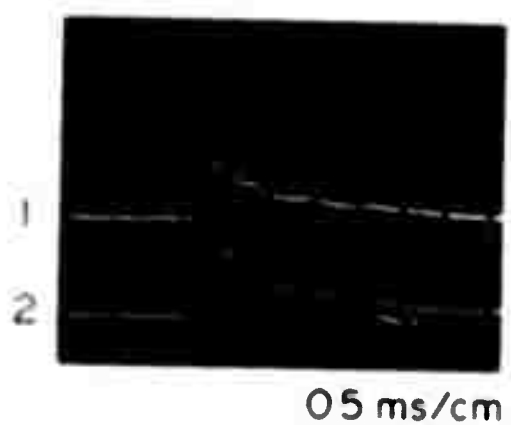
ROUND 68/70



ROUND 68/70



ROUND 75/70



ROUND 75/70

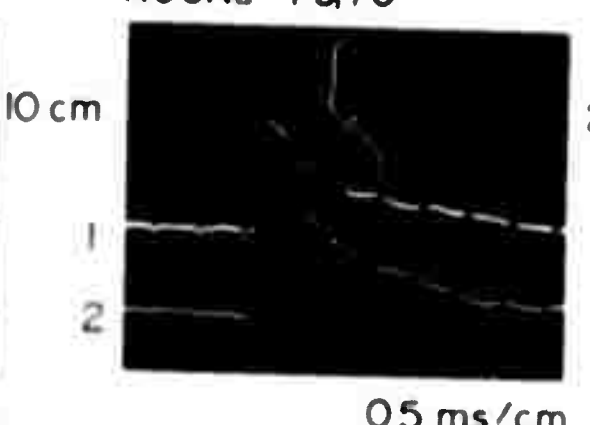


FIGURE 22 - Typical dual channel interferometer signals at 7.6 torr

ROUND 67/70



0.5 ms/cm

ROUND 67/70



0.5 ms/cm

ROUND 69/70



0.5 ms/cm

ROUND 69/70



0.5 ms/cm

ROUND 71/70



0.5 ms/cm

ROUND 71/70



0.5 ms/cm

UNCLASSIFIED

46

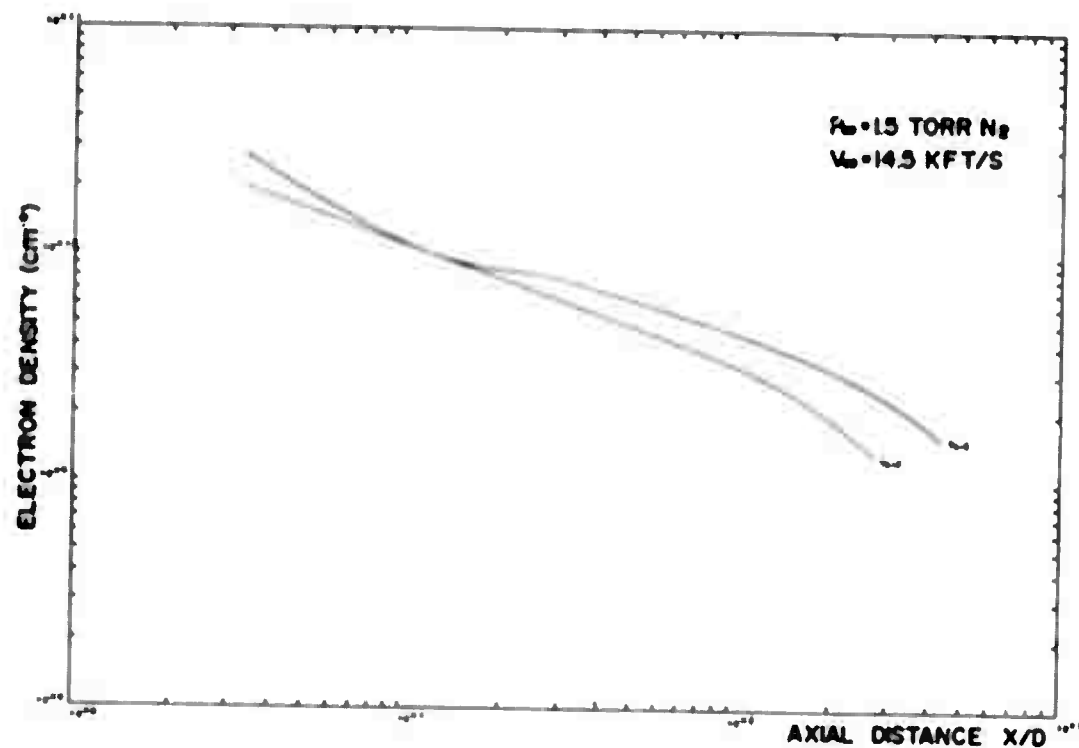


FIGURE 24 - Comparison of electron density estimates on the wake axis obtained by specifying the wake radius on a solitary 1.5 torr N_2 round.

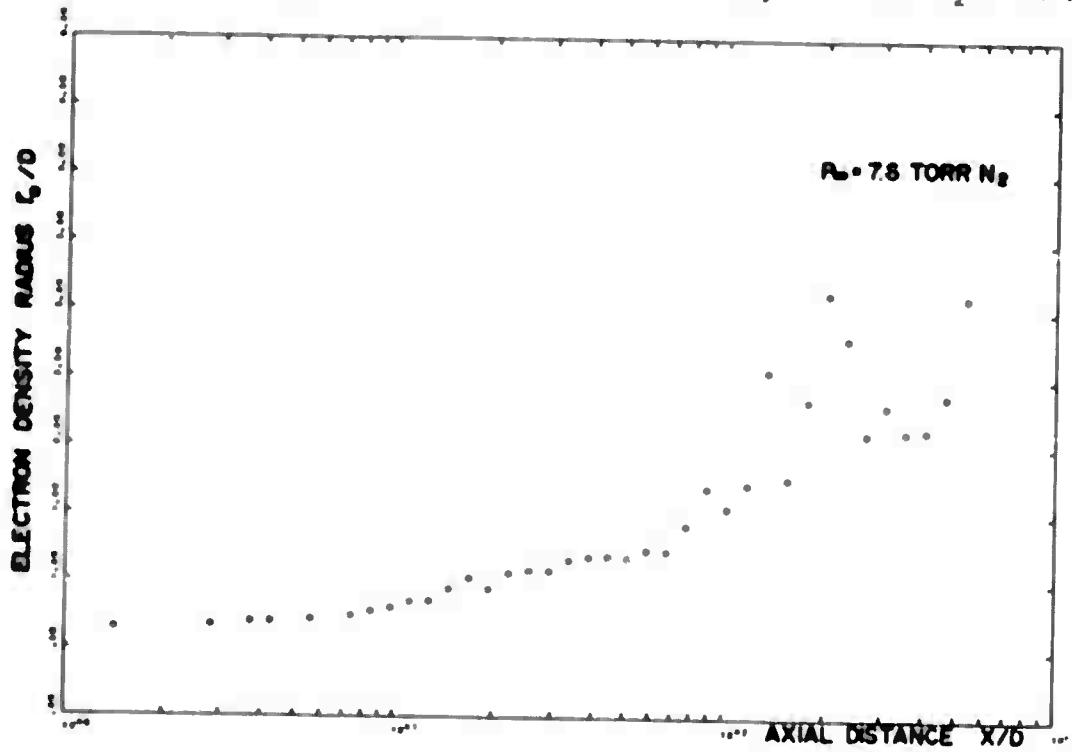


FIGURE 25 - Electron density wake radius obtained by averaging over the estimates of a number of 7.6 torr N_2 rounds.

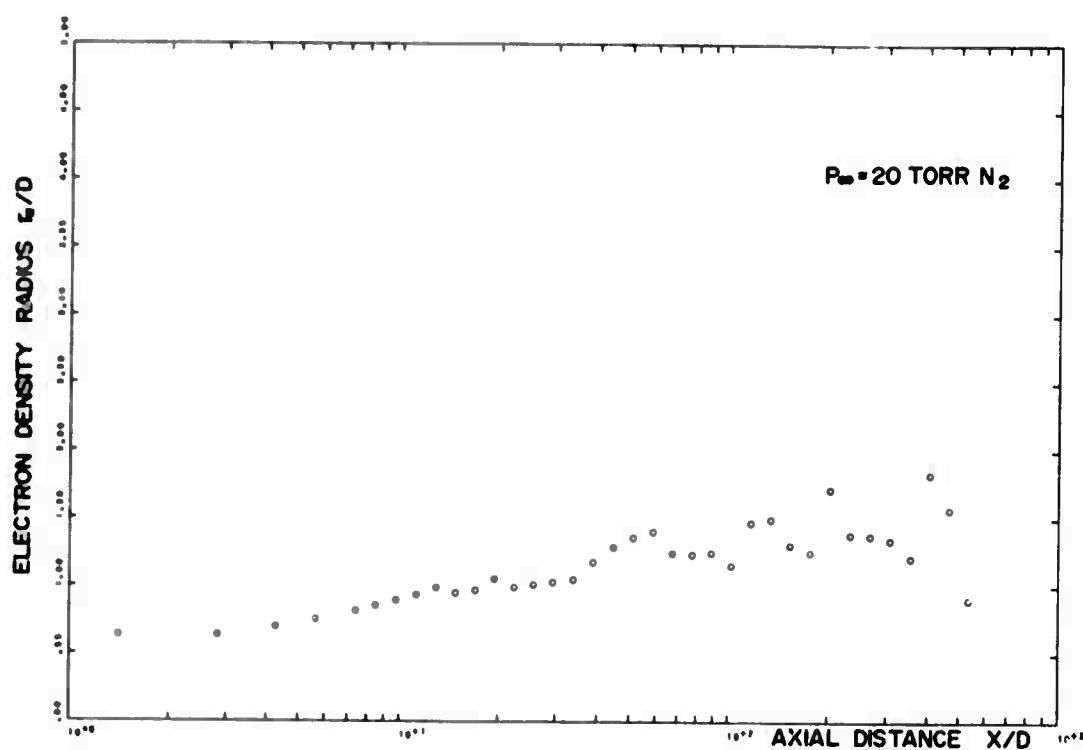


FIGURE 26 - Electron density wake radius obtained by averaging over the estimates of a number of 20 torr N₂ rounds.

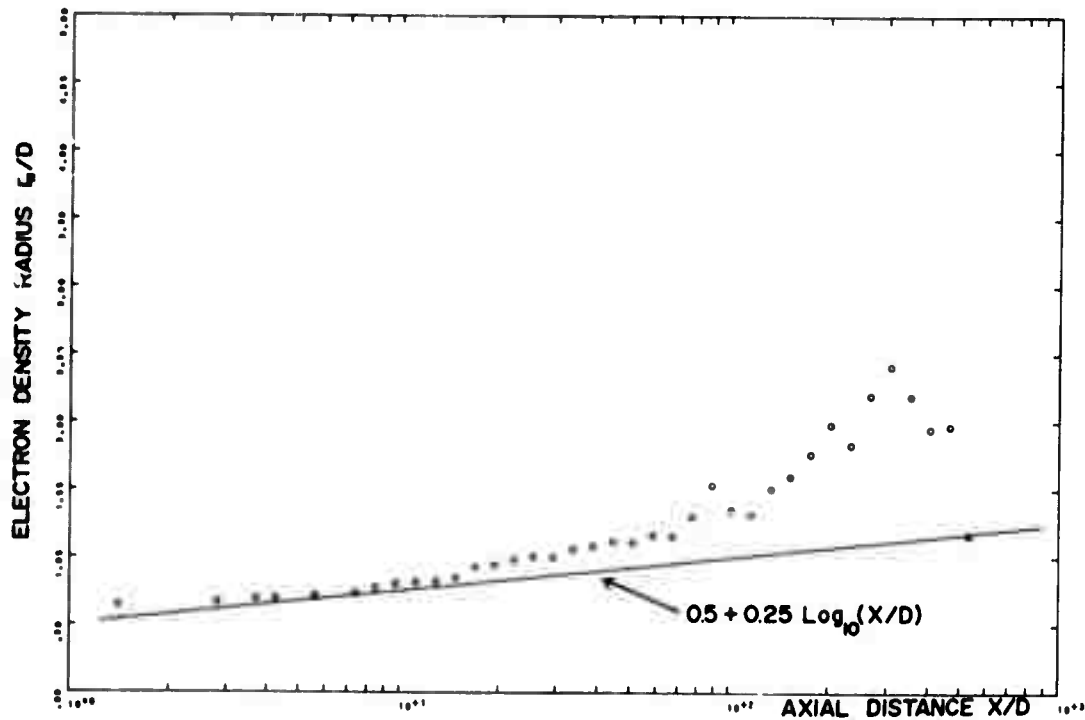


FIGURE 27 - Electron density radius obtained by averaging over the radius estimates of a number of rounds where the electron density radius obtained by simultaneous solutions as well defined.

UNCLASSIFIED

48

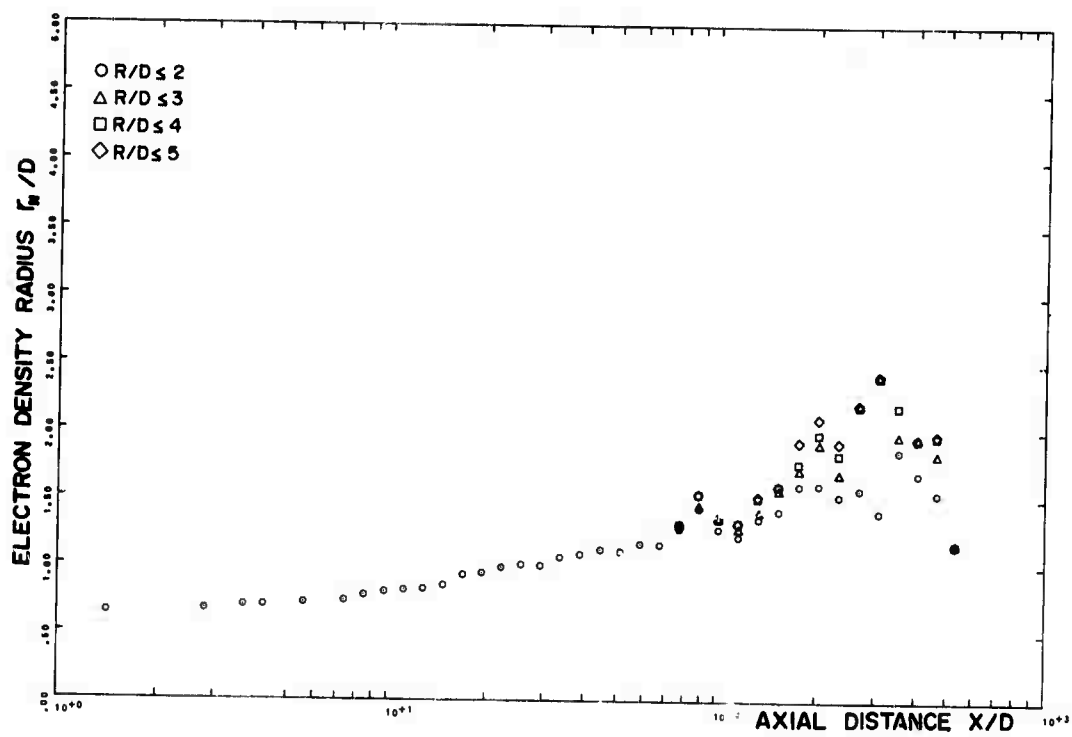


FIGURE 28 - The effect on the average electron density radius estimate if individual estimates exceeding various values of R/D are rejected.

APPENDICES A to F

The following six appendices have been included so that the interested reader may have access to reproductions of the original polaroid photographs used to record the dual channel interferometer signals and also to representations of the estimates of the electron density on the wake axis and the electron density radii derived from analysis of these signals. Appendices A to C refer to results obtained in air atmospheres while Appendices D to E refer to results from nitrogen atmospheres.

UNCLASSIFIED
51

APPENDIX A

Interferometer Firing Reports and SIN ϕ Displays Air Atmospheres

UNCLASSIFIED

52

INTERFEROMETER FIRING REPORT

ROUND 50.70

PROJECTILE 2.7" SPHERE

VELOCITY 14,500 ft/s

PRESSURE 10 Torr Air

INTERFEROMETER STATION 272

PROJECTILE POSITION AT STATION 272 0.30" High

DISTANCE TO UPPER BEAM (CH 2) 0.62"

DISTANCE TO LOWER BEAM (CH 1) 1.01"

FIGURE A-1(a)

UNCLASSIFIED

S3

INTERFEROMETER 3in & DISPLAYS

ROUND 50/70

CH 1

CH 2

Max Defl
10 cm

0.5 ns/cm

INTERFEROMETER 3in & 4 Cos & DISPLAYS ROUND 50/70

CH 1

CH 2

Max Defl
20 cm

Max Defl
10 cm

1.0 ns/cm

FIGURE A-1(b)

UNCLASSIFIED

54

INTERFEROMETER FIRING REPORT

ROUND 51.70

PROJECTILE 2.7" SPHERE

VELOCITY 14,600 ft/s

PRESSURE 10 Torr Air

INTERFEROMETER STATION 272

PROJECTILE POSITION AT STATION 272 0.99" HIGH

DISTANCE TO UPPER BEAM (CH 2) 0.07"

DISTANCE TO LOWER BEAM (CH 1) 1.70"

FIGURE A-2(a)

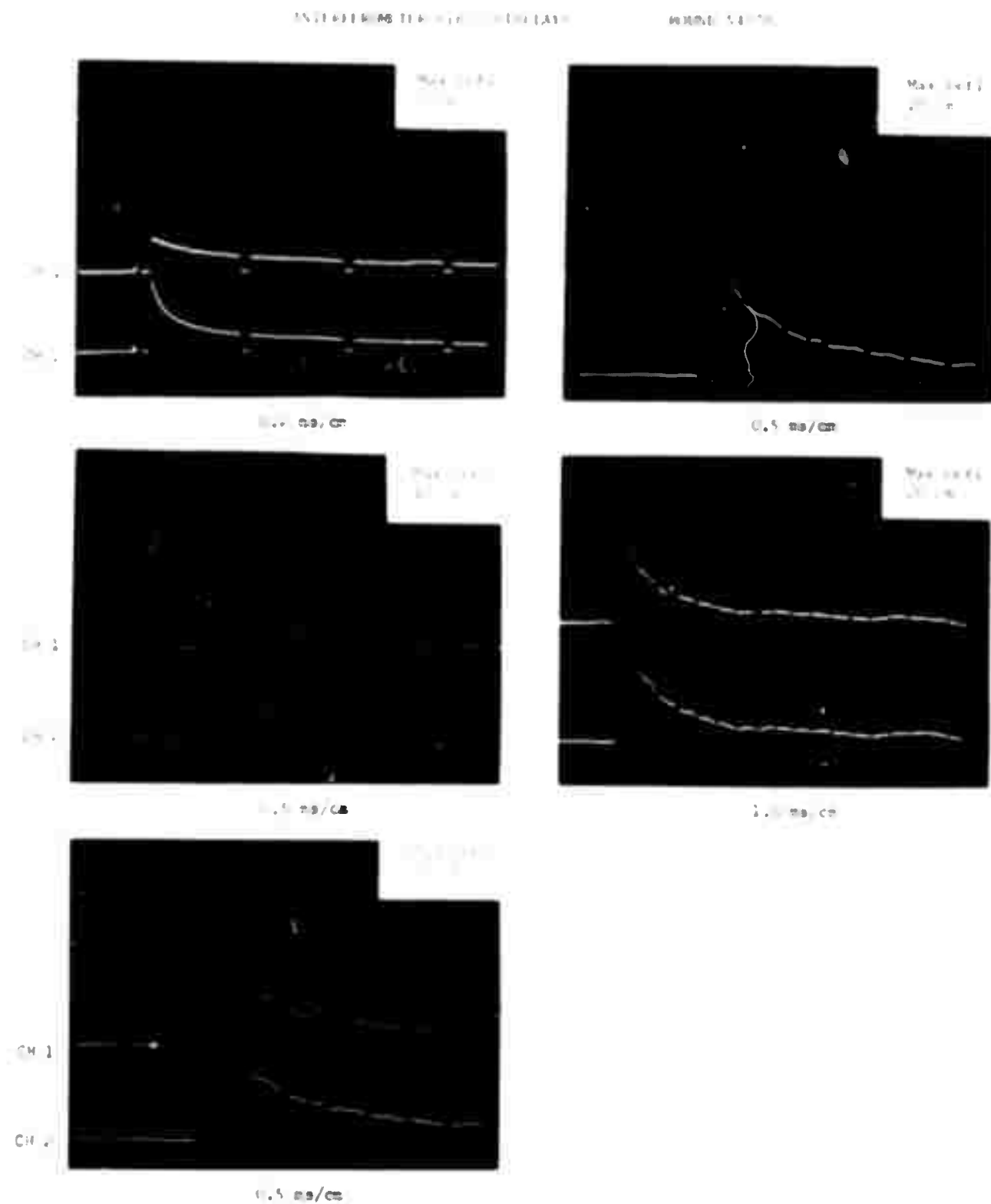


FIGURE A-2(b)

UNCLASSIFIED

56

INTERFEROMETER FIRING REPORT

ROUND 55.70

PROJECTILE 2.7" SPHERE

VELOCITY 14,600 ft/s

PRESSURE 9.9 Torr Air

INTERFEROMETER STATION 272

PROJECTILE POSITION AT STATION 272 1.50" HIGH

DISTANCE TO UPPER BEAM (CH 2) 0.58"

DISTANCE TO LOWER BEAM (CH 1) 2.20"

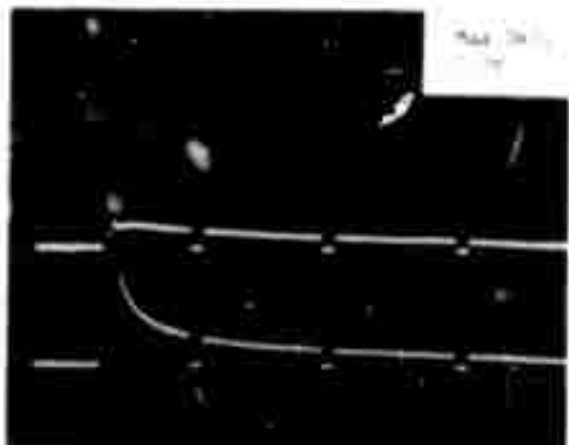
FIGURE A-3(a)

UNCLASSIFIED

67

15704700.70 510-00000000

510-00000000



0.5 sec/0.5 sec



0.5 sec/0.5 sec



0.5 sec/0.5 sec



0.5 sec/0.5 sec



0.5 sec/0.5 sec

FIGURE A-3(b)

UNCLASSIFIED
S8

INTERFEROMETER FIRING REPORT

ROUND → 59.70

PROJECTILE → 2.7" SPHERE

VELOCITY → 14,488 ft/s

PRESSURE → 10 Torr Air

INTERFEROMETER STATION → 272

PROJECTILE POSITION AT STATION 272 → 0.112" HIGH

DISTANCE TO UPPER BEAM (CH 2) → 0.808"

DISTANCE TO LOWER BEAM (CH 1) → 0.017"

FIGURE A-4(a)

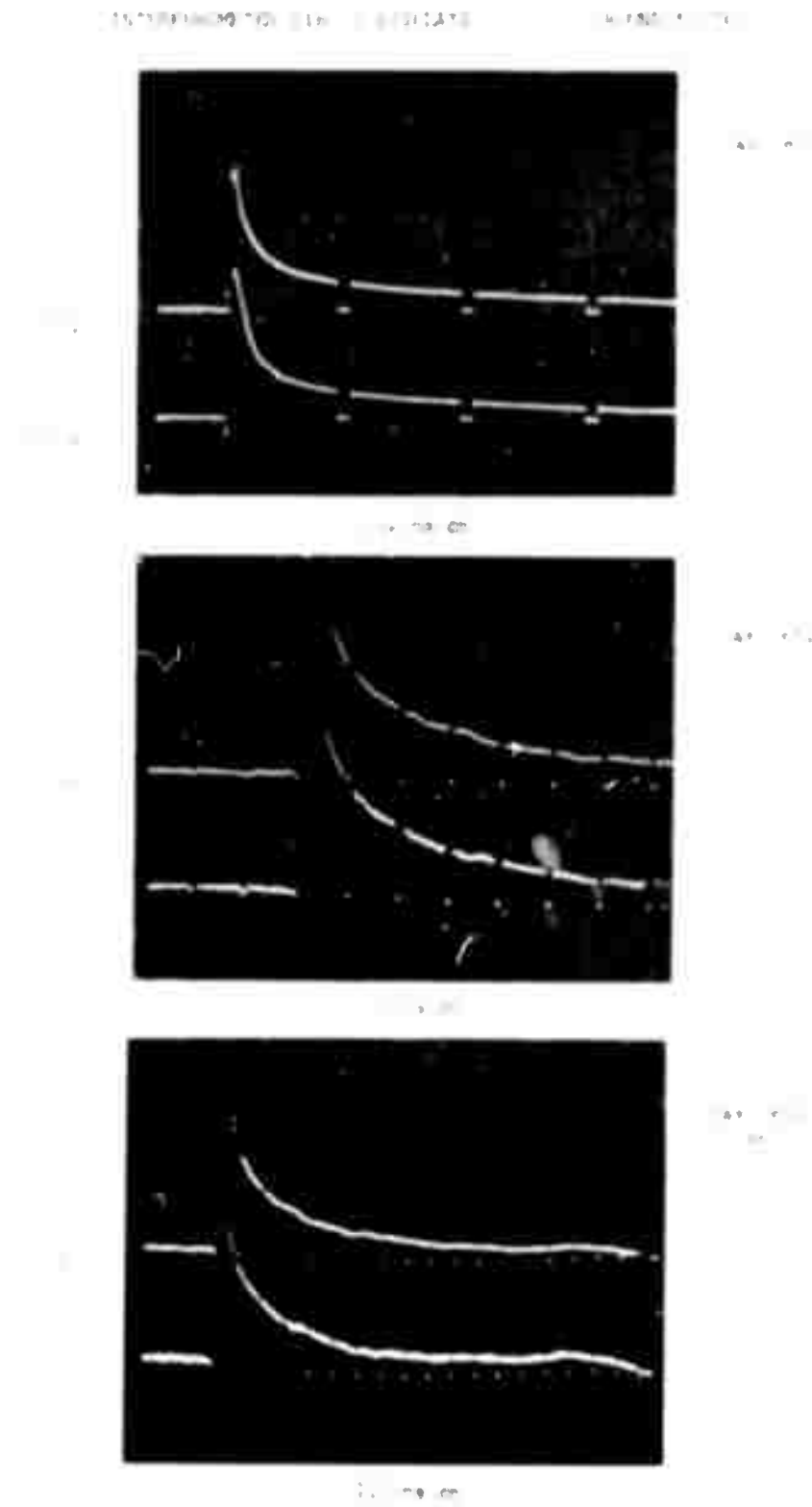


FIGURE A-4(b)

UNCLASSIFIED
60

INTERFEROMETER FIRING REPORT

ROUND → 60.70

PROJECTILE → 2.7" SPHERE

VELOCITY → 14,194 ft/s

PRESSURE → 10 Torr Air

INTERFEROMETER STATION → 272

PROJECTILE POSITION AT STATION 272 → 0.77" High

DISTANCE TO UPPER BEAM (CH 2) → 0.15"

DISTANCE TO LOWER BEAM (CH 1) → 1.48"

FIGURE A-5(a)

INTERFEROMETER 3in : DISPLAYS ROUND 60/70

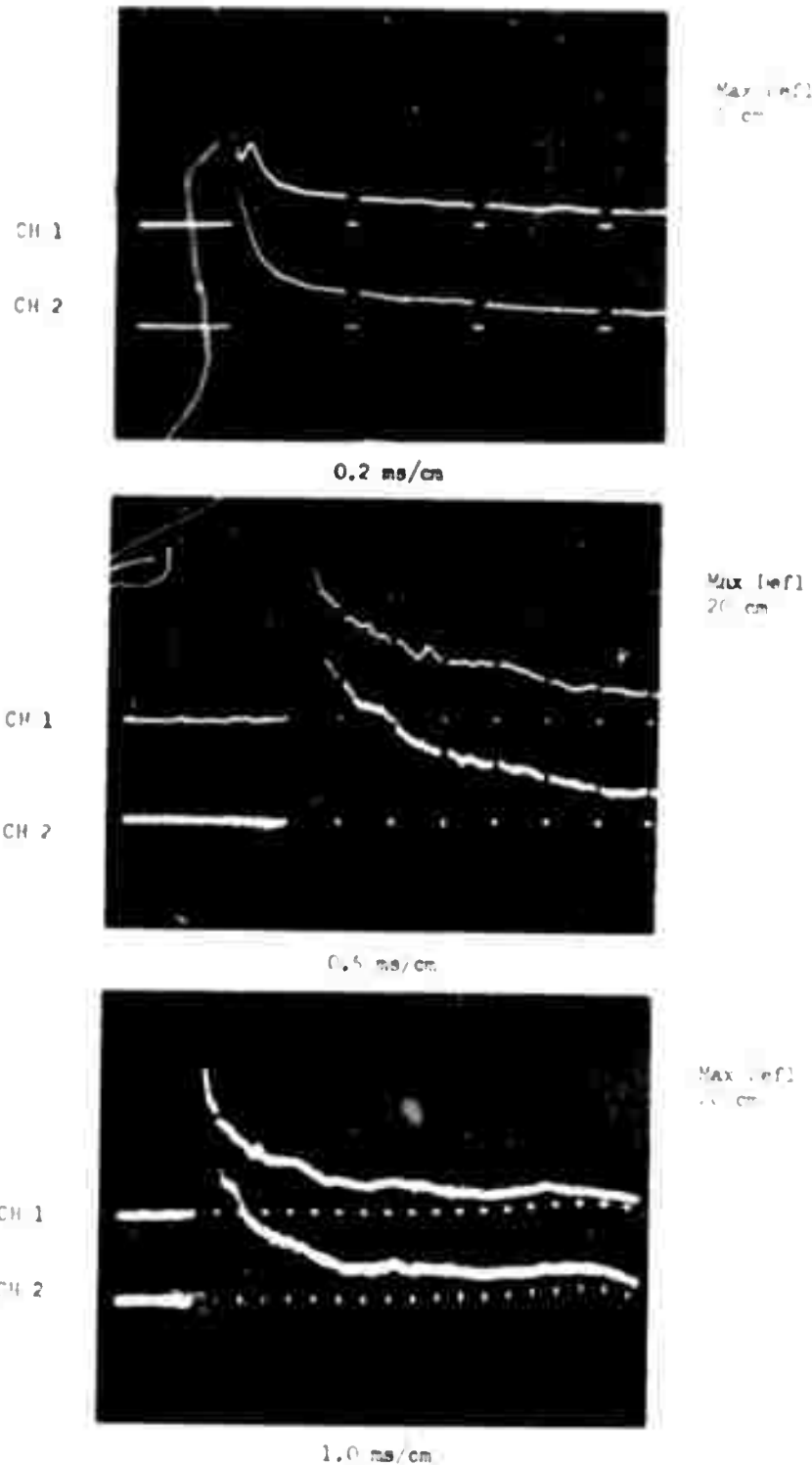


FIGURE A-5 (b)

UNCLASSIFIED

62

INTERFEROMETER FIRING REPORT

ROUND 72.70

PROJECTILE 2.7" SPHERE

VELOCITY 14,400 ft/s

PRESSURE 10 Torr Air

INTERFEROMETER STATION 272

PROJECTILE POSITION AT STATION 272 0.72" High

DISTANCE TO UPPER BEAM (CH 2) 0.20"

DISTANCE TO LOWER BEAM (CH 1) 1.43"

FIGURE A-6(a)

INTERFEROMETER $\sin \phi$ DISPLAYS

ROUND 72/70

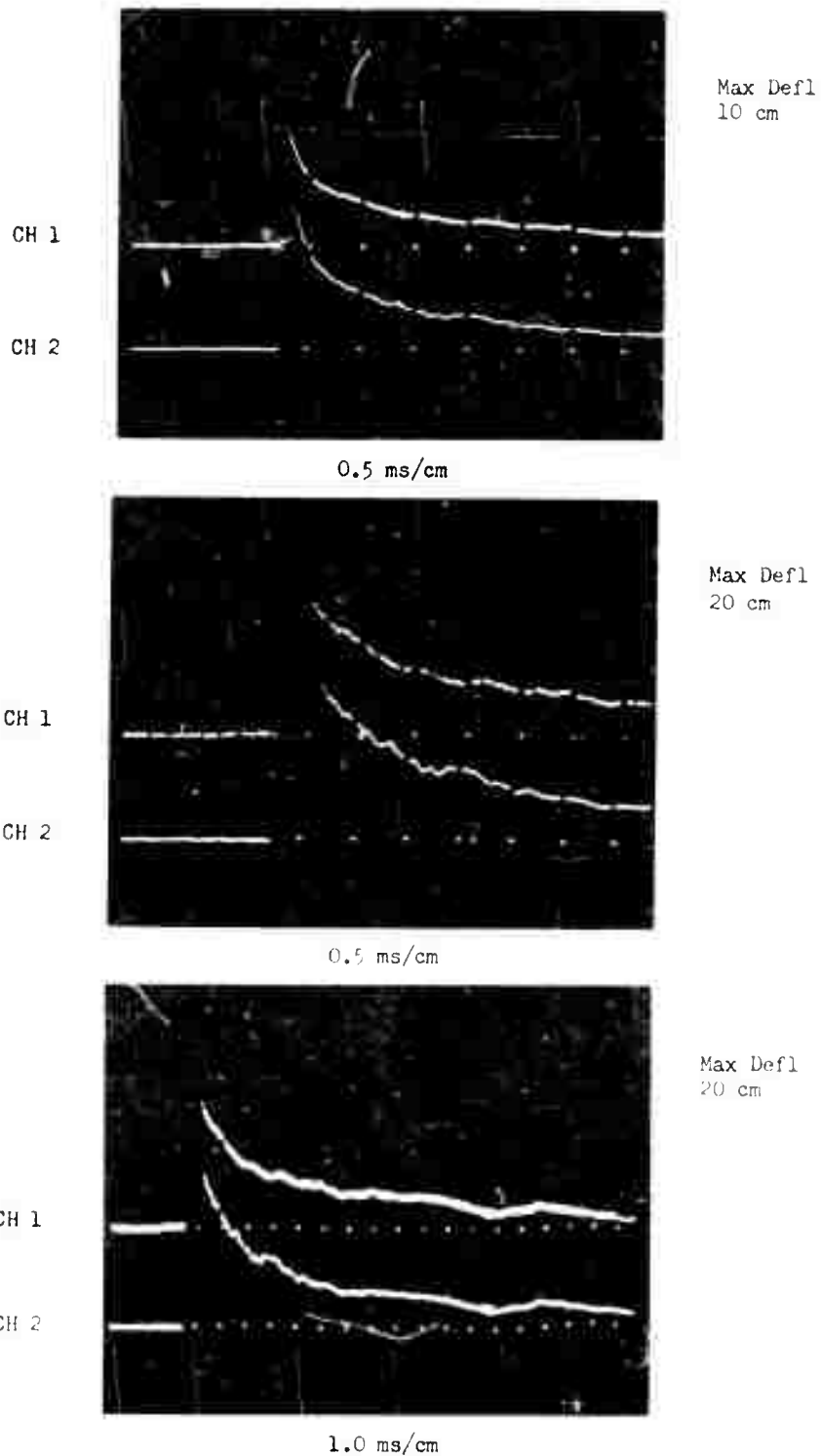


FIGURE A-6(b)

UNCLASSIFIED
64

INTERFEROMETER FIRING REPORT

ROUND → 73.70

PROJECTILE → 2.7" SPHERE

VELOCITY → 14,600 ft/s

PRESSURE → 7.6 Torr Air

INTERFEROMETER STATION → 272

PROJECTILE POSITION AT STATION 272 → 0.35" Low

DISTANCE TO UPPER BEAM (CH 2) → 1.27"

DISTANCE TO LOWER BEAM (CH 1) → 0.35"

FIGURE A-7(a)

INTERFEROMETER Sin ϕ DISPLAYS

ROUND 73/70

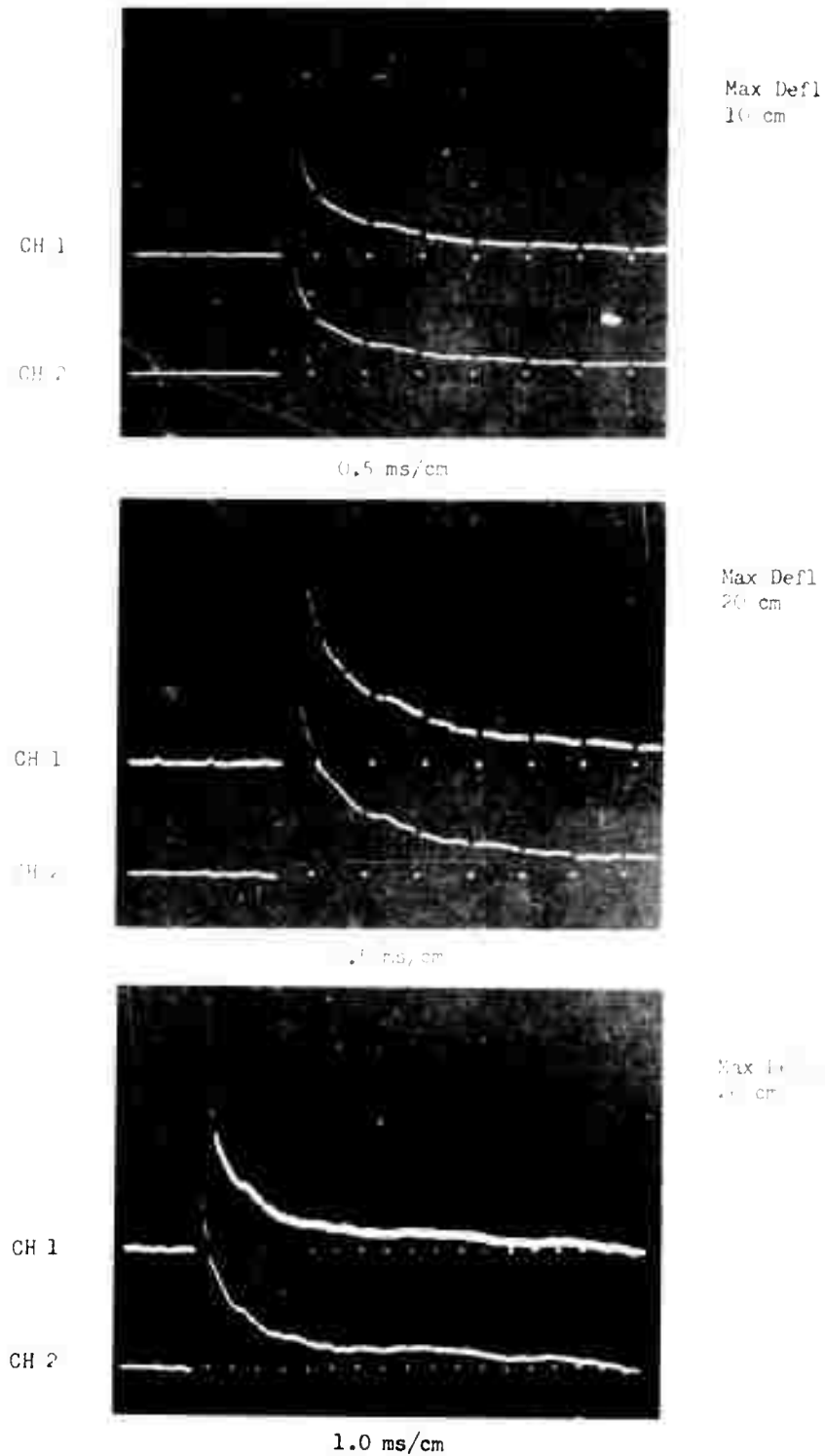


FIGURE A-7(b)

UNCLASSIFIED

66

INTERFEROMETER FIRING REPORT

ROUND 76.70

PROJECTILE 2.7" SPHERE

VELOCITY 14,500 ft/s

PRESSURE 20 Torr Air

INTERFEROMETER STATION 272

PROJECTILE POSITION AT STATION 272 0.99" Low

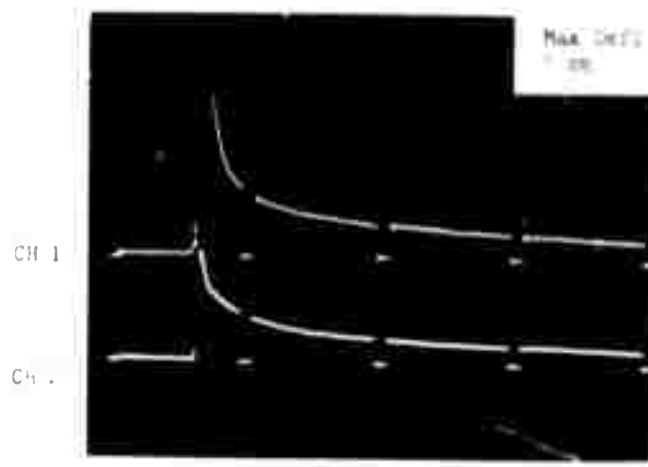
DISTANCE TO UPPER BEAM (CH 2) 1.91"

DISTANCE TO LOWER BEAM (CH 1) 0.28"

FIGURE A-8(a)

INTERFEROMETER SCA & DISPLAYS

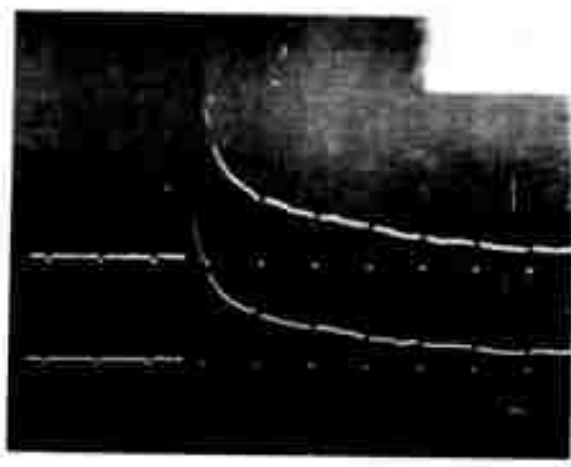
ROUND 7/70



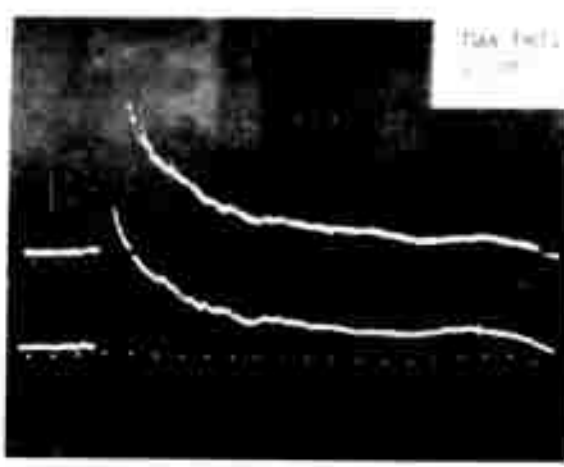
0.5 ms/cm



0.5 ms/cm



0.5 ms/cm



1.0 ms/cm

FIGURE A-8(b)

UNCLASSIFIED

68

INTERFEROMETER FIRING REPORT

ROUND 91.70

PROJECTILE 2.7" SPHERE

VELOCITY 14,500 ft/s

PRESSURE 10 Torr Air

INTERFEROMETER STATION 272

PROJECTILE POSITION AT STATION 272 1.18" High

DISTANCE TO UPPER BEAM (CH 2) 0.26"

DISTANCE TO LOWER BEAM (CH 1) 1.88"

FIGURE A-9(a)

UNCLASSIFIED

69

INTERFEROMETER SIN ♦ DISPLAYS

ROUND 91/70

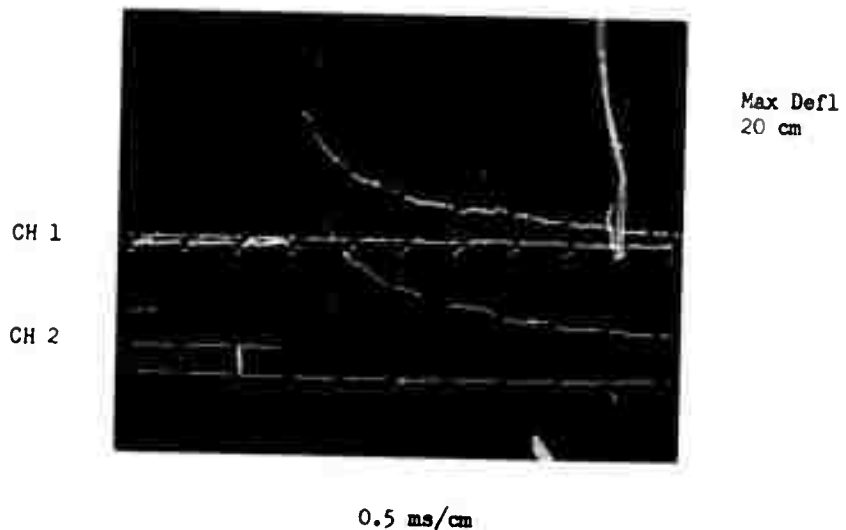
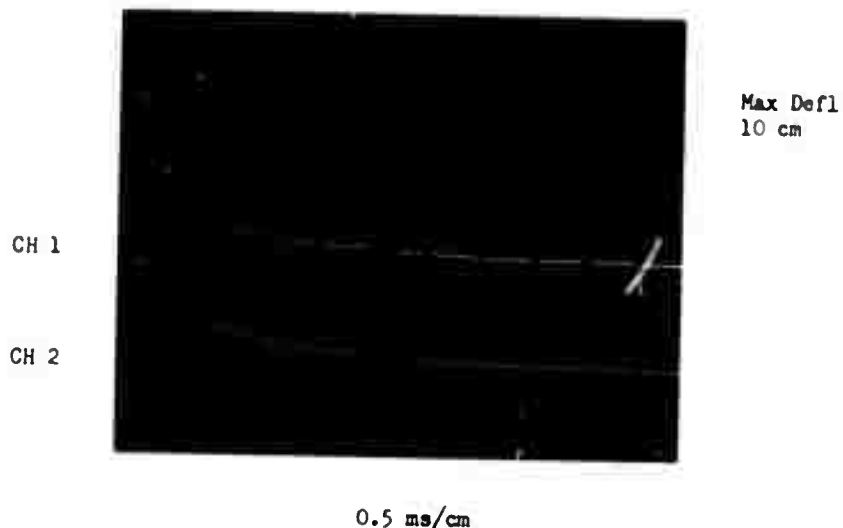


FIGURE A-9(b)

UNCLASSIFIED

70

INTERFEROMETER FIRING REPORT

ROUND → 93.70

PROJECTILE → 2.7" SPHERE

VELOCITY → 14.5 Kft/s

PRESSURE → 10 Torr Air

INTERFEROMETER STATION → 272

PROJECTILE POSITION AT STATION 272 → 0.34" Low

DISTANCE TO UPPER BEAM (CH 2) → 1.260"

DISTANCE TO LOWER BEAM (CH 1) → 0.365"

FIGURE A-10(a)

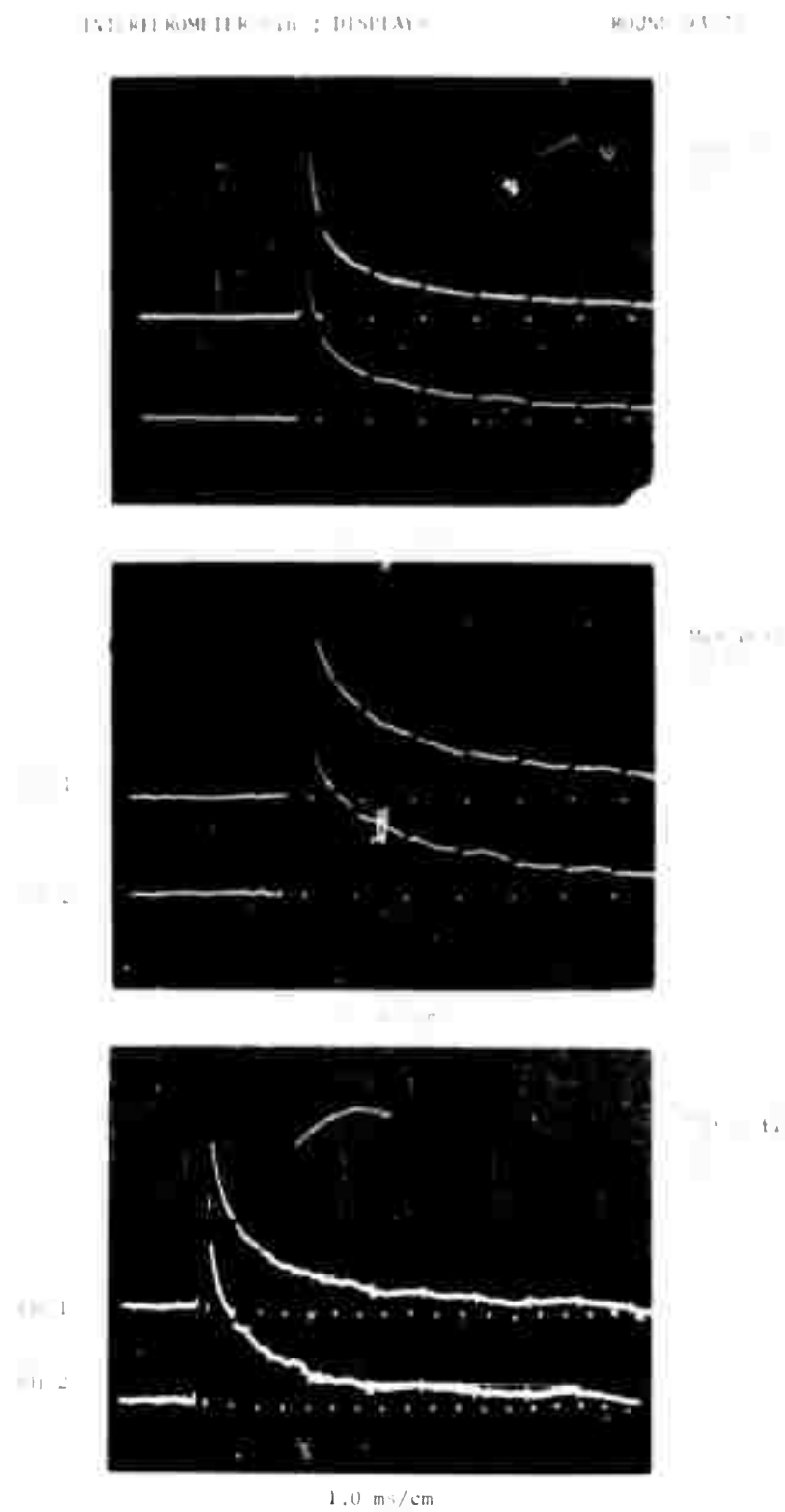


FIGURE A-10(b)

UNCLASSIFIED

72

INTERFEROMETER FIRING REPORT

ROUND → 94.70

PROJECTILE → 2.7" SPHERE

VELOCITY → 14.5 Kft/s

PRESSURE → 10 Torr Air

INTERFEROMETER STATION → 272

PROJECTILE POSITION AT STATION 272 → 0.174" Low

DISTANCE TO UPPER BEAM (CH 2) → 1.094"

DISTANCE TO LOWER BEAM (CH 1) → 0.531"

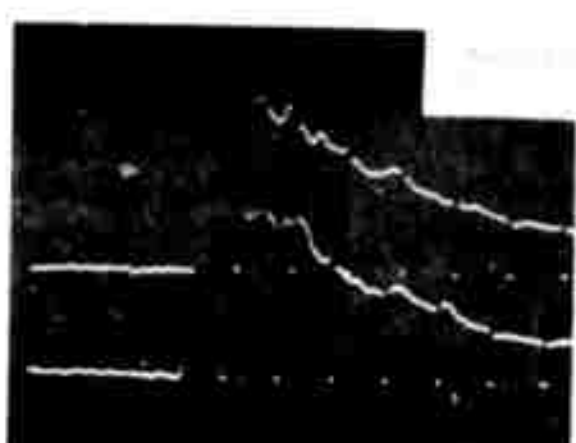
FIGURE A-11(a)

INTERFEROMETER DISPLAYS

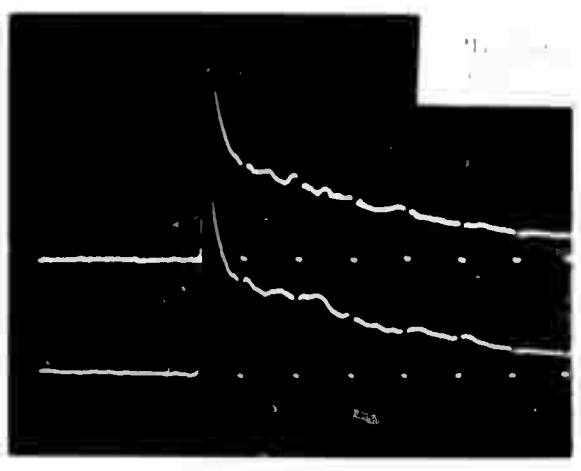
ROUND 94-70



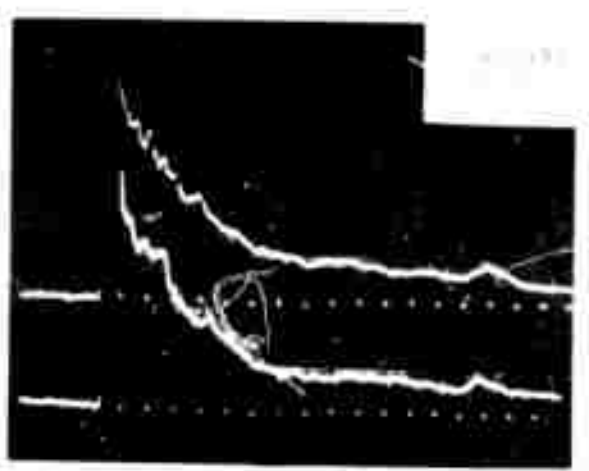
0.2 ms/cm



0.1 ms/cm



0.5 ms/cm



1.0 ms/cm

FIGURE A-11(b)

UNCLASSIFIED

74

INTERFEROMETER FIRING REPORT

ROUND → 95.70

PROJECTILE → 2.7" SPHERE

VELOCITY → 14,500 ft/s

PRESSURE → 10 Torr Air

INTERFEROMETER STATION → 272

PROJECTILE POSITION AT STATION 272 → 1.30" High

DISTANCE TO UPPER BEAM (CH 2) → 0.38"

DISTANCE TO LOWER BEAM (CH 1) → 2.00"

FIGURE A-12(a)

UNCLASSIFIED

75

INTERFEROMETER Sin φ DISPLAYS

ROUND 95/70

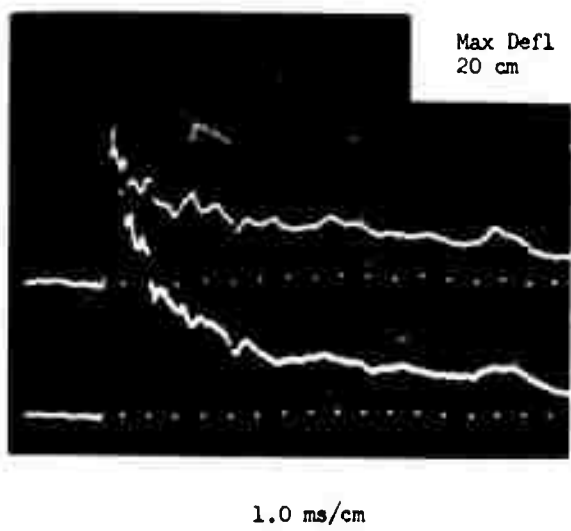
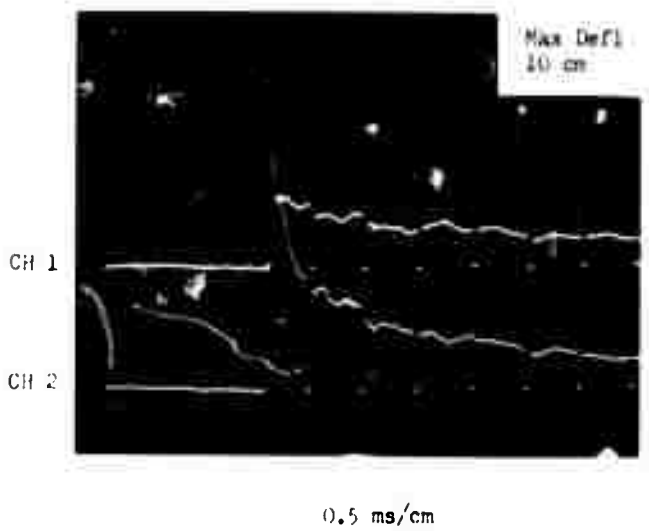
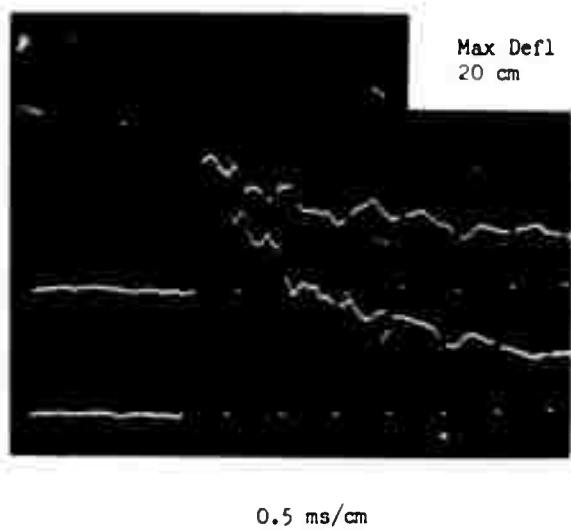
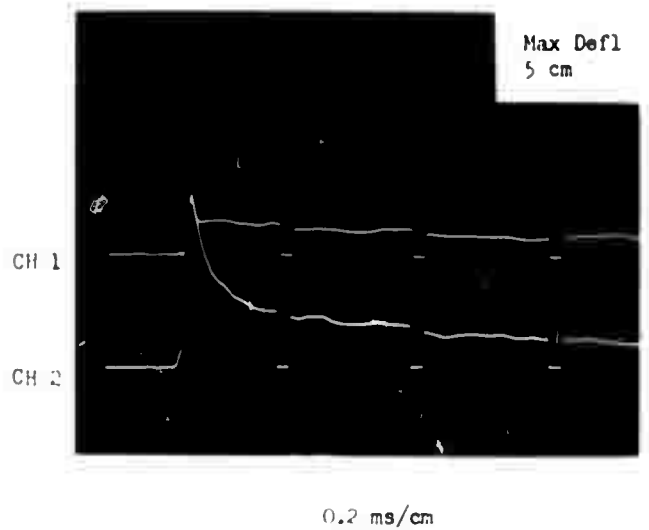


FIGURE A-12(b)

UNCLASSIFIED

76

INTERFEROMETER FIRING REPORT

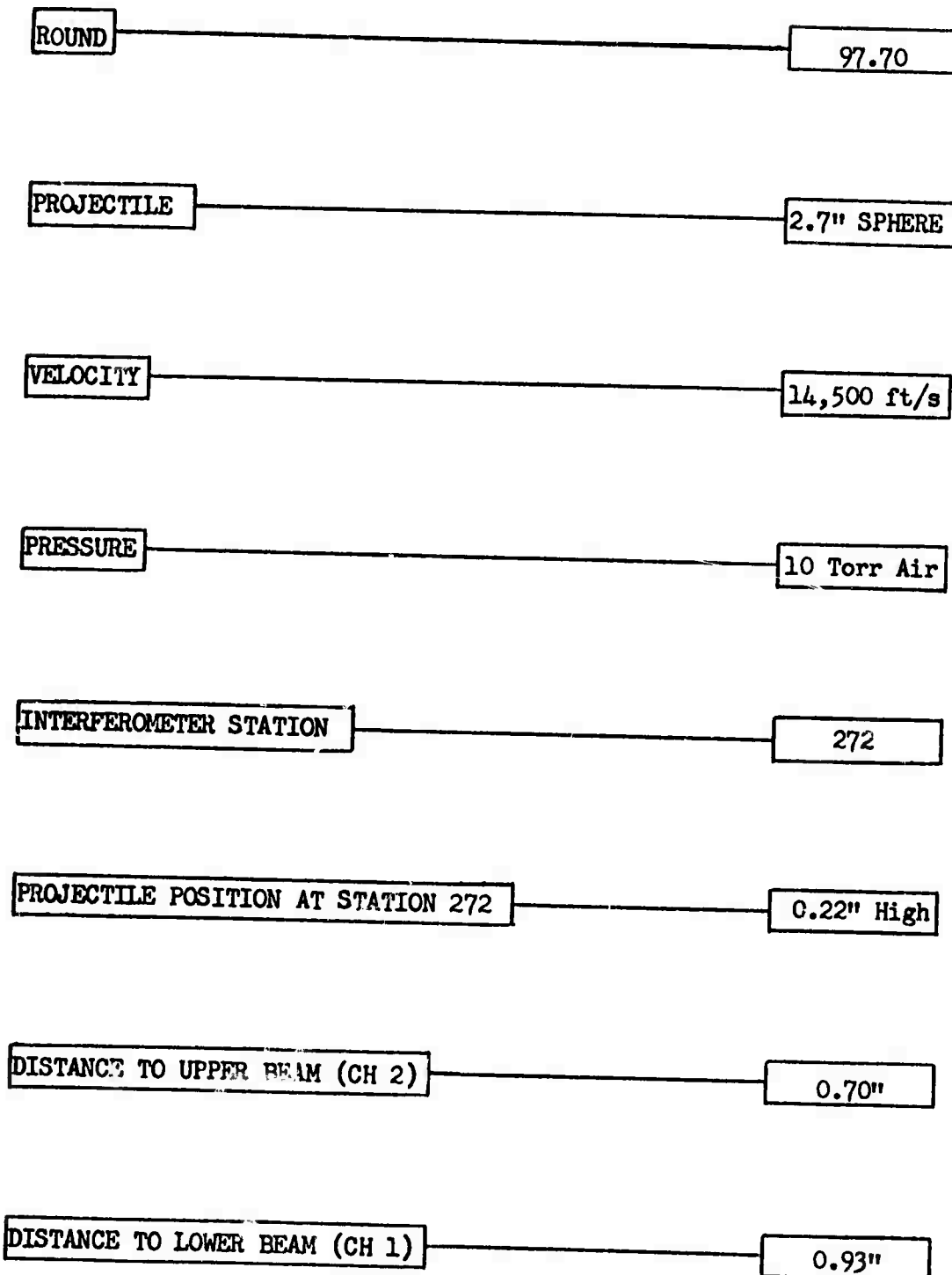


FIGURE A-13(a)

INTERFEROMETER $\sin \phi$ DISPLAYS

ROUND 97/70

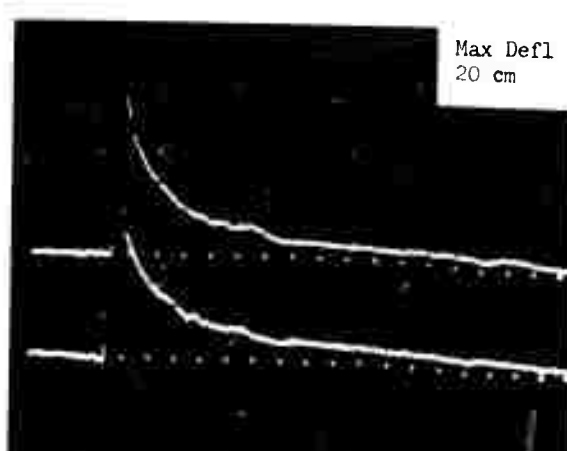
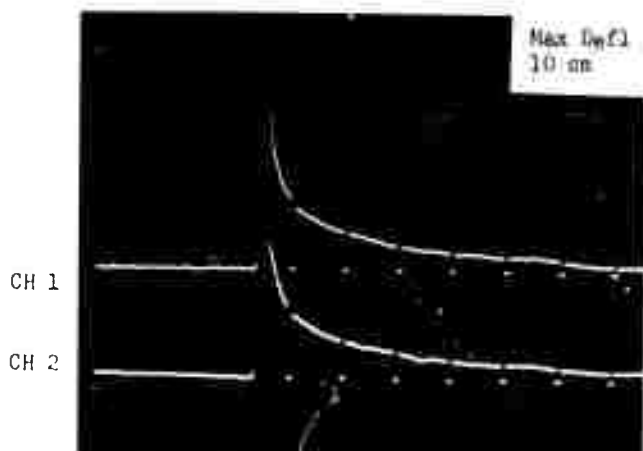
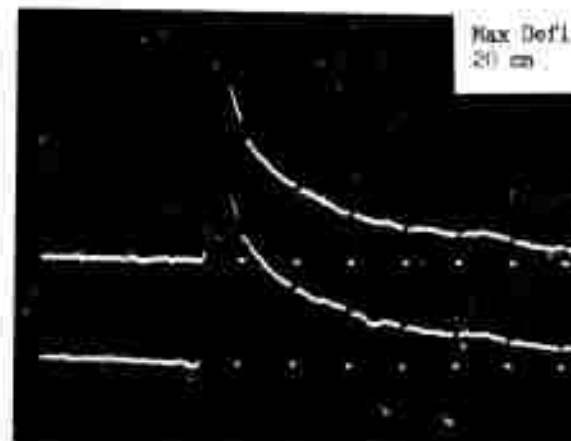


FIGURE A-13(b)

UNCLASSIFIED

78

INTERFEROMETER FIRING REPORT

ROUND → 98.70

PROJECTILE → 2.7" SPHERE

VELOCITY → 14,500 ft/s

PRESSURE → 10 Torr Air

INTERFEROMETER STATION → 272

PROJECTILE POSITION AT STATION 272 → 0.38" High

DISTANCE TO UPPER BEAM (CH 2) → 0.54"

DISTANCE TO LOWER BEAM (CH 1) → 1.08"

FIGURE A-14(a)

INTERFEROMETER Sin φ DISPLAYS

ROUND 98/70

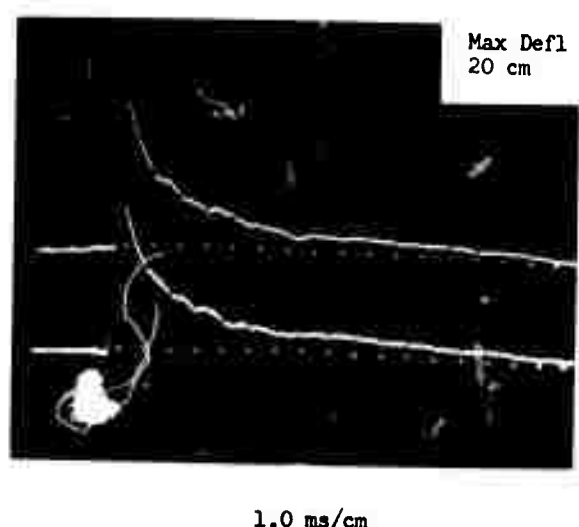
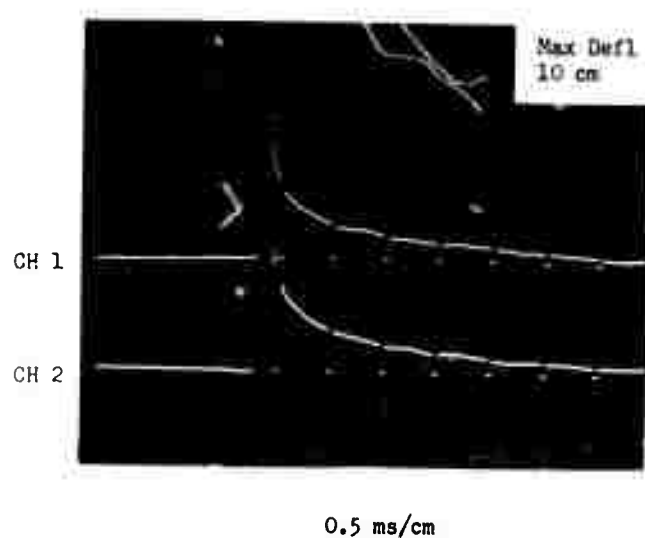
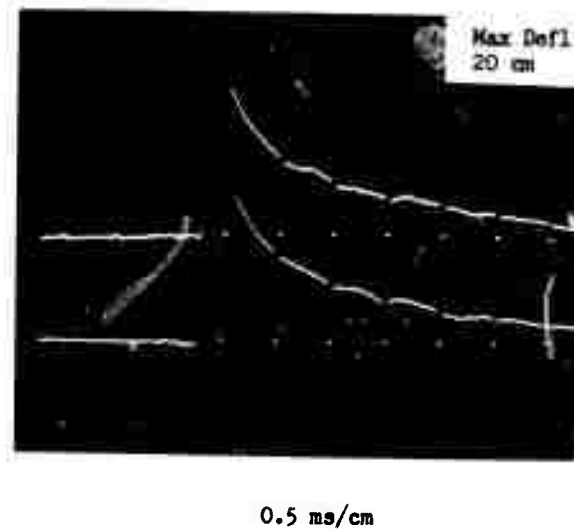
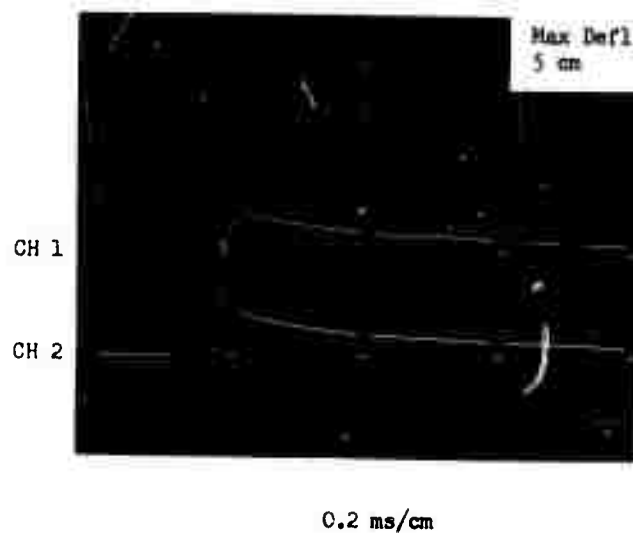


FIGURE A-14(b)

UNCLASSIFIED

80

INTERFEROMETER FIRING REPORT

ROUND 99.70

PROJECTILE 2.7" SPHERE

VELOCITY 14,413 ft/s

PRESSURE 10 Torr Air

INTERFEROMETER STATION 272

PROJECTILE POSITION AT STATION 272 1.18" High

DISTANCE TO UPPER BEAM (CH 2) 0.26"

DISTANCE TO LOWER BEAM (CH 1) 1.28"

FIGURE A-15(a)

INTERFEROMETER $\sin \phi$ DISPLAYS

ROUND 99/70

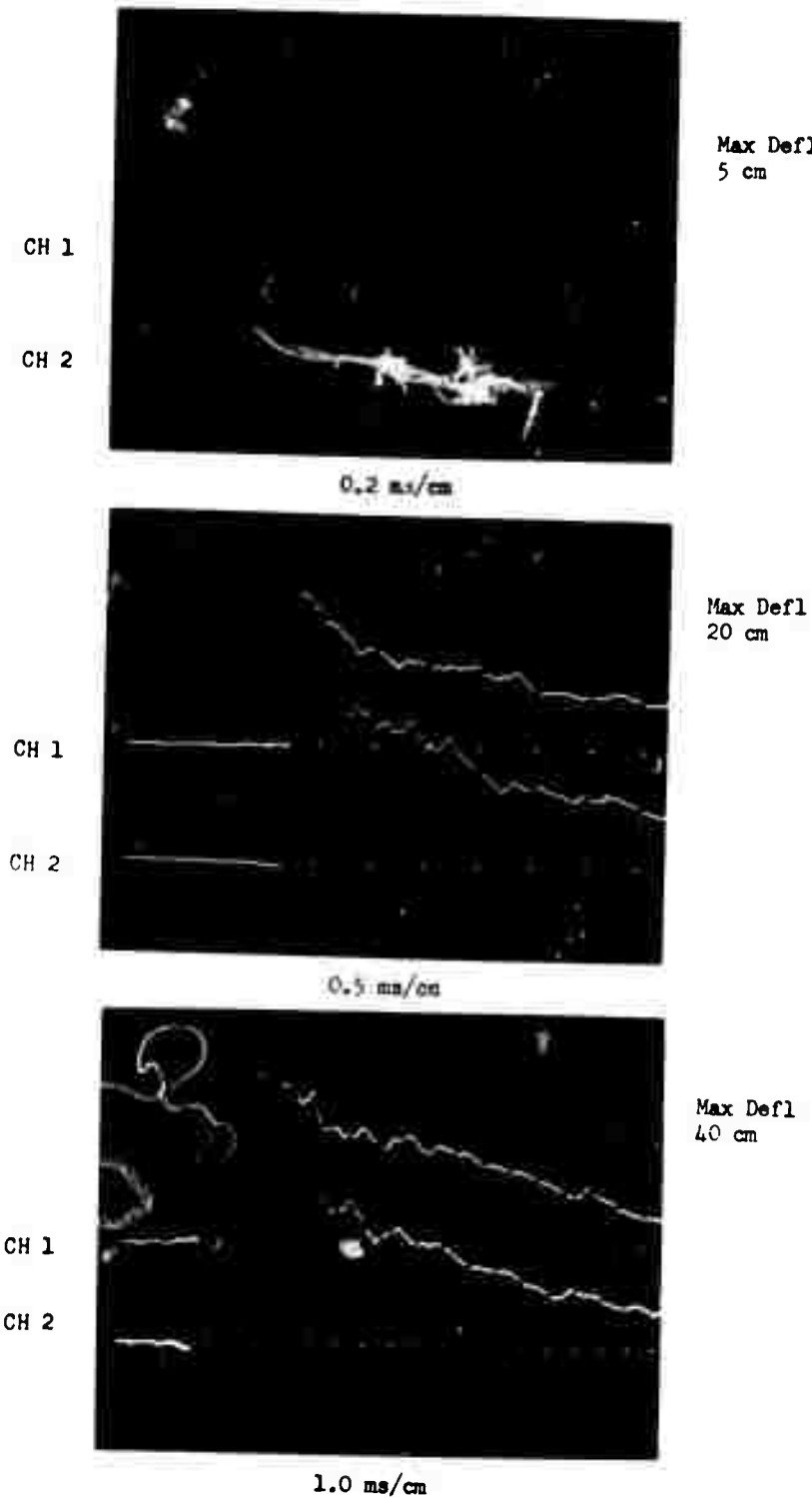


FIGURE A-15(b)

UNCLASSIFIED
82

INTERFEROMETER FIRING REPORT

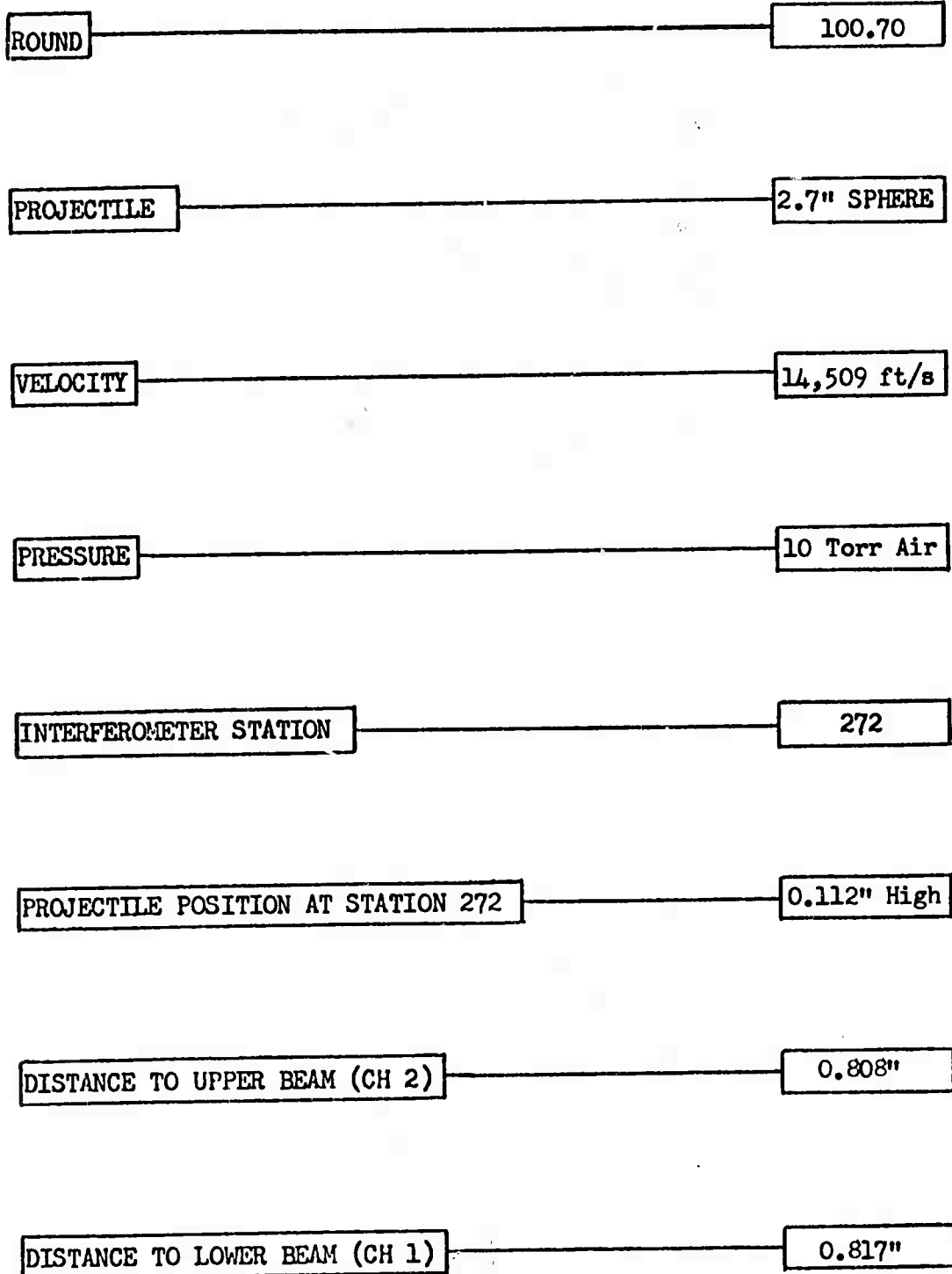


FIGURE A-16(a)

INTERFEROMETER $\sin \phi$ DISPLAYS

ROUND 100/70

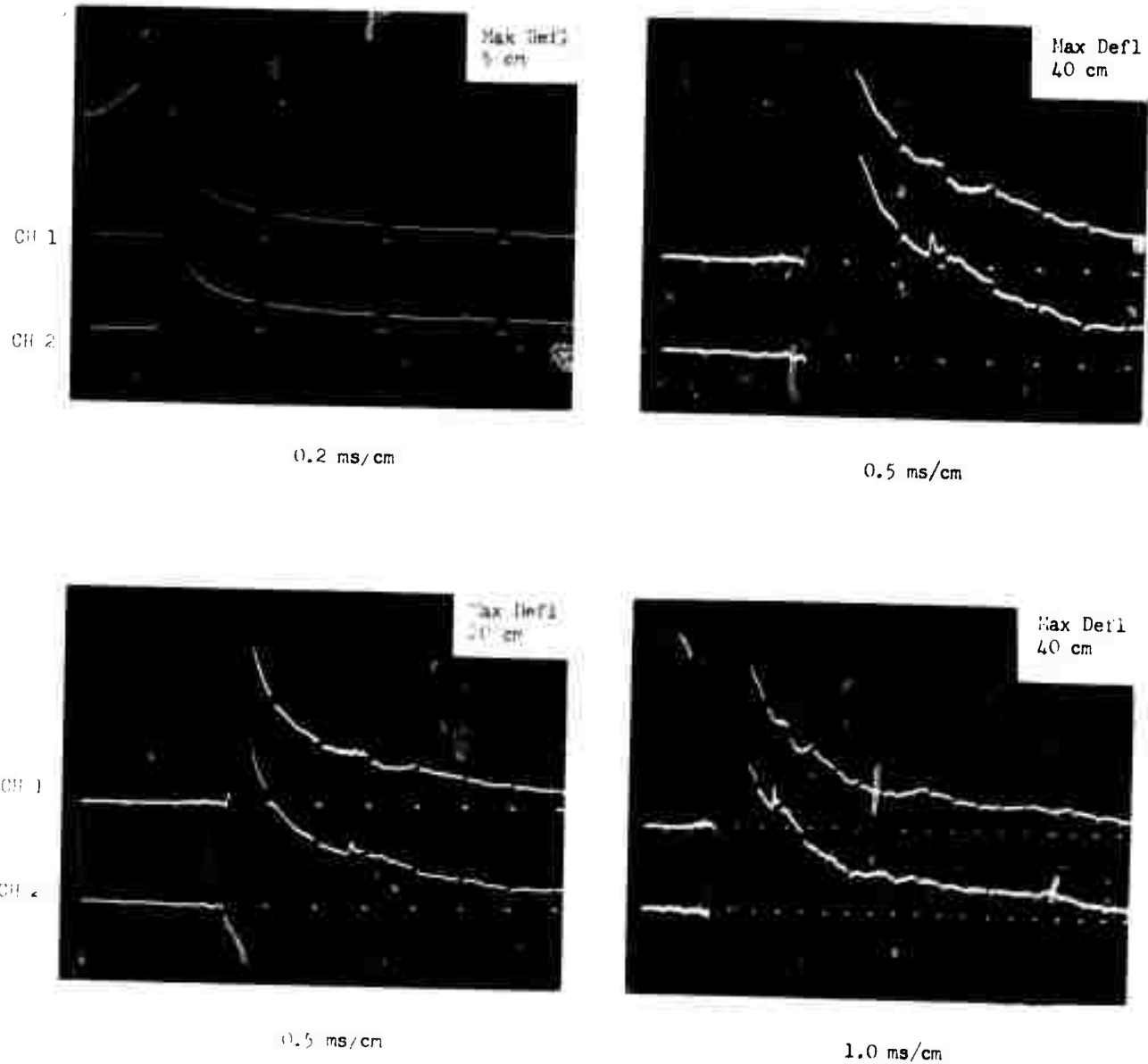


FIGURE A-16(b)

APPENDIX B

**Electron Densities on the axis and Electron Density Radii
from Simultaneous Solutions Air Atmospheres**

The figure numbers in this appendix correspond
to the figure numbers in Appendix A.

Figures B-4b, 4d, 7d, 10b, 10d, 11b, 11d, 16b,
16d are unavailable

UNCLASSIFIED

86

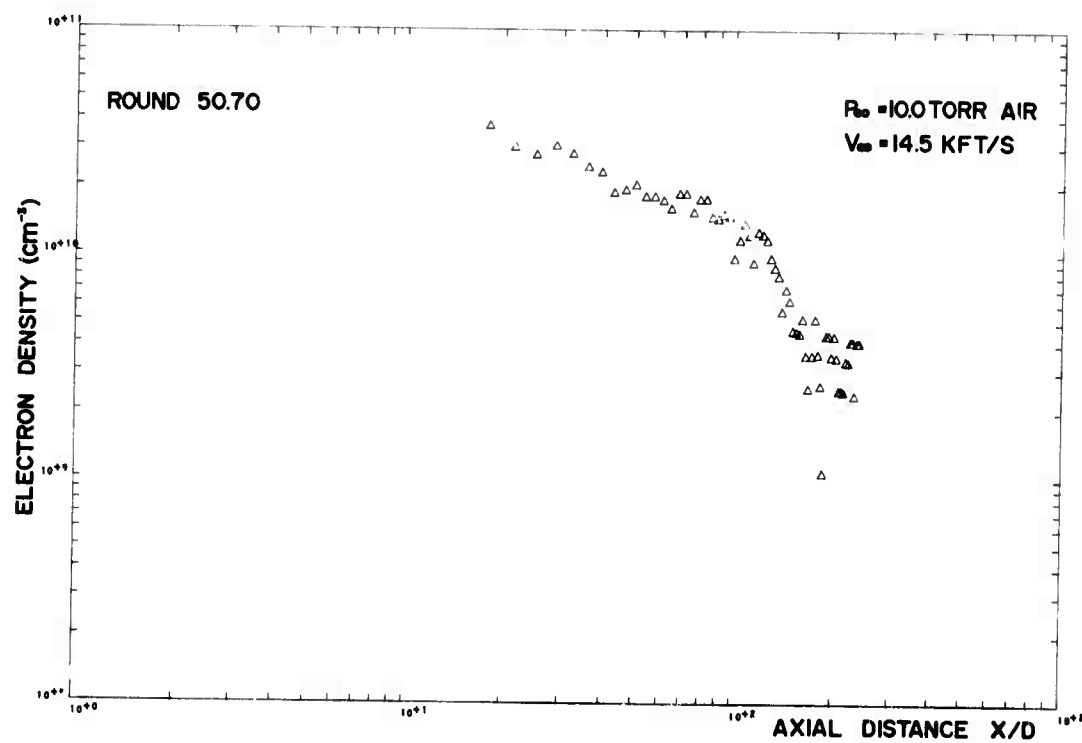


FIGURE B-1(a)

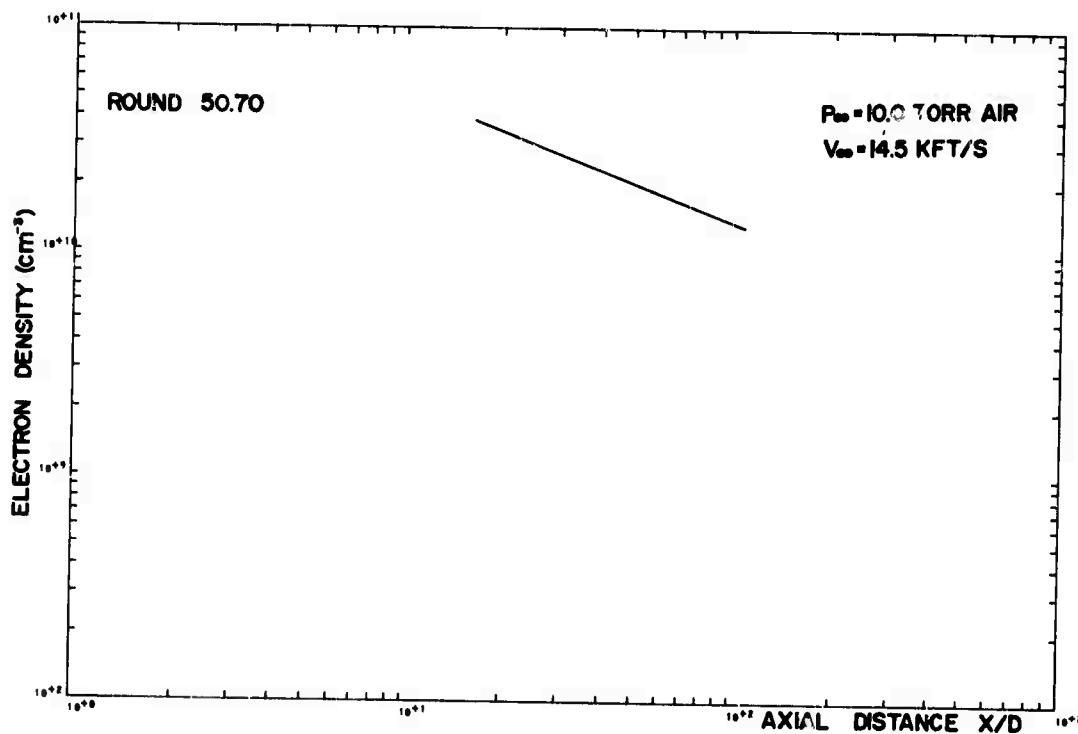


FIGURE B-1(b)

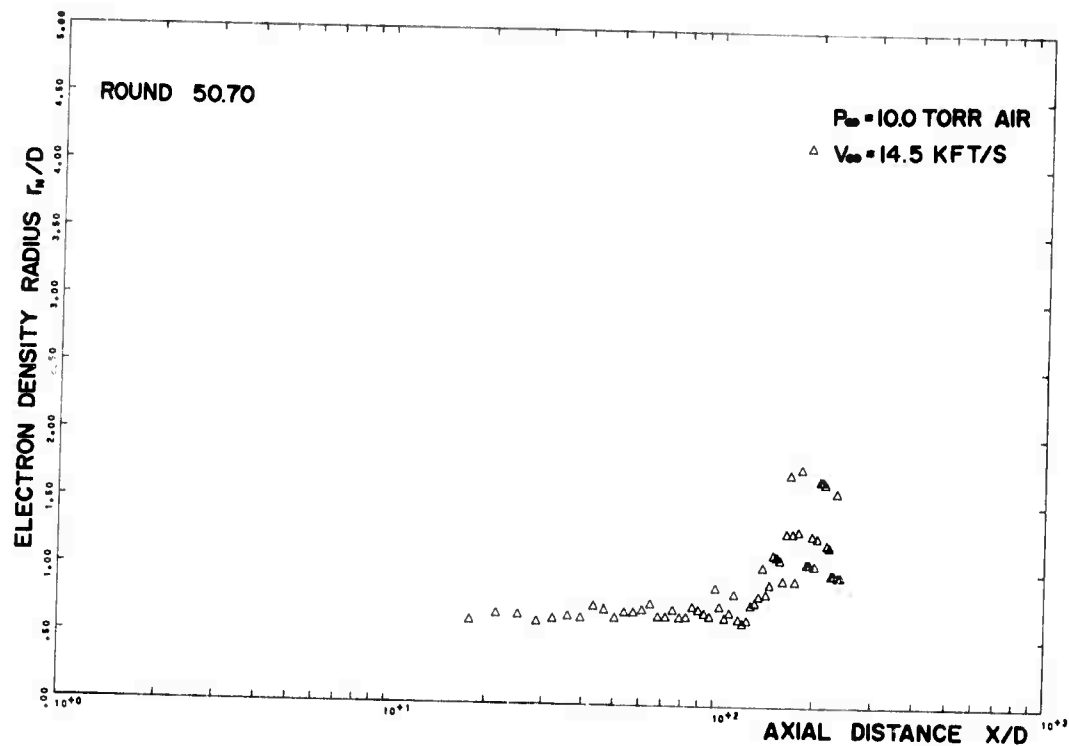


FIGURE B-1(c)

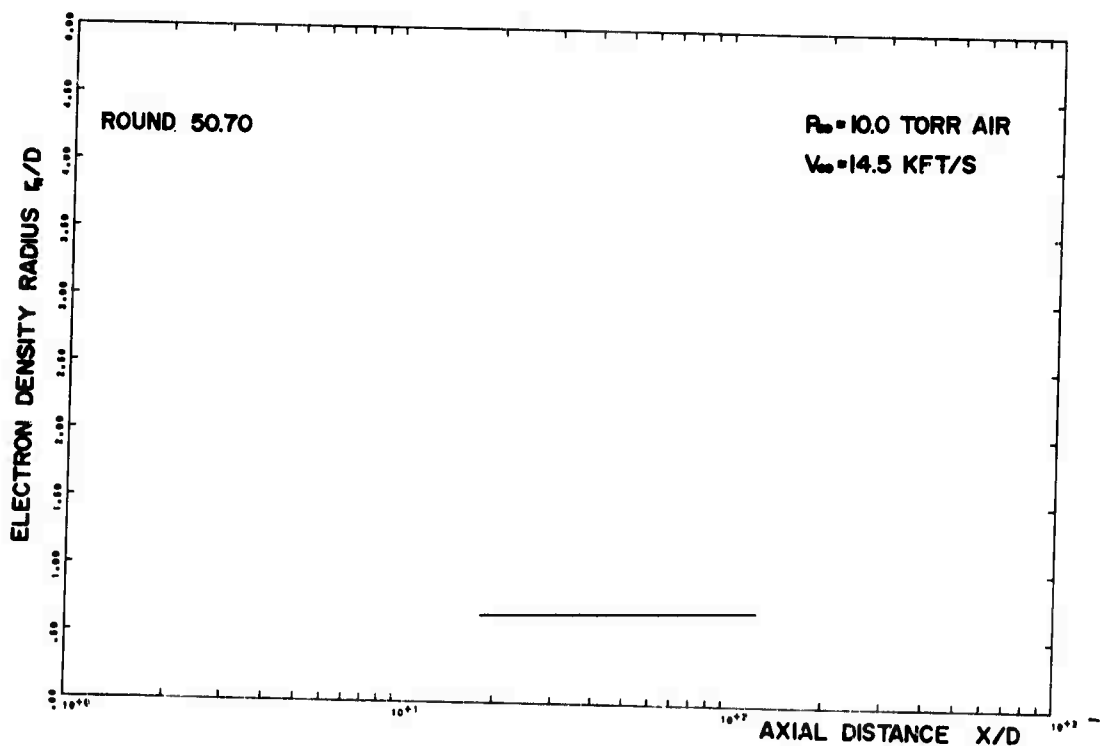


FIGURE B-1(d)

UNCLASSIFIED

88

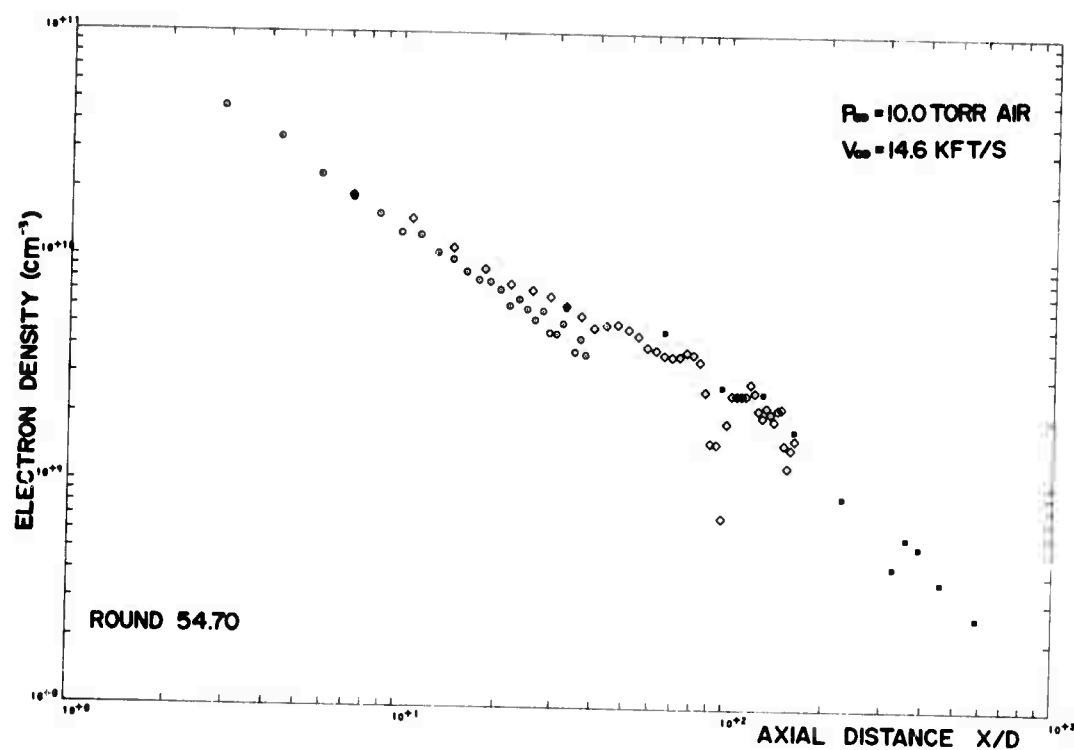


FIGURE B-2(a)

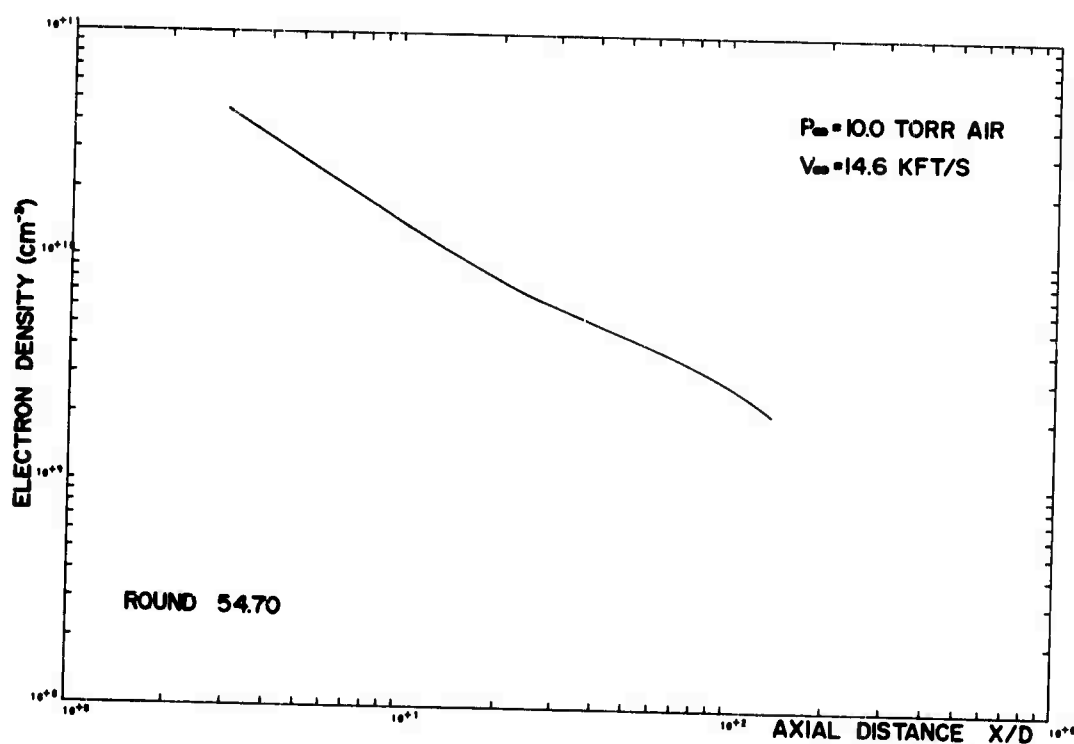


FIGURE B-2(b)

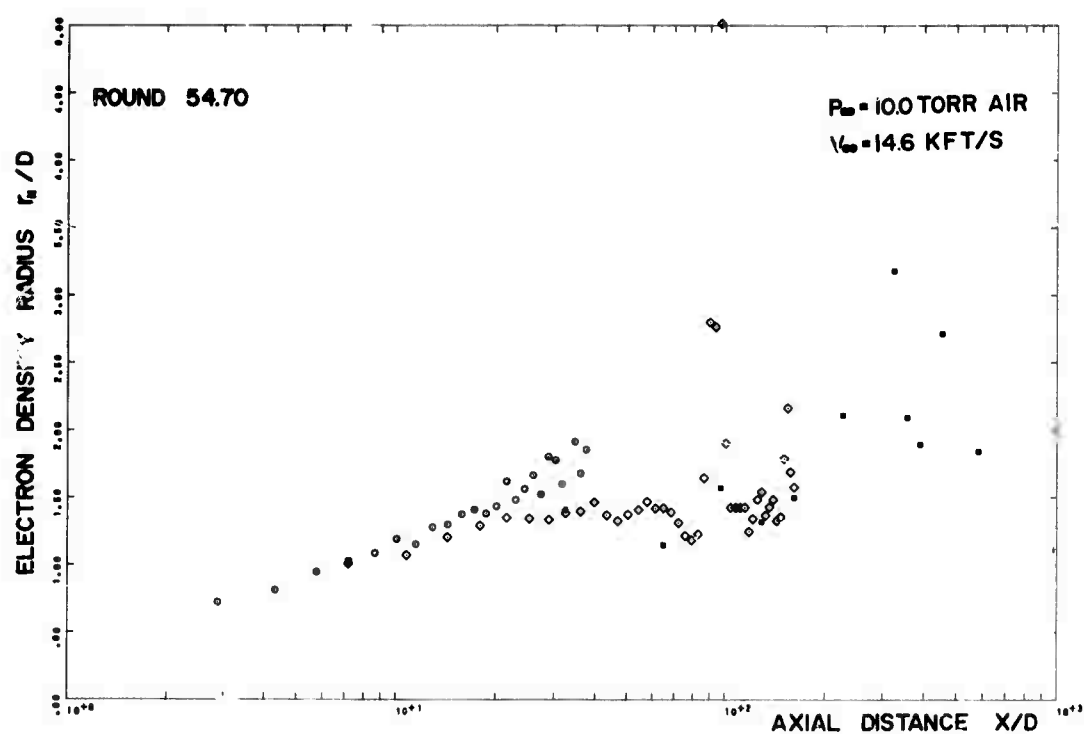


FIGURE B-2(c)

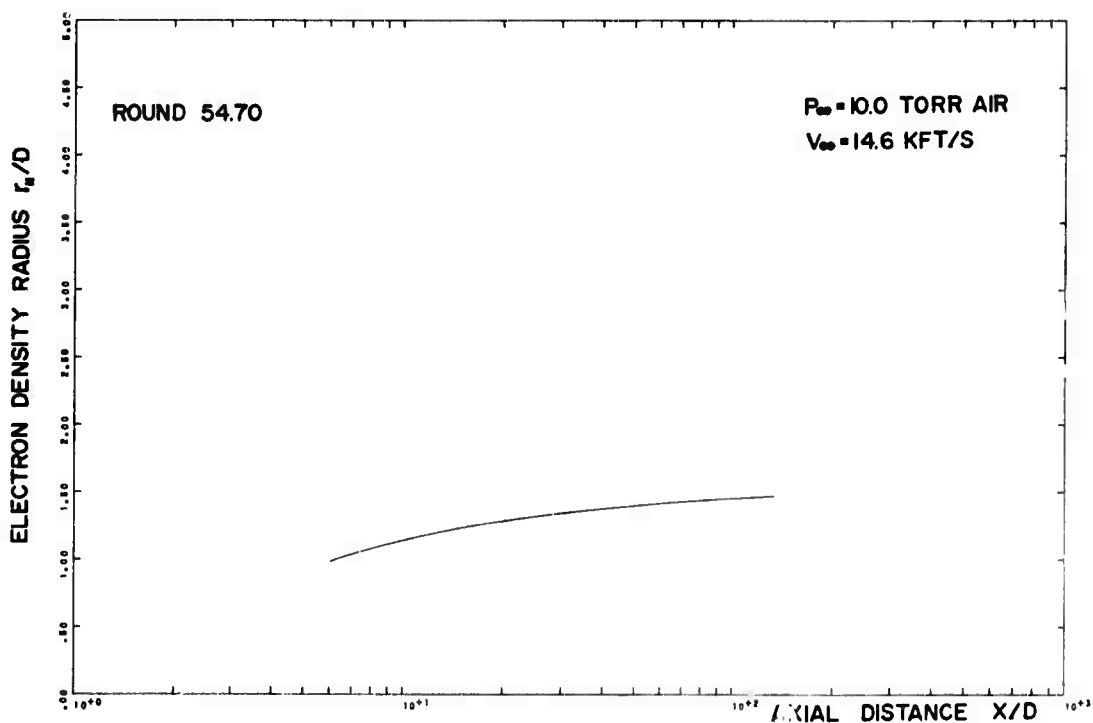


FIGURE B-2(d)

UNCLASSIFIED

90

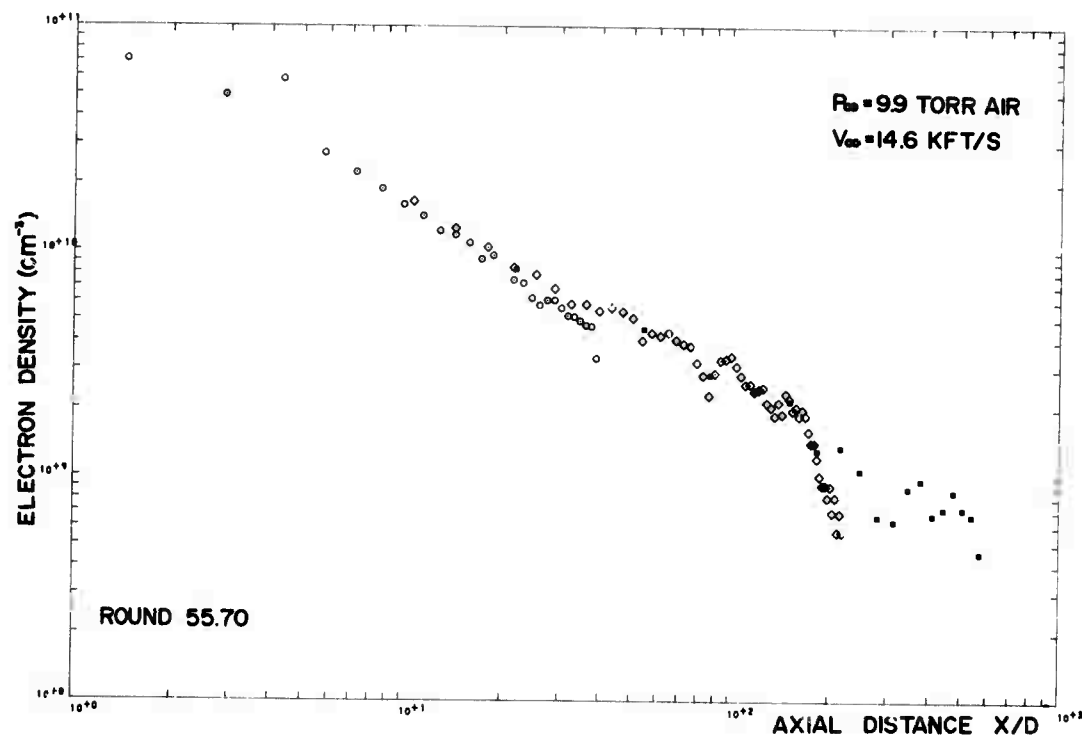


FIGURE B-3(a)

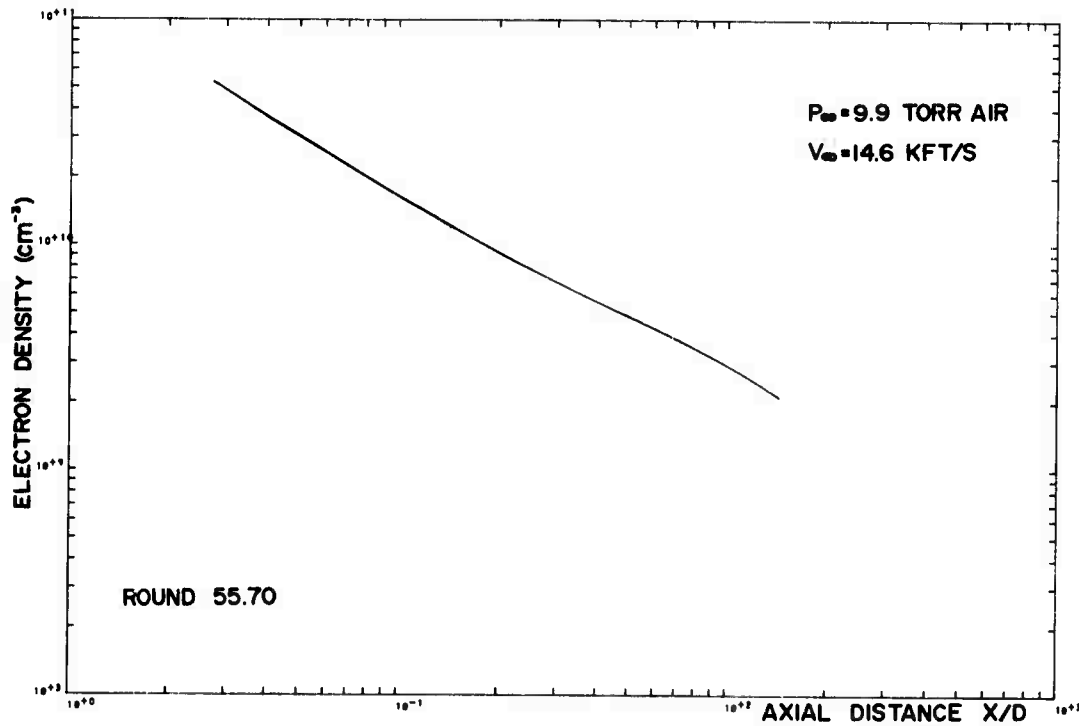


FIGURE B-3(b)

UNCLASSIFIED

91

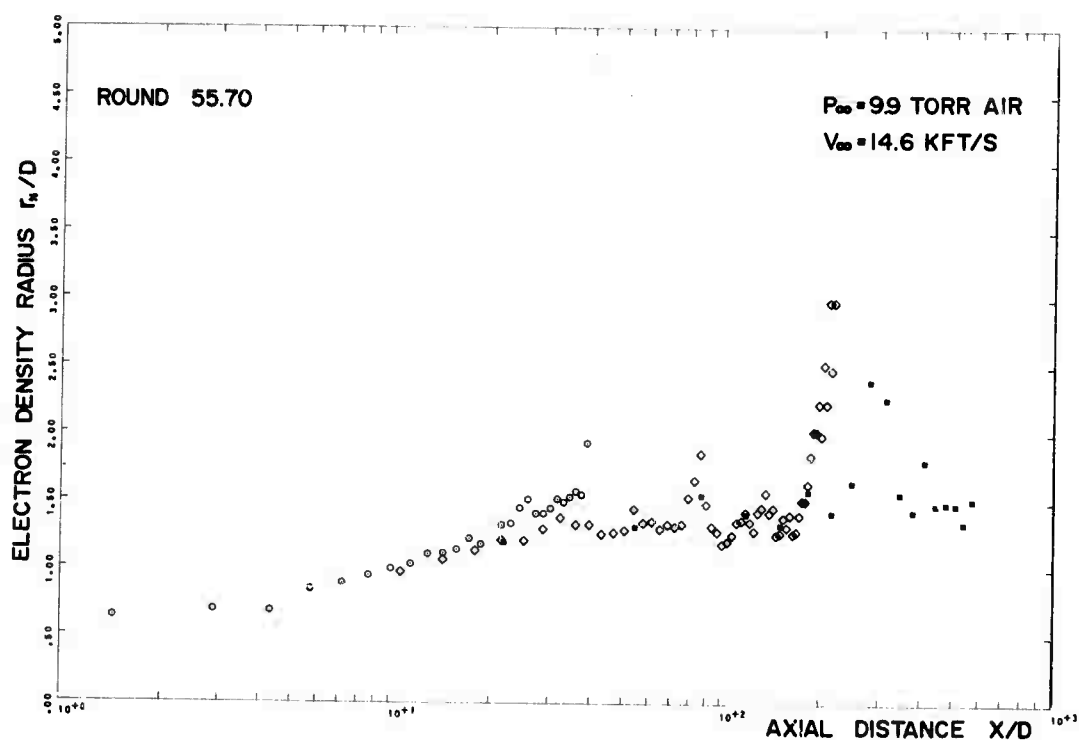


FIGURE B-3(c)

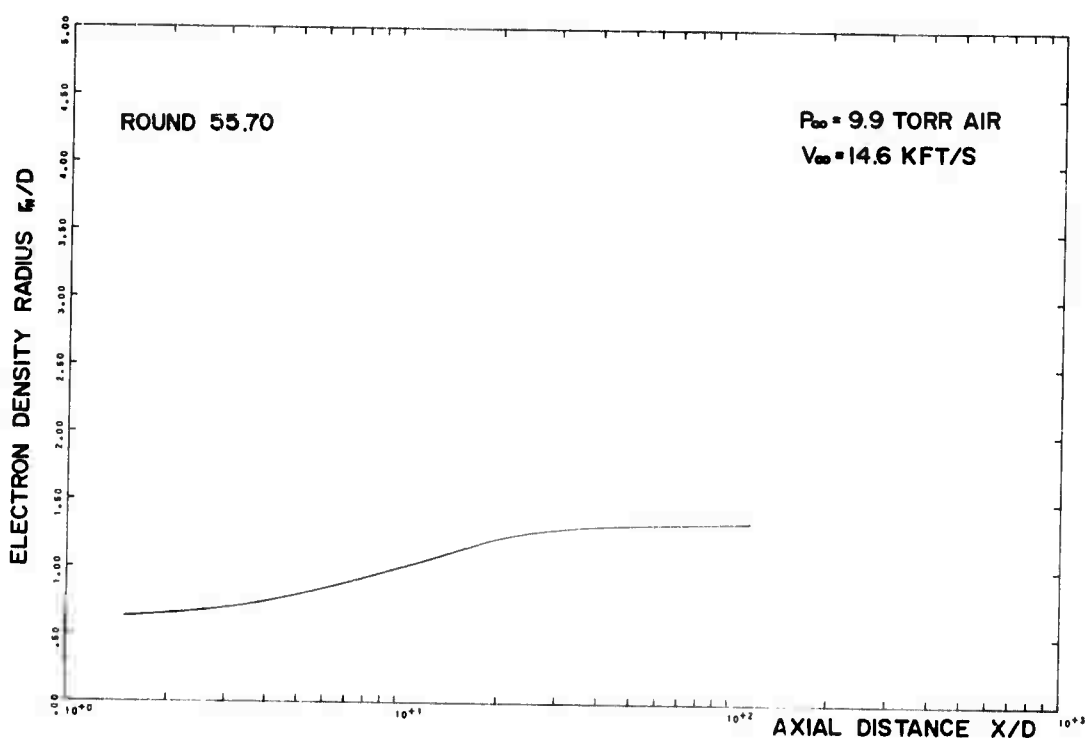


FIGURE B-3(d)

UNCLASSIFIED
92

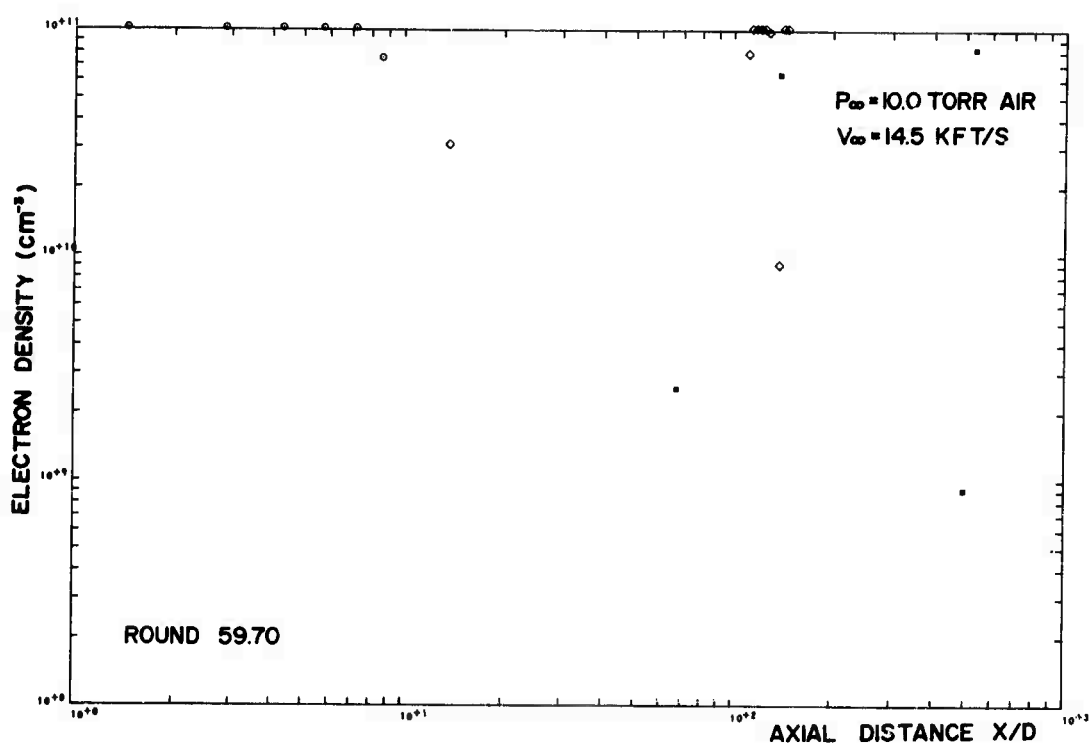


FIGURE B-4(a)

UNCLASSIFIED
93

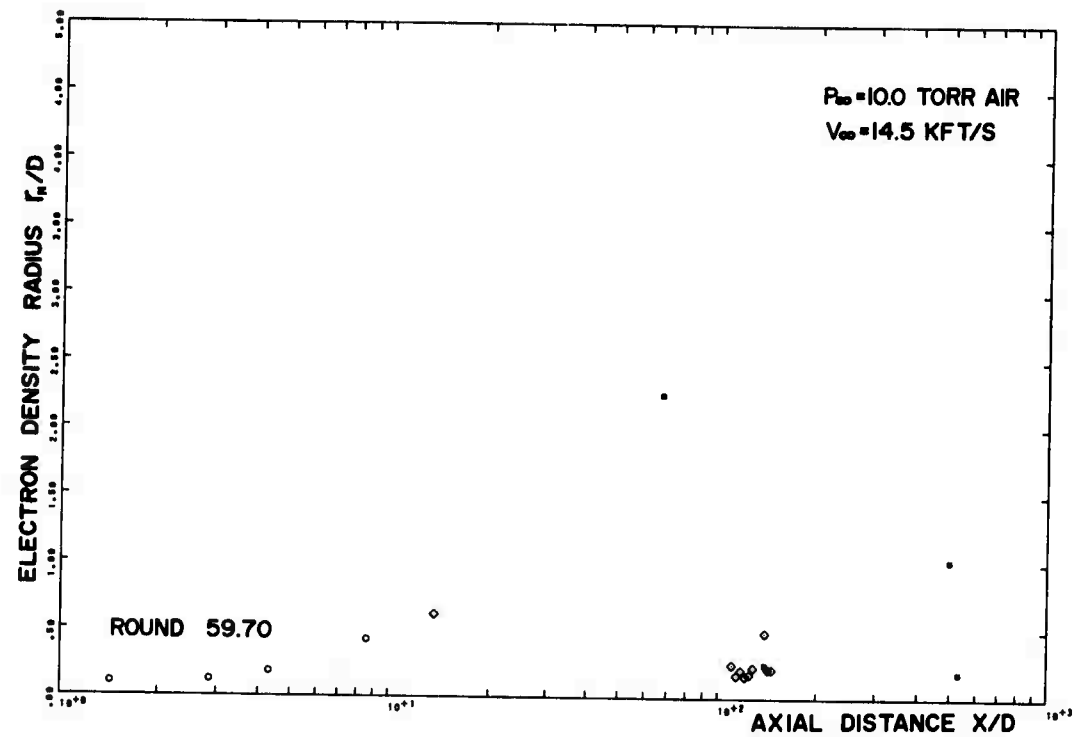


FIGURE B-4(c)

UNCLASSIFIED

94

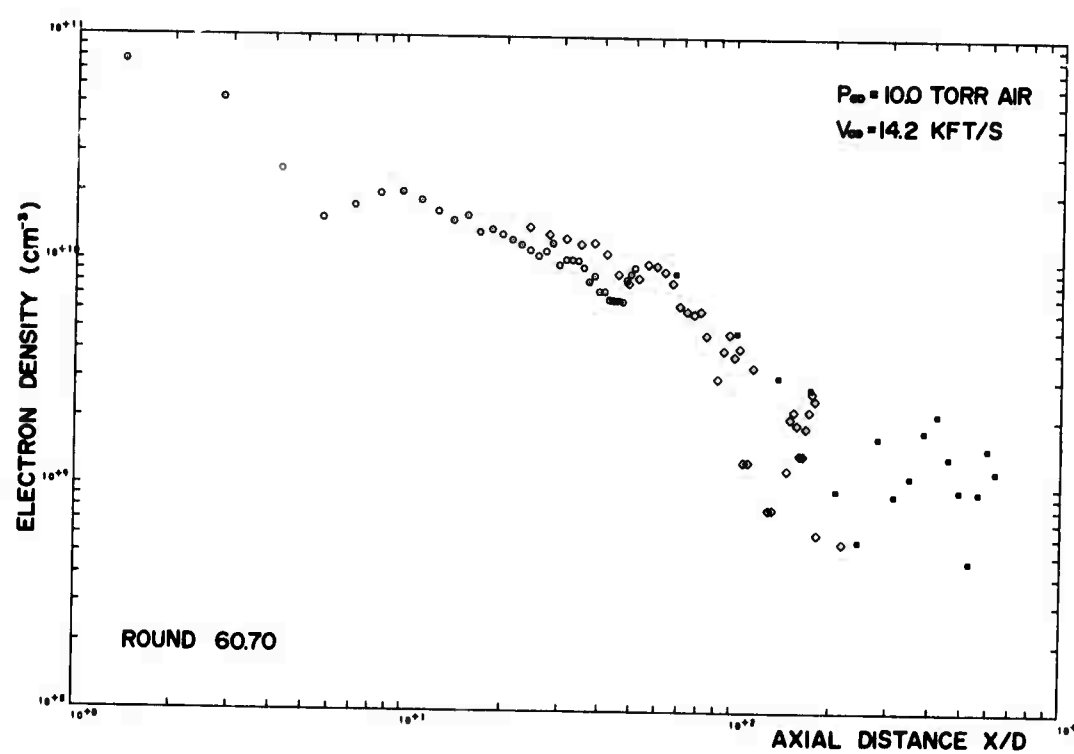


FIGURE B-5(a)

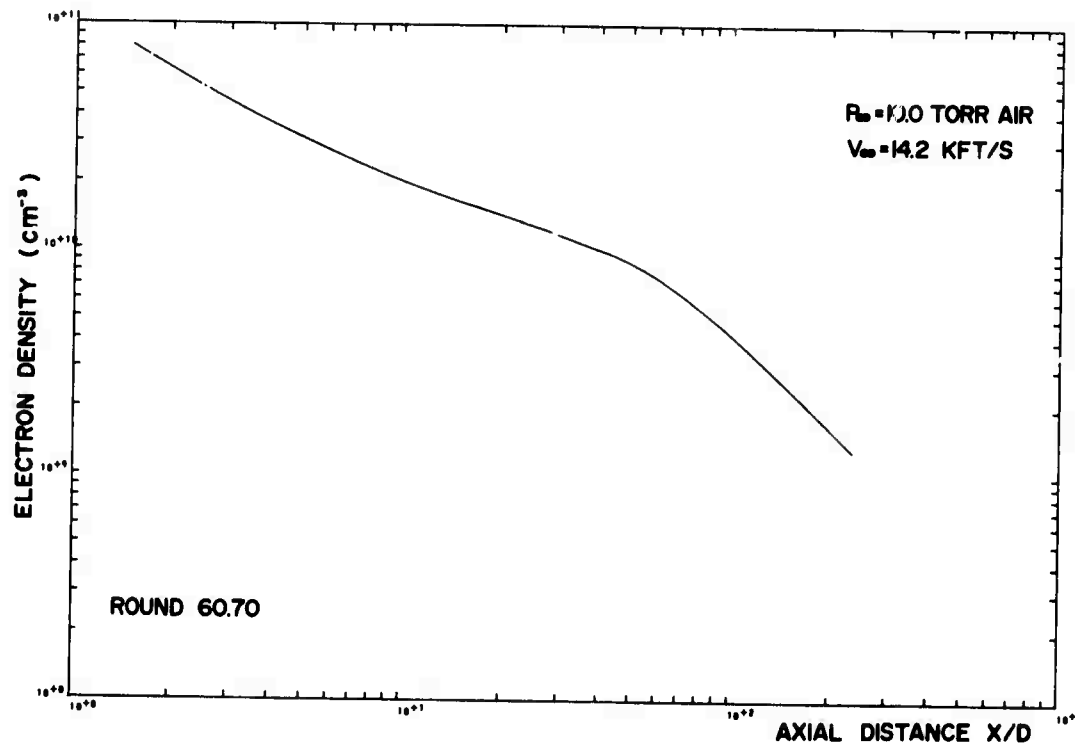


FIGURE B-5(b)

UNCLASSIFIED

95

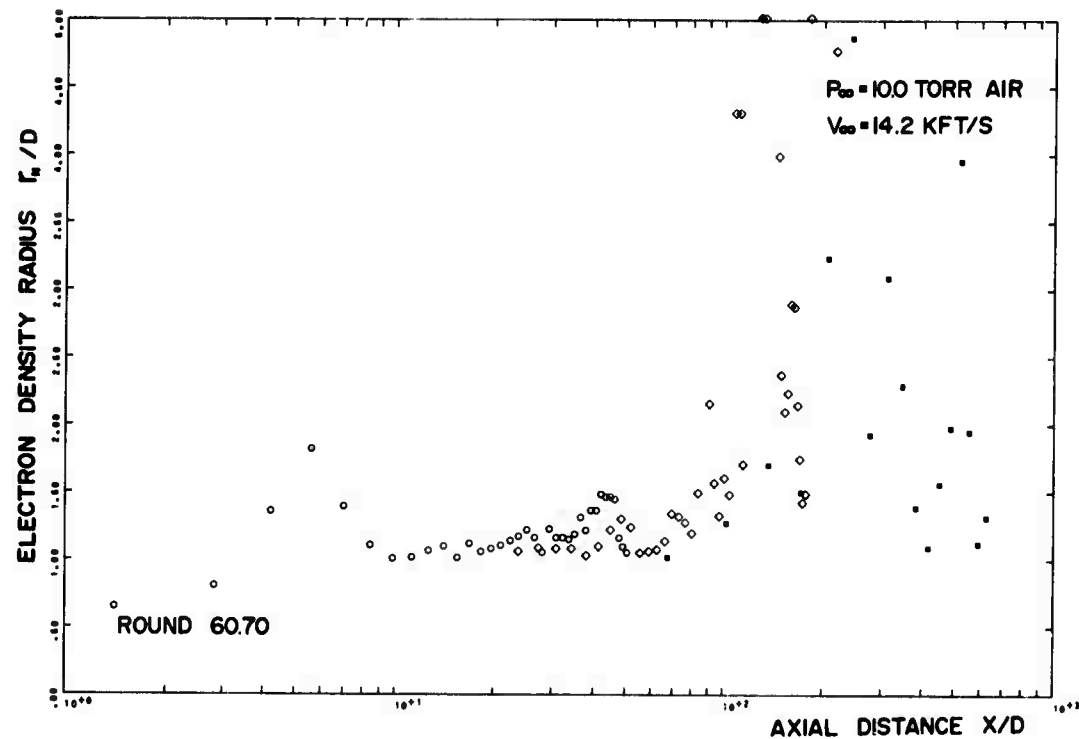


FIGURE B-5(c)

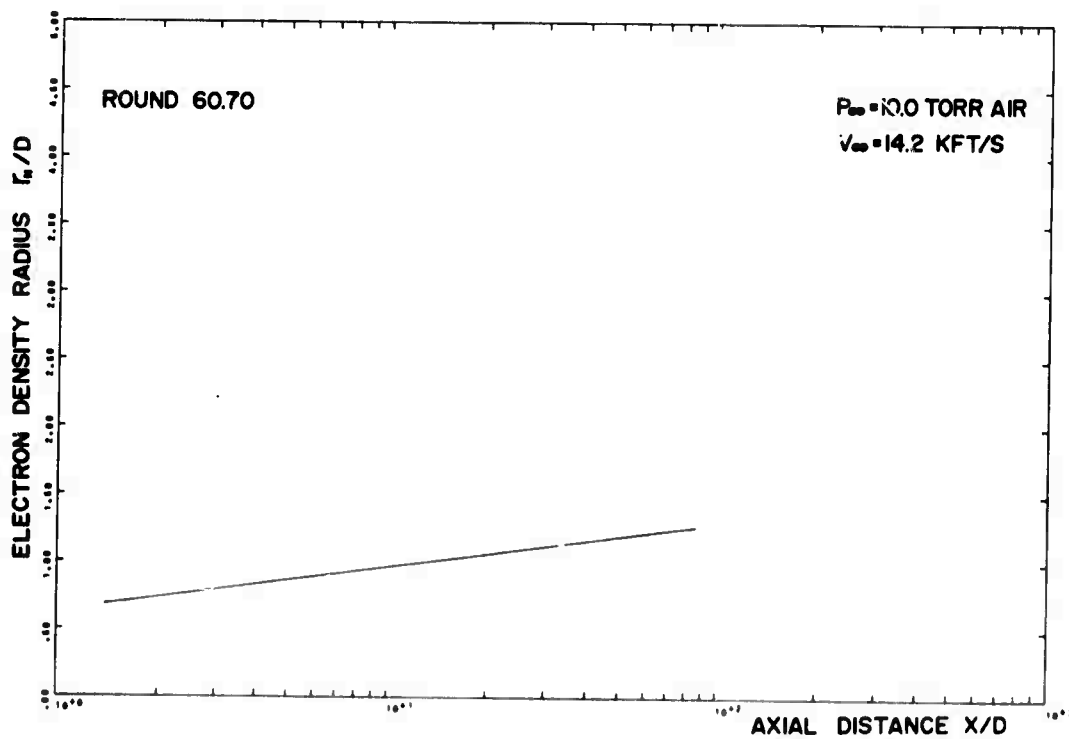


FIGURE B-5(d)

UNCLASSIFIED
96

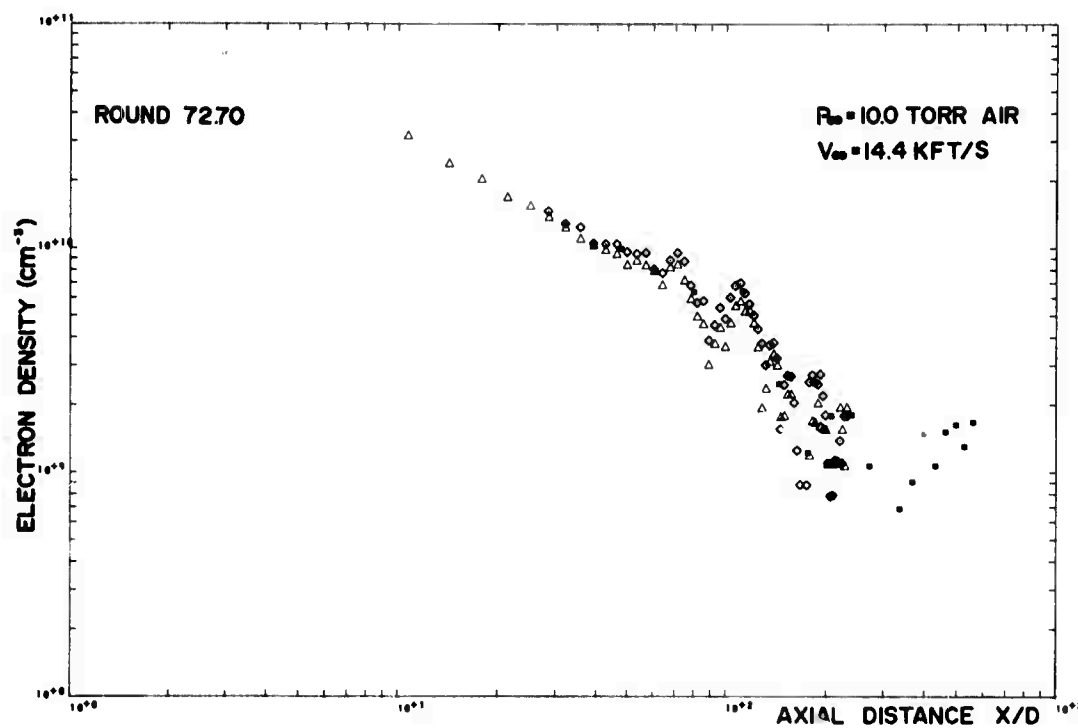


FIGURE B-6(a)

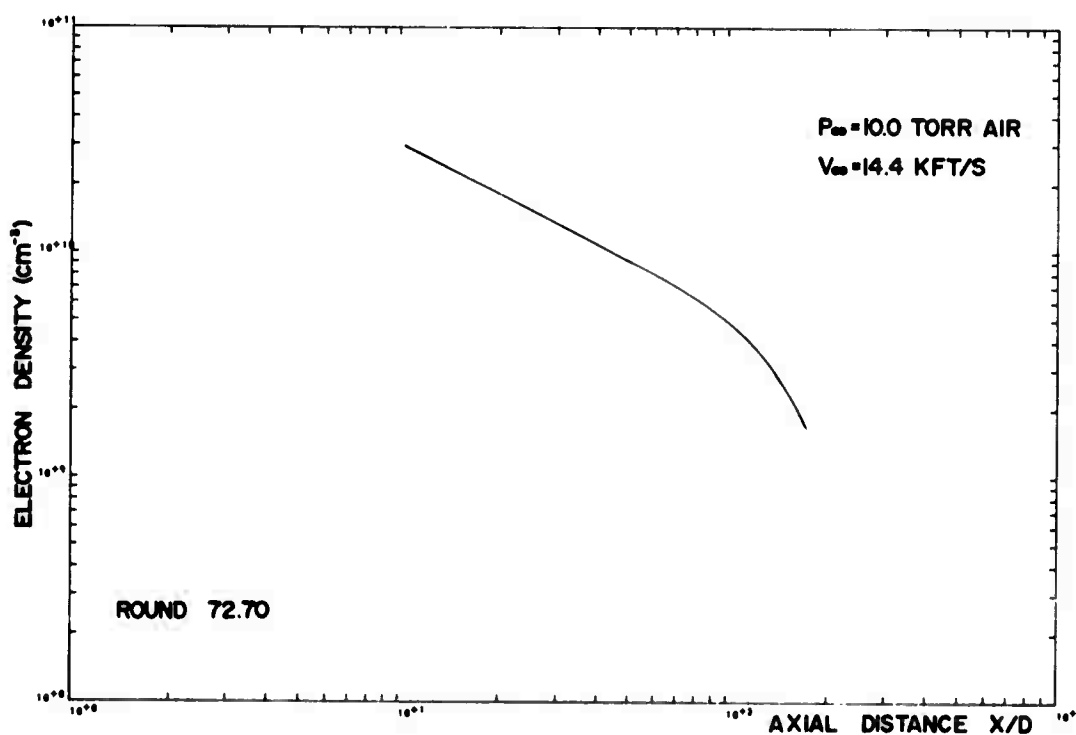


FIGURE B-6(b)

UNCLASSIFIED

97

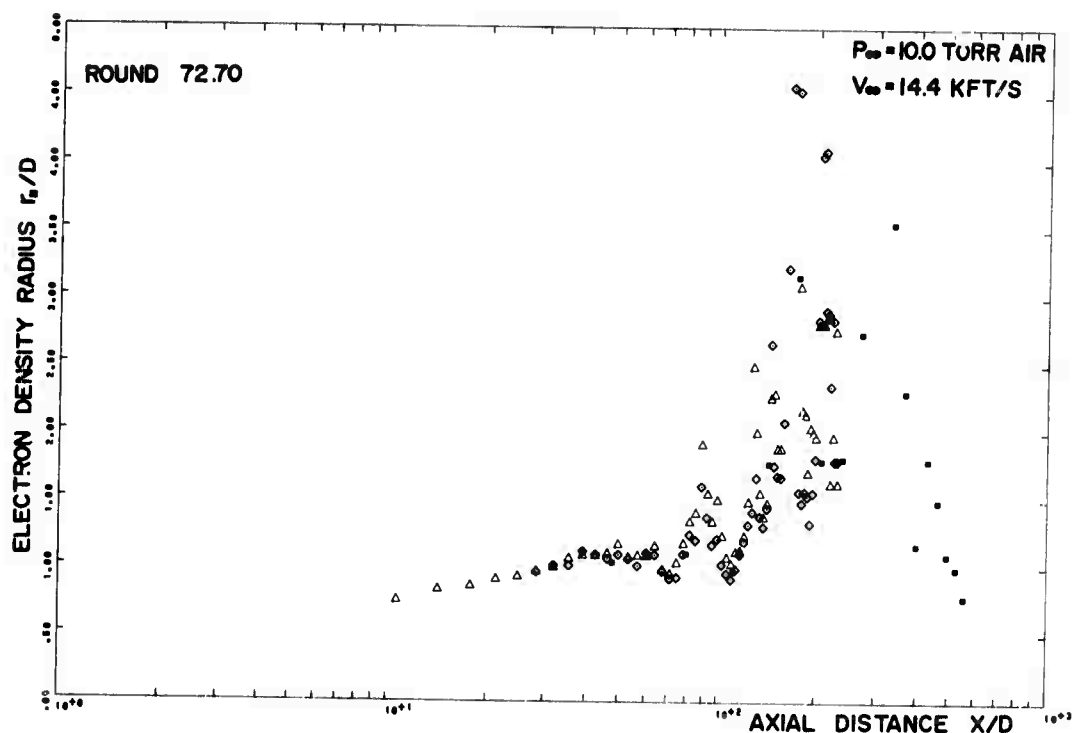


FIGURE B-6(c)

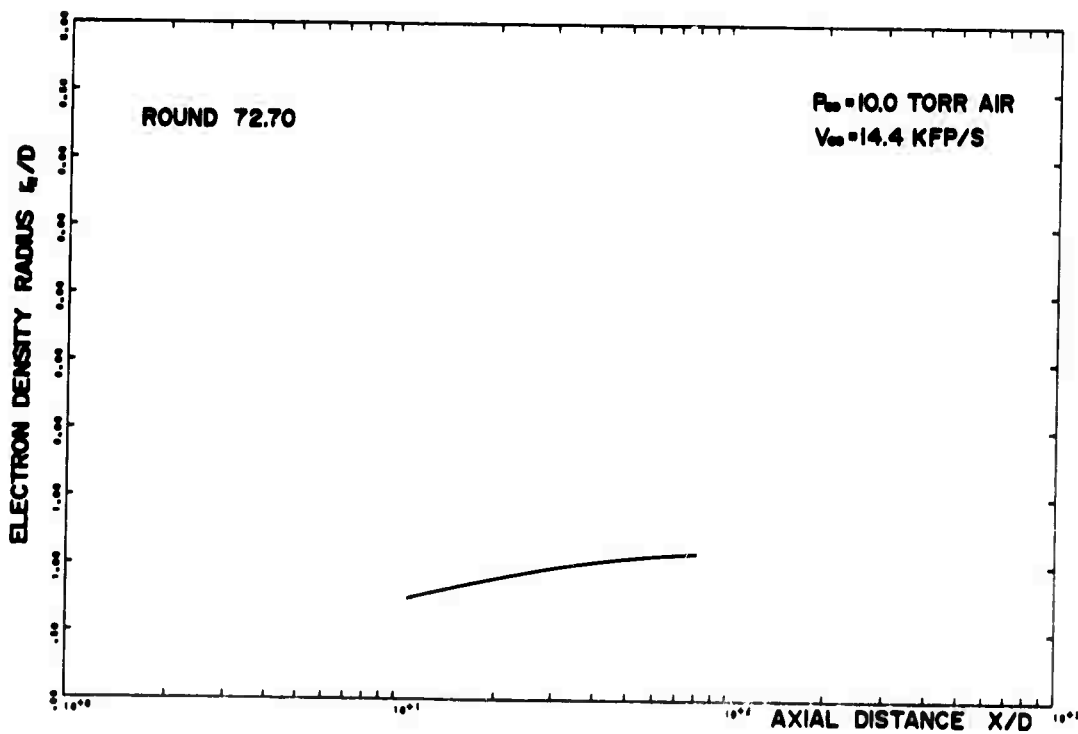


FIGURE B-6(d)

UNCLASSIFIED

98

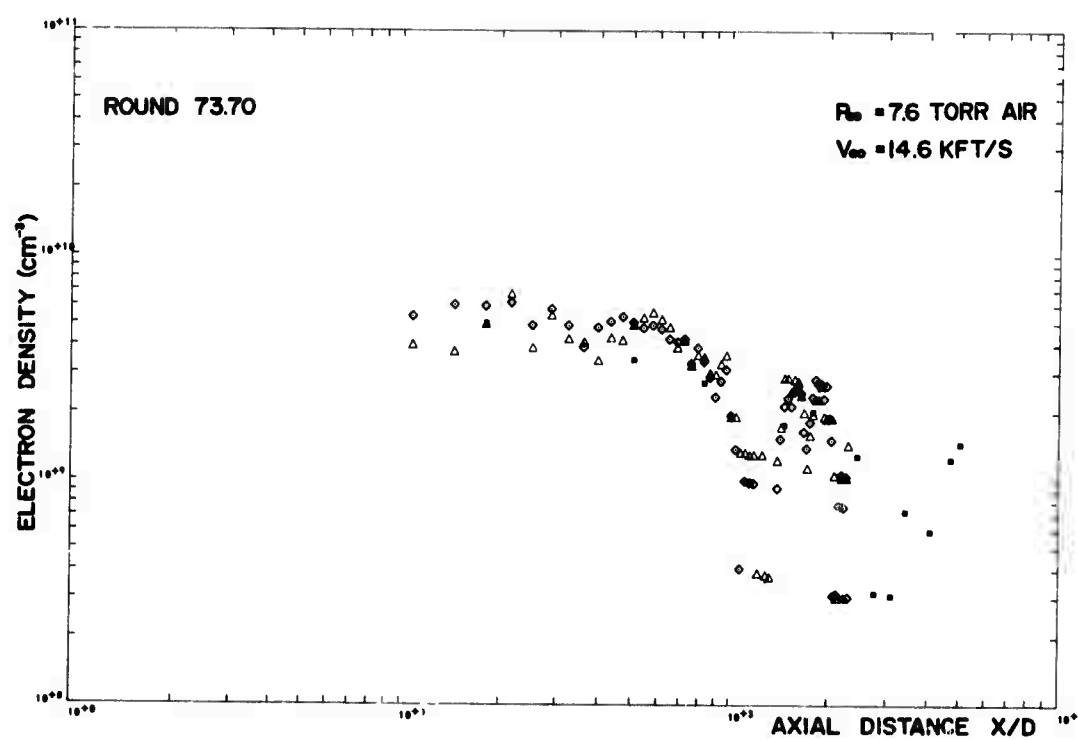


FIGURE B-7(a)

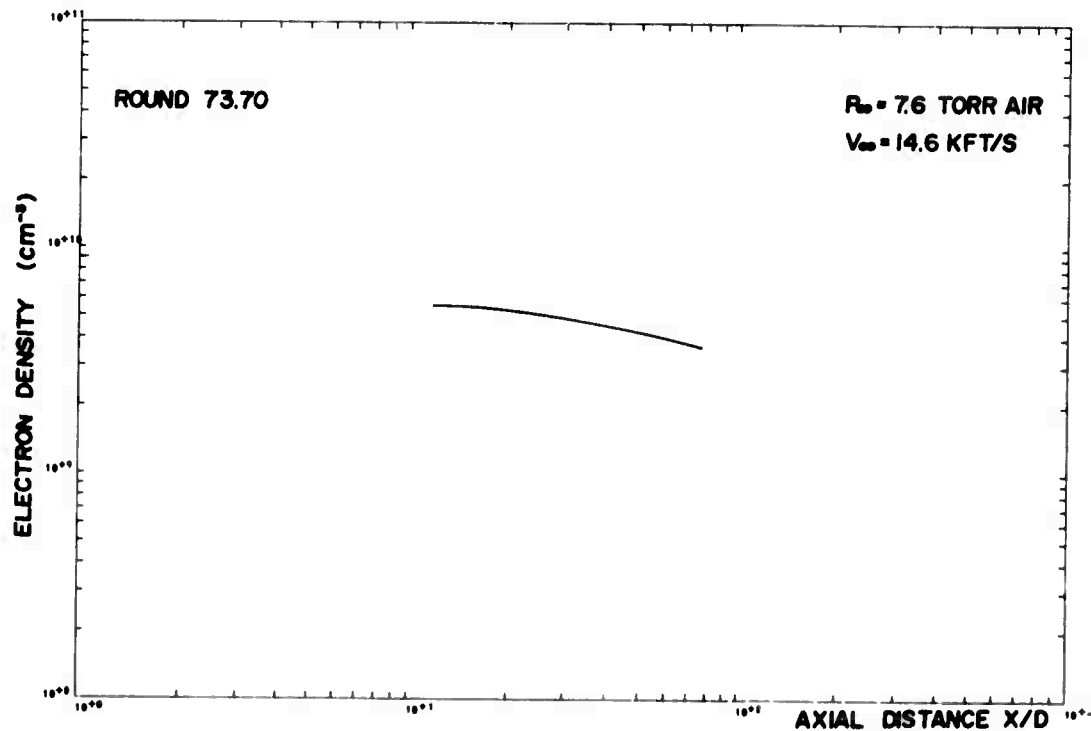


FIGURE B-7(b)

UNCLASSIFIED
99

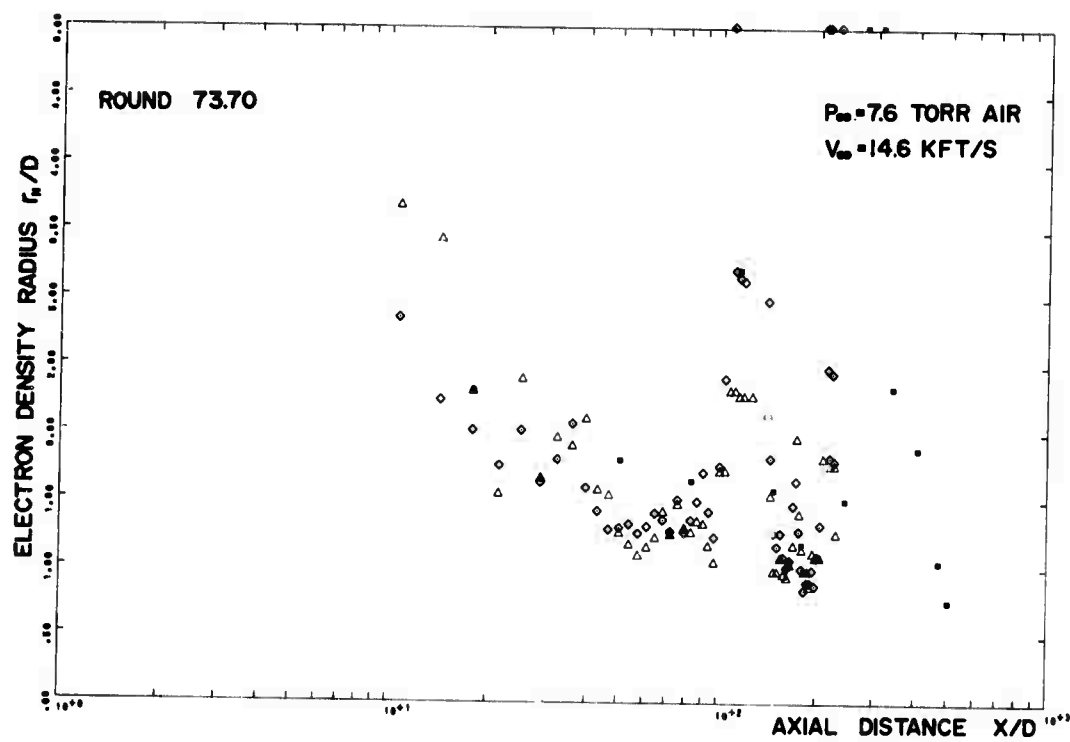


FIGURE B-7(c)

UNCLASSIFIED
100

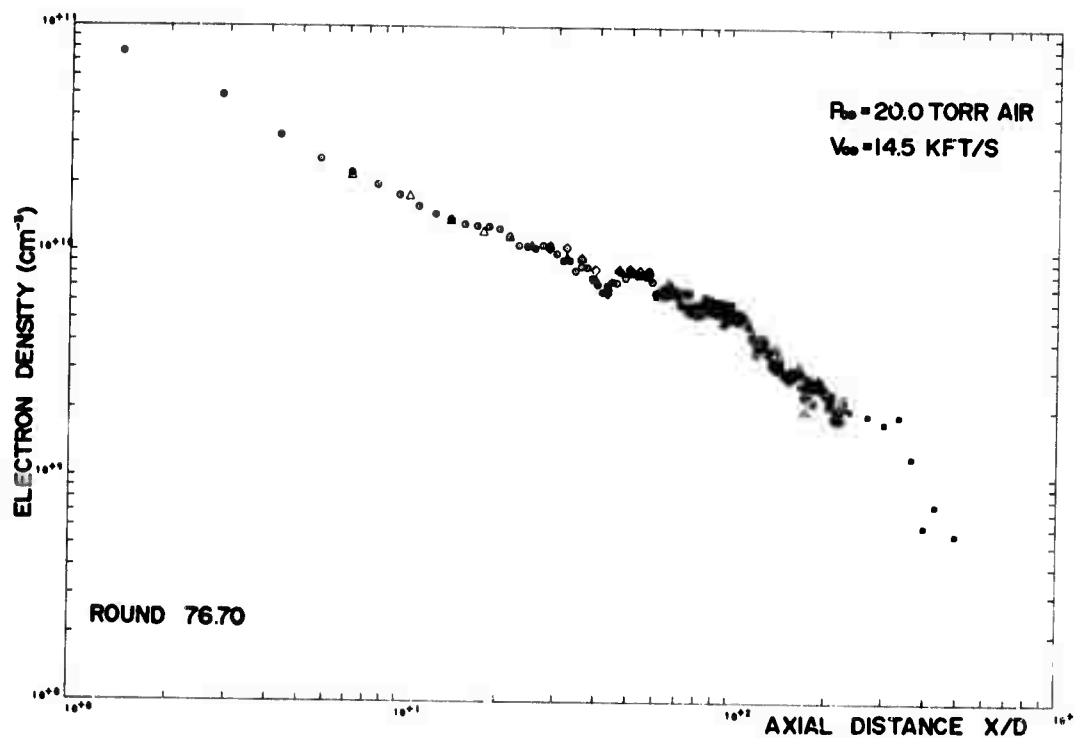


FIGURE B-8(a)

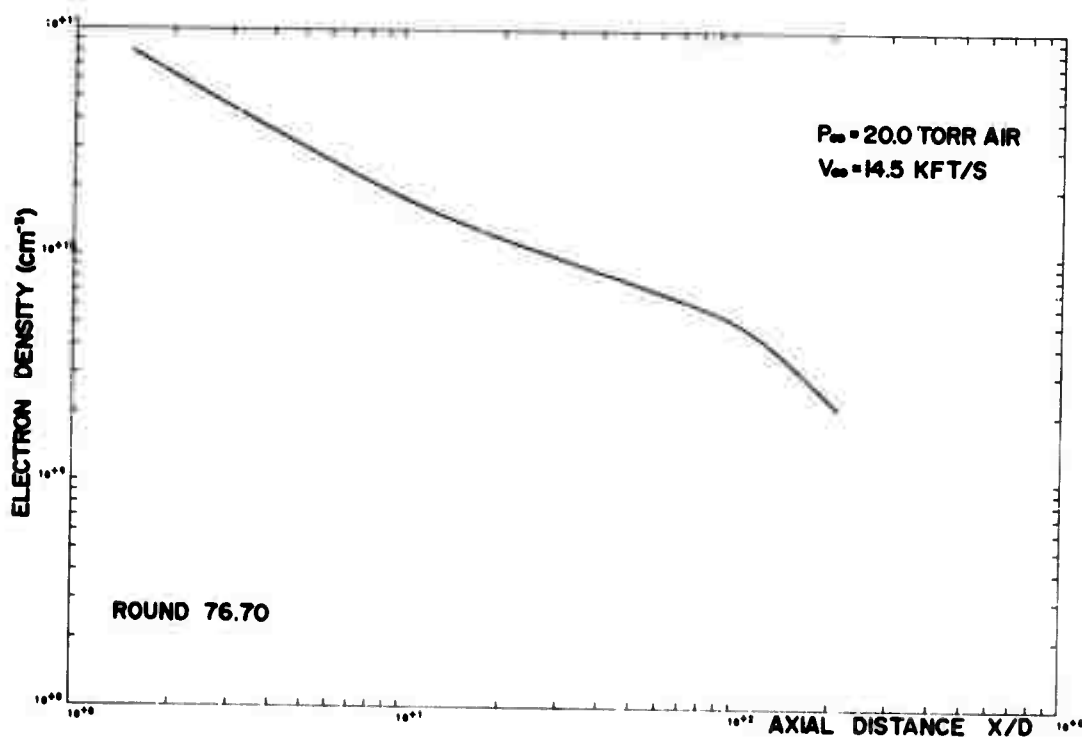


FIGURE B-8(b)

UNCLASSIFIED

101

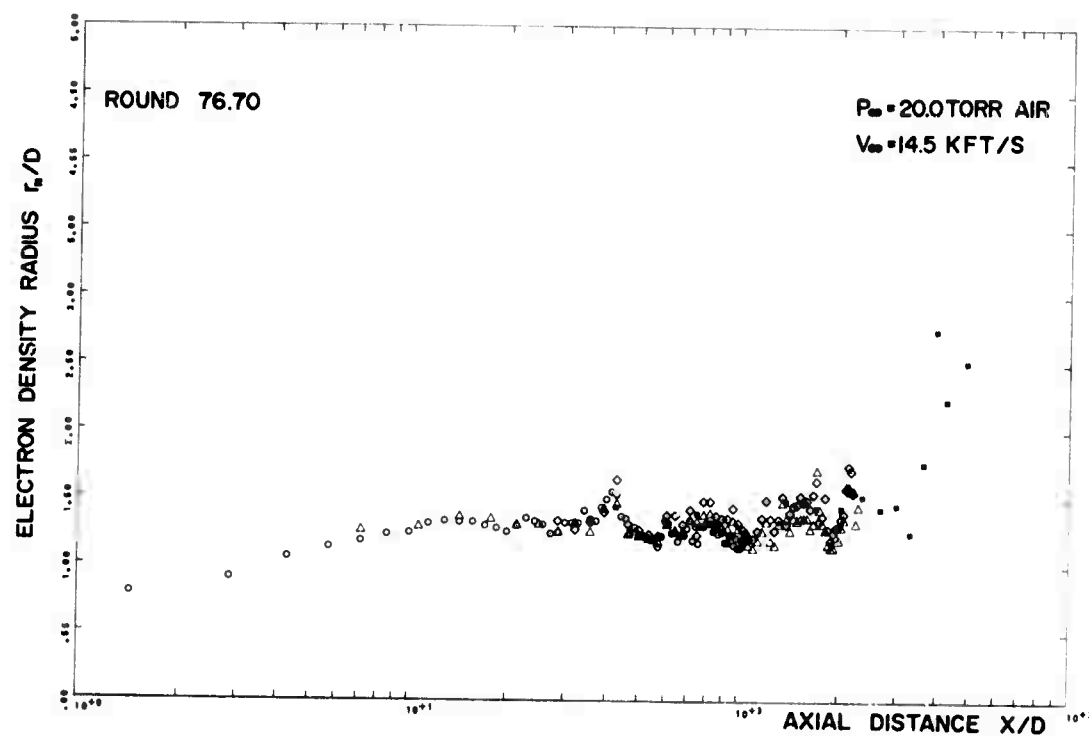


FIGURE B-8(c)

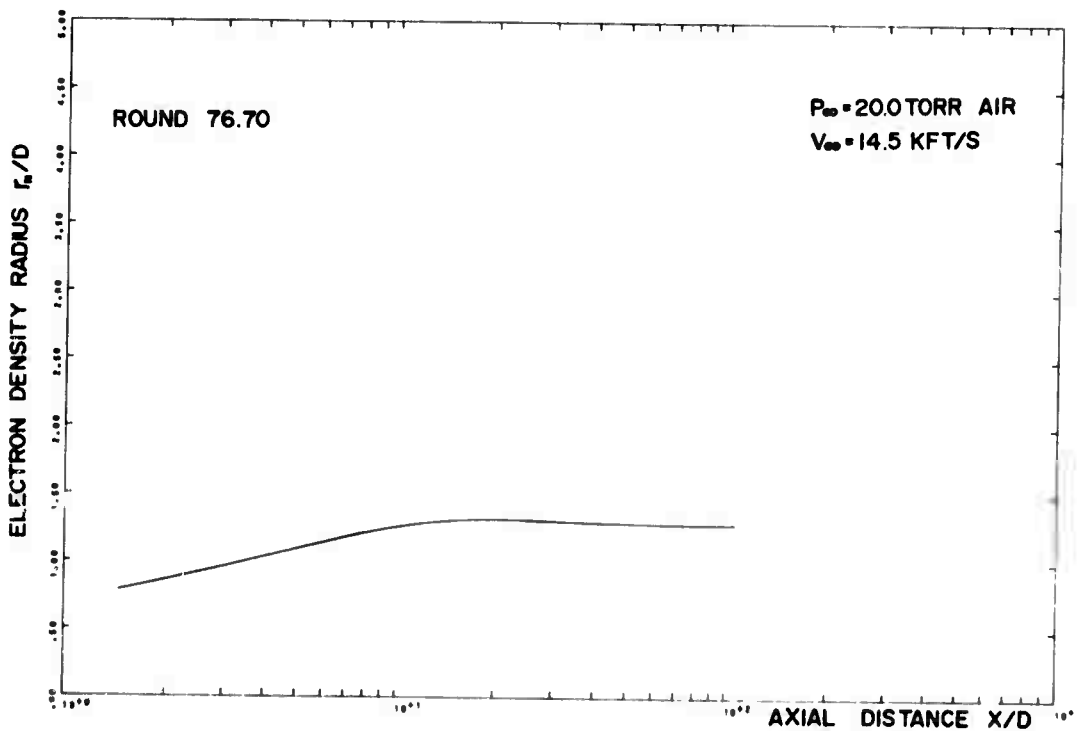


FIGURE B-8(d)

UNCLASSIFIED

102

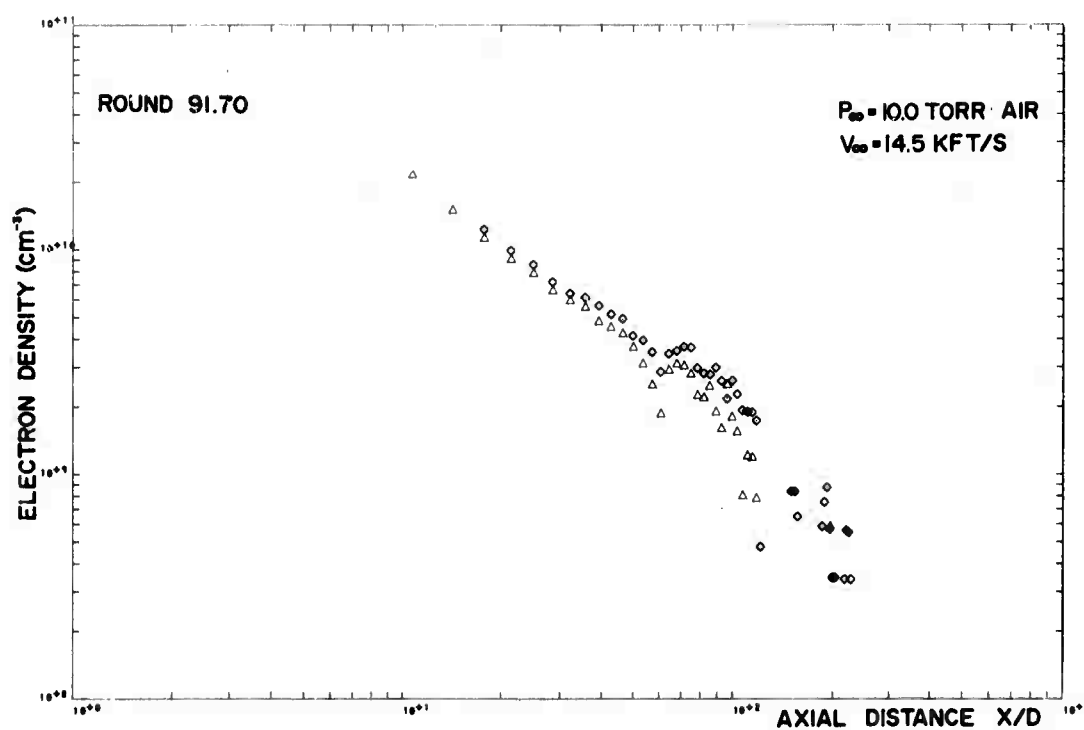


FIGURE B-9(a)

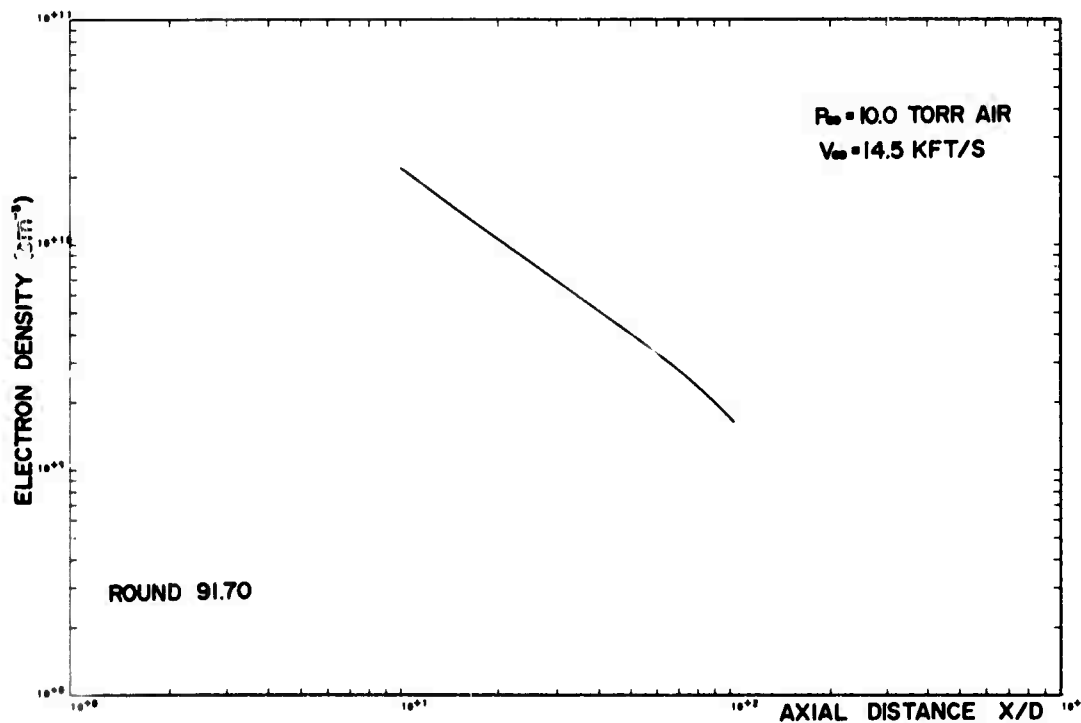


FIGURE B-9(b)

UNCLASSIFIED
103

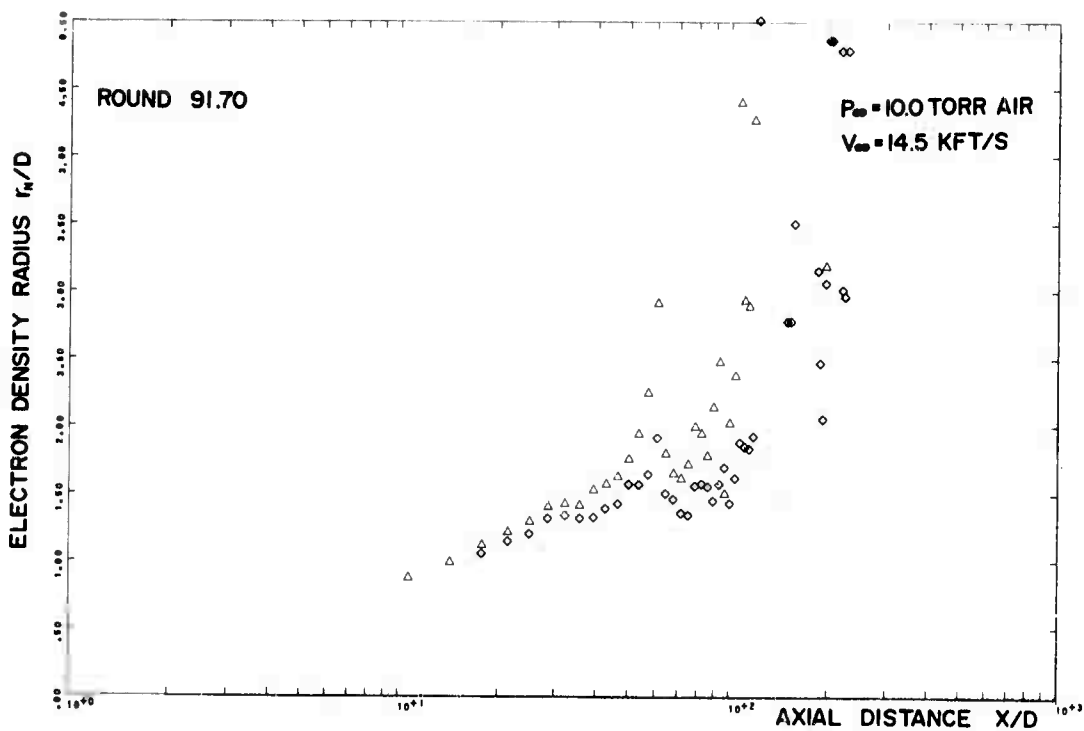


FIGURE B-9(c)

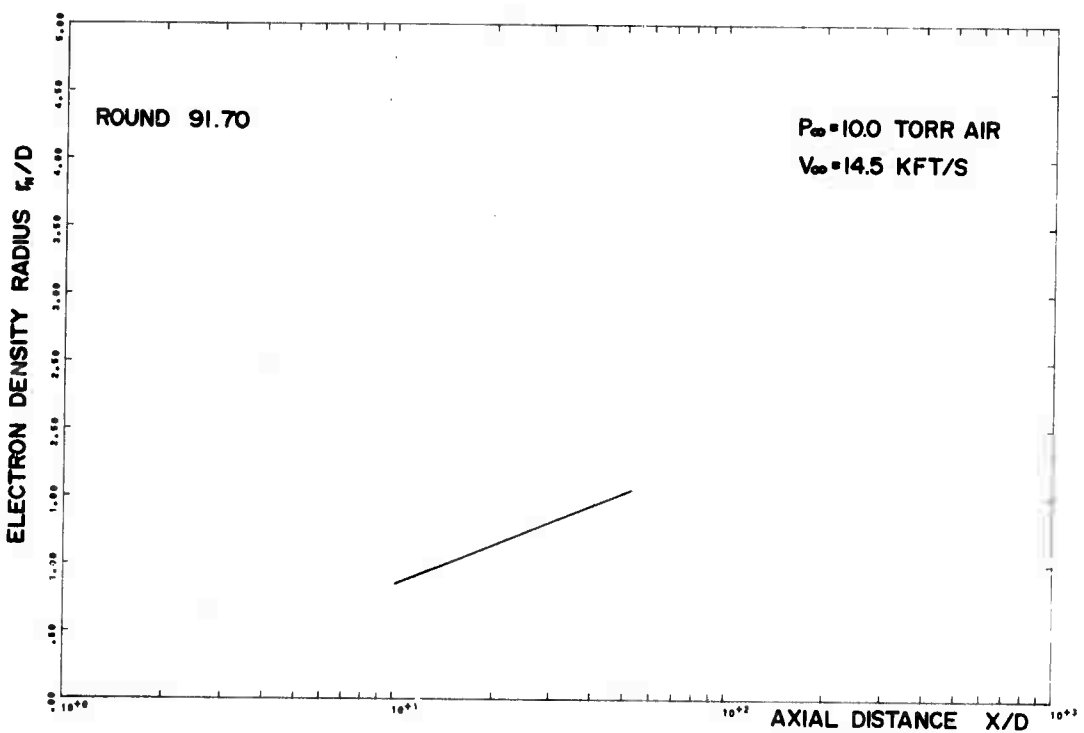


FIGURE B-9(d)

UNCLASSIFIED
104

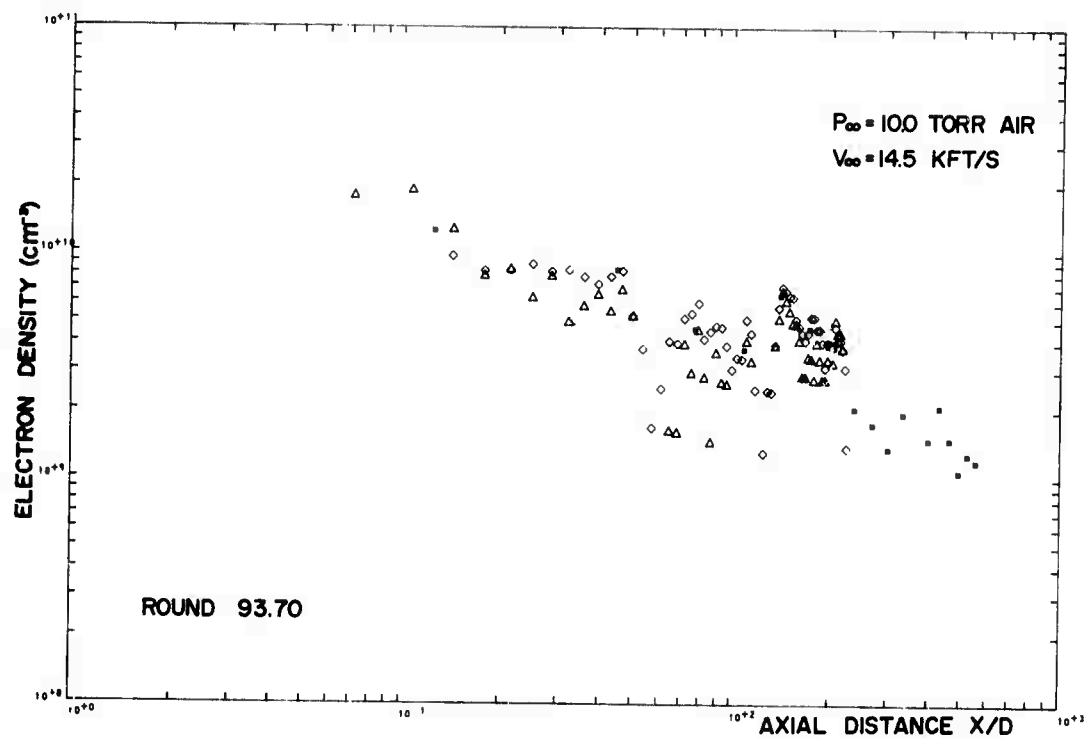


FIGURE B-10(a)

UNCLASSIFIED
105

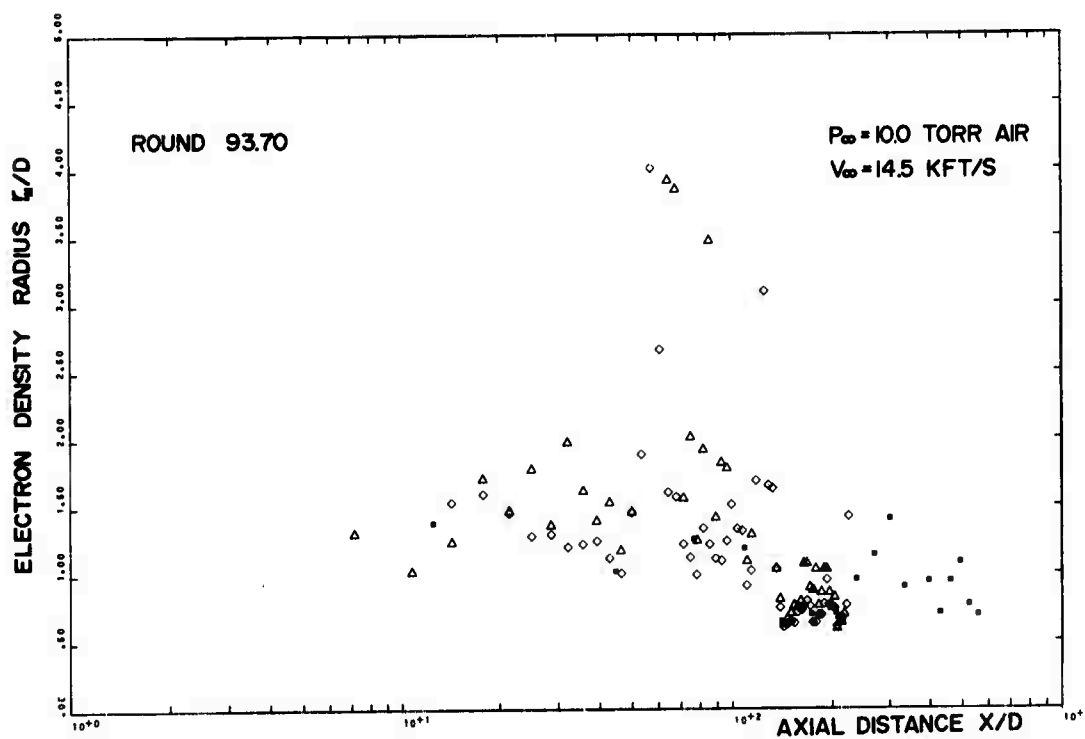


FIGURE B-10(c)

UNCLASSIFIED

106

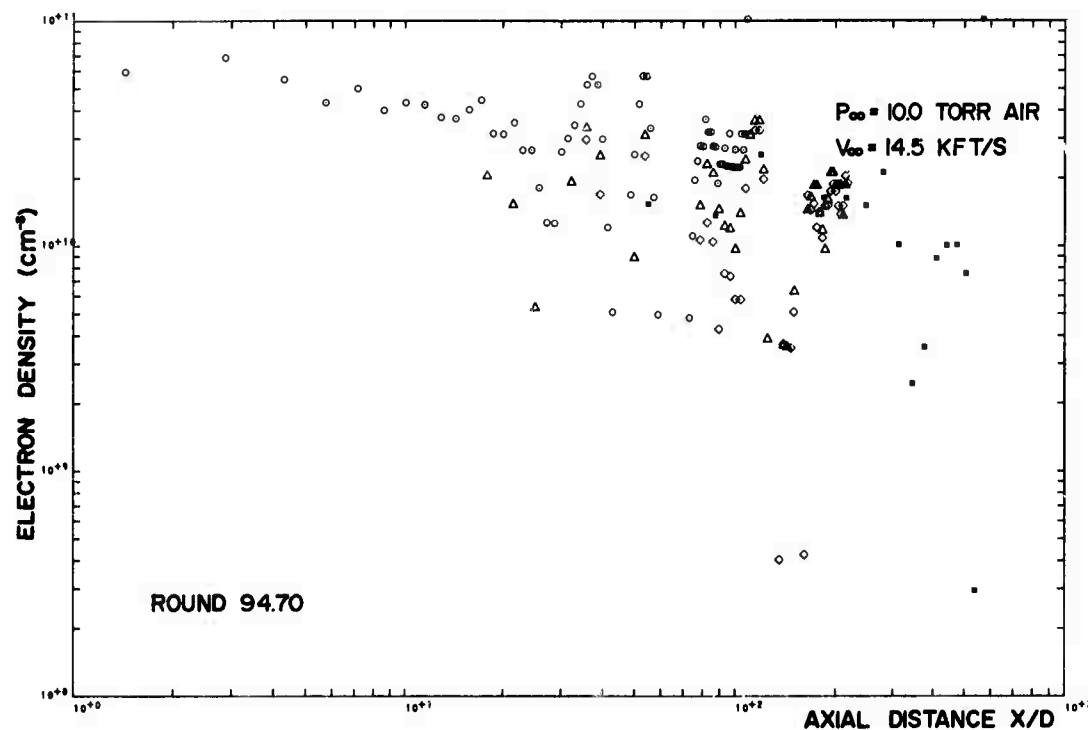


FIGURE B-11(a)

UNCLASSIFIED
107

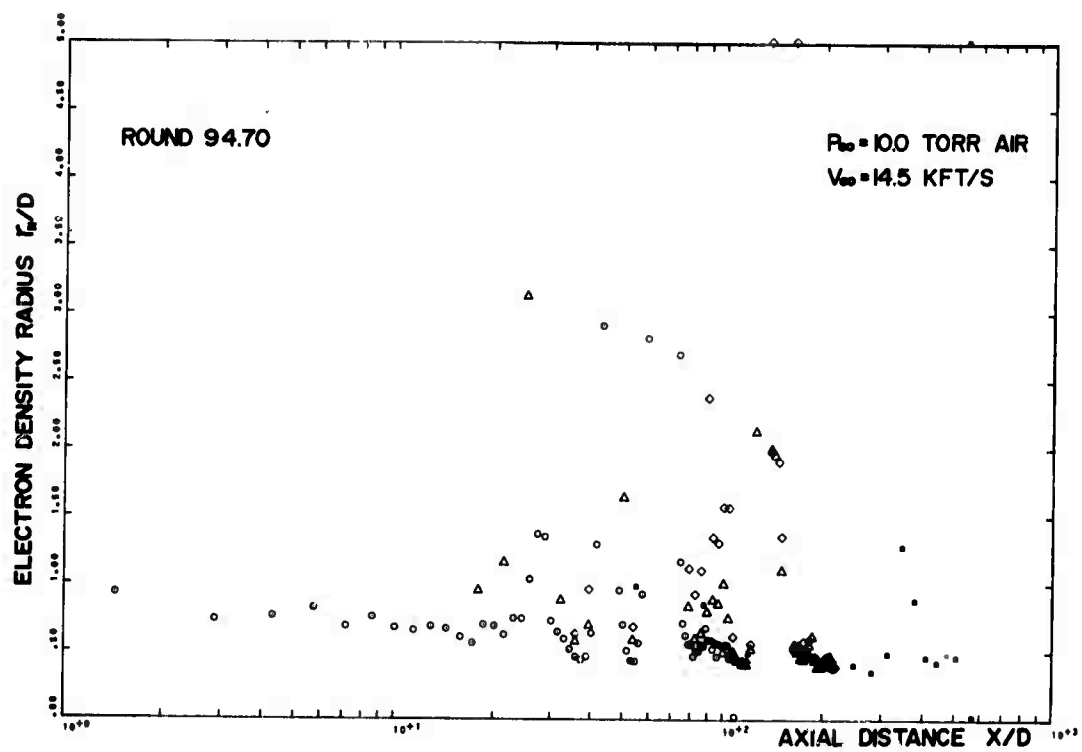


FIGURE B-11(c)

UNCLASSIFIED
108

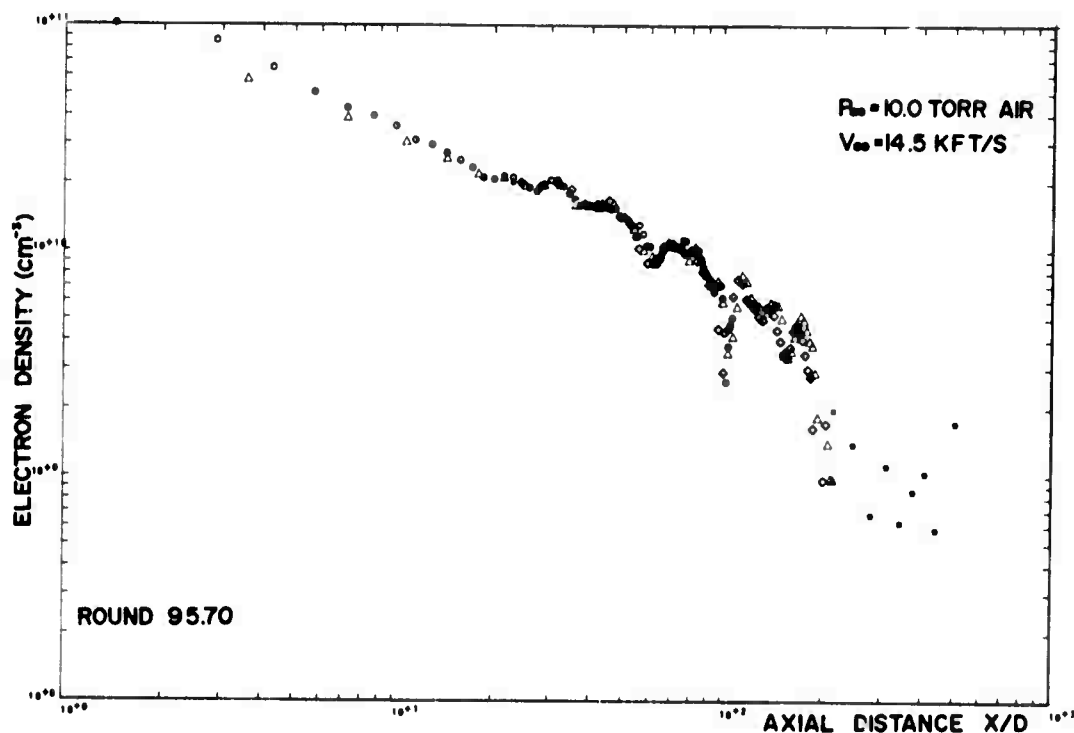


FIGURE B-12(a)

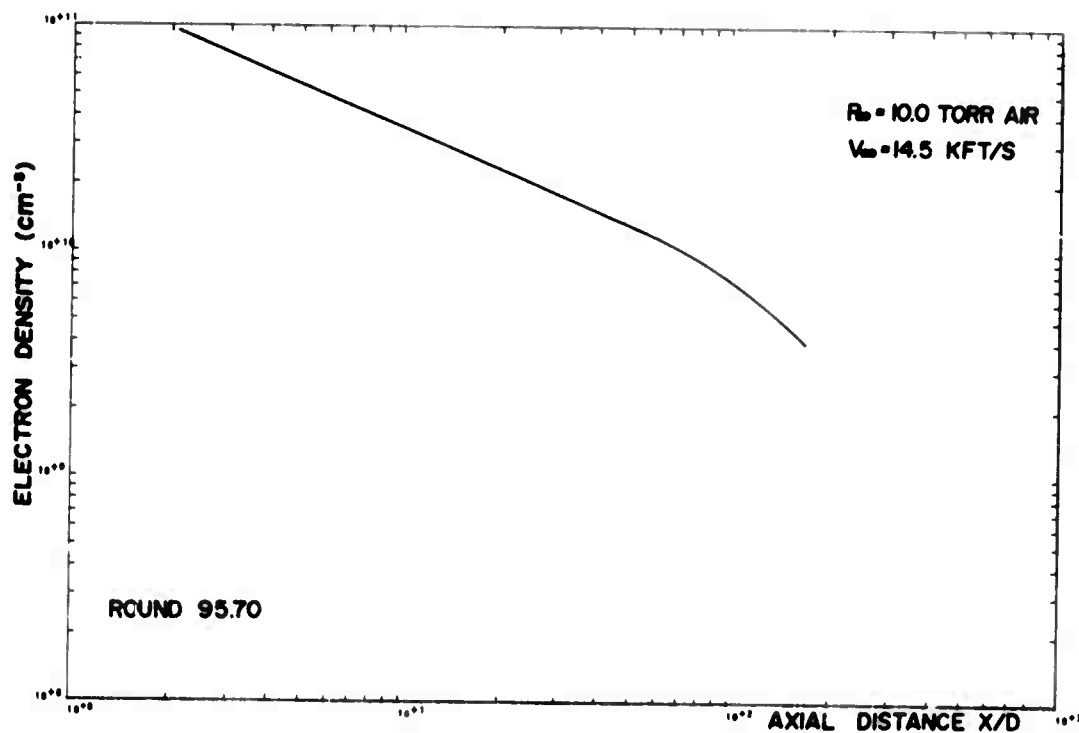


FIGURE B-12(b)

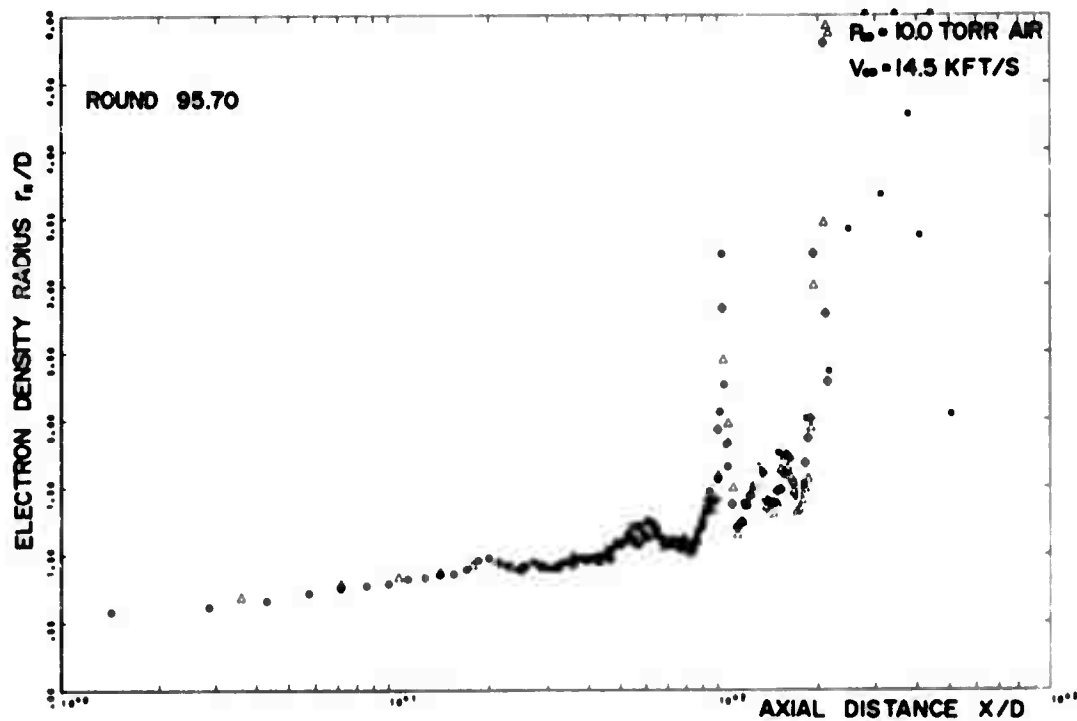


FIGURE B-12(c)

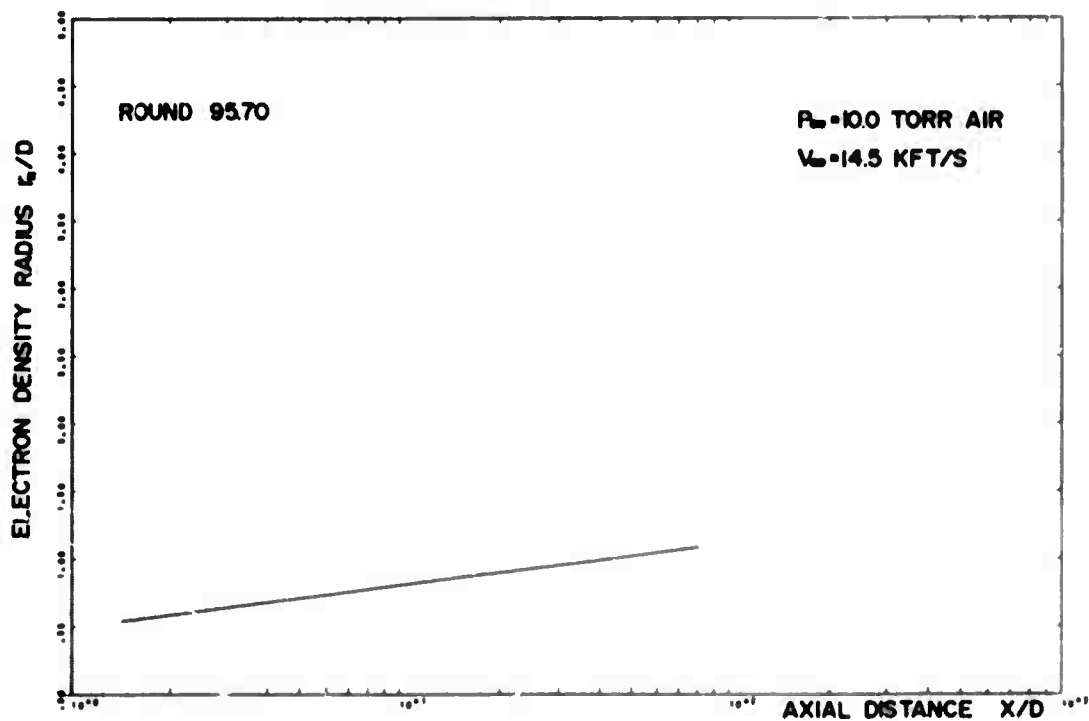


FIGURE B-12(d)

UNCLASSIFIED
110

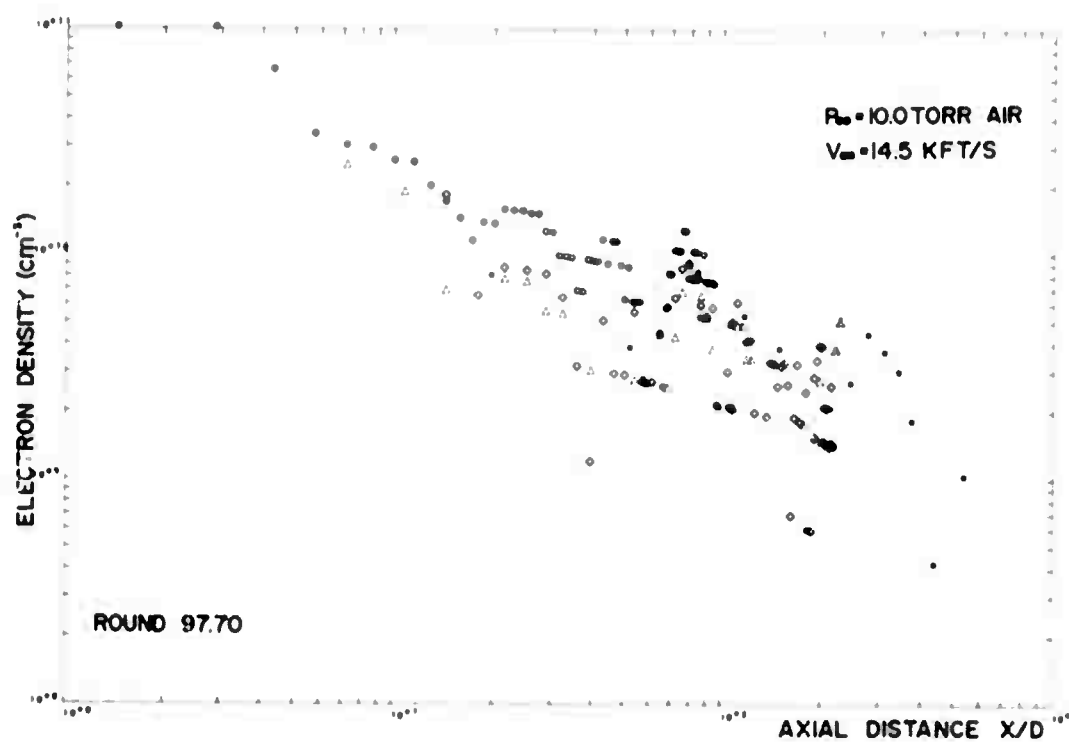


FIGURE B-13(a)

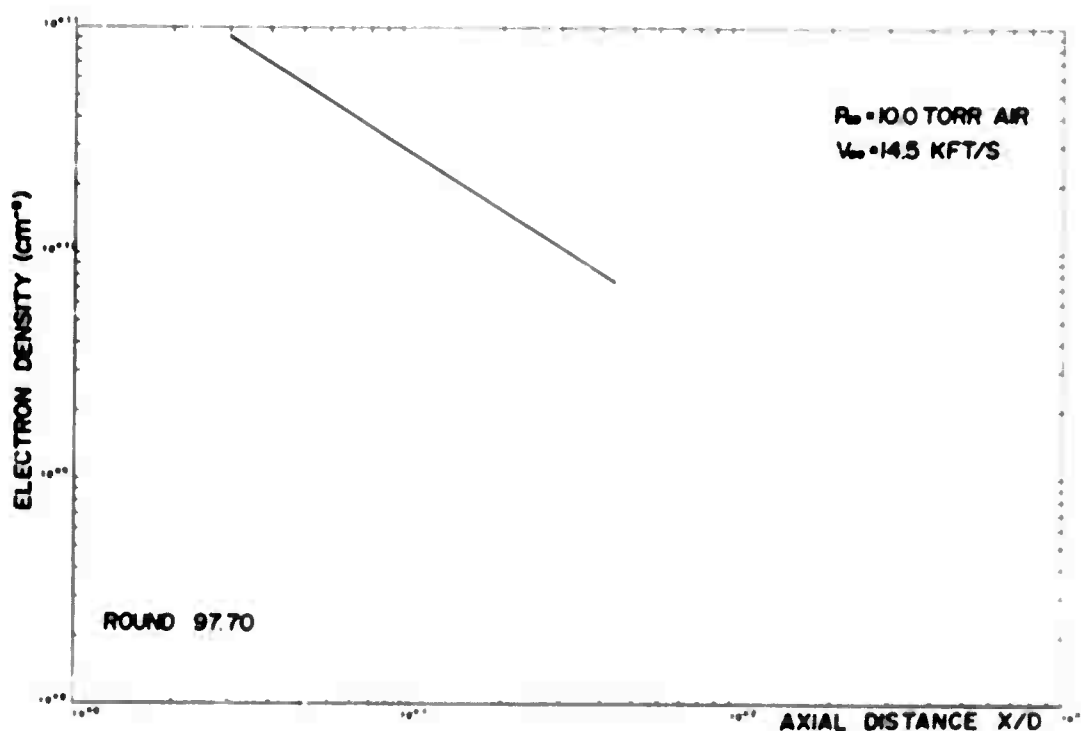


FIGURE B-13(b)

UNCLASSIFIED
111

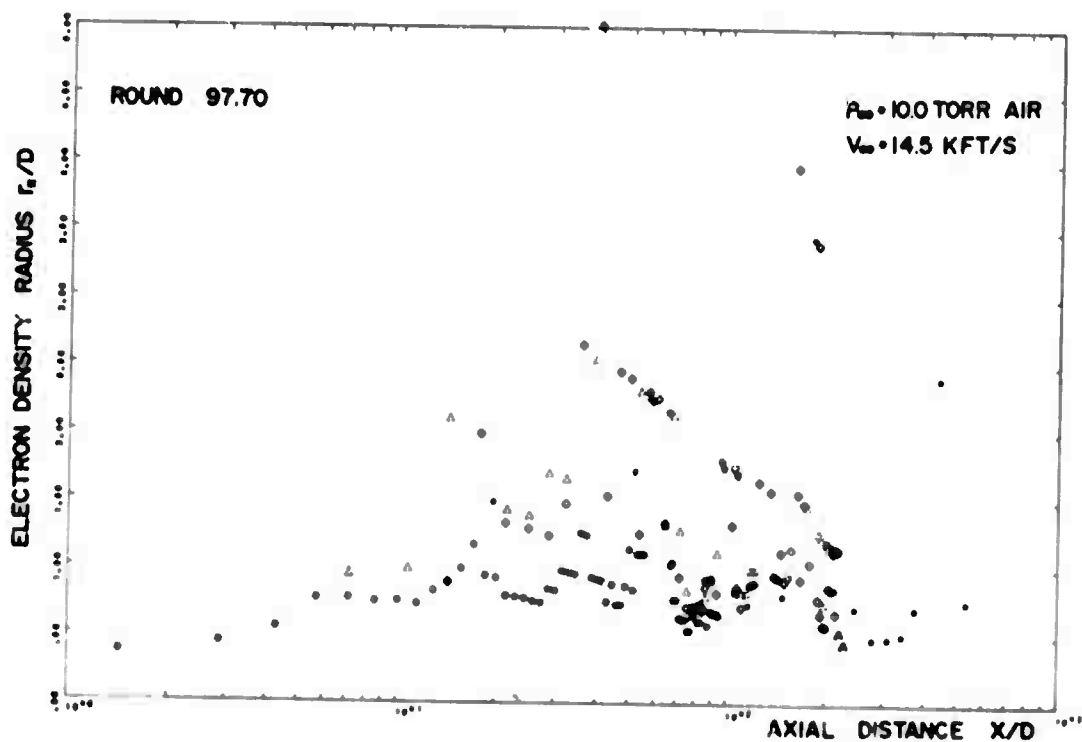


FIGURE B-13(c)

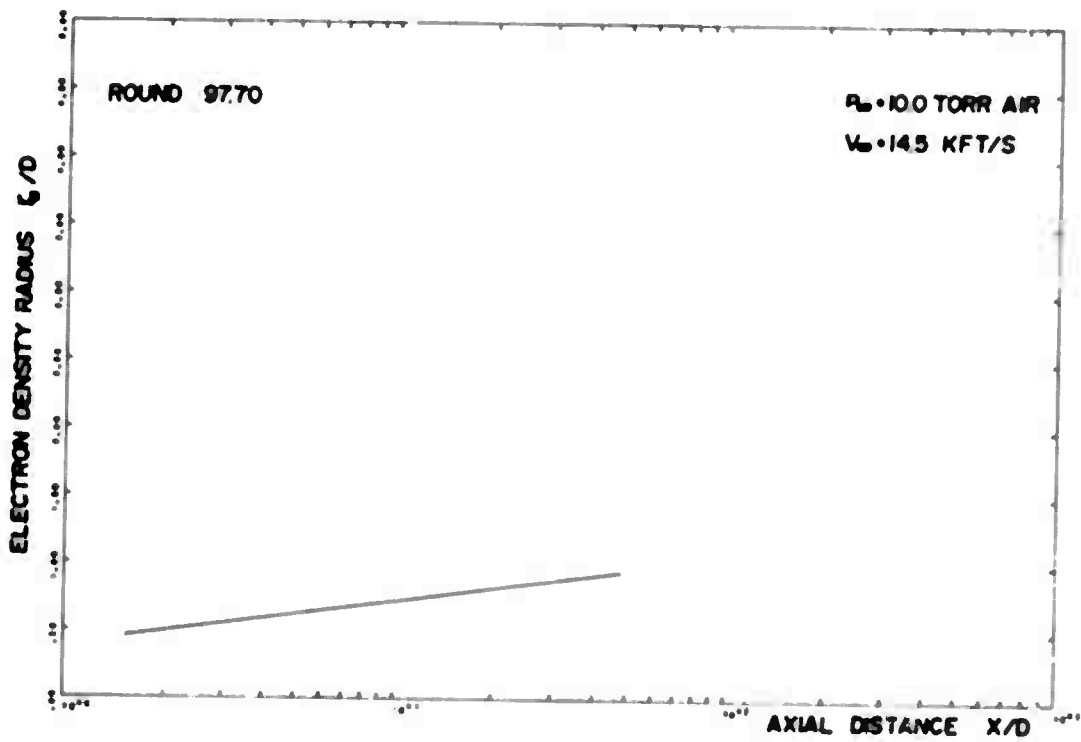


FIGURE B-13(d)

UNCLASSIFIED

112

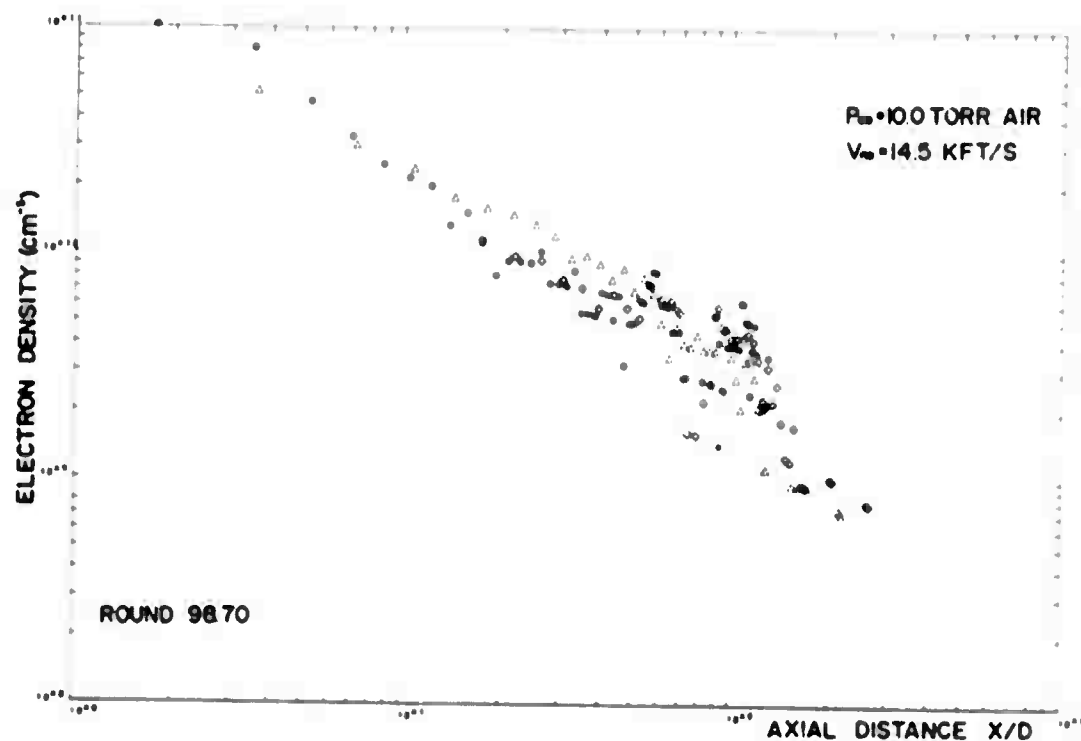


FIGURE B-14(a)

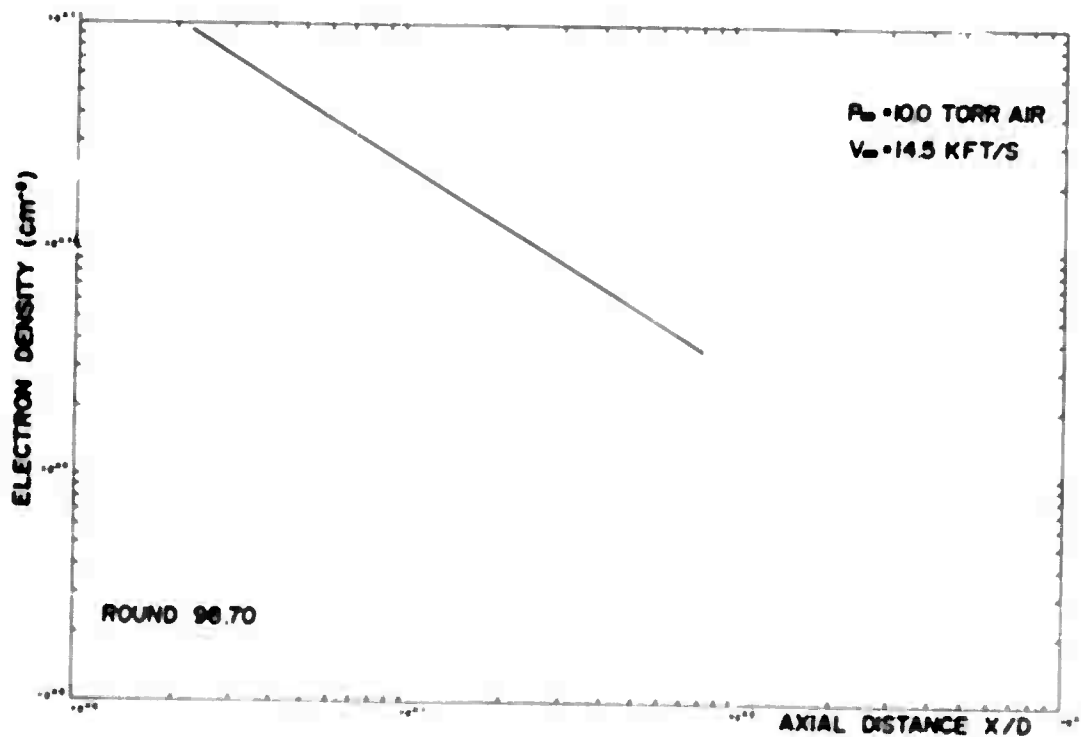


FIGURE B-14(b)

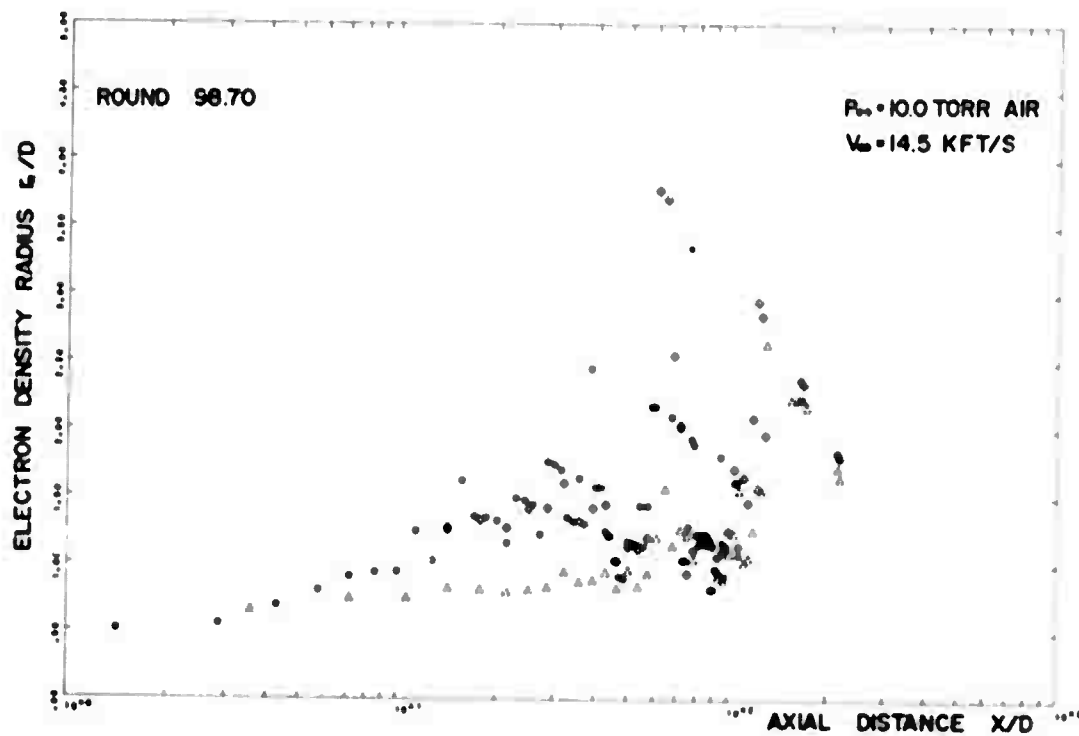


FIGURE B-14(c)

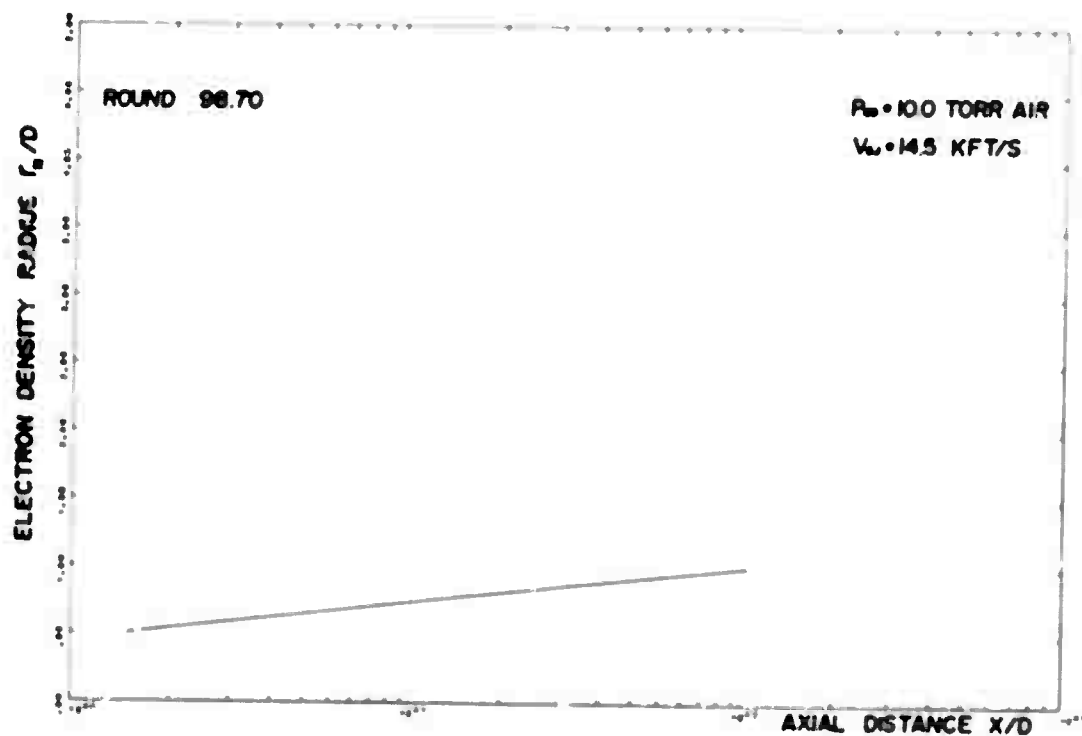


FIGURE B-14(d)

UNCLASSIFIED
114

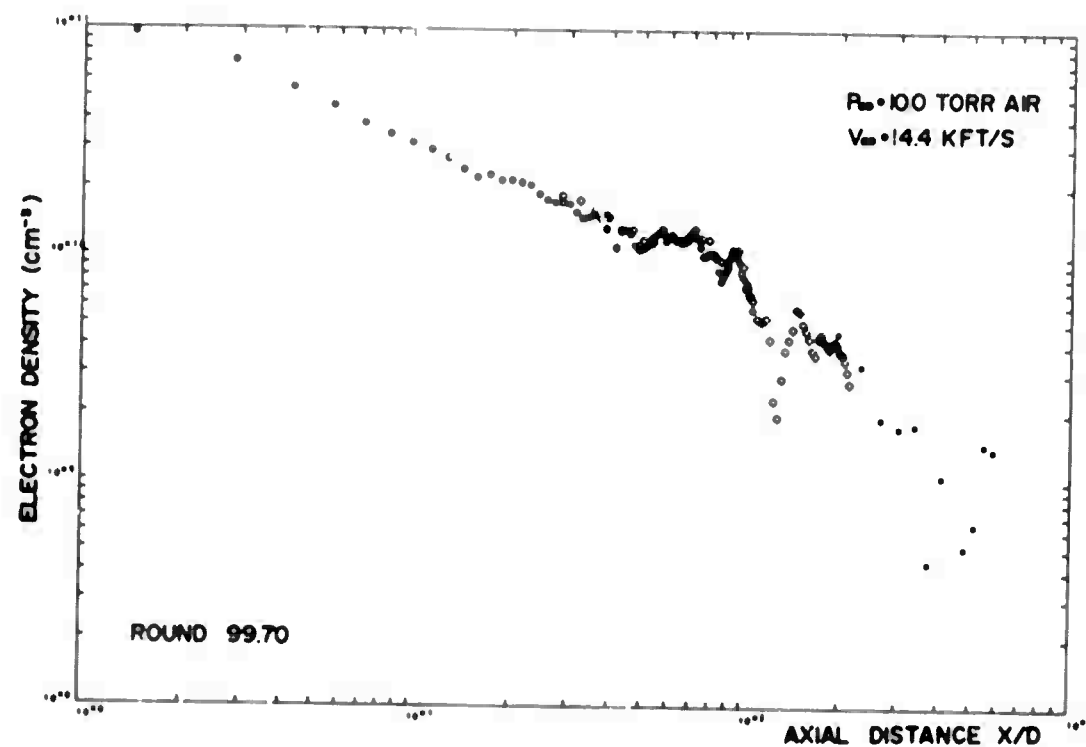


FIGURE B-15(a)

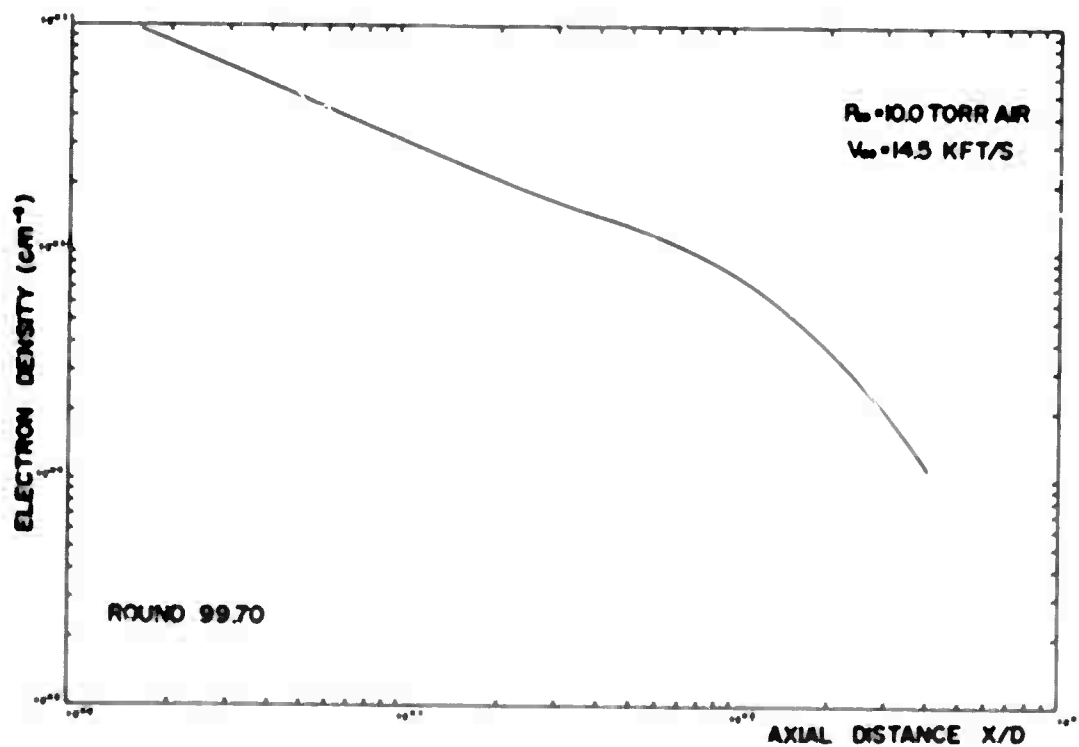


FIGURE B-15(b)

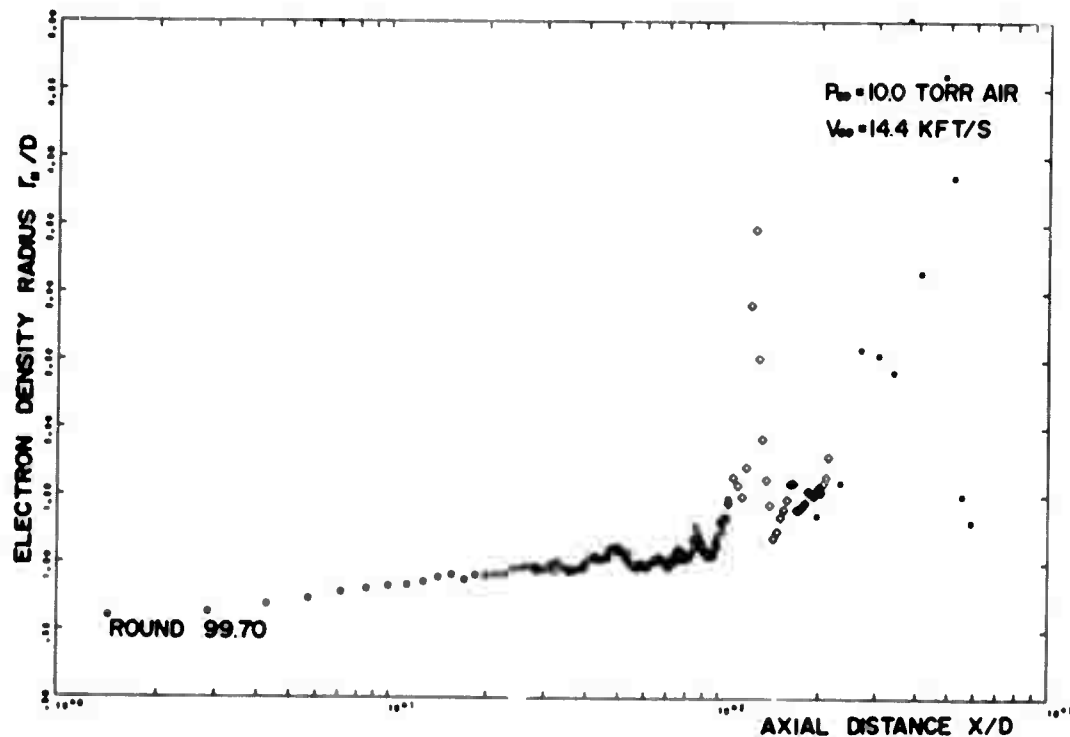


FIGURE B-15(c)

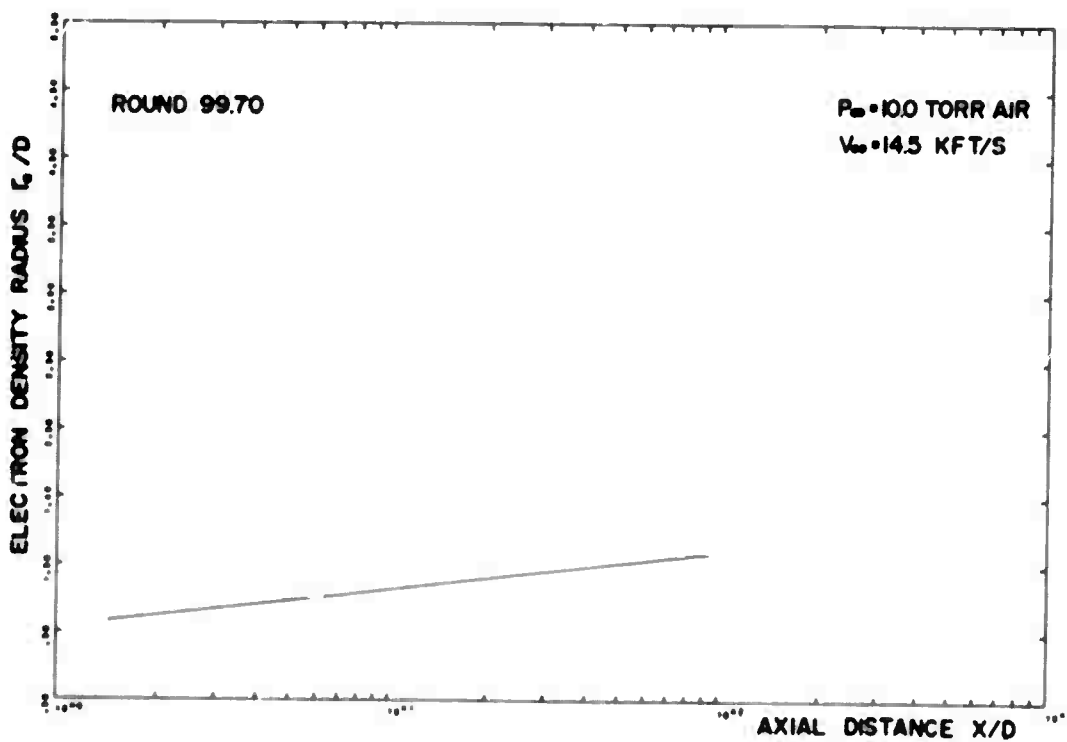


FIGURE B-15(d)

UNCLASSIFIED

116

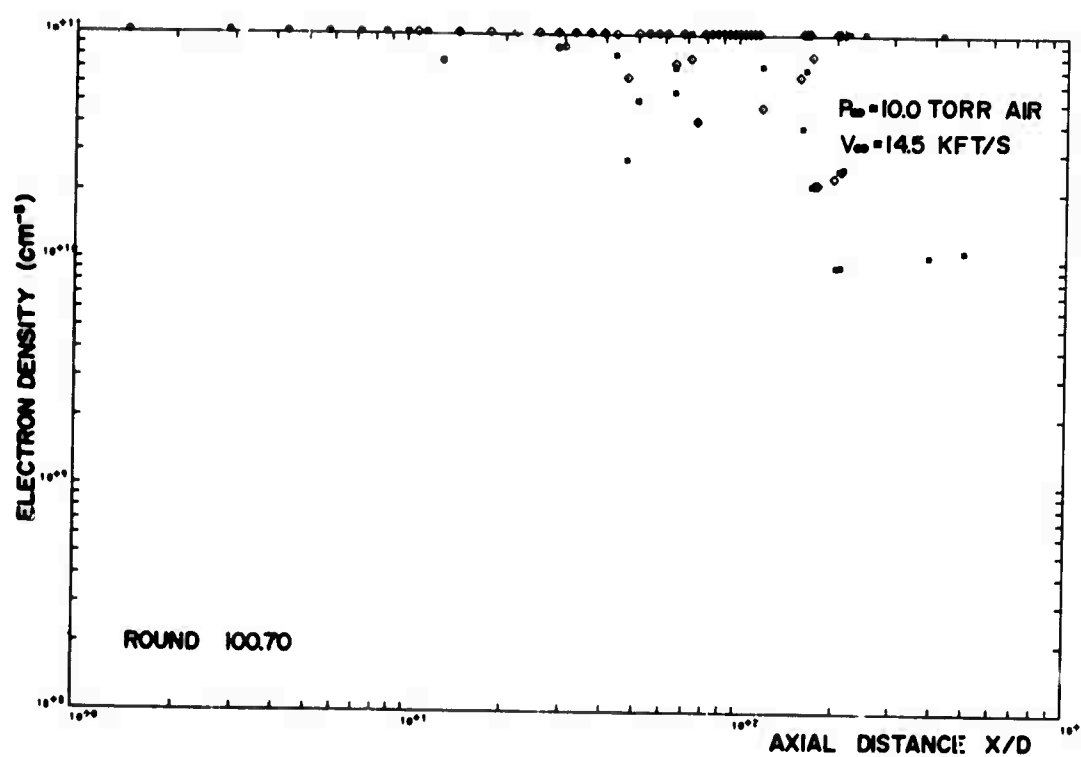


FIGURE B-16(a)

UNCLASSIFIED

117

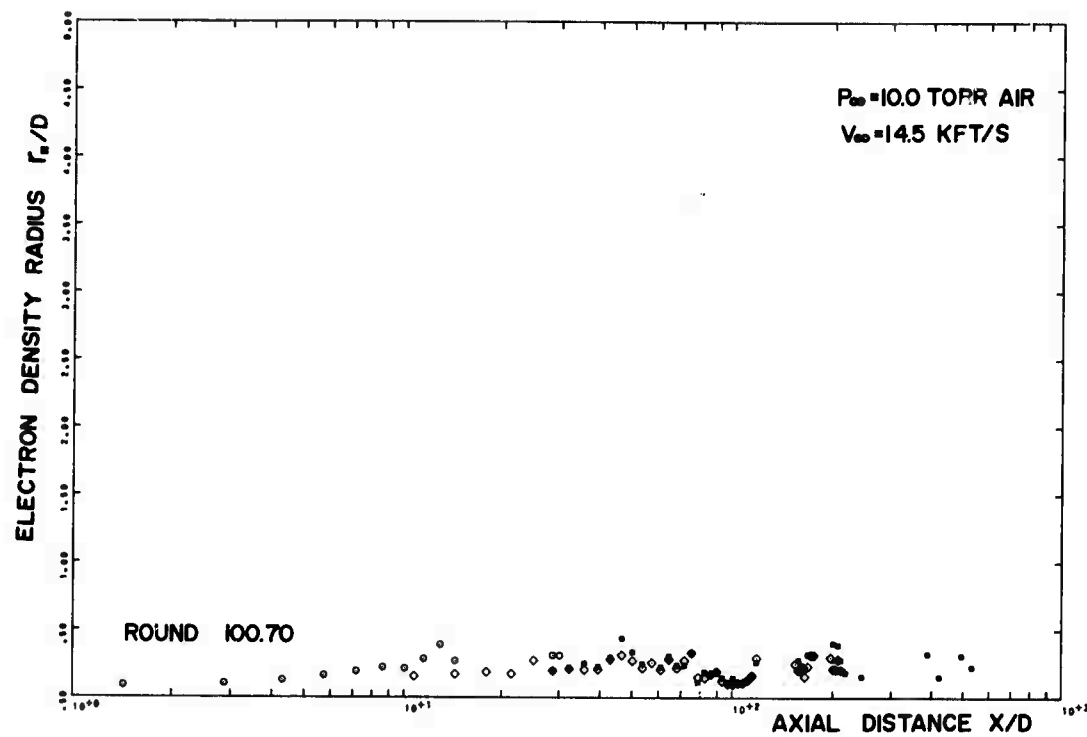


FIGURE B-16(c)

APPENDIX C

**Electron Densities on the Axis Computed with a Prescribed
Electron Density Radius Air Atmospheres**

The figure numbers in this appendix correspond
to the figure numbers in Appendices A and B.

Figures C-7a, 7b, 8a, 8b are unavailable

UNCLASSIFIED
120

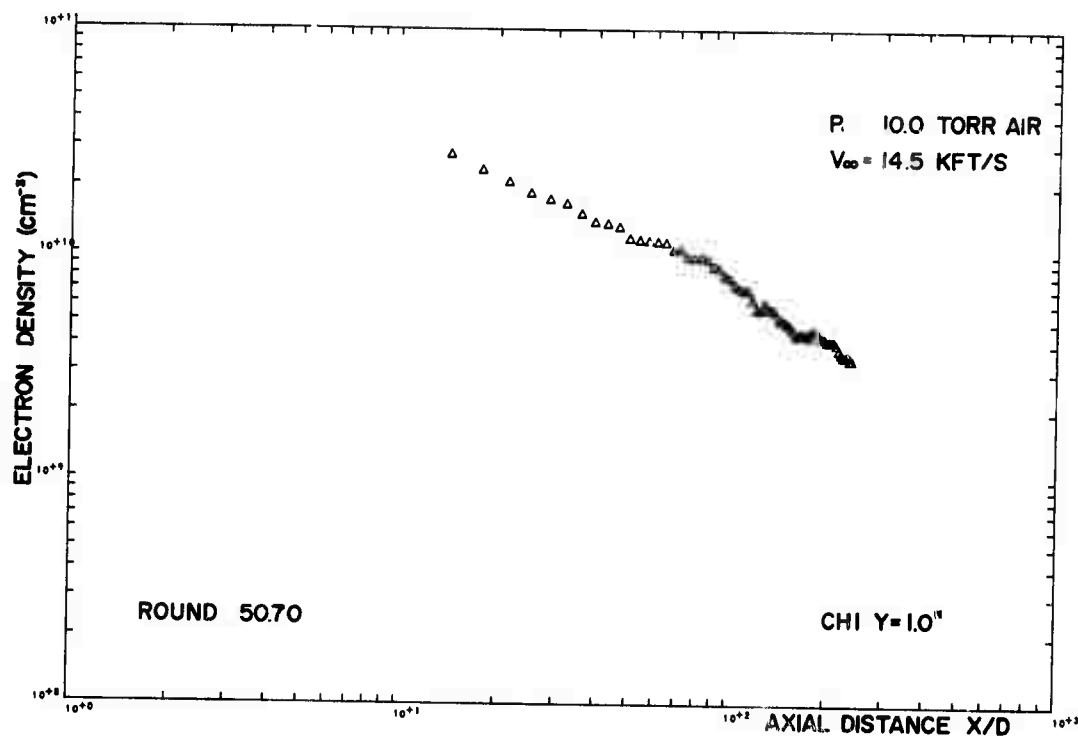


FIGURE C-1(a)

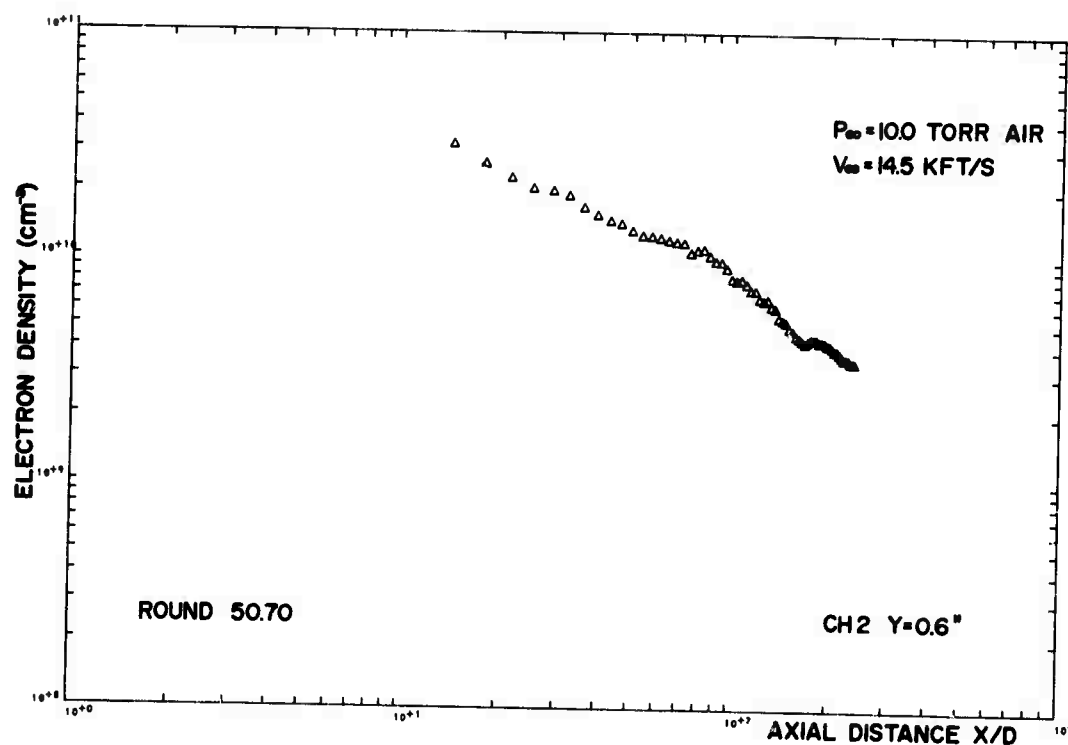


FIGURE C-1(b)

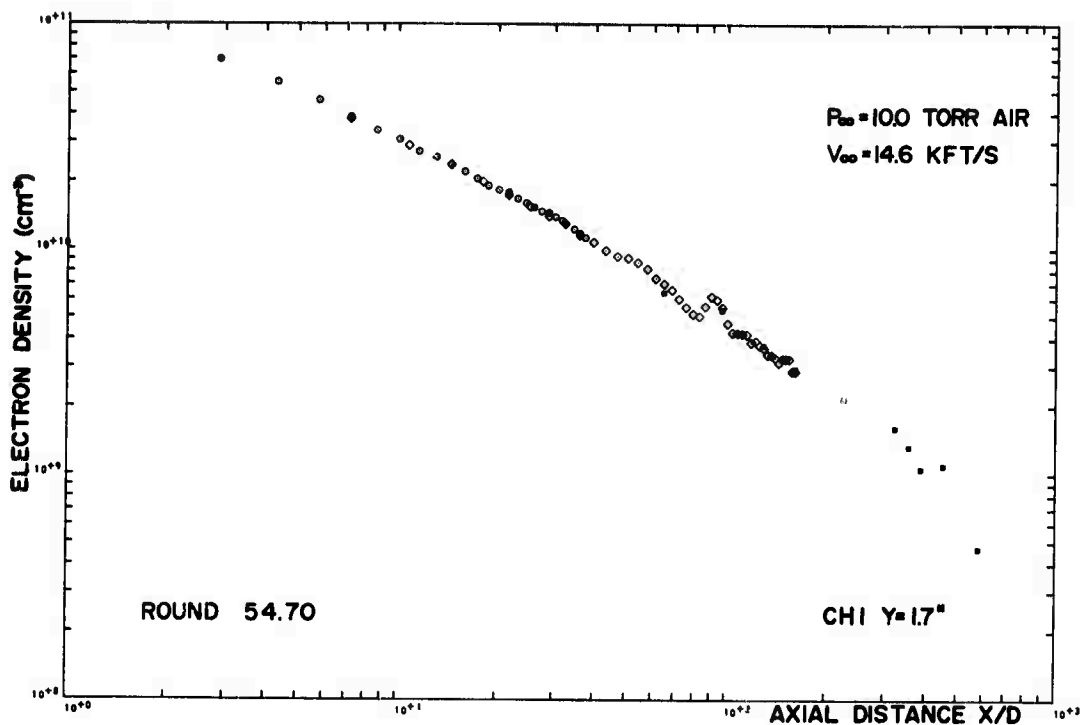


FIGURE C-2(a)

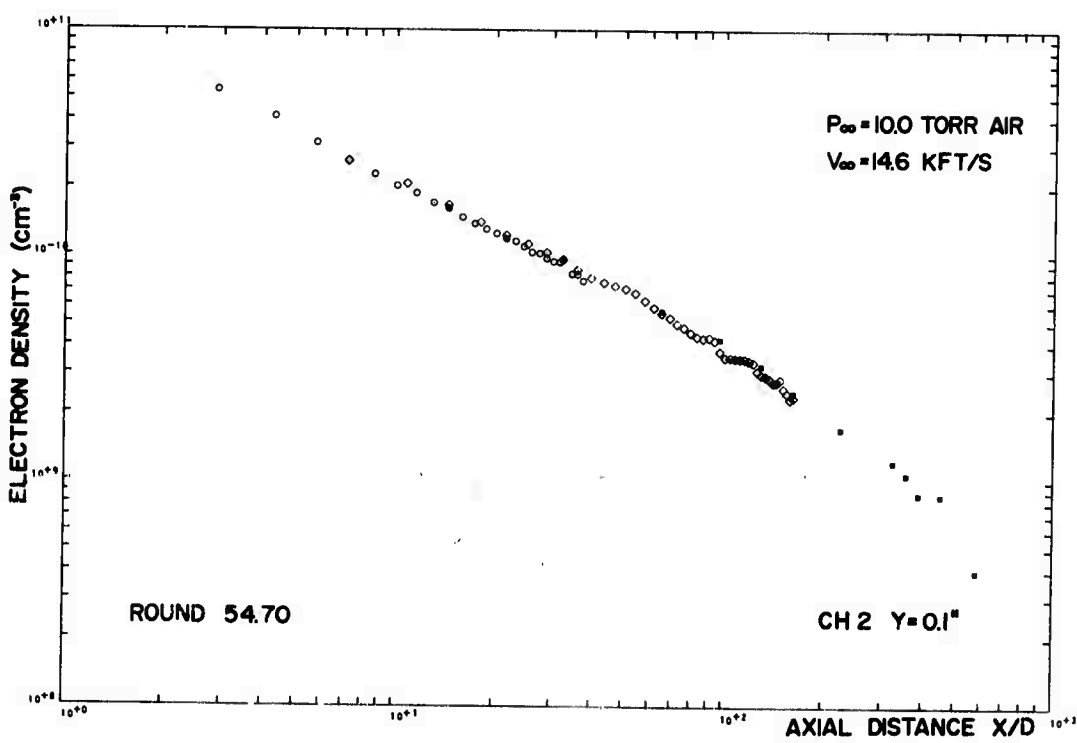


FIGURE C-2(b)

UNCLASSIFIED
122

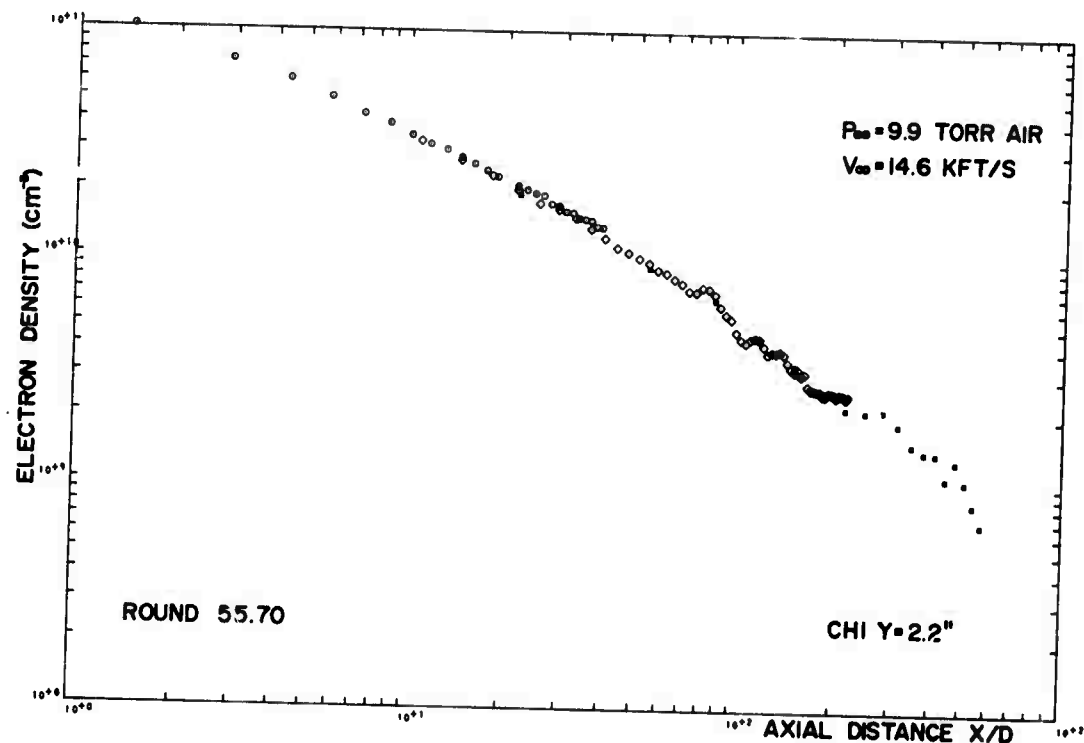


FIGURE C-3(a)

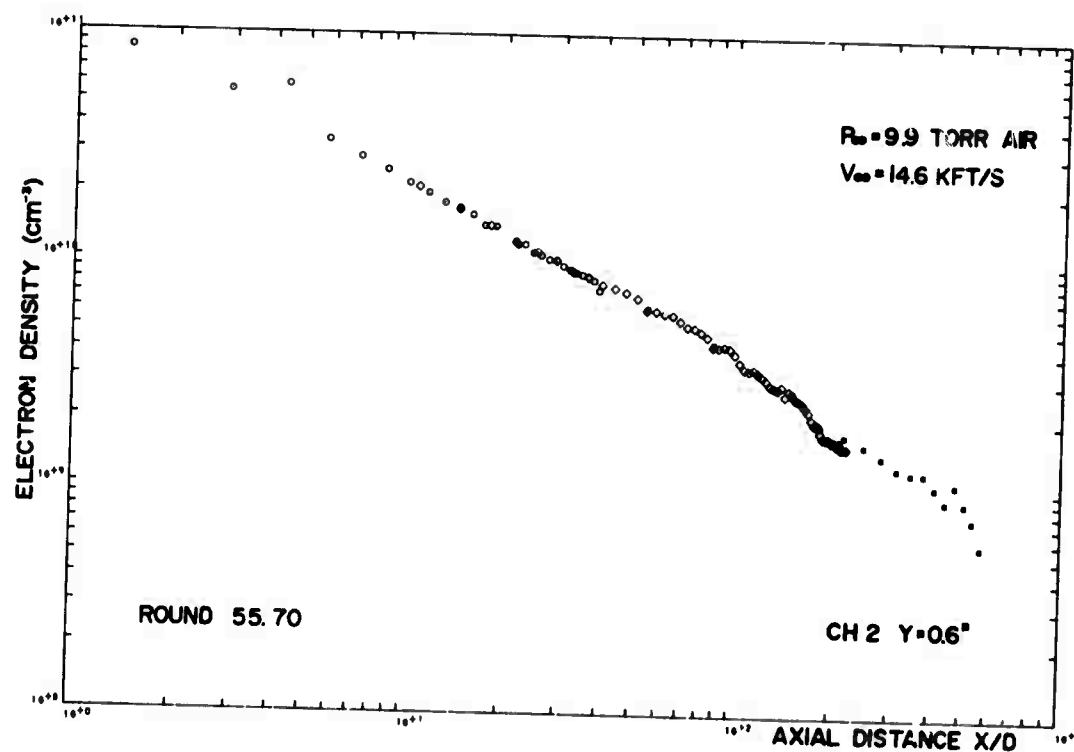


FIGURE C-3(b)

UNCLASSIFIED

123

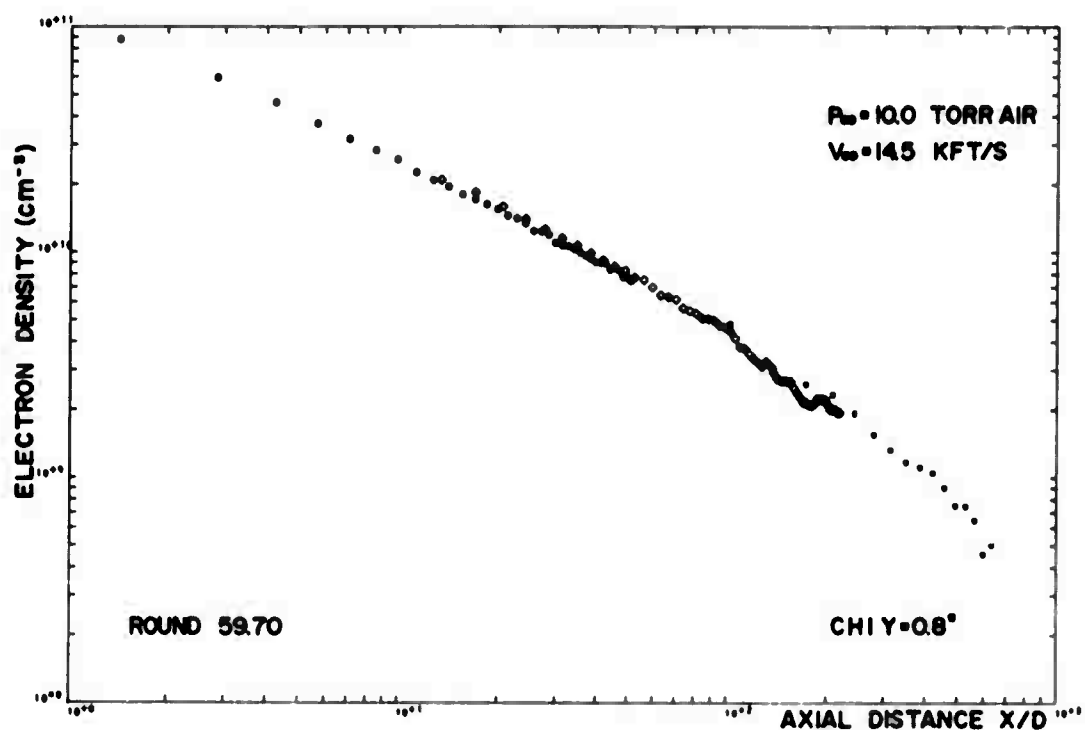


FIGURE C-4(a)

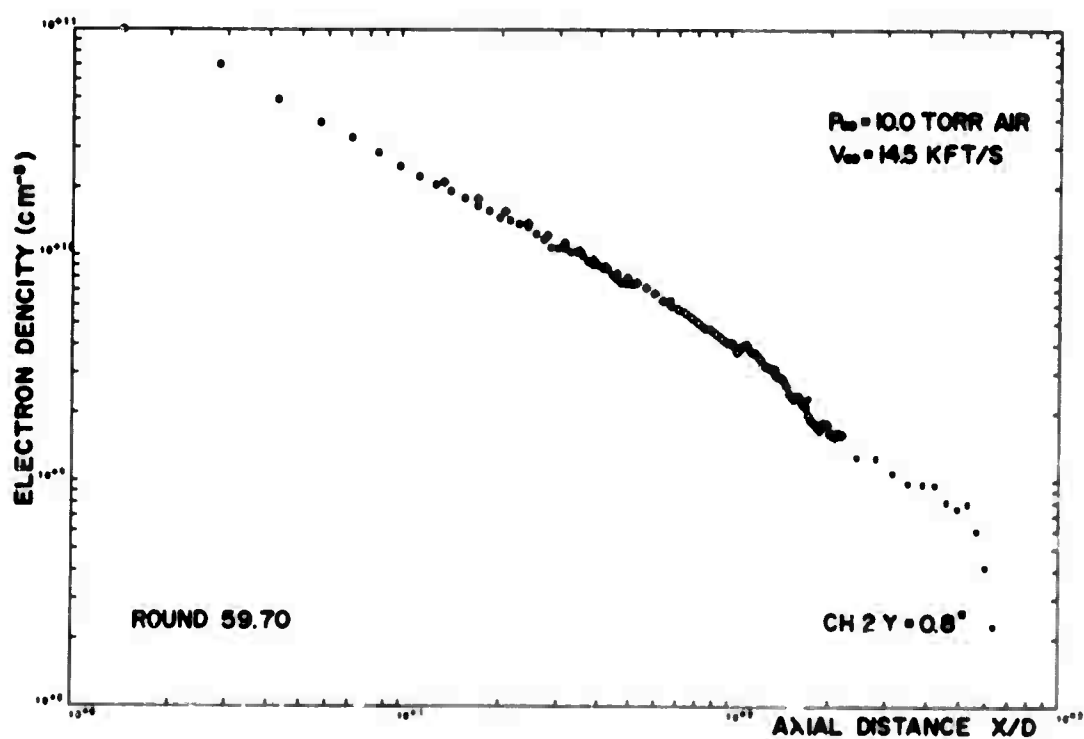


FIGURE C-4(b)

UNCLASSIFIED
124

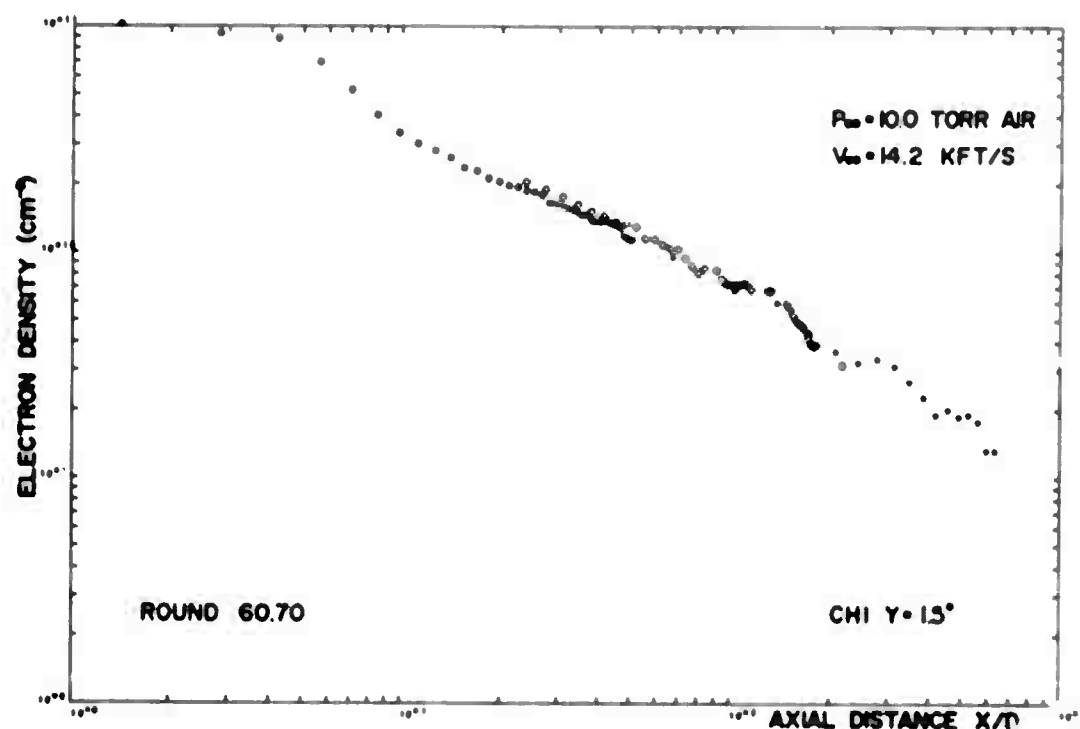


FIGURE C-5(a)

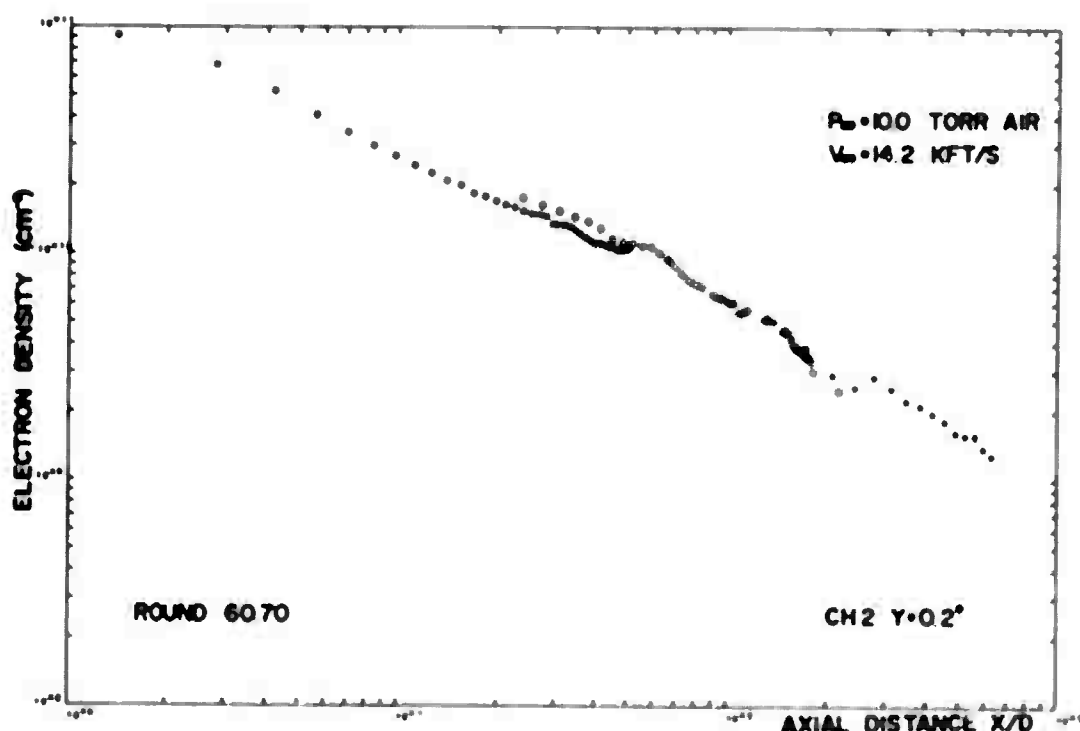


FIGURE C-5(b)

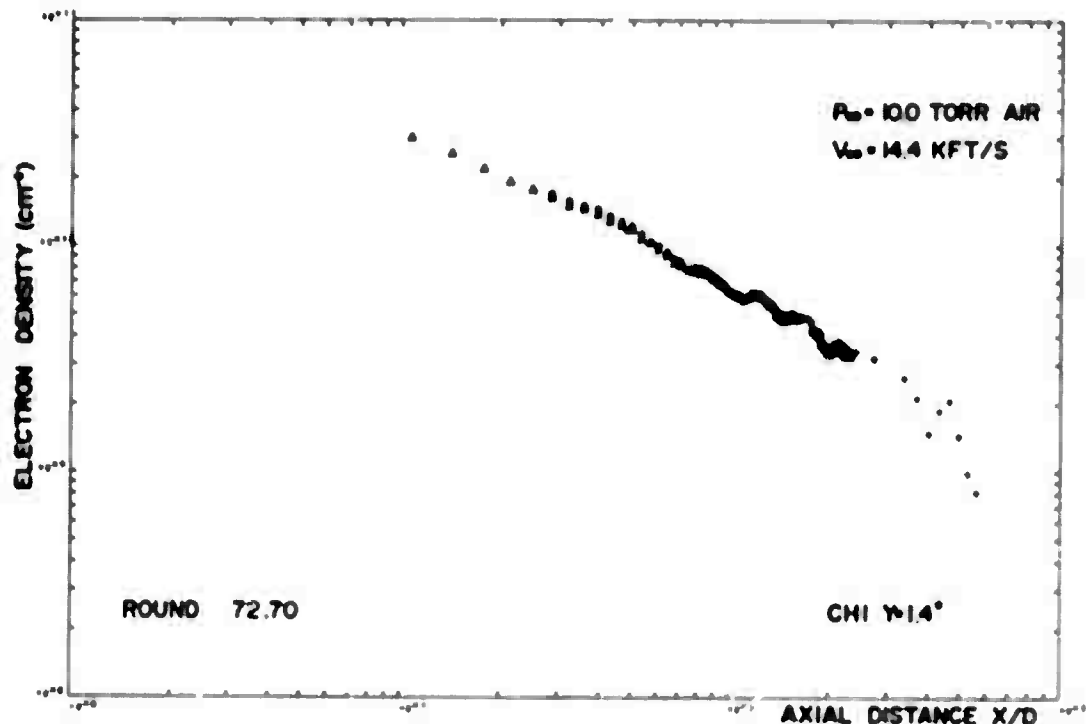


FIGURE C-6(a)

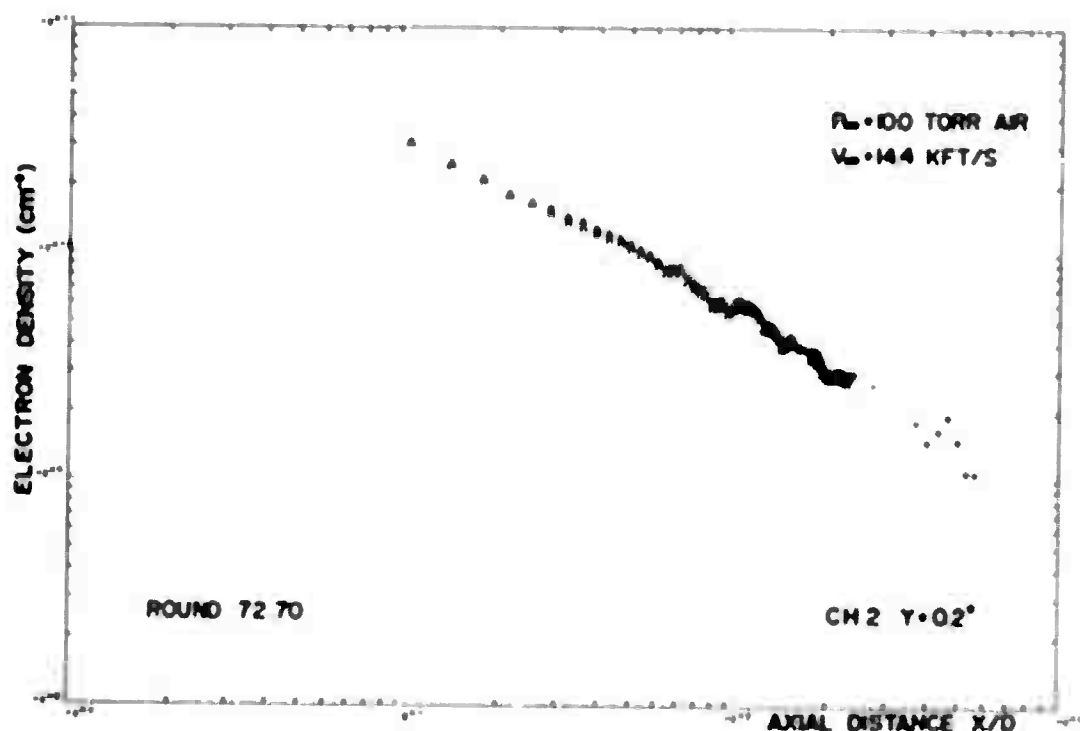


FIGURE C-6(b)

UNCLASSIFIED

126

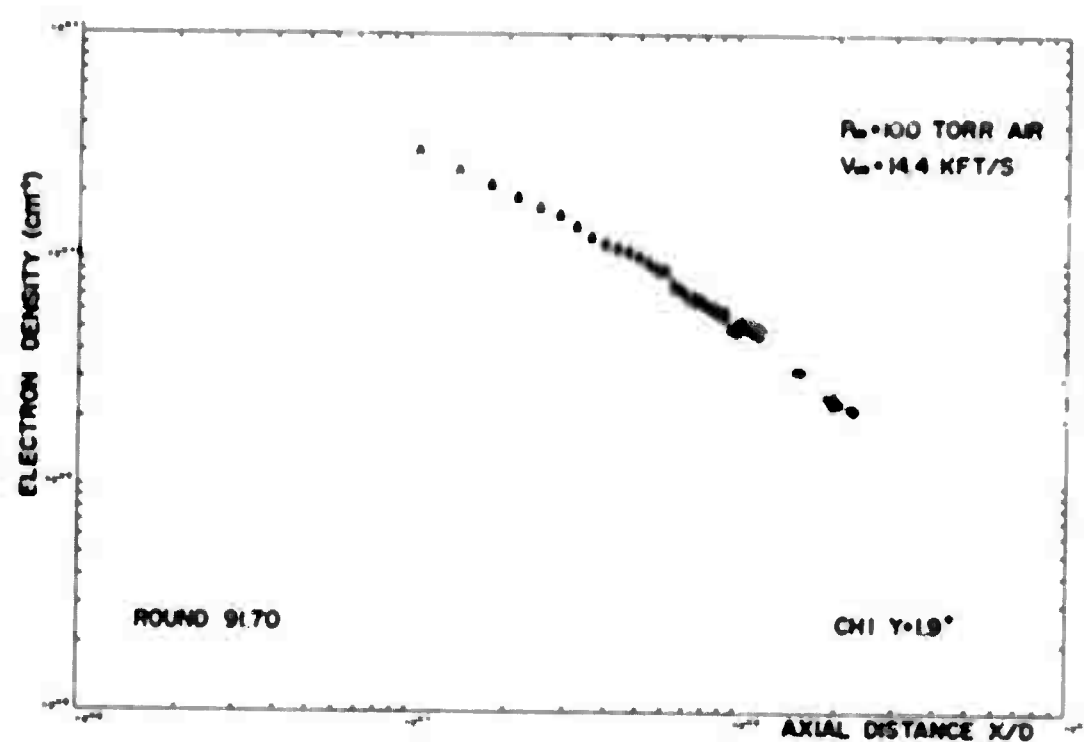


FIGURE C-9(a)

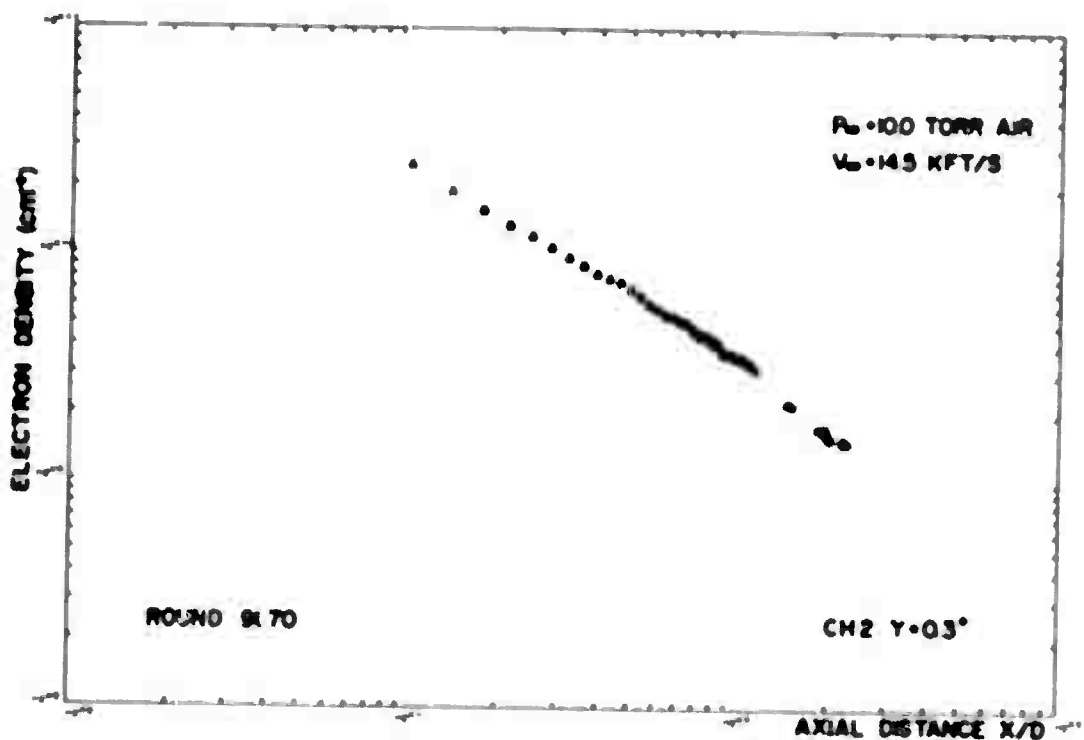


FIGURE C-9(b)

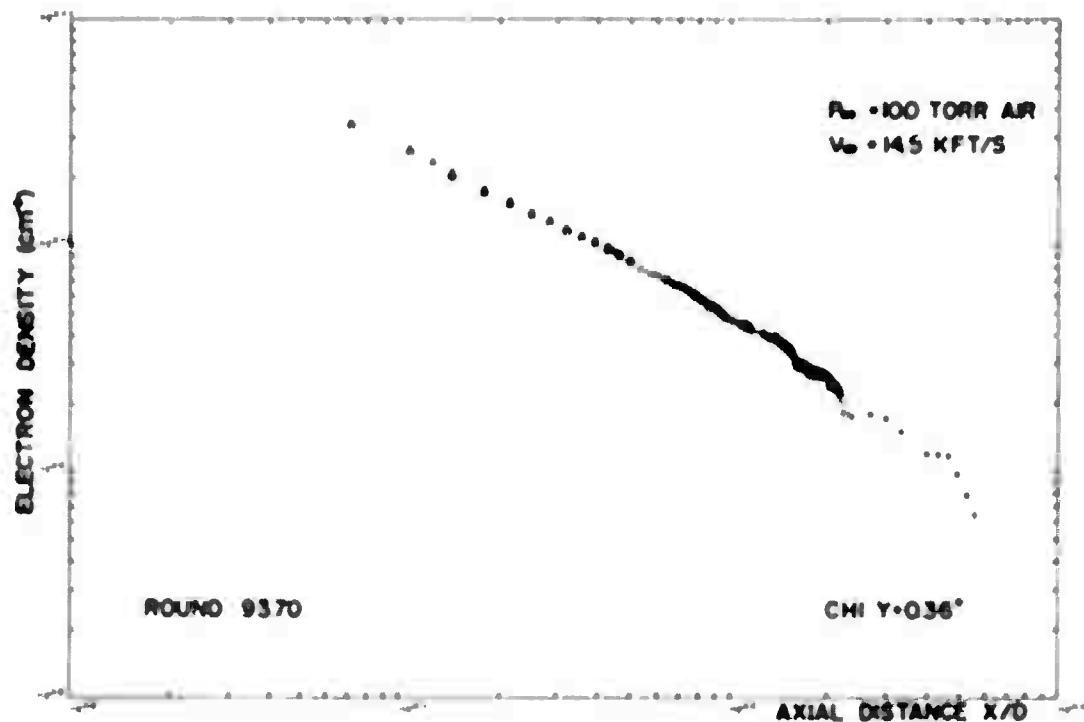


FIGURE C-10(a)

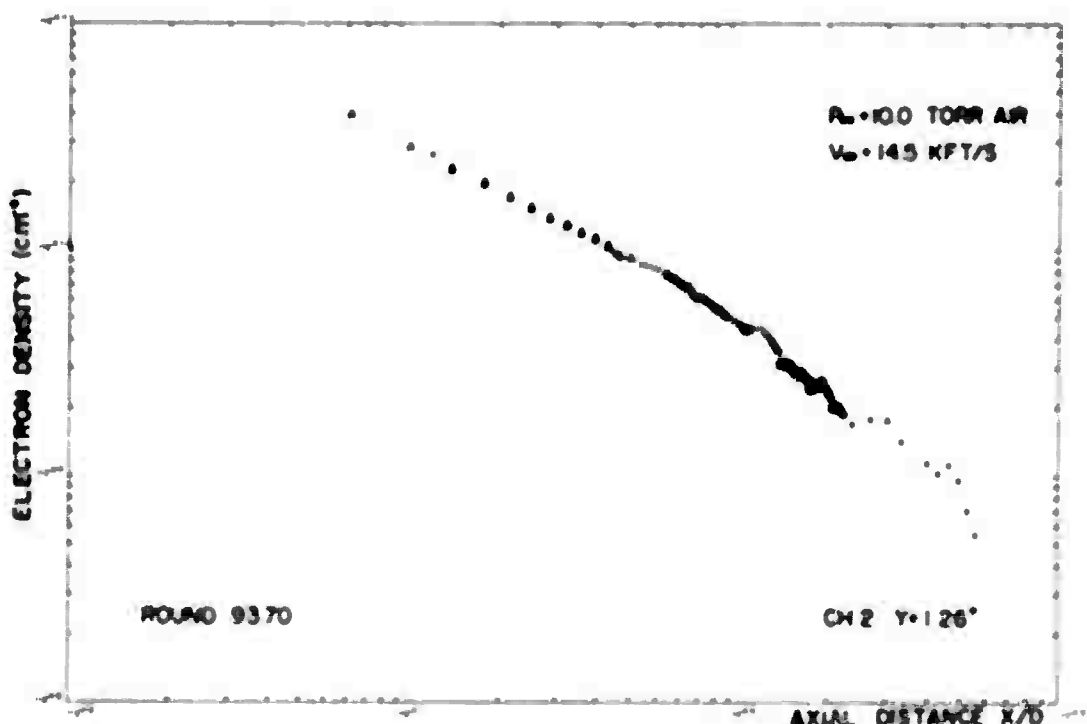


FIGURE C-10(b)

UNCLASSIFIED

128

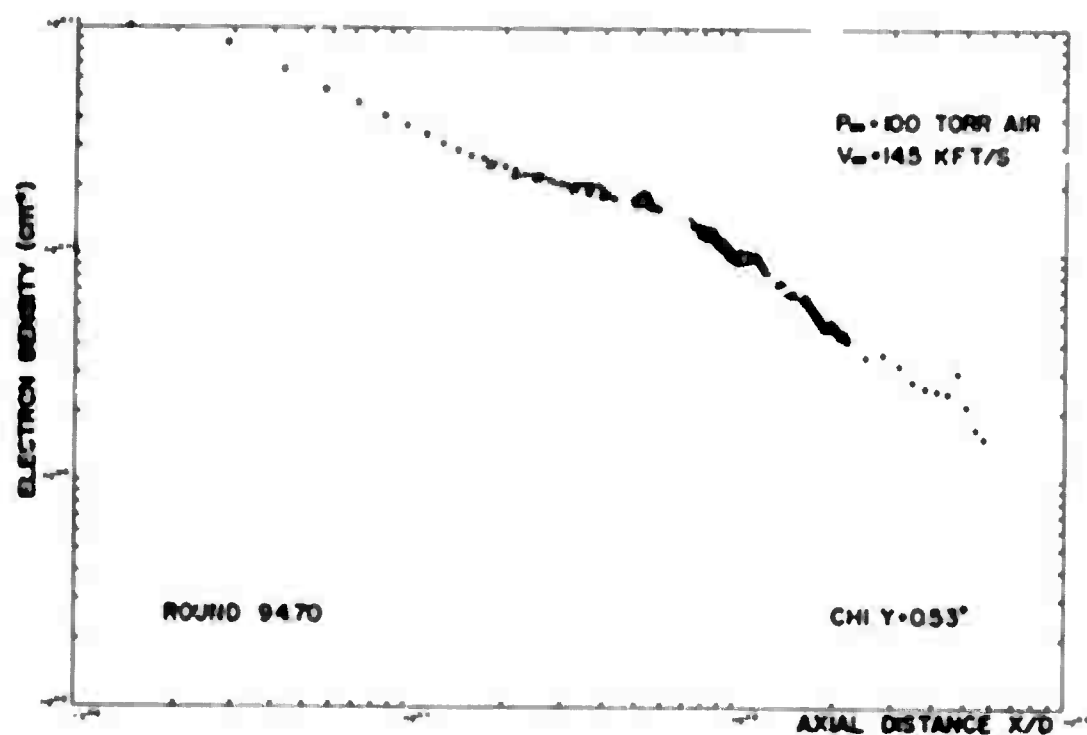


FIGURE C-11(a)

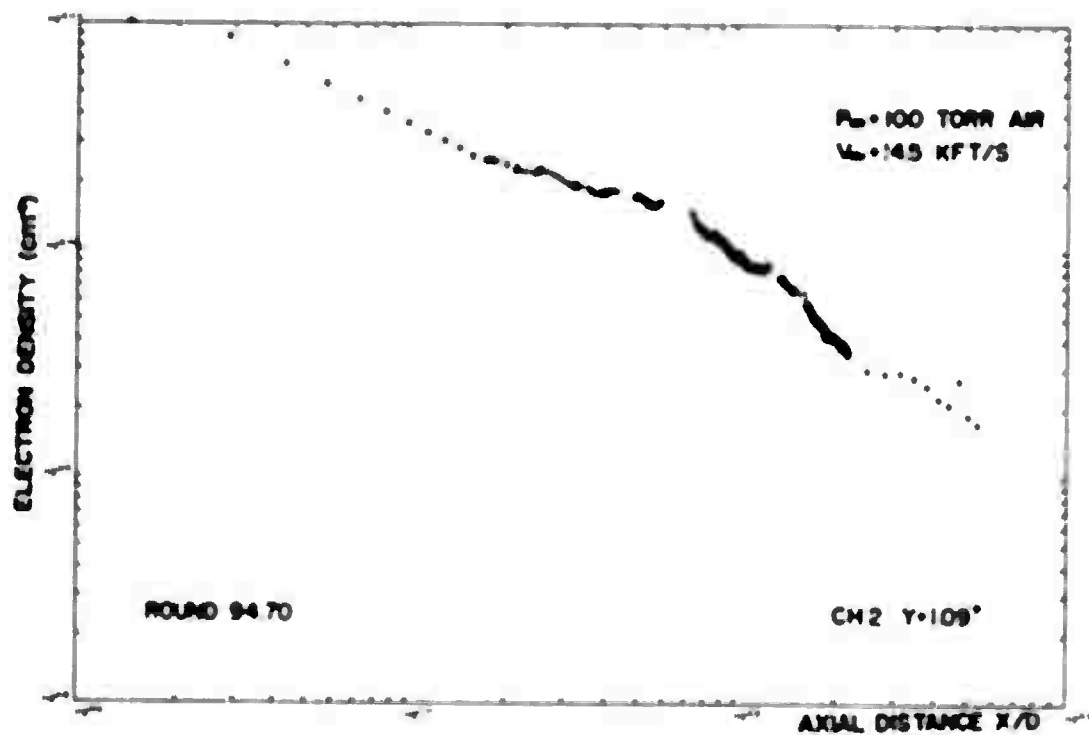


FIGURE C-11(b)

UNCLASSIFIED
129

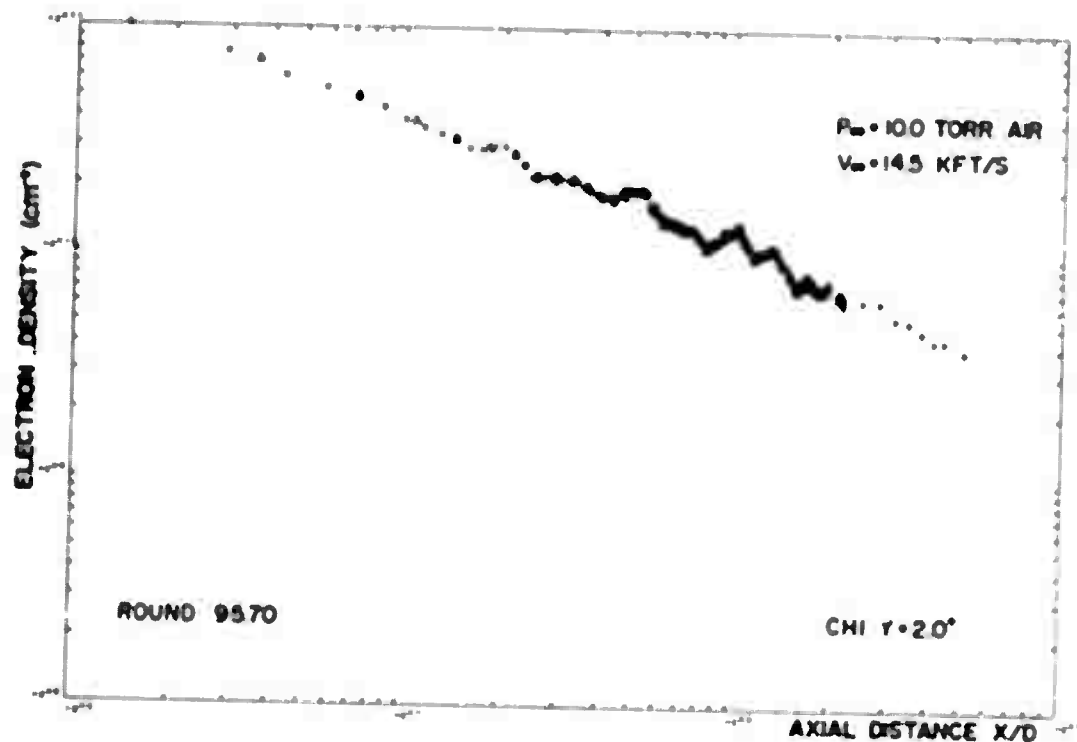


FIGURE C-12(a)

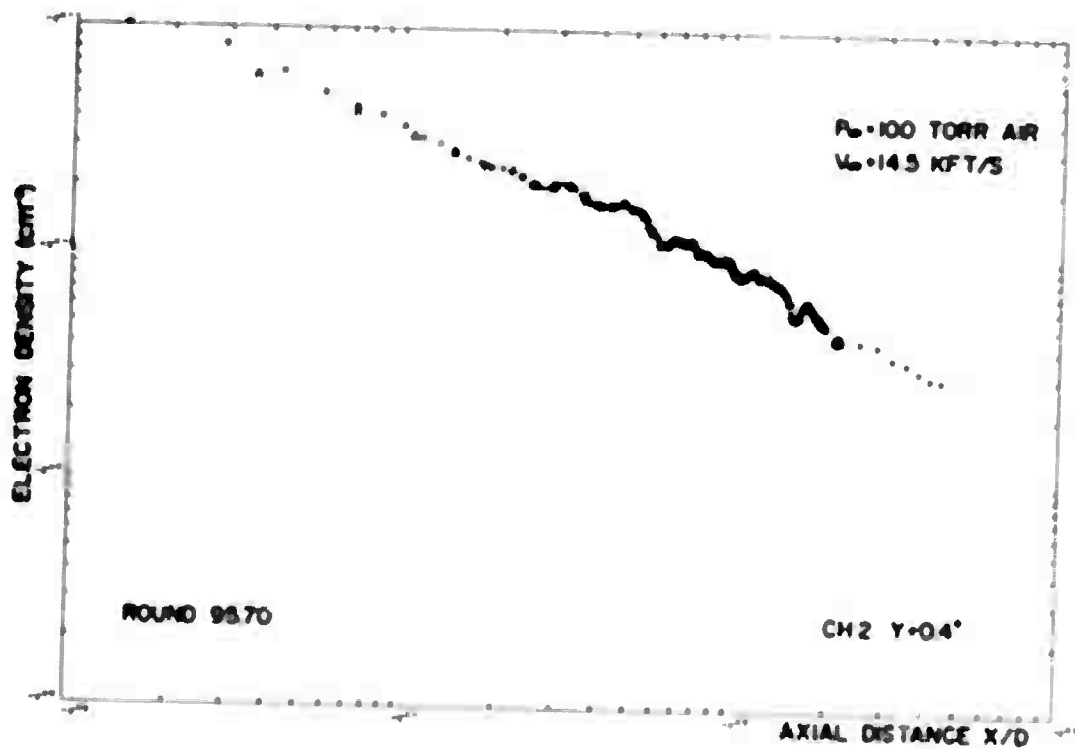


FIGURE C-12(b)

UNCLASSIFIED
130

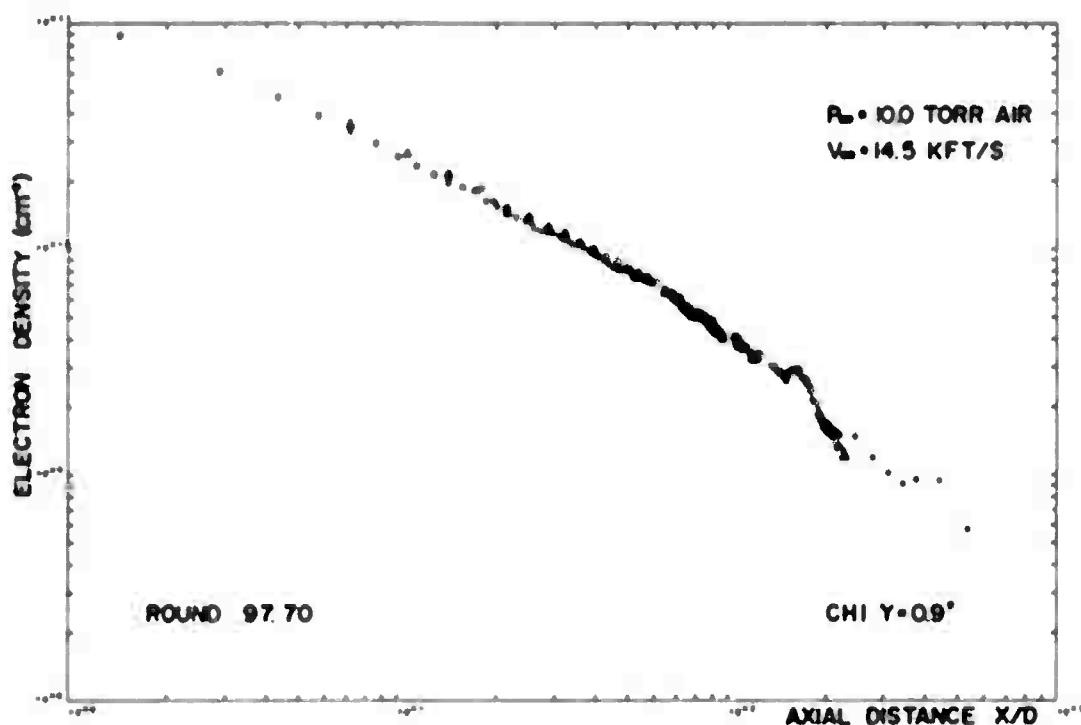


FIGURE C-13(a)

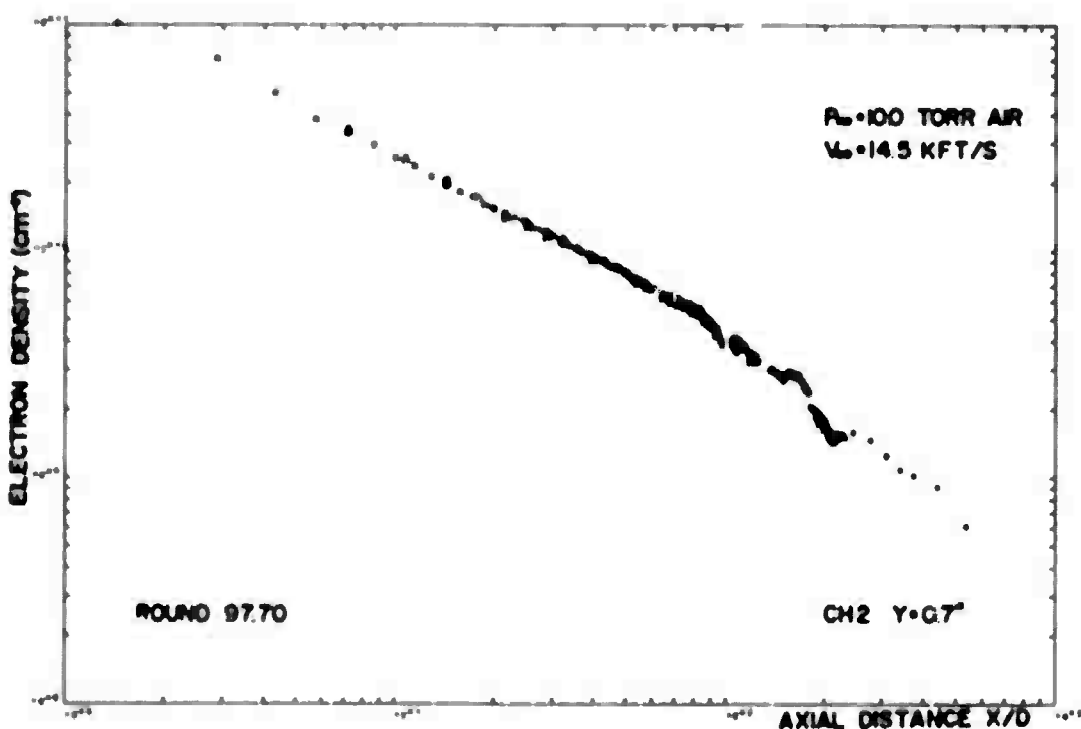


FIGURE C-13(b)

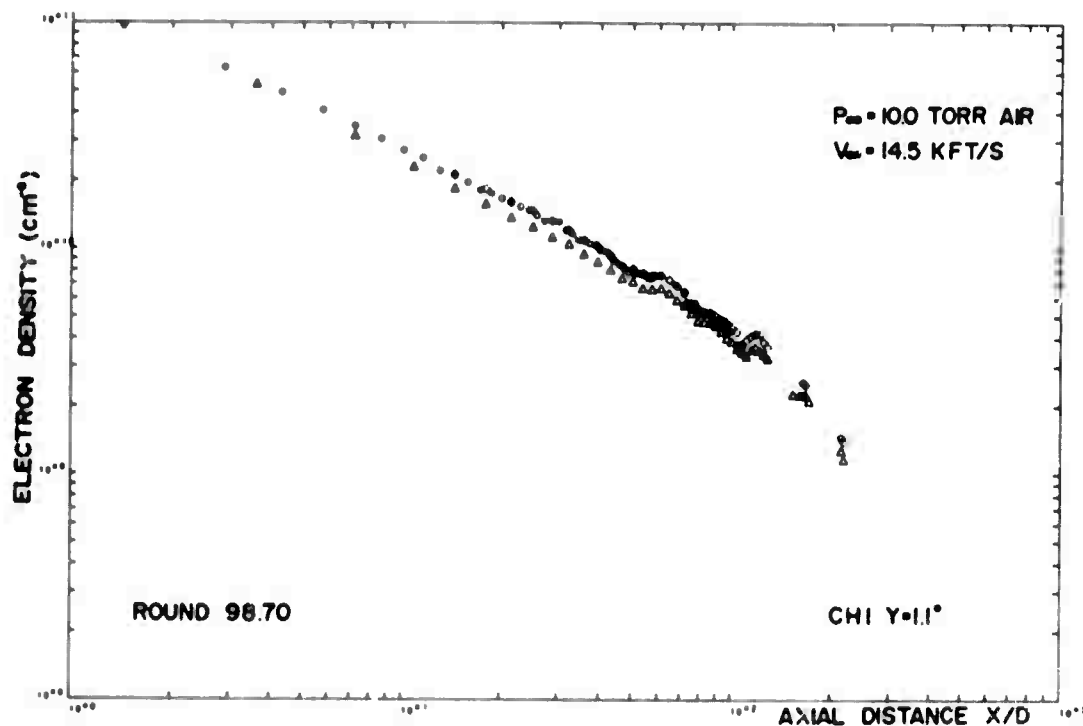


FIGURE C-14(a)

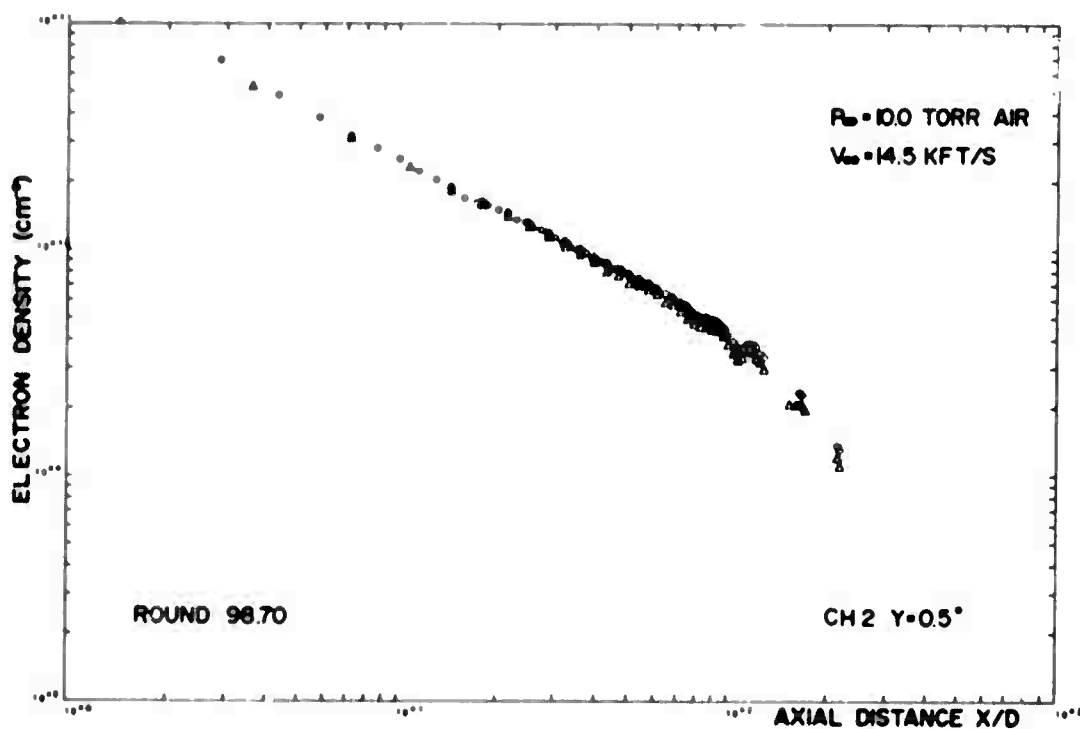


FIGURE C-14(b)

UNCLASSIFIED

132

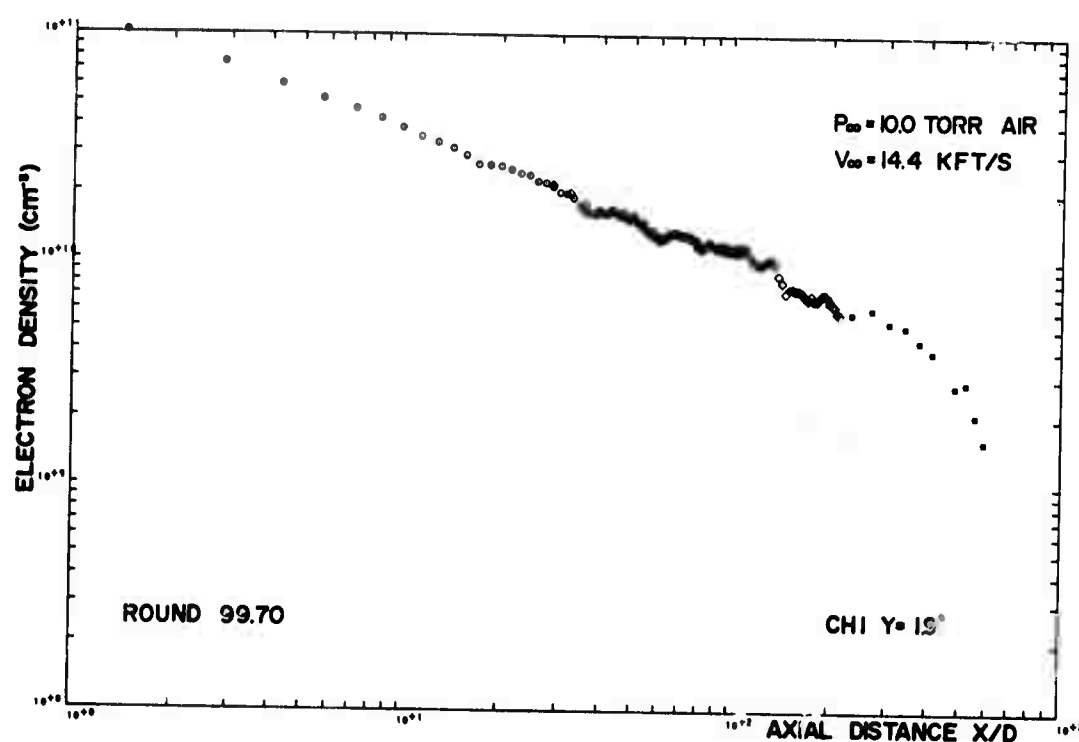


FIGURE C-15(a)

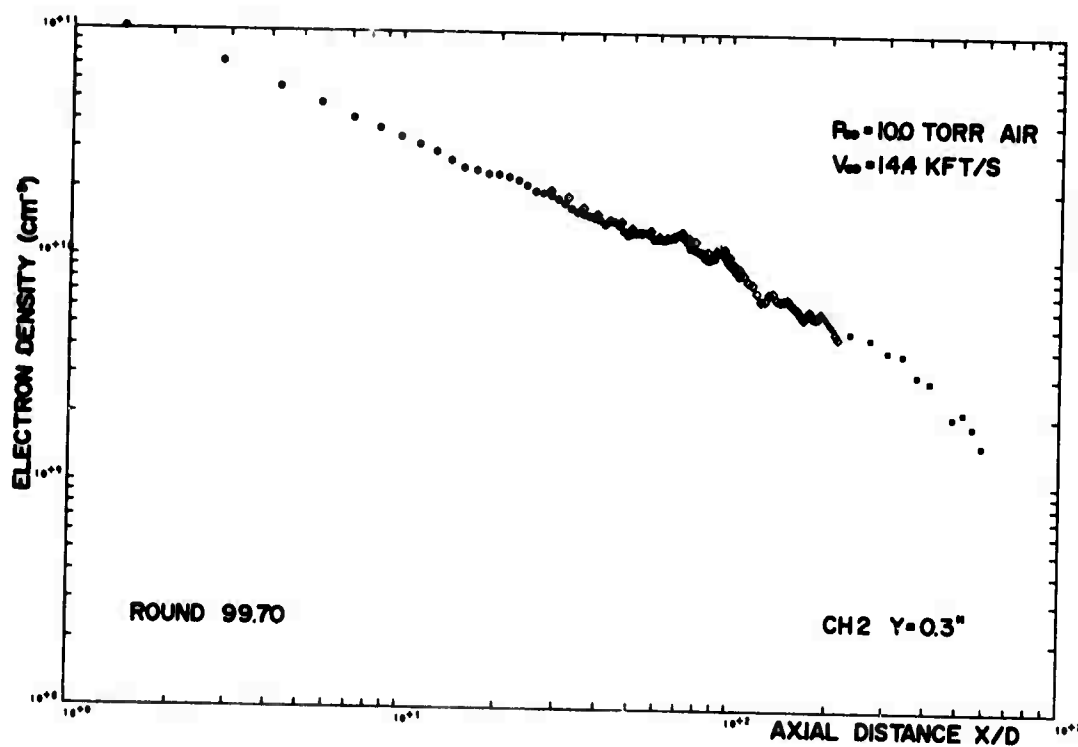


FIGURE C-15(b)

UNCLASSIFIED

133

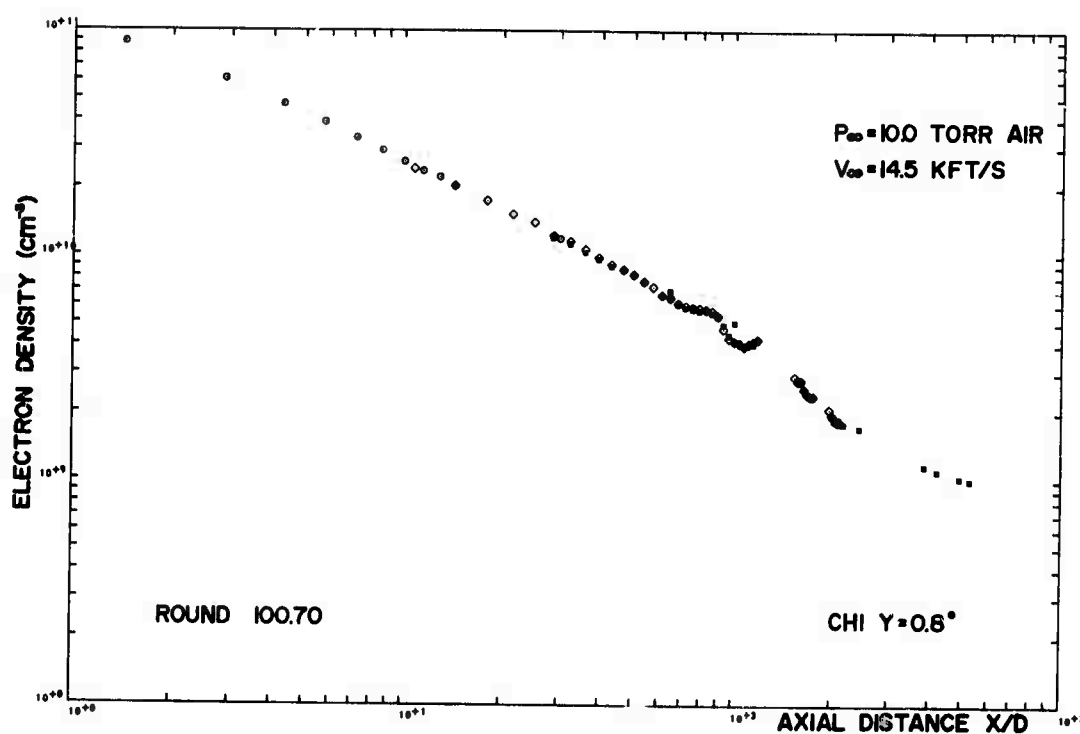


FIGURE C-16(a)

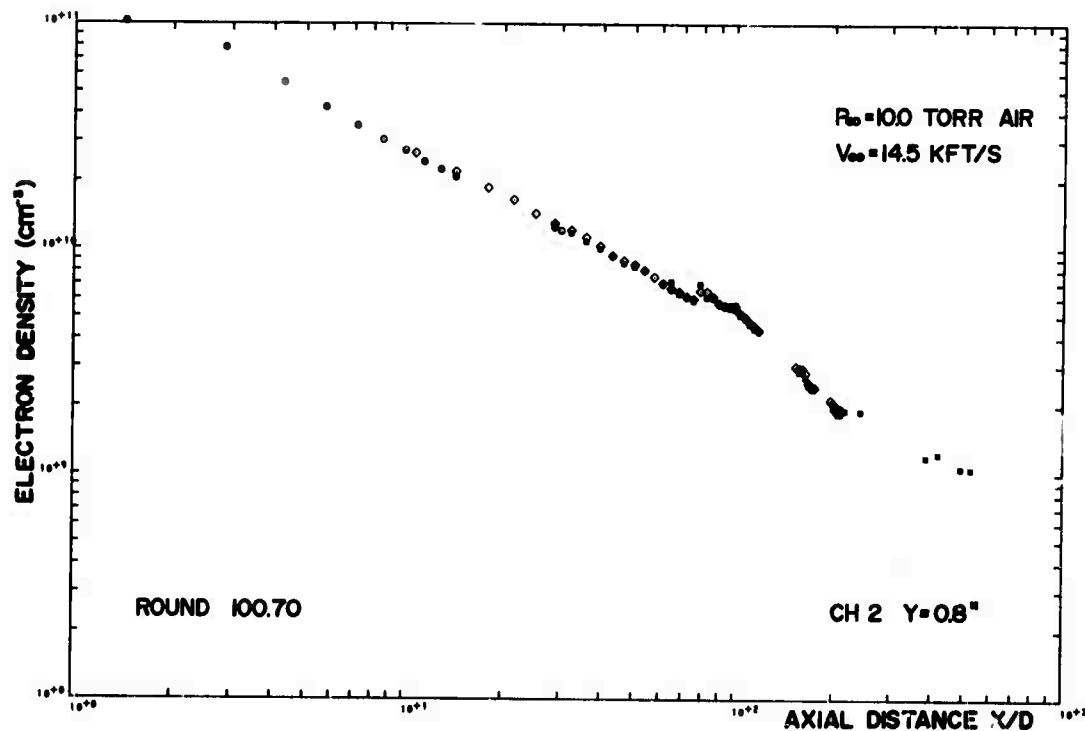


FIGURE C-16(b)

UNCLASSIFIED
135

APPENDIX D

Interferometer Firing Reports and SIN ϕ Displays Nitrogen Atmospheres

UNCLASSIFIED
136

INTERFEROMETER FIRING REPORT

ROUND 62.70

PROJECTILE 2.7" SPHERE

VELOCITY 14.5 Kft/s

PRESSURE 7.6 Torr N₂

INTERFEROMETER STATION 272

PROJECTILE POSITION AT STATION 272 0.148" Low

DISTANCE TO UPPER BEAM (CH 2) 1.068"

DISTANCE TO LOWER BEAM (CH 1) 0.853"

FIGURE D-1(a)

UNCLASSIFIED

137

INTERFEROMETER $\sin \phi$ DISPLAYS

ROUND 62/70

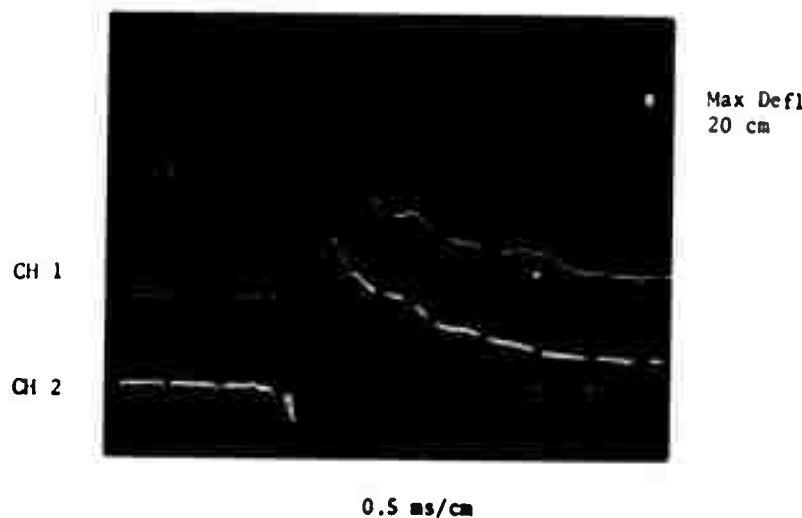


FIGURE D-1(b)

UNCLASSIFIED

138

INTERFEROMETER FIRING REPORT

ROUND 65.70

PROJECTILE 2.7" SPHERE

VELOCITY 14,500 ft/s

PRESSURE 7.6 Torr N₂

INTERFEROMETER STATION 272

PROJECTILE POSITION AT STATION 272 0.71" Low

DISTANCE TO UPPER BEAM (CH 2) 1.63"

DISTANCE TO LOWER BEAM (CH 1) 0.00"

FIGURE D-2(a)

EXTENSIMETRIC 5in x DISPLAY

ROUND 65/70

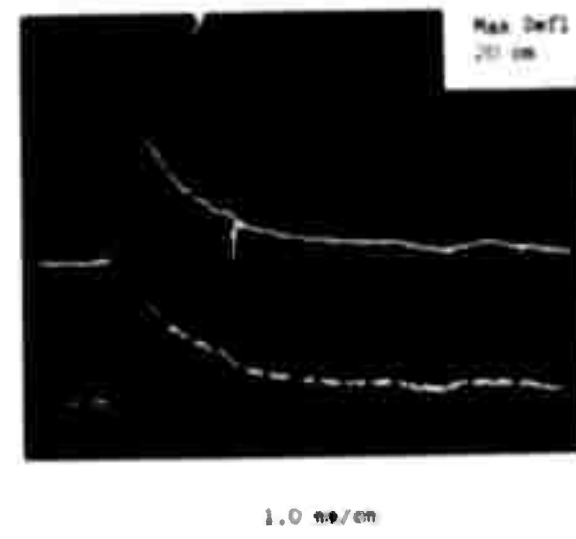
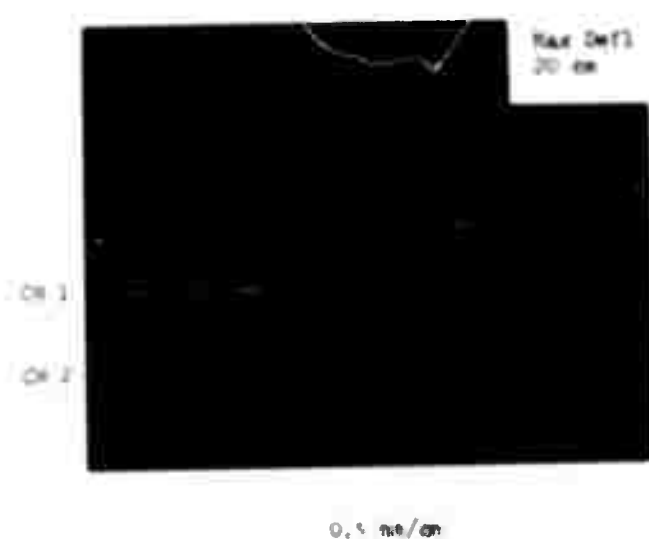
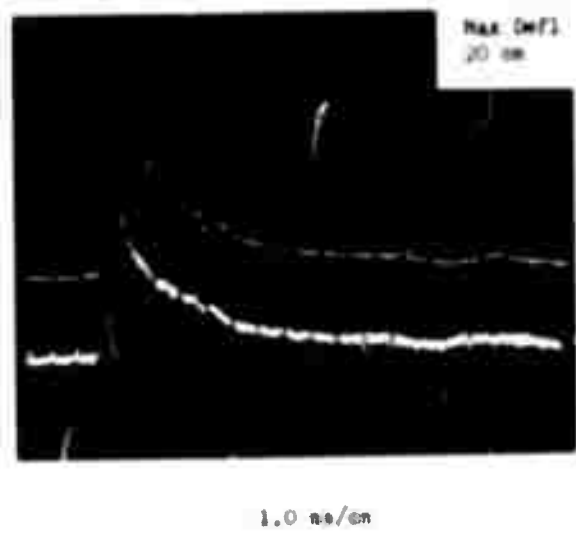
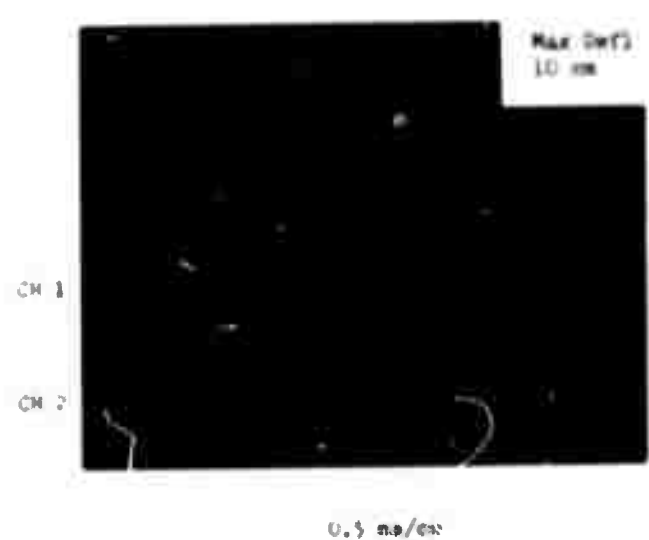


FIGURE D-2(b)

UNCLASSIFIED
140

INTERFEROMETER FIRING REPORT

ROUND 66.70

PROJECTILE 2.7" SPHERE

VELOCITY 14,500 ft/s

PRESSURE 7.6 Torr E_2

INTERFEROMETER STATION 272

PROJECTILE POSITION AT STATION 272 2.56" HIGH

DISTANCE TO UPPER BEAM (CH 2) 1.64"

DISTANCE TO LOWER BEAM (CH 1) 3.26"

FIGURE D-3(a)

INTERFEROMETER 81A + DISPLATE

RECORD 14/70

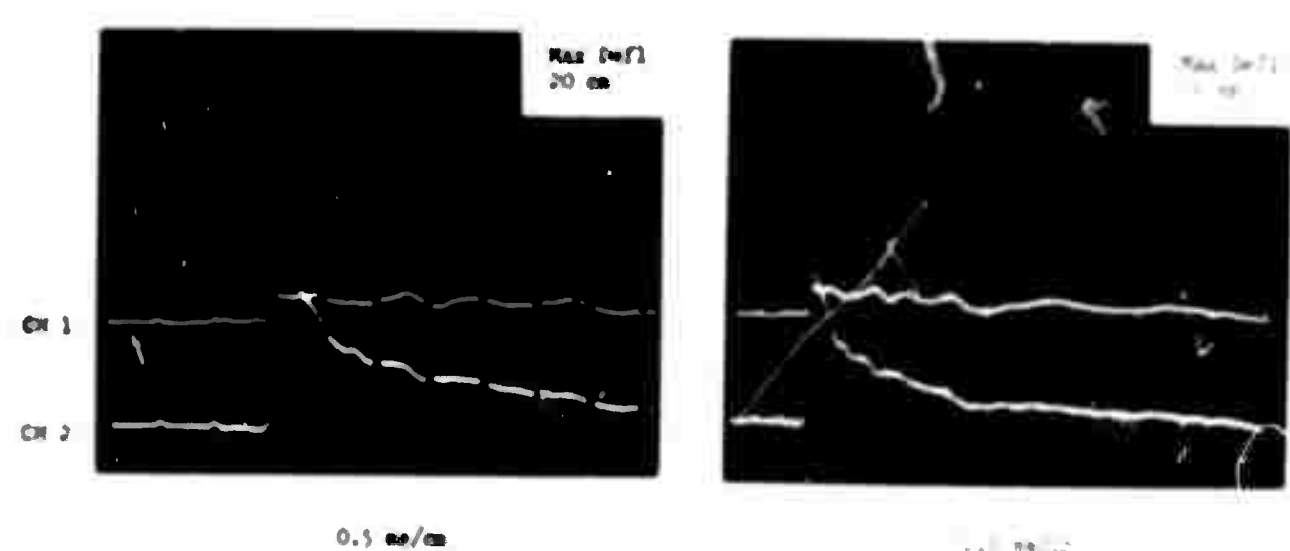
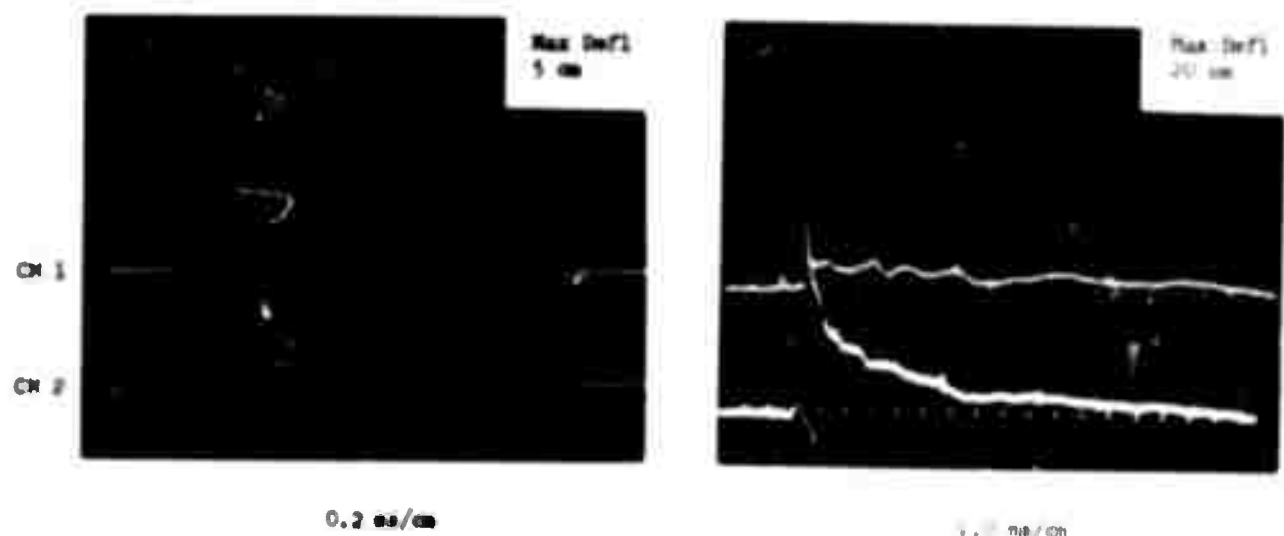


FIGURE D-3(b)

UNCLASSIFIED

142

INTERFEROMETER FIRING REPORT

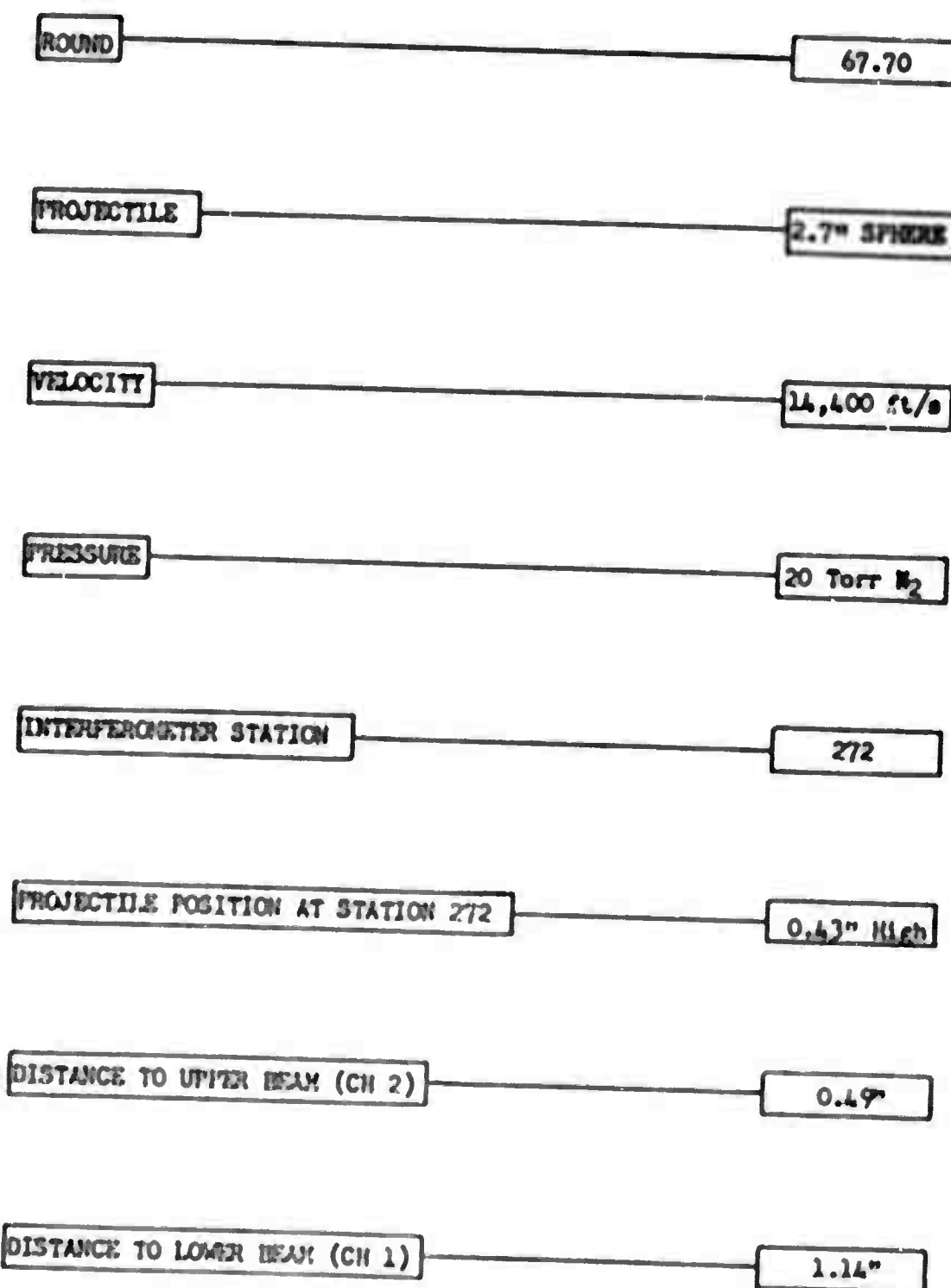
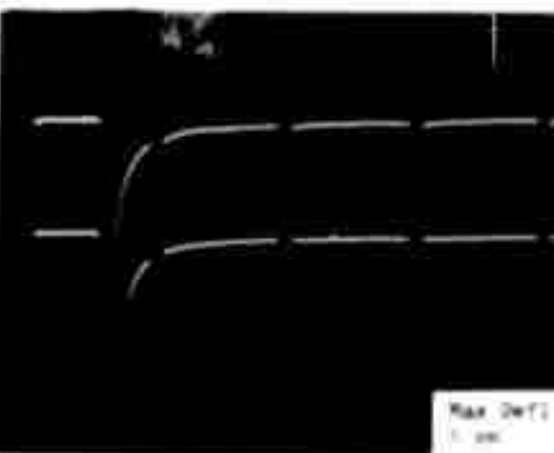
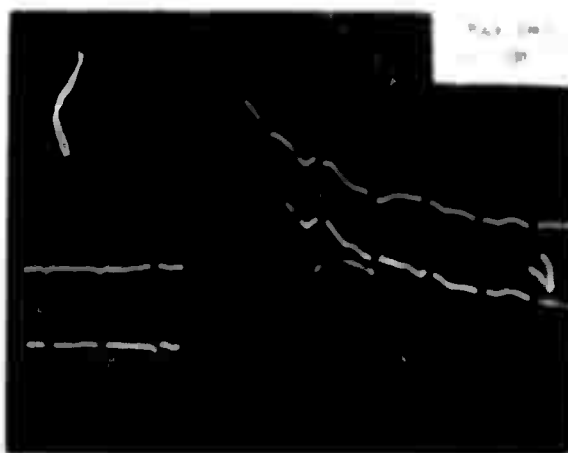
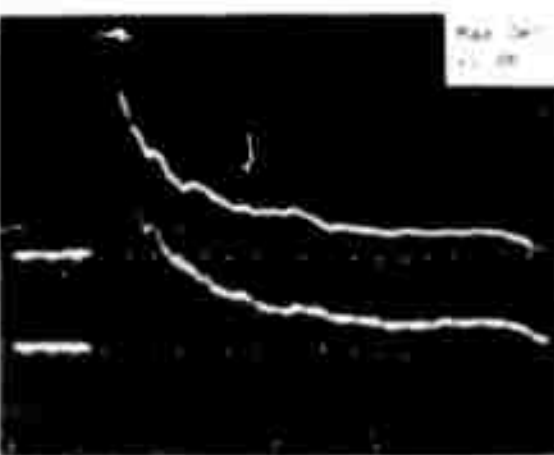
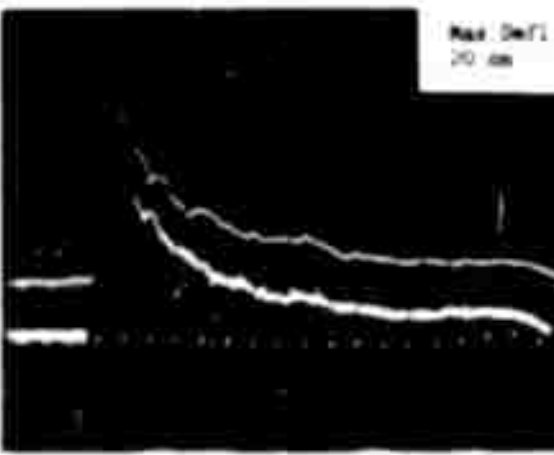
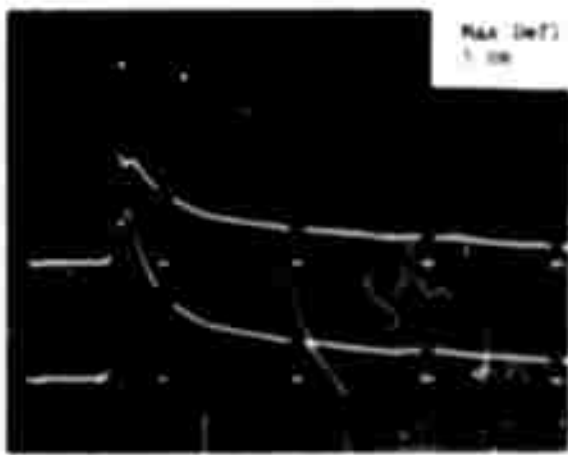


FIGURE D-4(a)

INTERFEROMETER SCAN & DISPLAYS

ROUND 67/70



0.5 ms/cm

0.5 ms/cm

FIGURE D-4(b)

UNCLASSIFIED
144

INTERFEROMETER FIRING REPORT

ROUND

68.70

PROJECTILE

2.7" SPHECO

VELOCITY

14,400 ft/s

PRESSURE

7.6 Torr N₂

INTERFEROMETER STATION

272

PROJECTILE POSITION AT STATION 272

0.90" High

DISTANCE TO UPPER BEAM (CH 2)

0.02"

DISTANCE TO LOWER BEAM (CH 1)

1.60"

FIGURE D-5(a)

UNCLASSIFIED
145

INTERFACULTY 5IN X DISPLAYS

ROUND 64/70

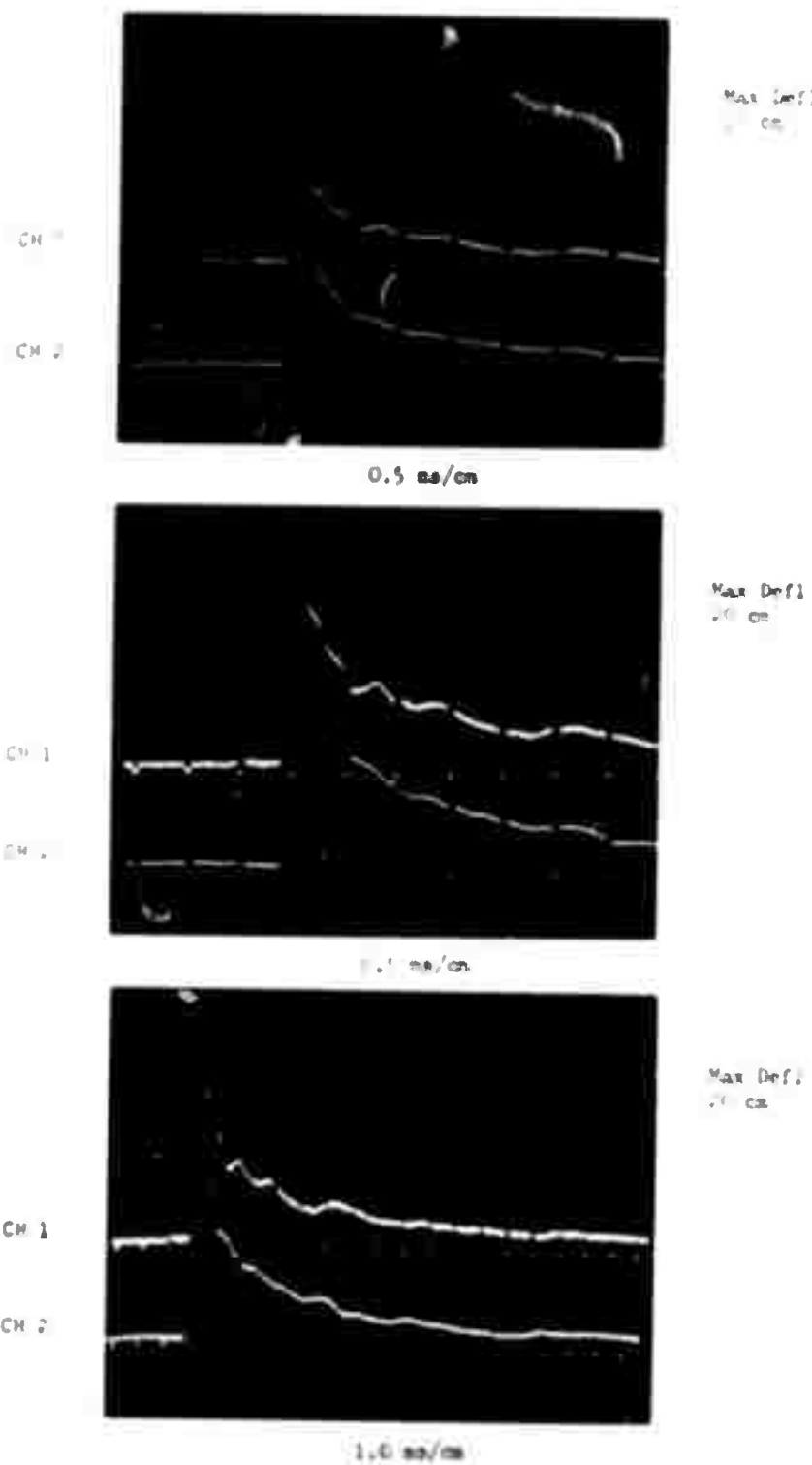


FIGURE D-5(b)

UNCLASSIFIED
146

INTERFEROMETER FIRING REPORT

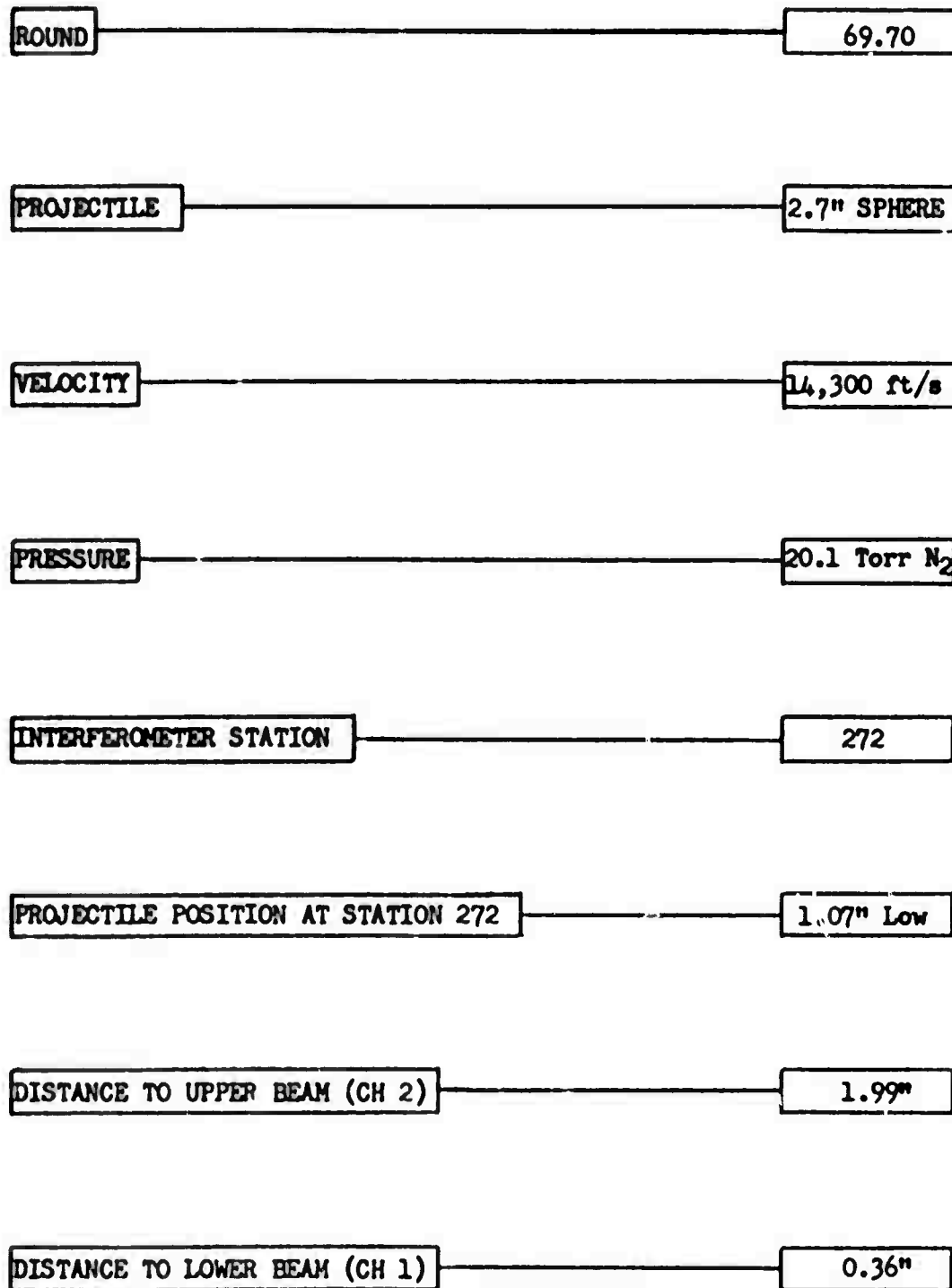


FIGURE D-6(a)

UNCLASSIFIED
147

INTERFEROMETER Sin φ DISPLAYS

ROUND 69/70

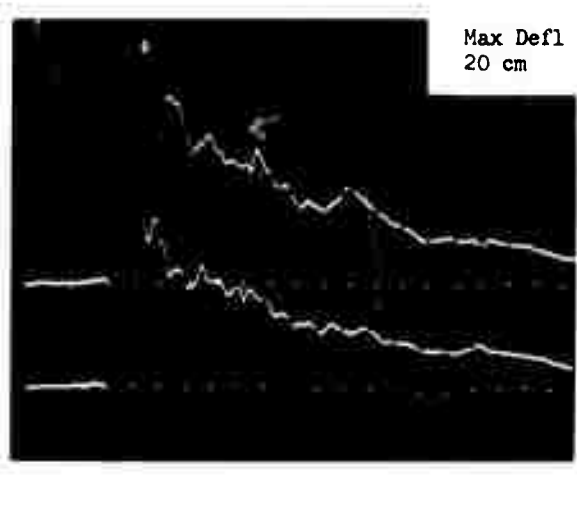
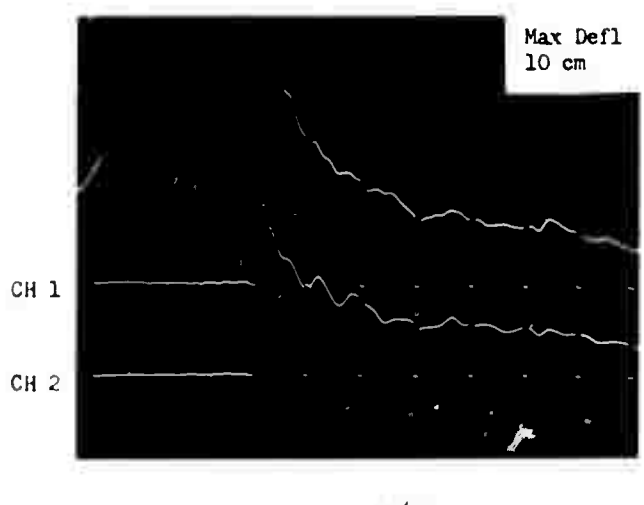
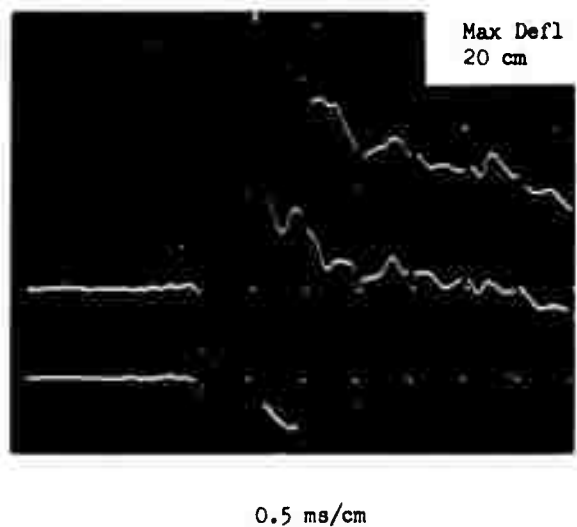
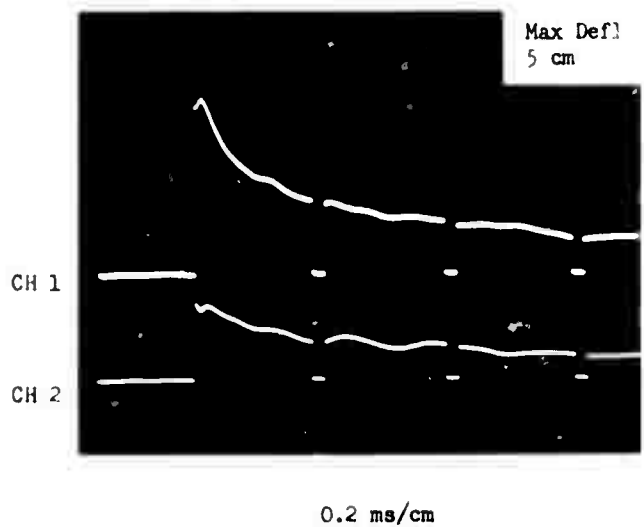


FIGURE D-6(b)

UNCLASSIFIED
148

INTERFEROMETER FIRING REPORT

ROUND 71.70

PROJECTILE 2.7" SPHERE

VELOCITY 14,400 ft/s

PRESSURE 20 Torr N₂

INTERFEROMETER STATION 272

PROJECTILE POSITION AT STATION 272 0.75" High

DISTANCE TO UPPER BEAM (CH 2) 0.17"

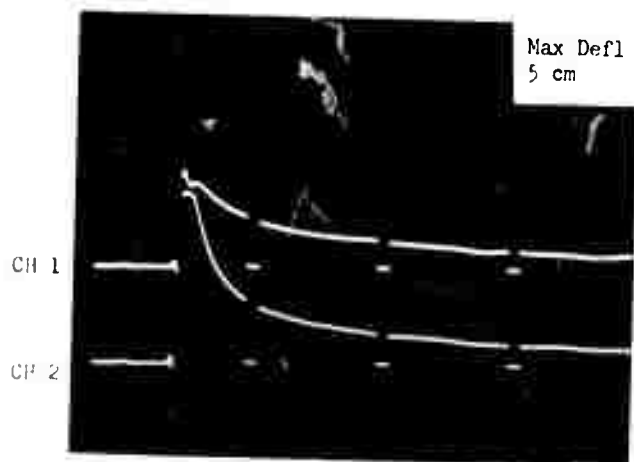
DISTANCE TO LOWER BEAM (CH 1) 1.46"

FIGURE D-7(a)

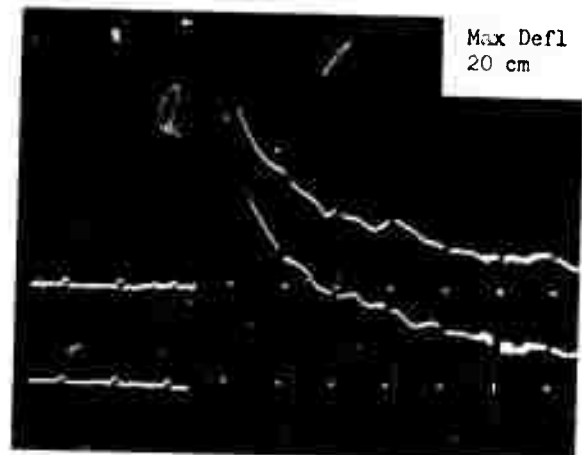
UNCLASSIFIED
149

INTERFEROMETER Sin ϕ DISPLAYS

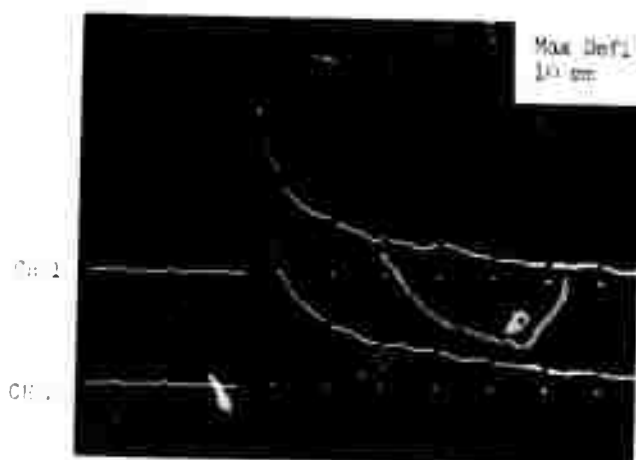
ROUND 71/70



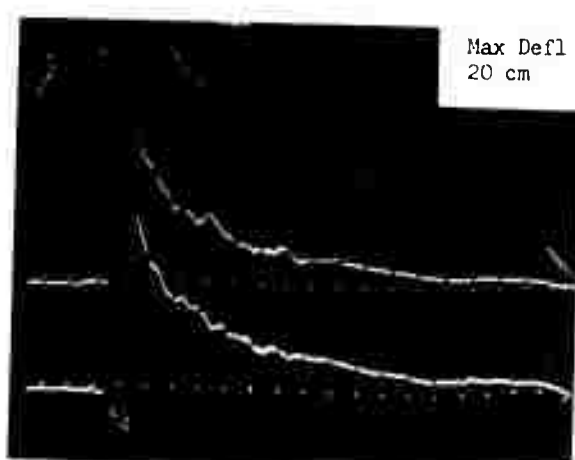
0.2 ms/cm



0.5 ms/cm



0.5 ms/cm



1.0 ms/cm

FIGURE D-7(b)

UNCLASSIFIED
150

INTERFEROMETER FIRING REPORT

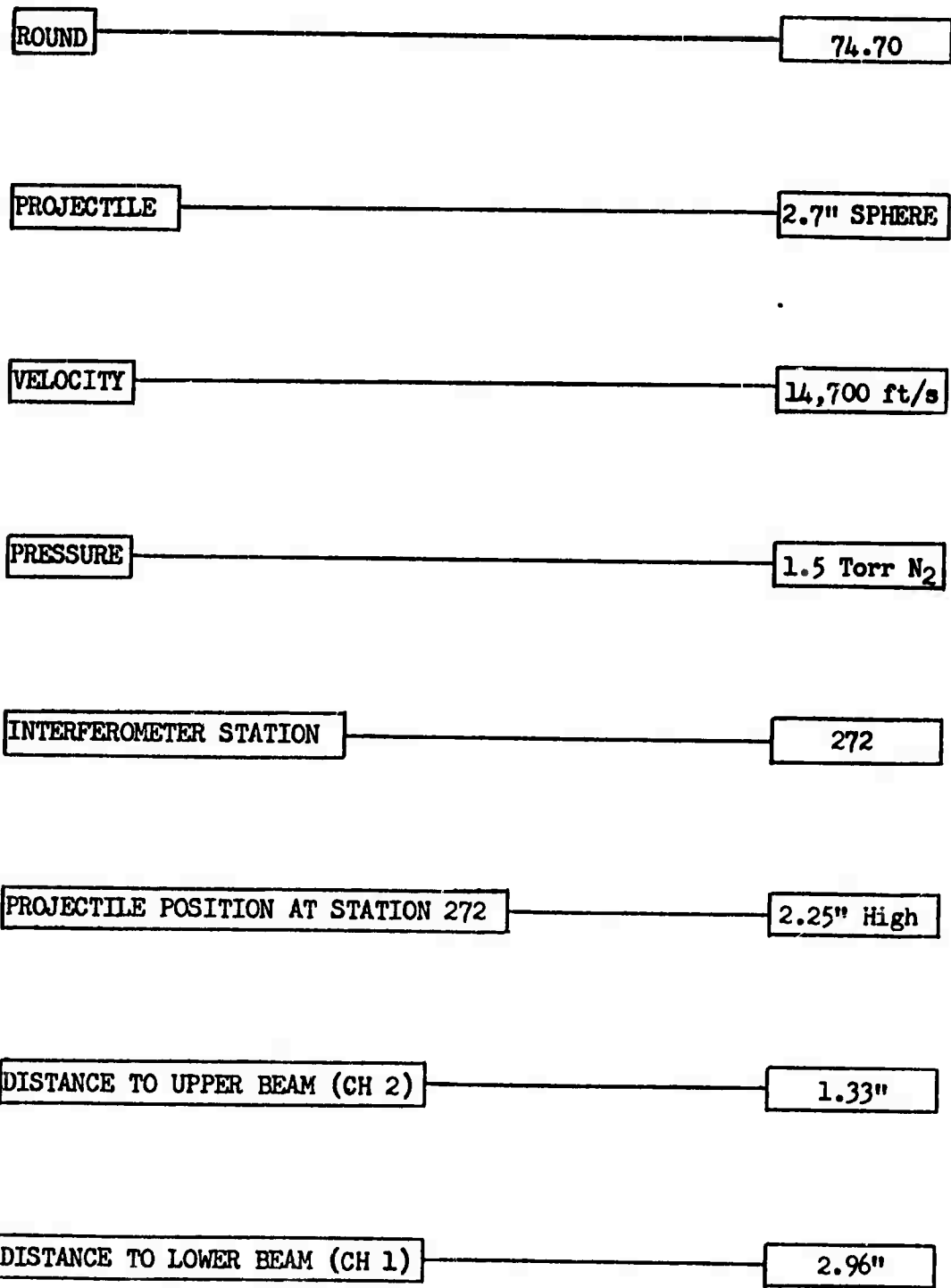


FIGURE D-8(a)

UNCLASSIFIED
151

INTERFEROMETER $\sin \phi$ DISPLAYS

ROUND 74/70

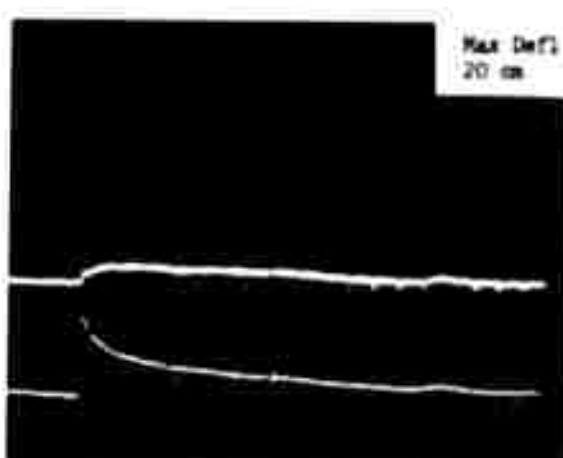
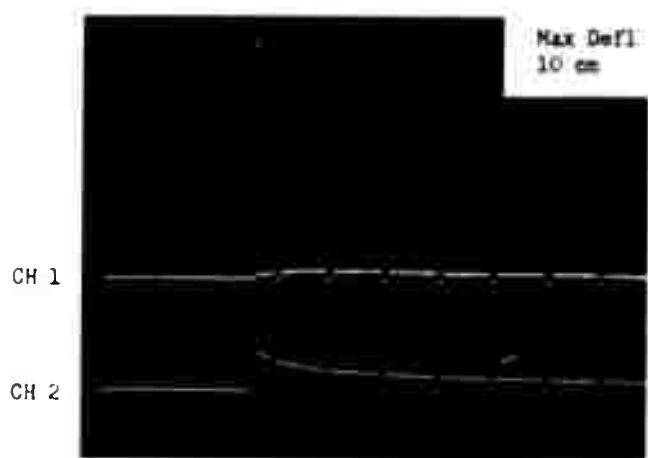
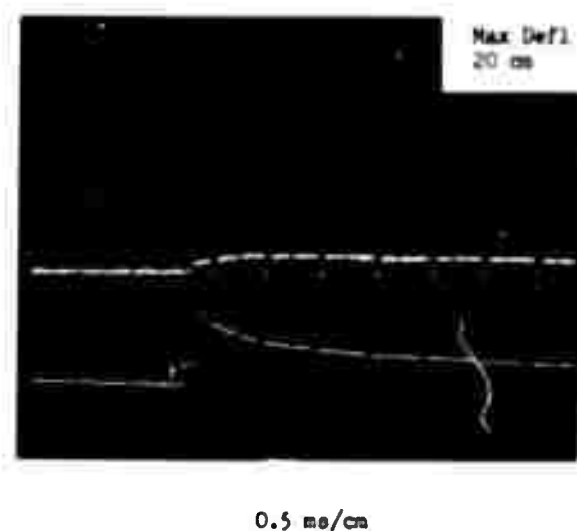
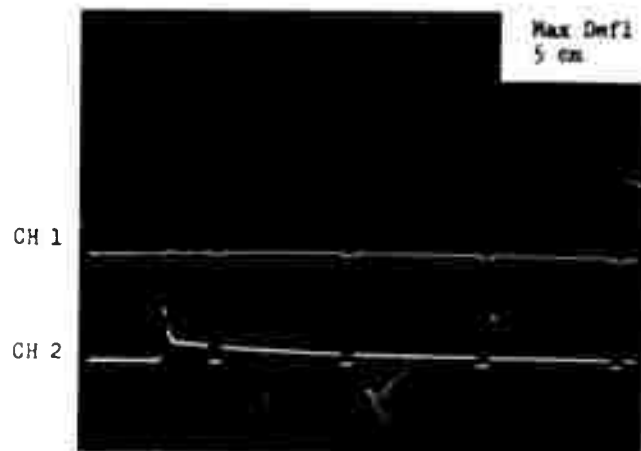


FIGURE D-8(b)

UNCLASSIFIED
152

INTERFEROMETER FIRING REPORT

ROUND 75.70

PROJECTILE 2.7" SPHERE

VELOCITY 14,600 ft/s

PRESSURE 7.6 Torr N₂

INTERFEROMETER STATION 272

PROJECTILE POSITION AT STATION 272 1.42" HIGH

DISTANCE TO UPPER BEAM (CH 2) 0.50"

DISTANCE TO LOWER BEAM (CH 1) 2.12"

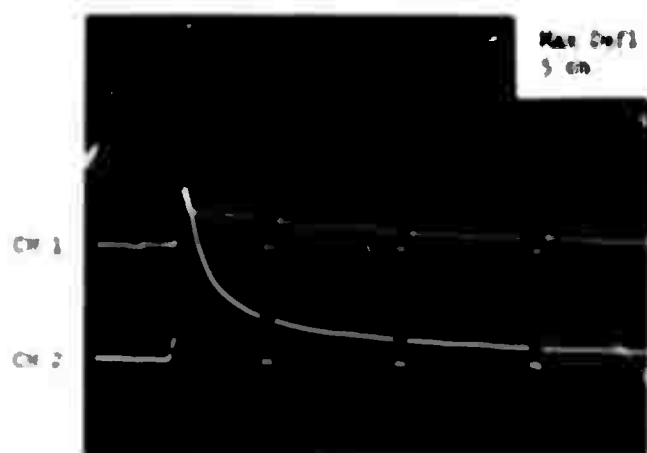
FIGURE D-9(a)

UNCLASSIFIED

153

INTERFACETRON 51A • DISPLAY

ROUND 73/10



0.2 ns/cm



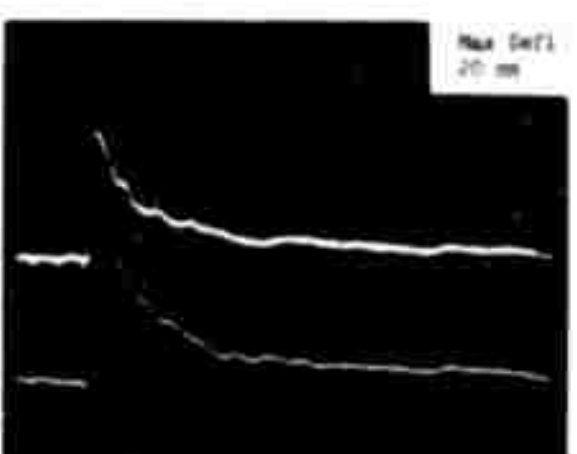
0.5 ns/cm



CH 1

CH 2

0.5 ns/cm



1.0 ns/cm

FIGURE D-9(b)

APPENDIX E

Electron Densities on the Axis and Electron Density Radii
from Simultaneous Solutions Nitrogen Atmospheres

The figure numbers in this appendix correspond
to the figure numbers in Appendix D.

Figures E-1b and 1d are unavailable.

UNCLASSIFIED

156

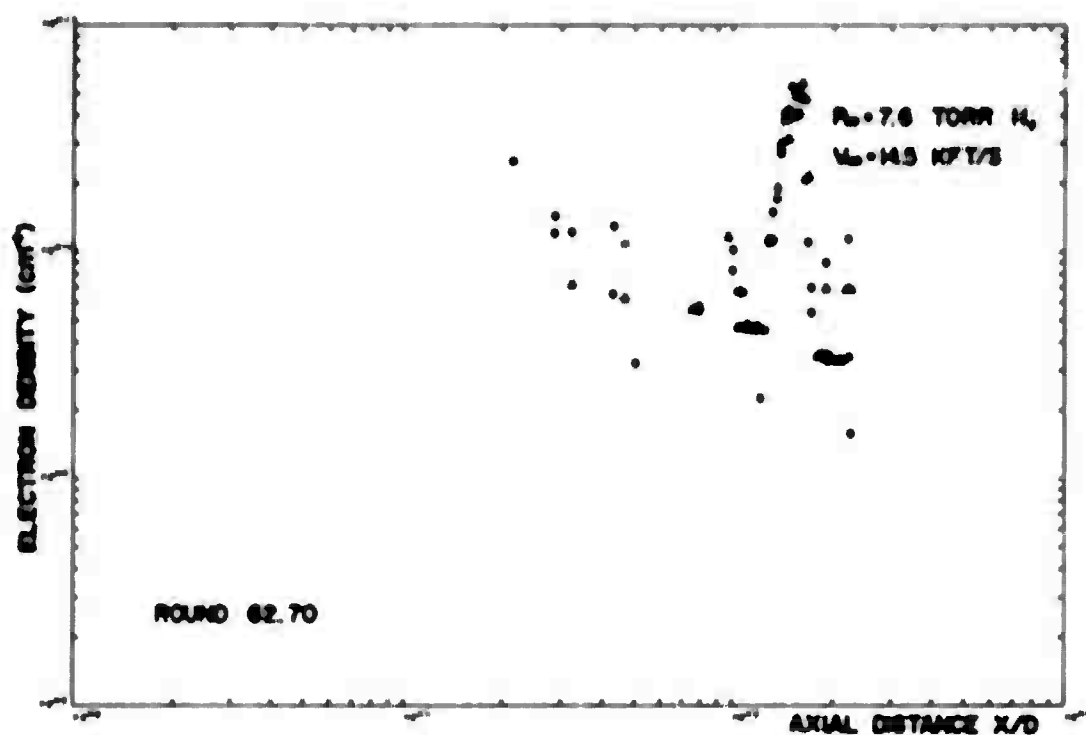


FIGURE E-1(a)

UNCLASSIFIED
157

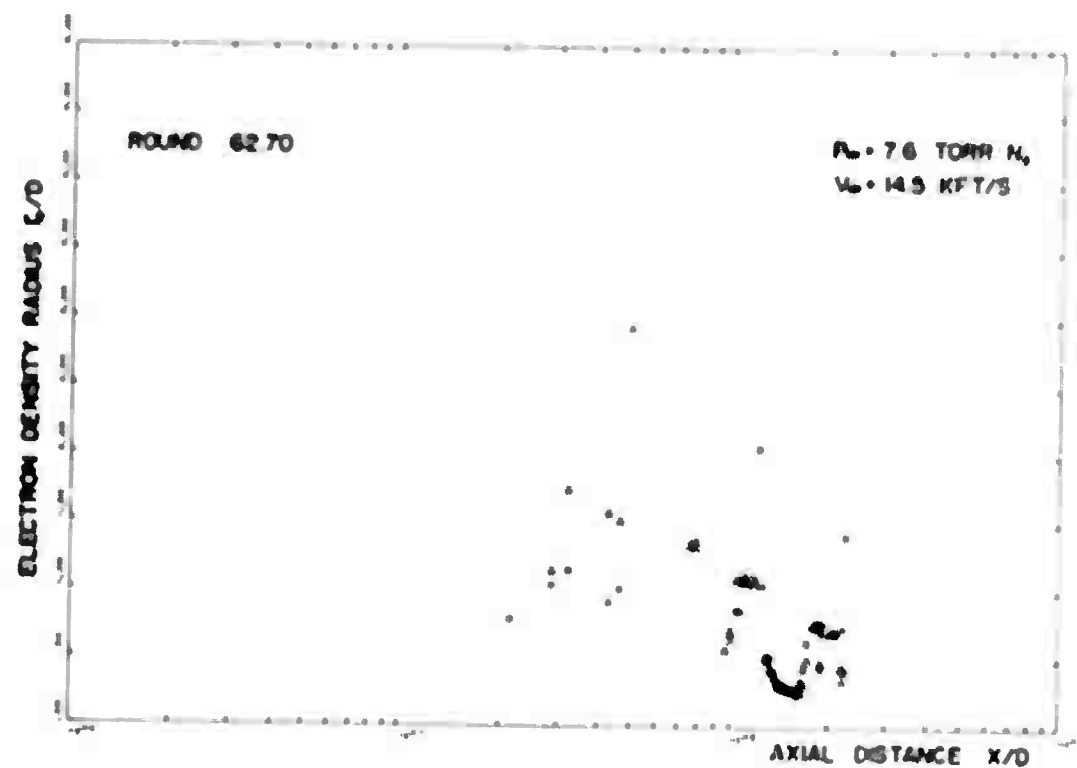


FIGURE E-1(c)

UNCLASSIFIED
158

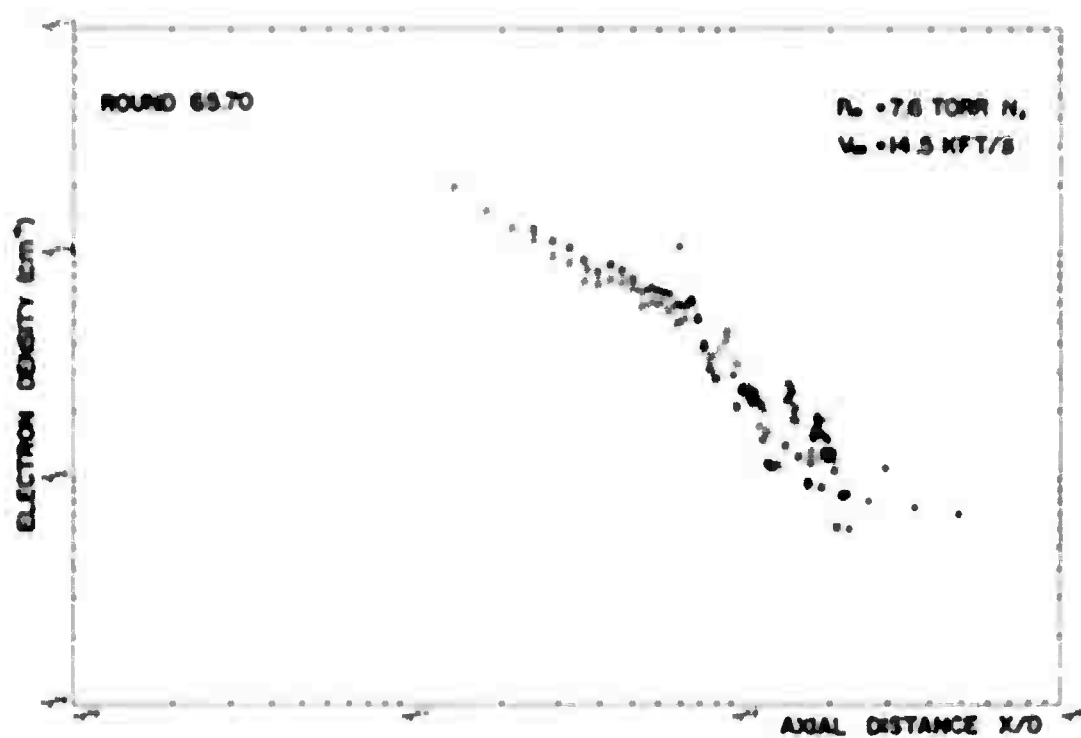


FIGURE E-2(a)

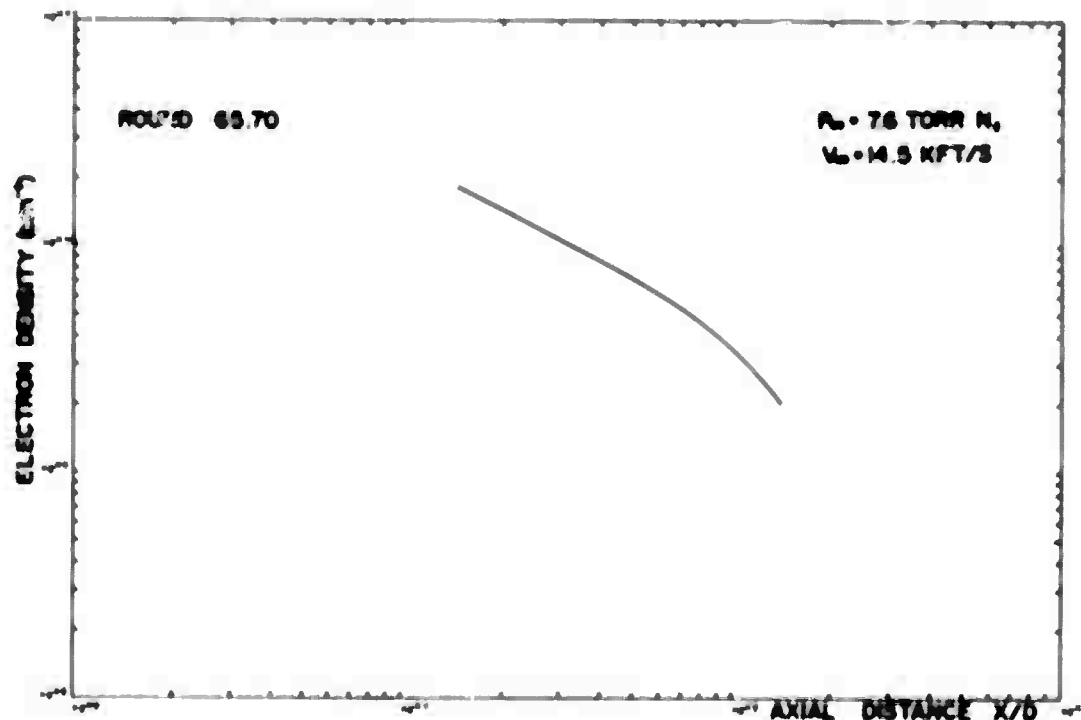


FIGURE E-2(b)

UNCLASSIFIED

159

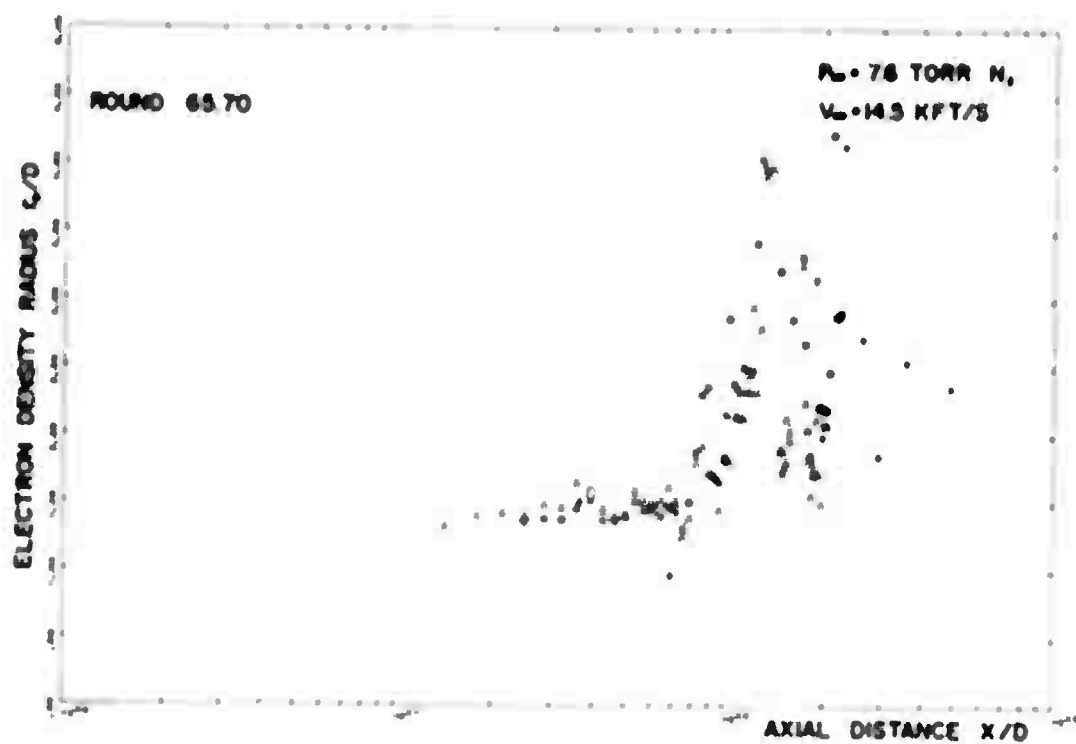


FIGURE E-2(c)

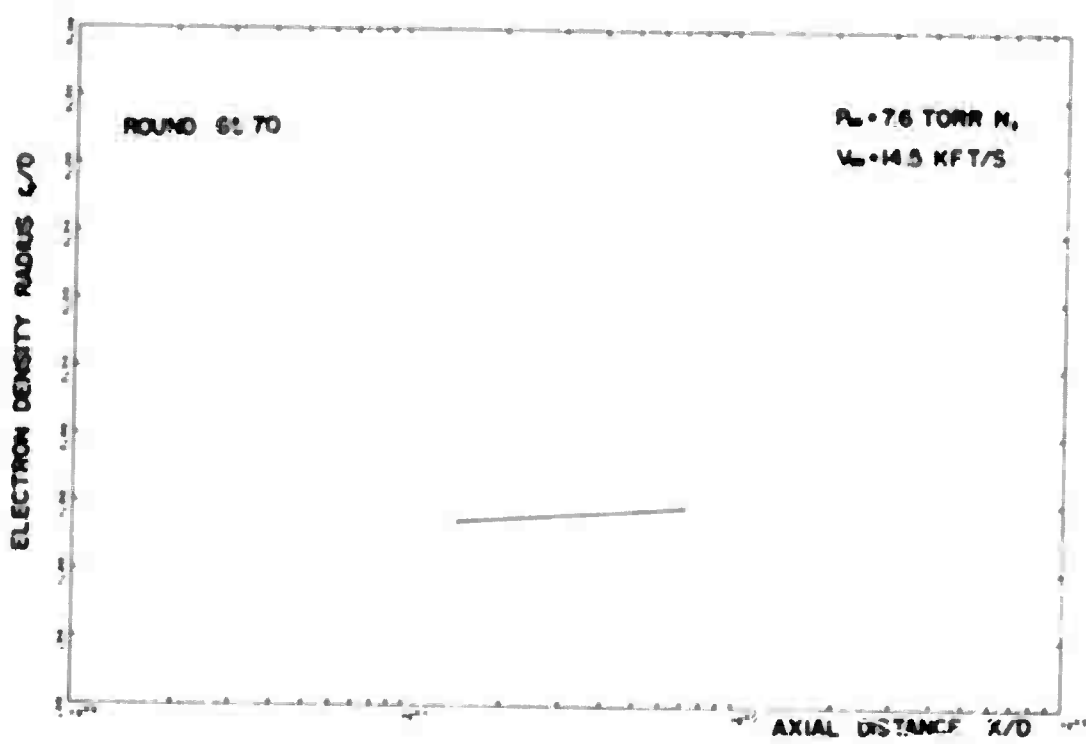


FIGURE E-2(d)

UNCLASSIFIED

160

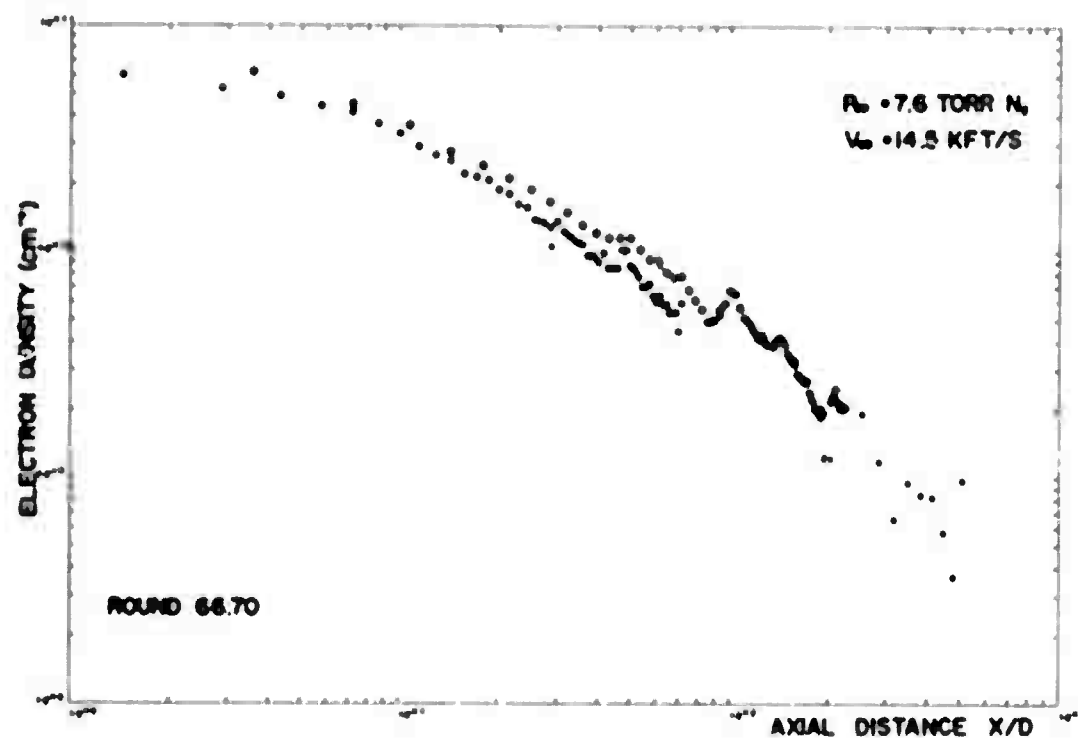


FIGURE E-3(a)

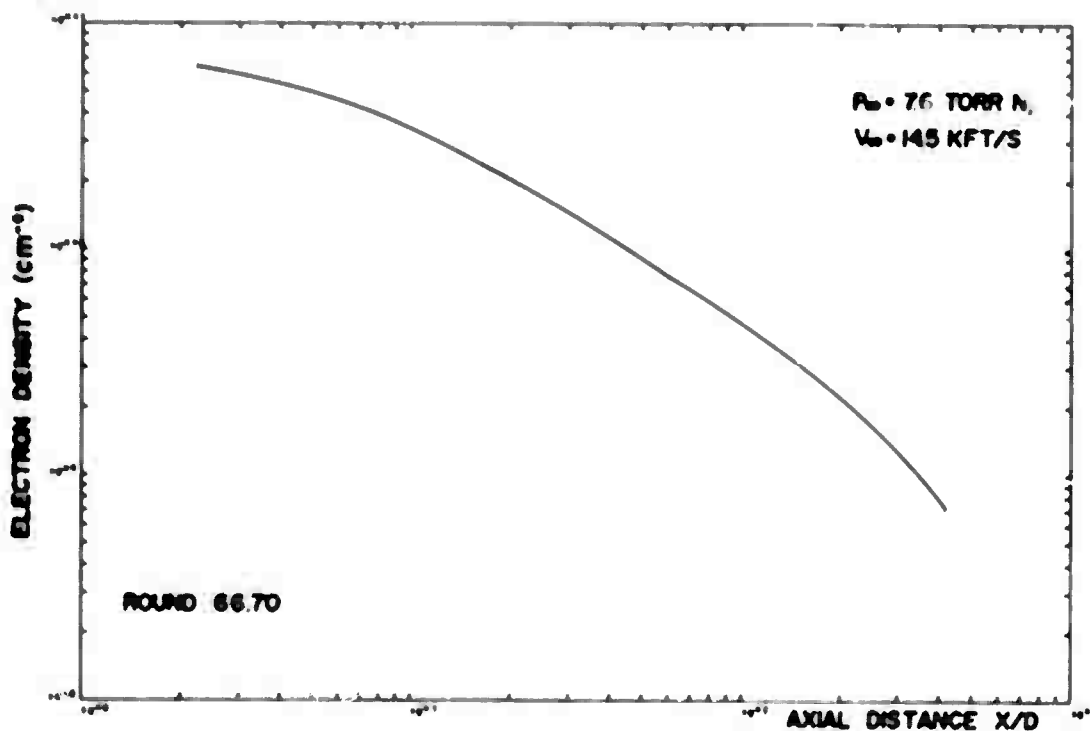


FIGURE E-3(b)

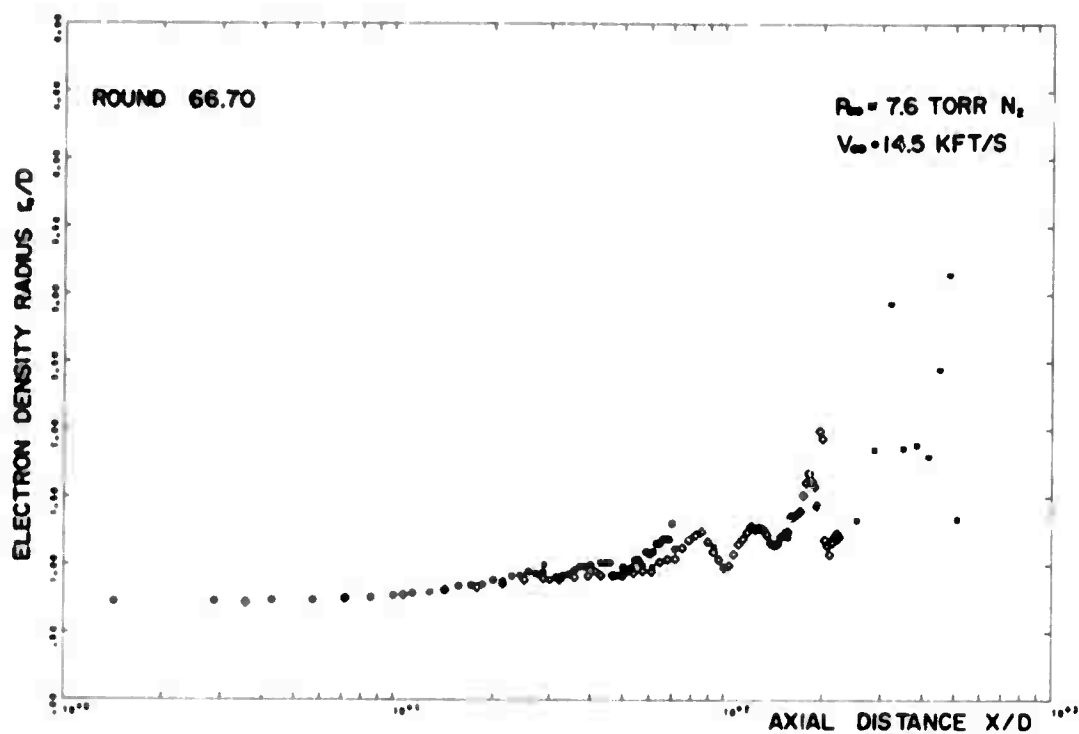


FIGURE E-3(c)

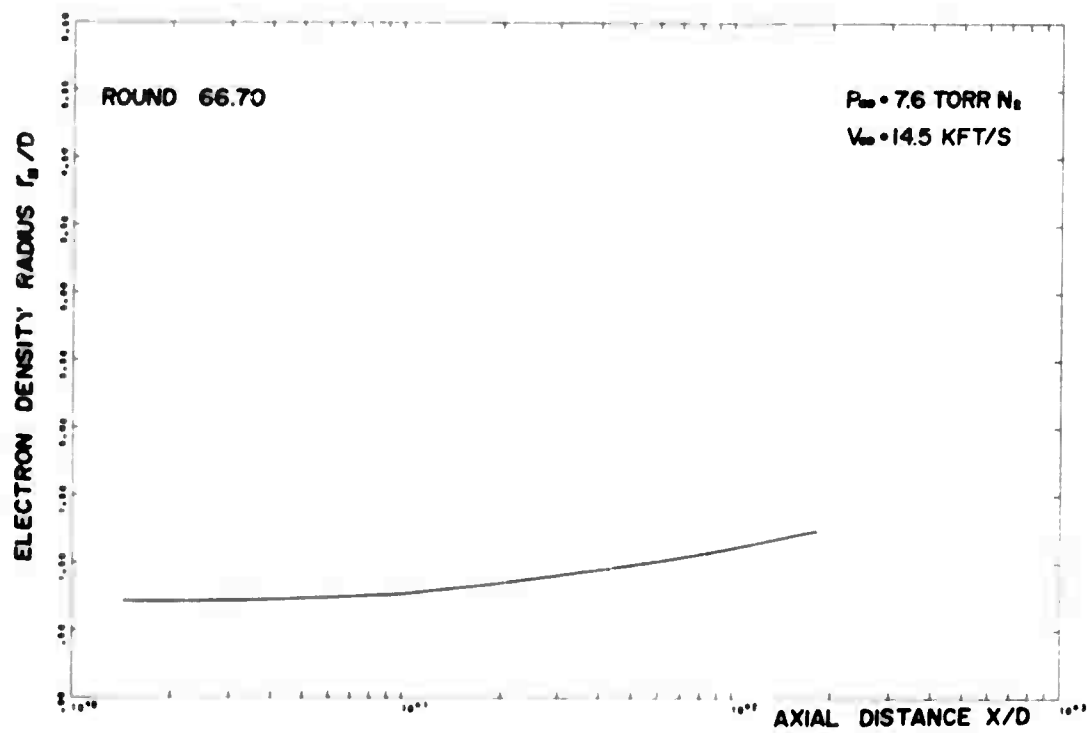


FIGURE E-3(d)

UNCLASSIFIED
162

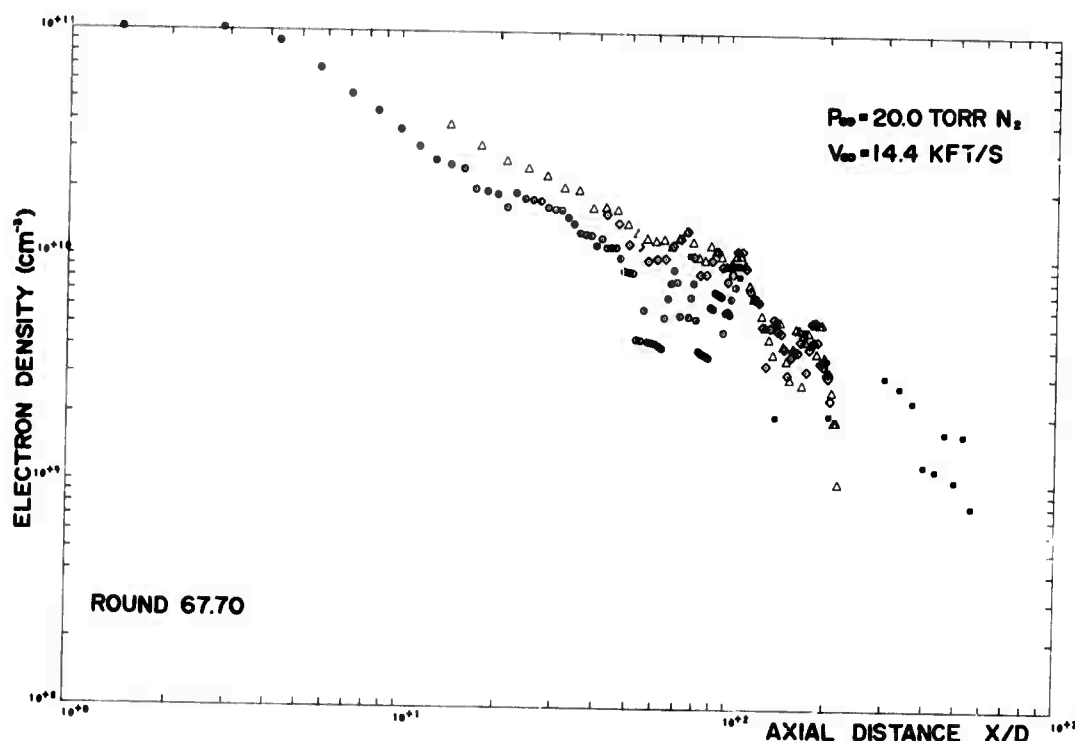


FIGURE E-4(a)

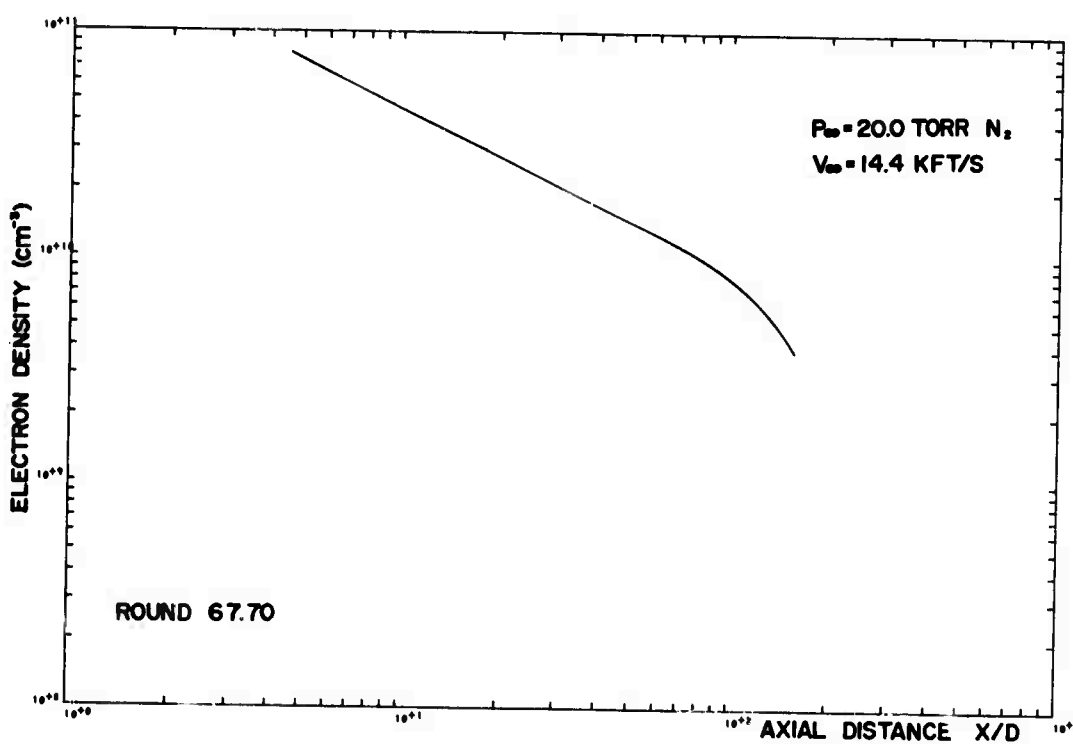


FIGURE E-4(b)

UNCLASSIFIED

163

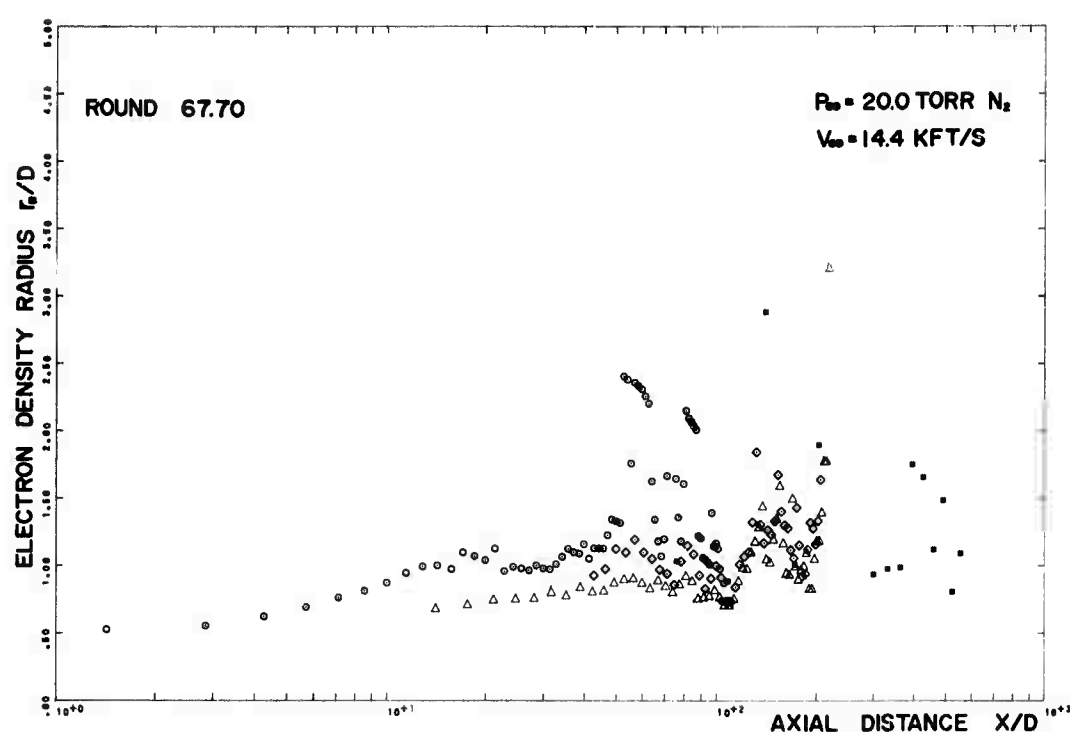


FIGURE E-4(c)

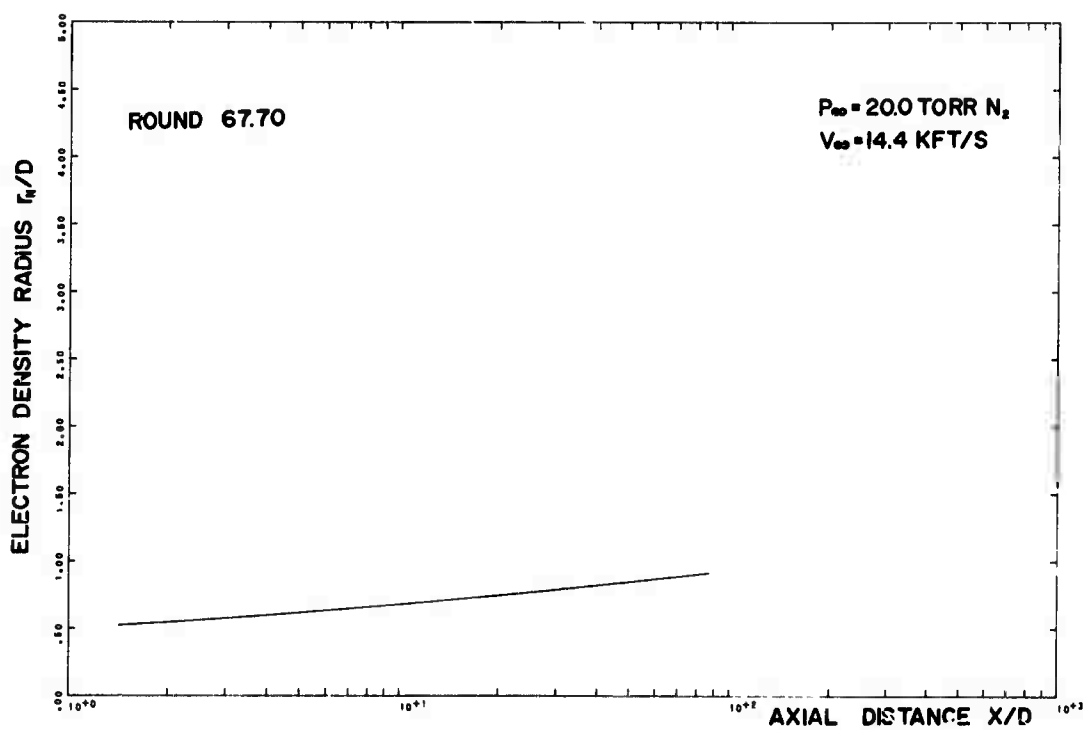


FIGURE E-4(d)

UNCLASSIFIED
164

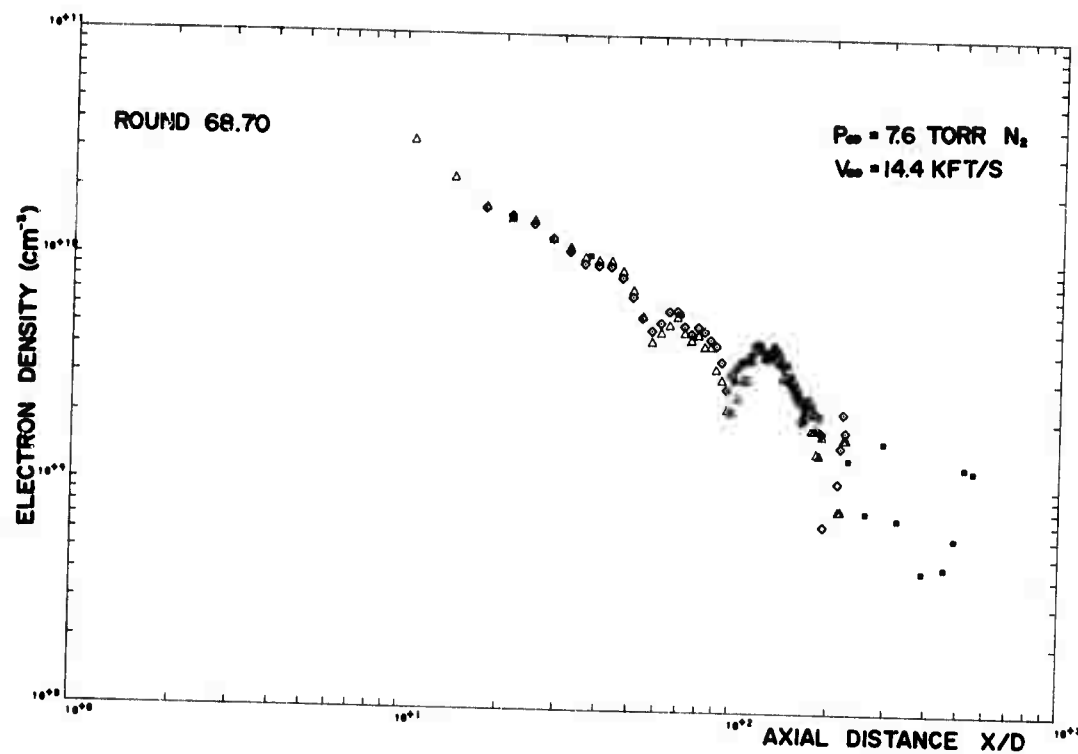


FIGURE E-5(a)

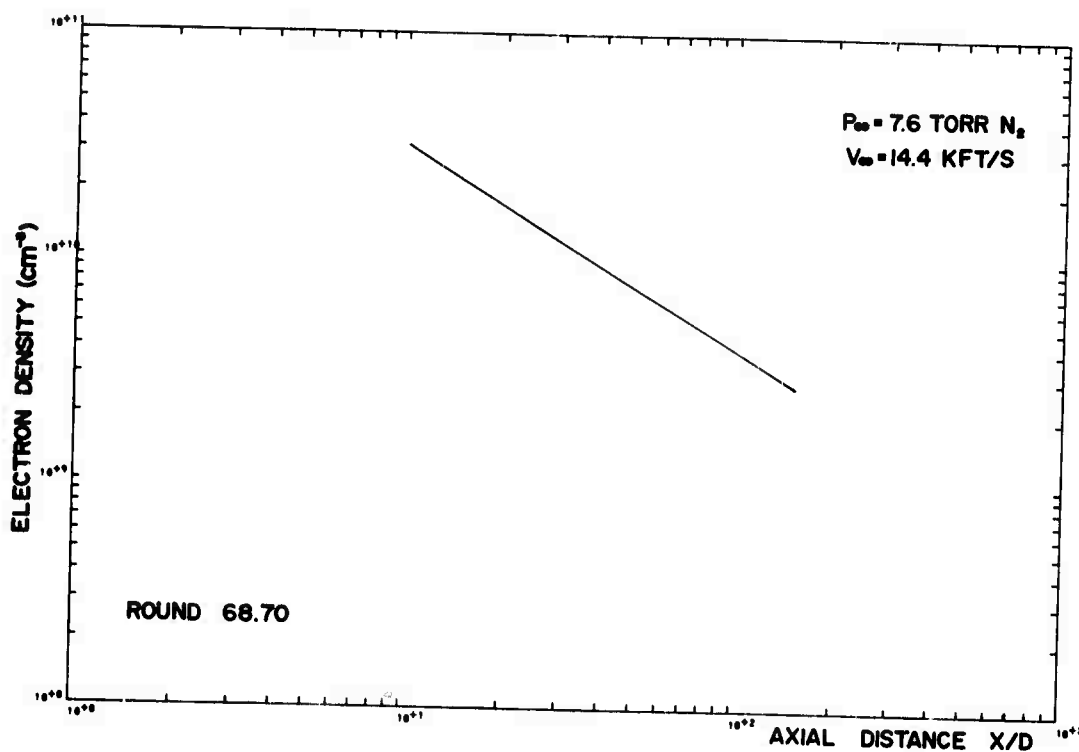


FIGURE E-5(b)

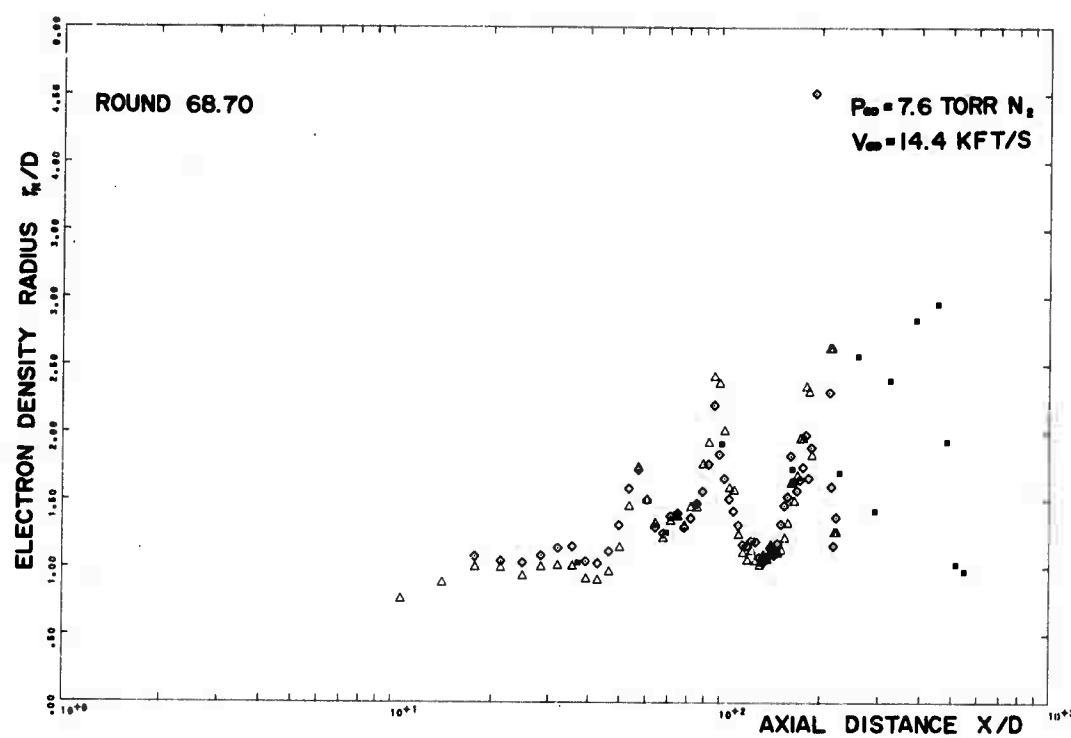


FIGURE E-5(c)

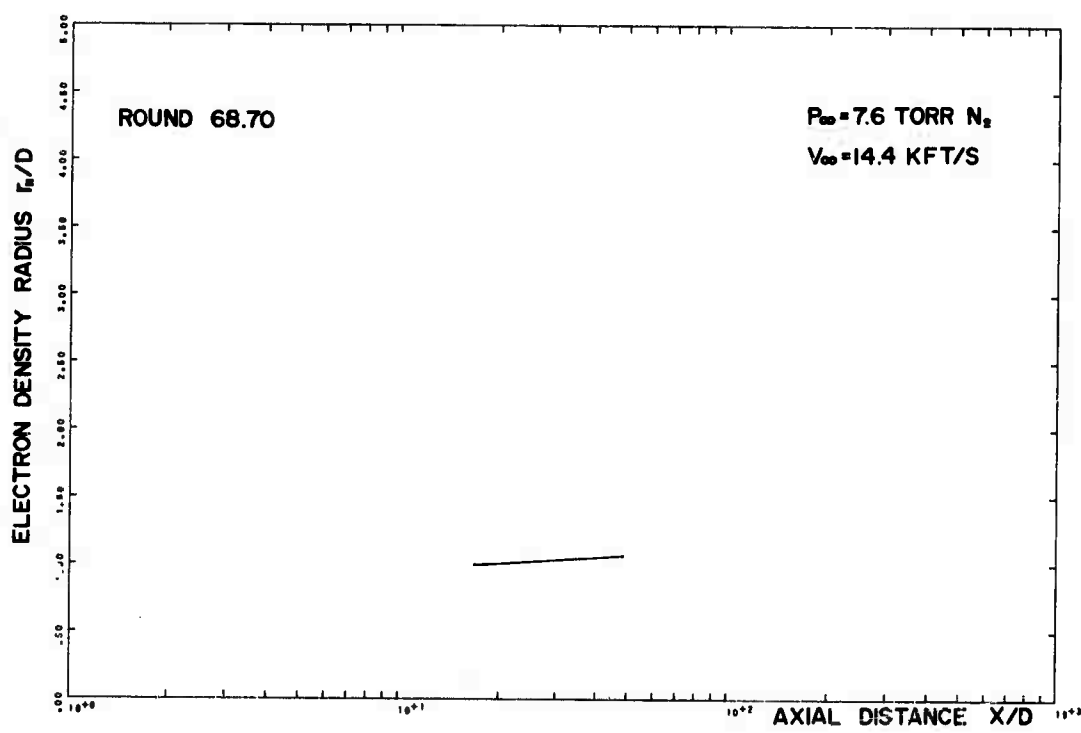


FIGURE E-5(d)

UNCLASSIFIED

166

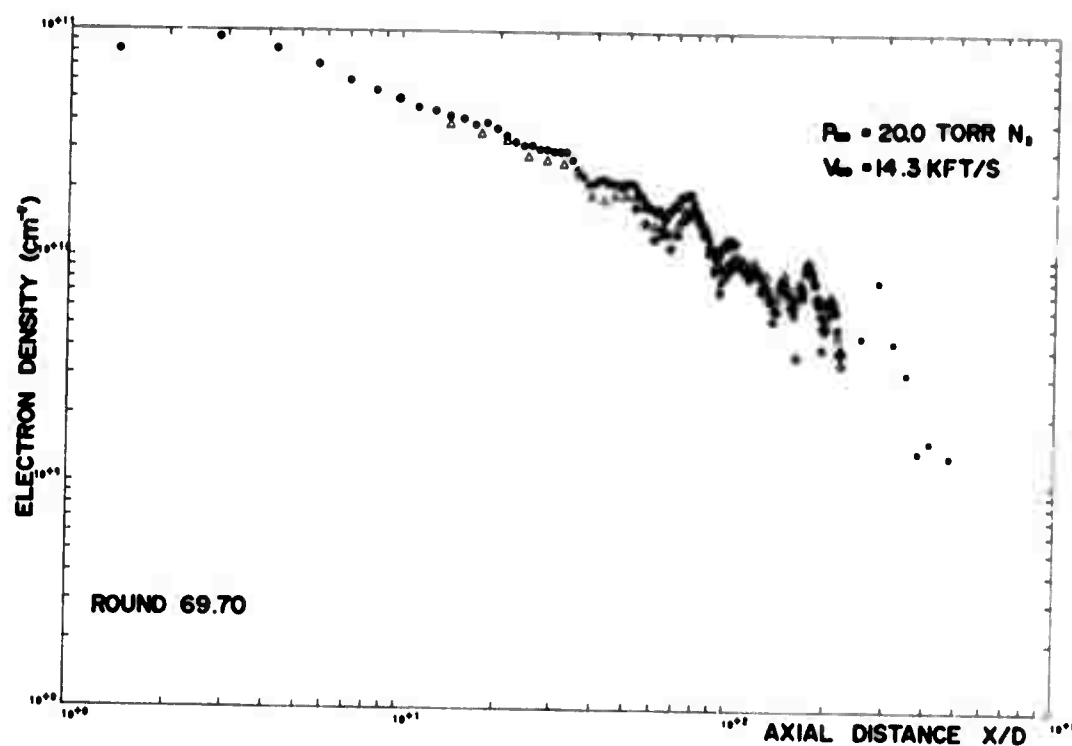


FIGURE E-6(a)

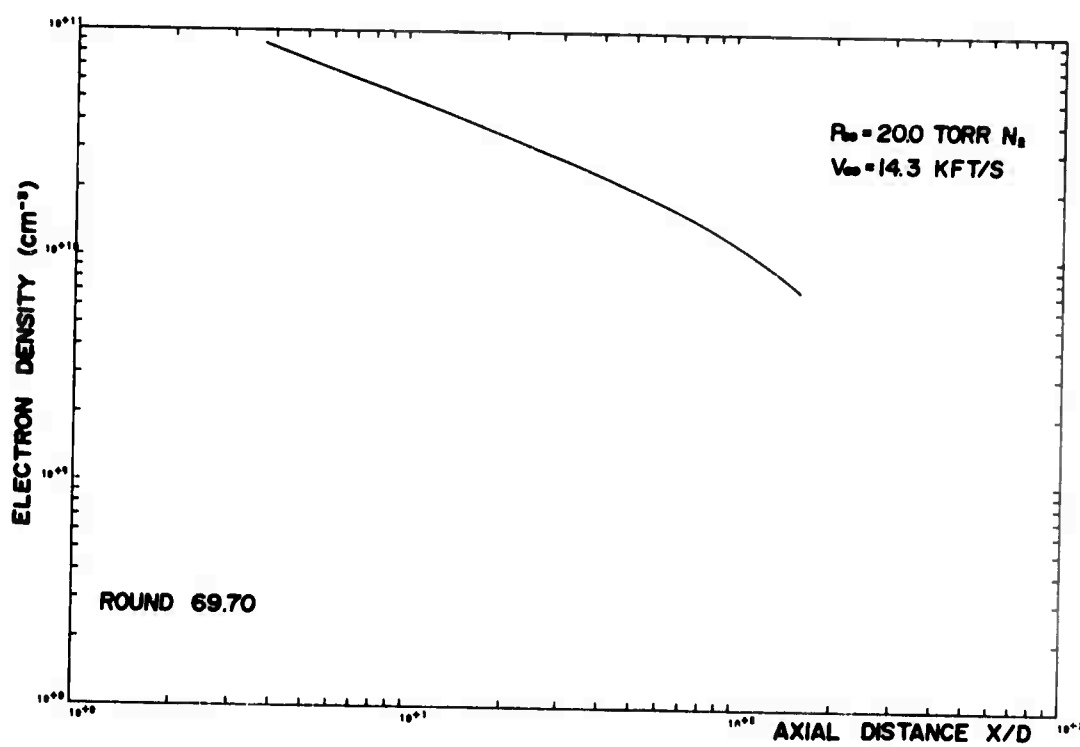


FIGURE E-6(b)

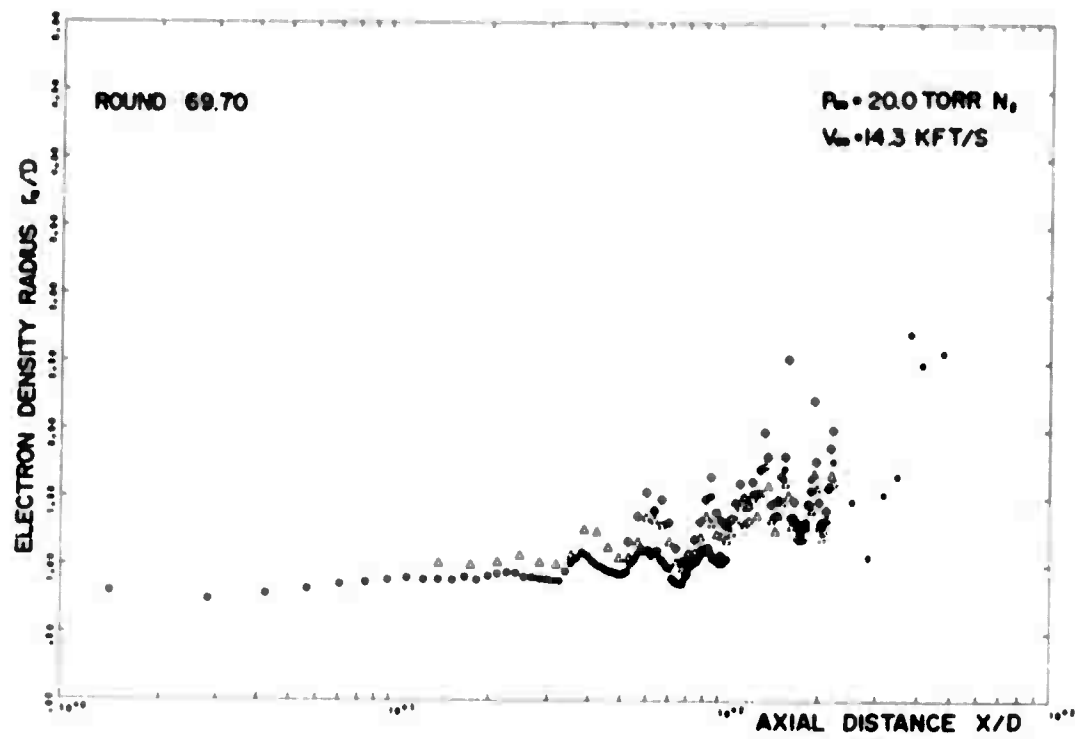


FIGURE E-6(c)

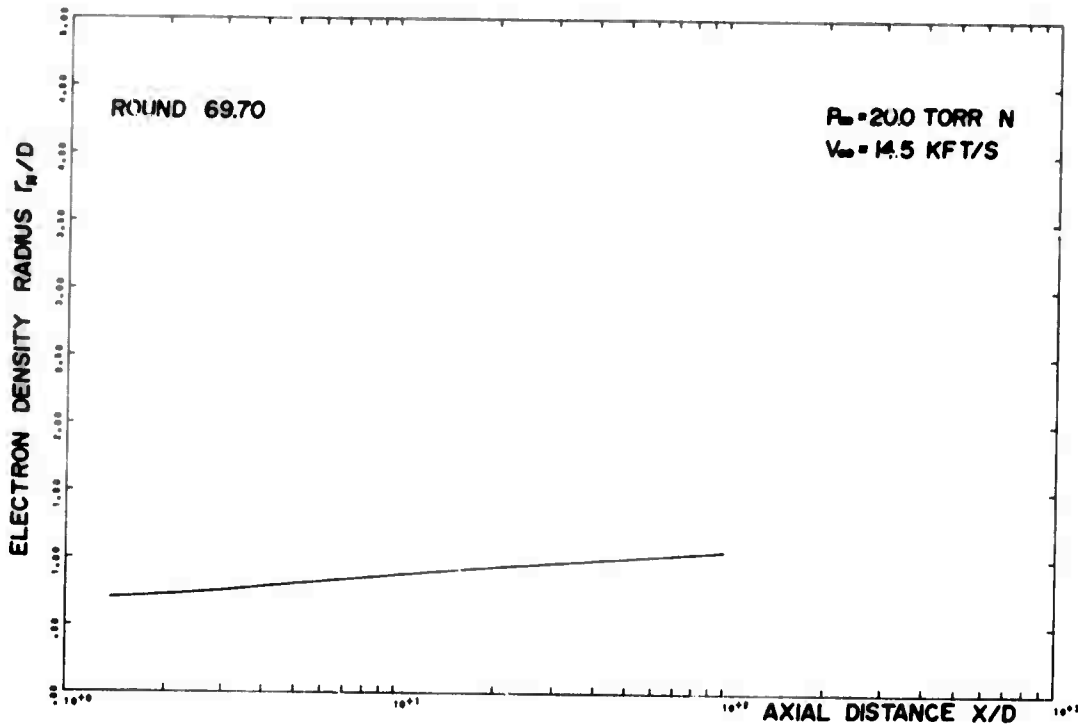


FIGURE E-6(d)

UNCLASSIFIED

168

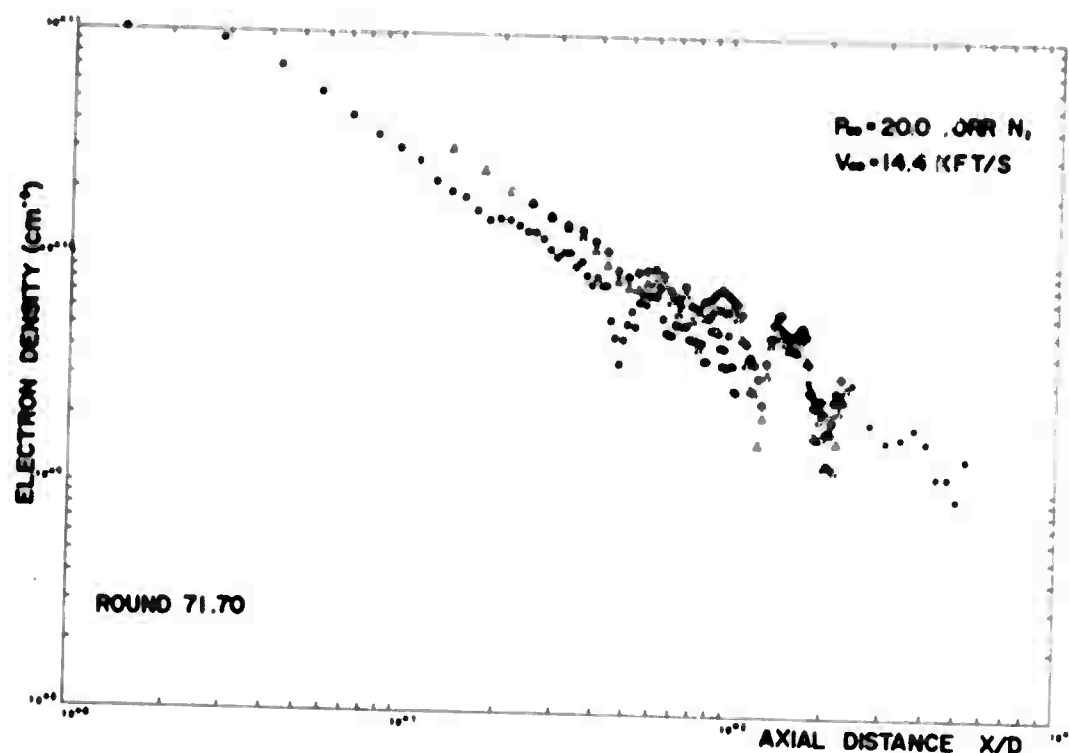


FIGURE E-7(a)

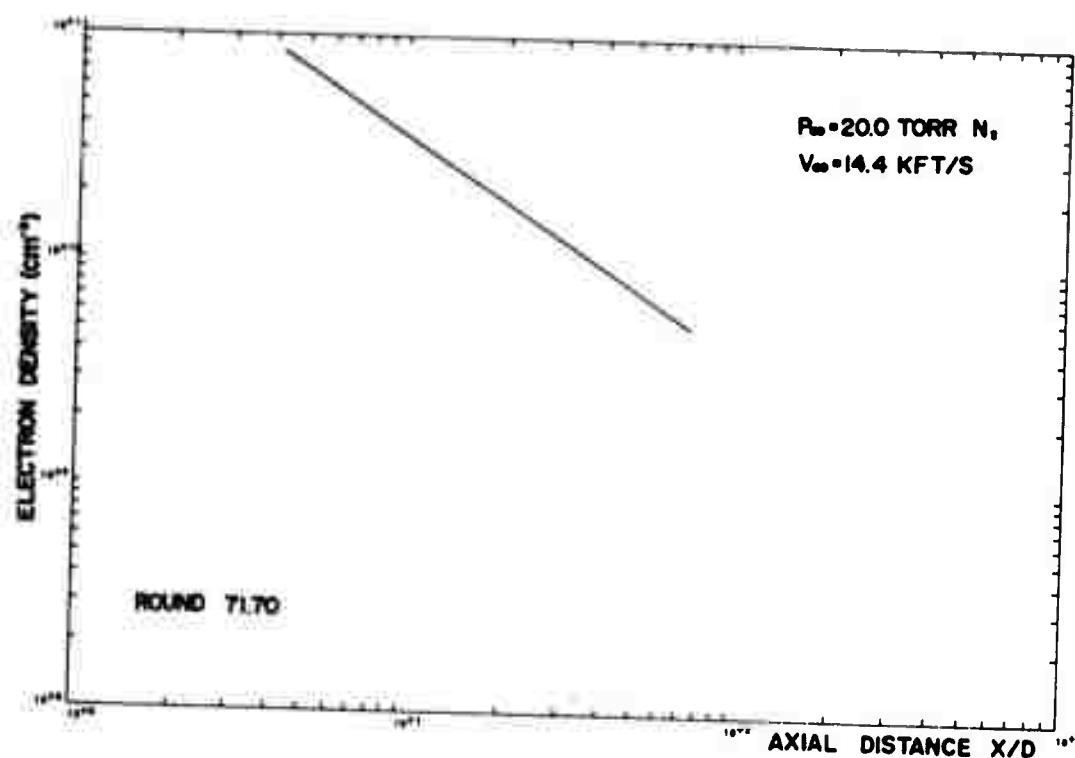


FIGURE E-7(b)

UNCLASSIFIED

169

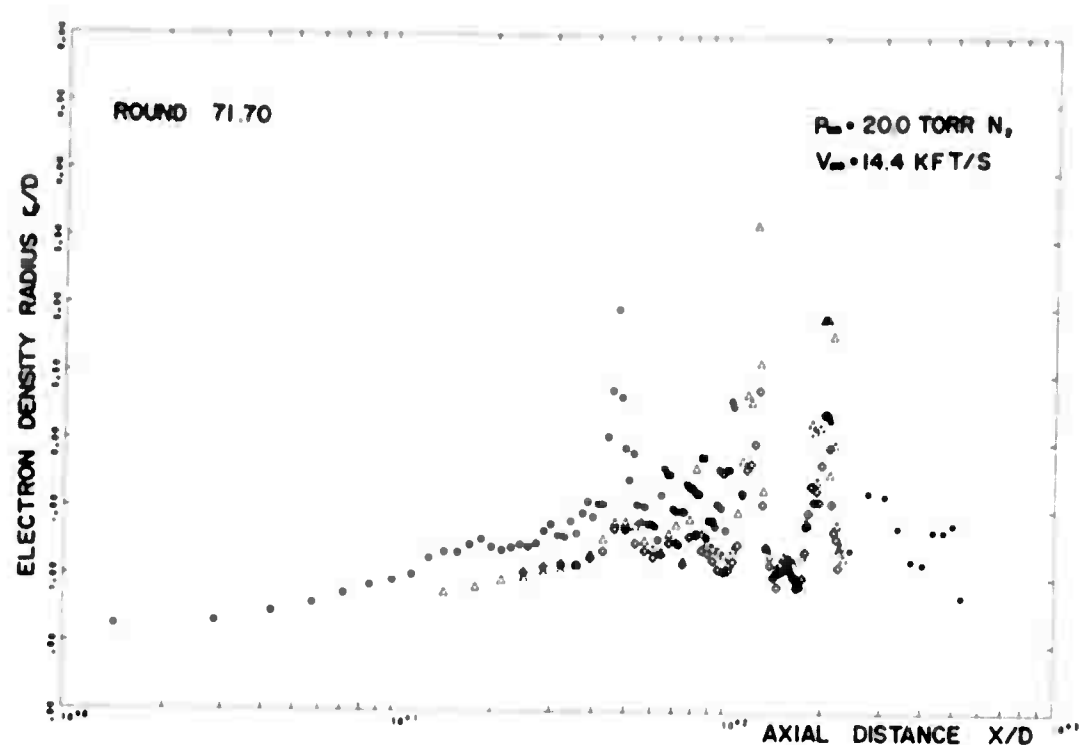


FIGURE E-7(c)

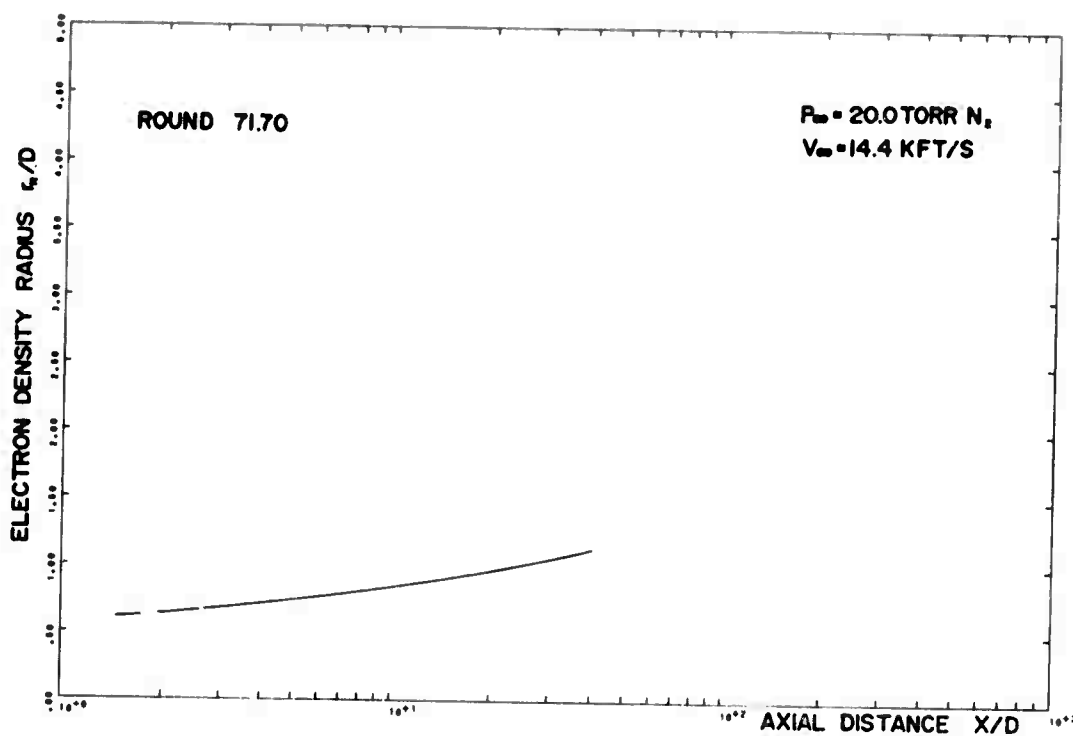


FIGURE E-7(d)

UNCLASSIFIED
170

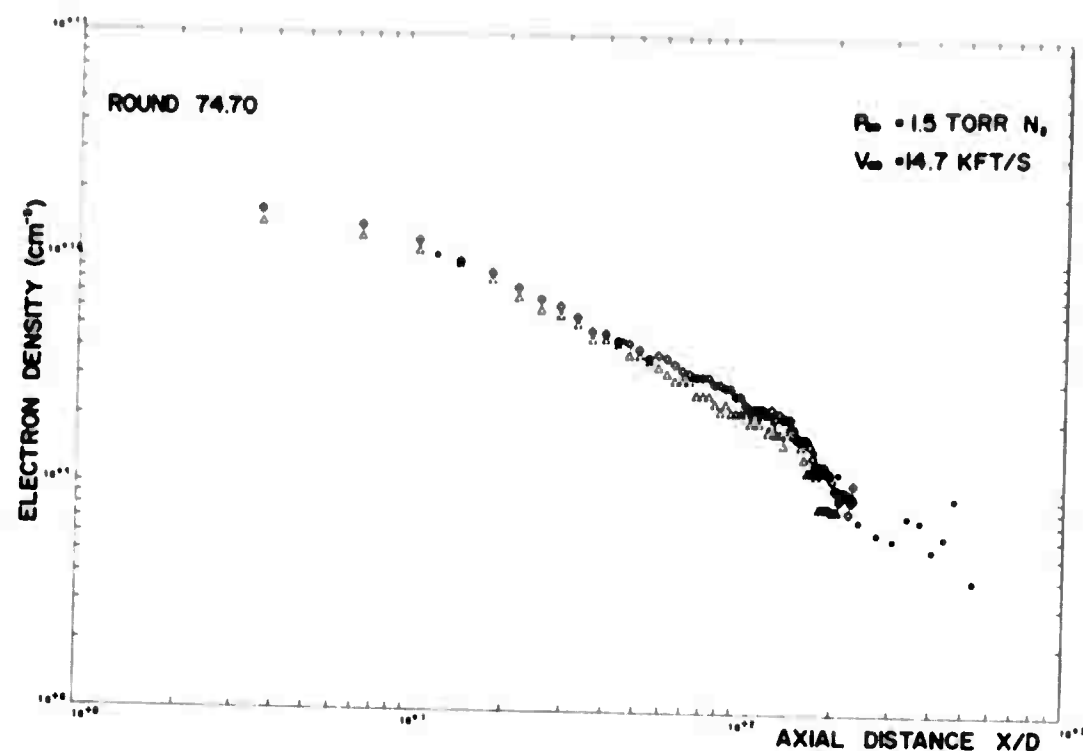


FIGURE E-8(a)

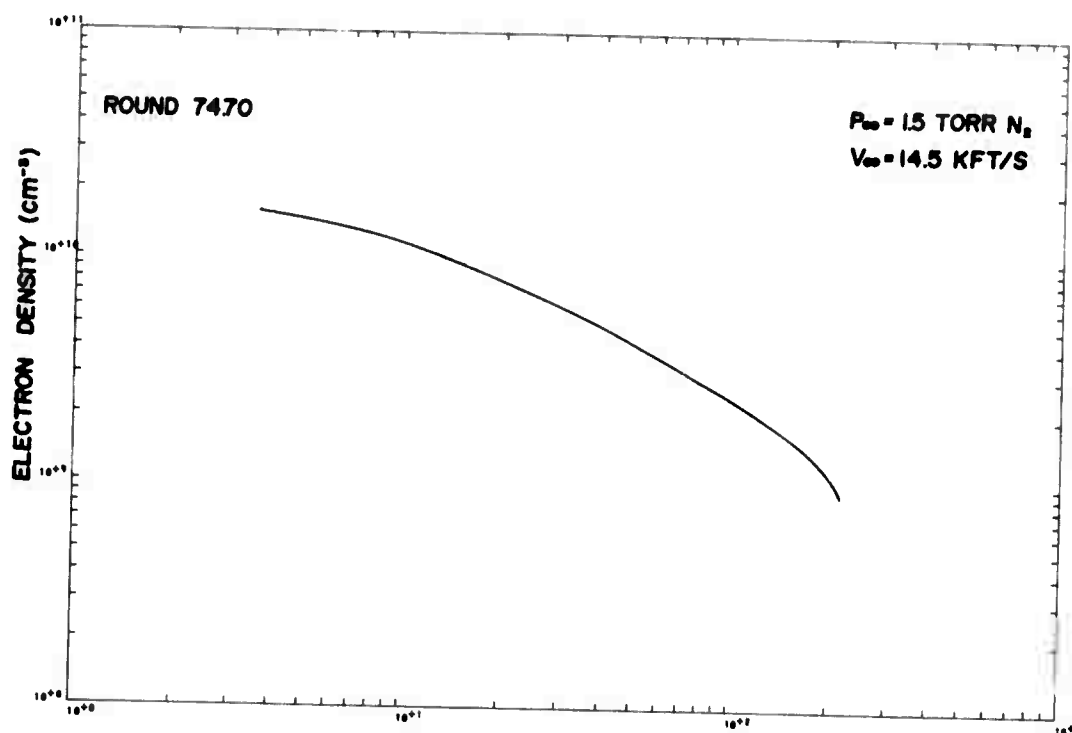


FIGURE E-8(b)

UNCLASSIFIED
171

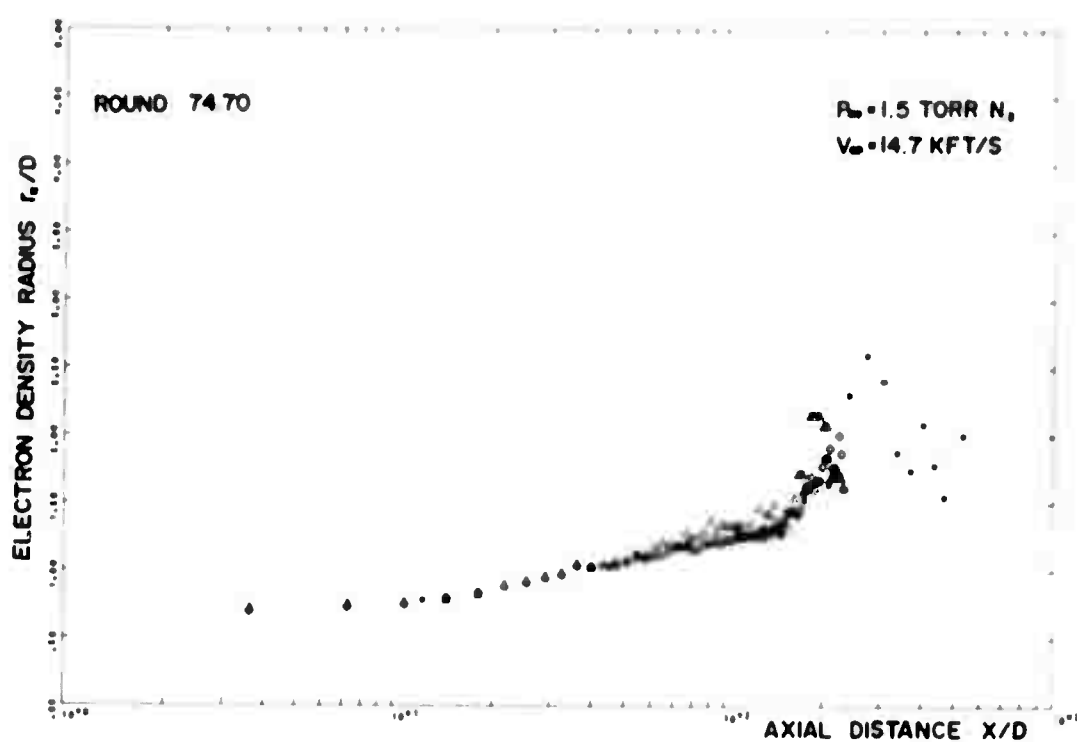


FIGURE E-8(c)

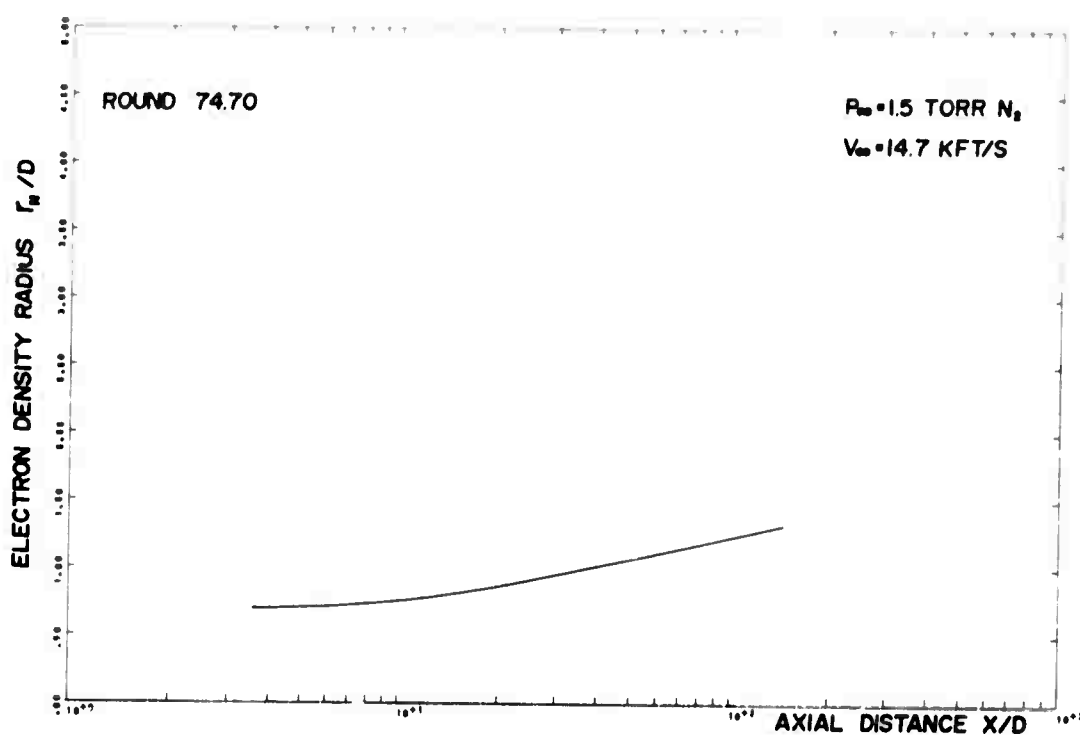


FIGURE E-8(d)

UNCLASSIFIED
172

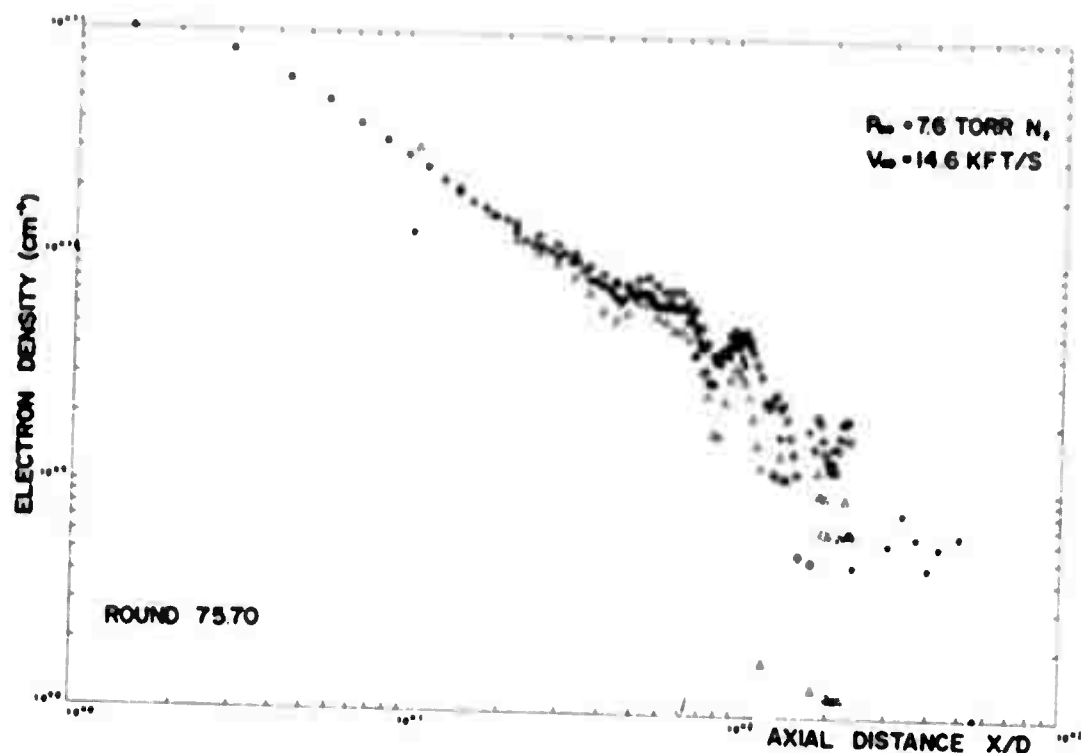


FIGURE E-9(a)

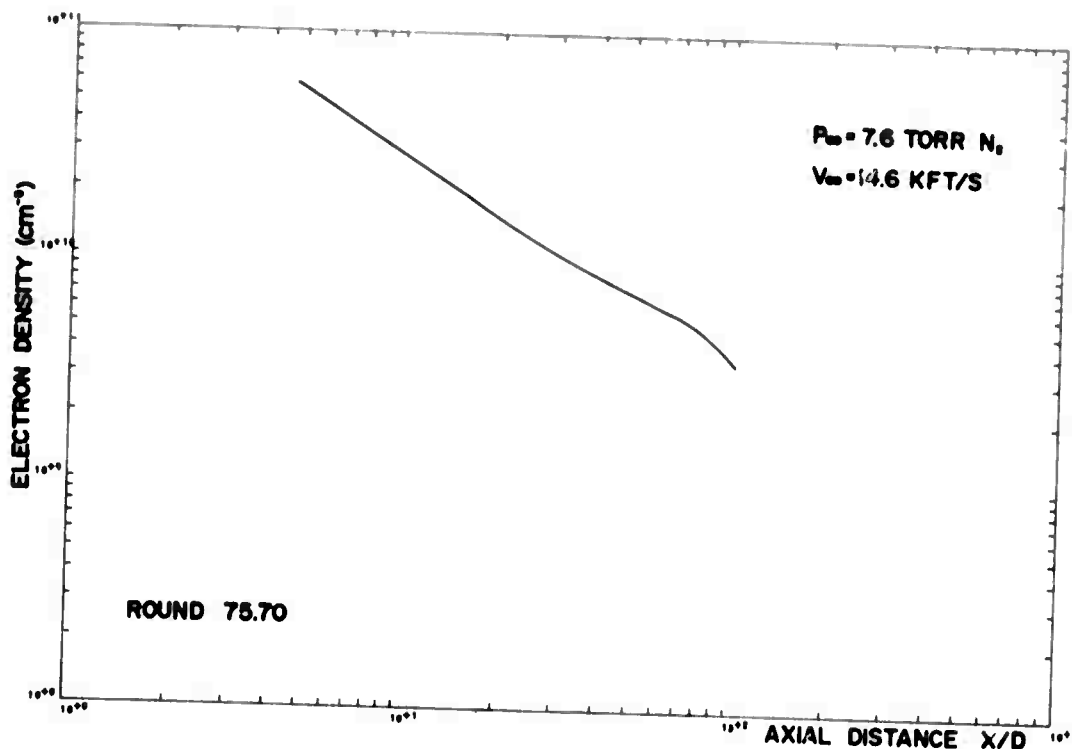


FIGURE E-9(b)

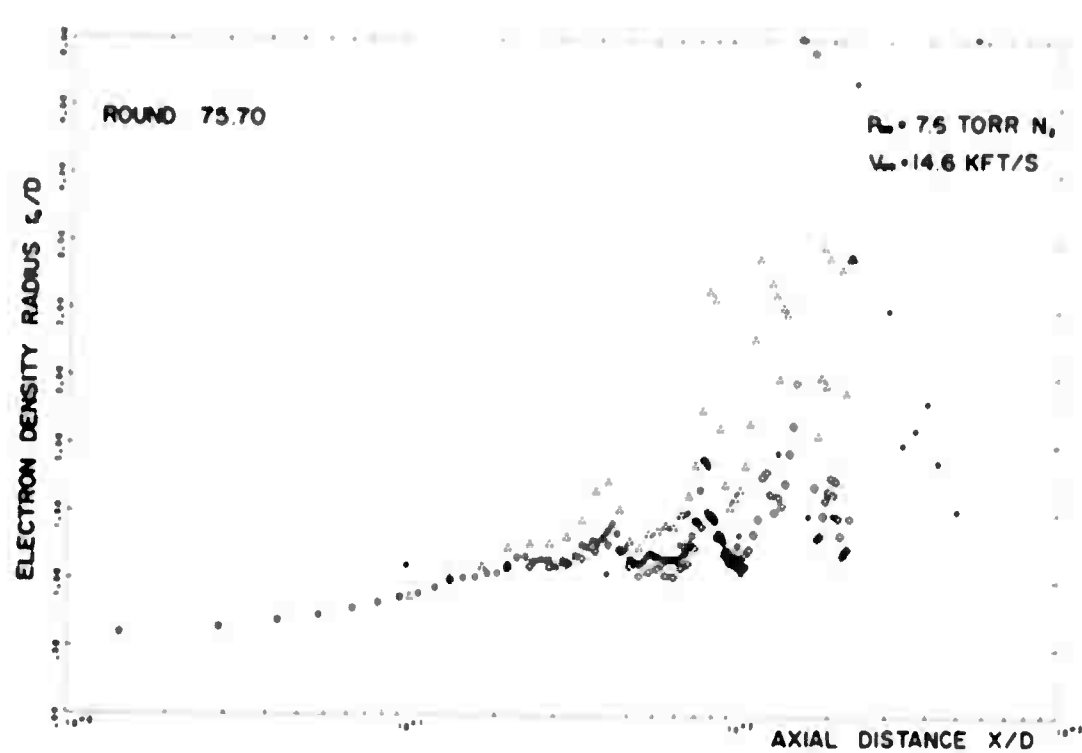


FIGURE E-9(c)

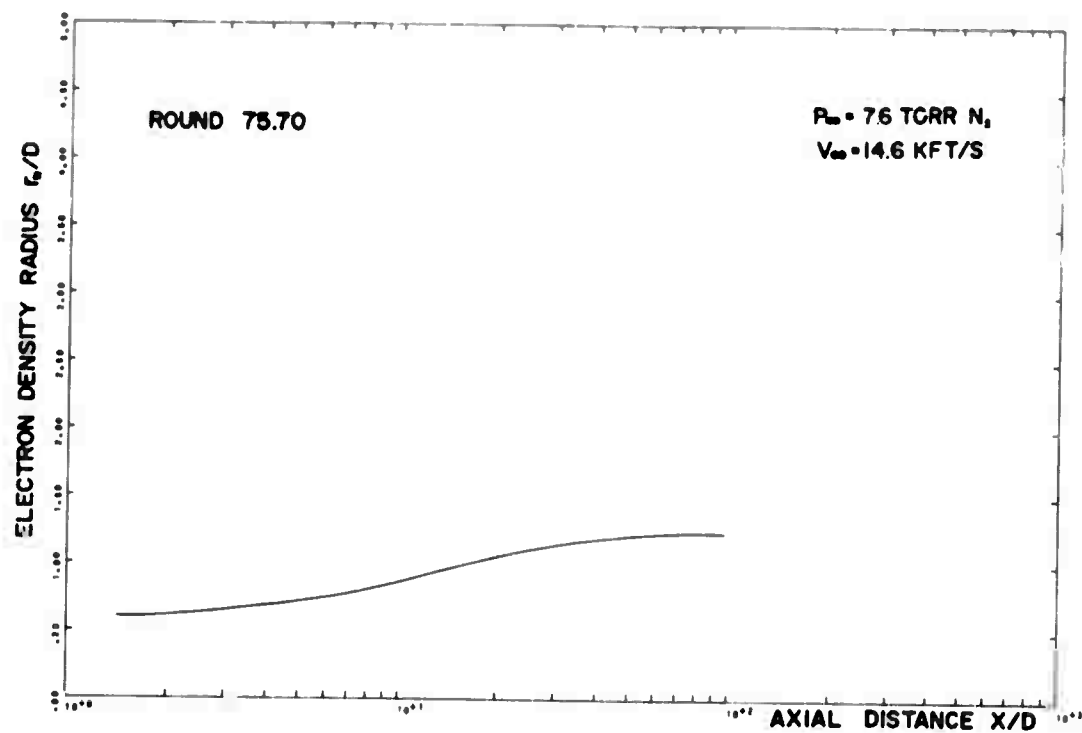


FIGURE E-9(d)

UNCLASSIFIED
174

APPENDIX F

Electron Densities on the Axis Computed with a Prescribed
Electron Density Radius Nitrogen Atmospheres

The figure numbers in this appendix correspond
to the figure numbers in Appendices D and E.

UNCLASSIFIED

176

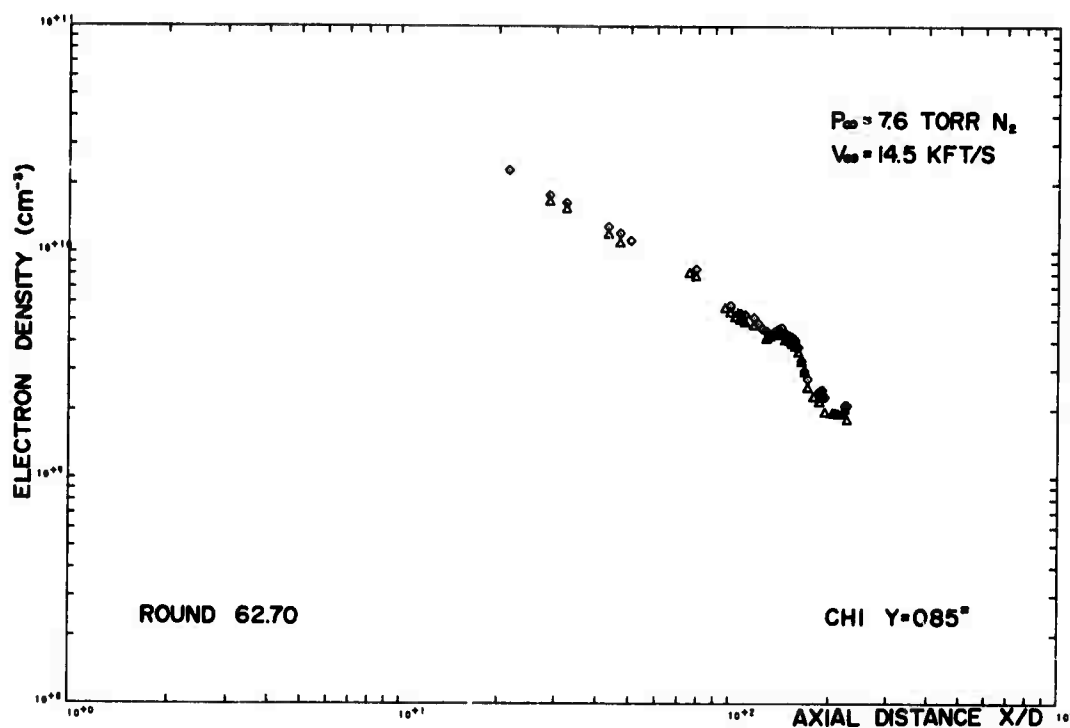


FIGURE F-1(a)

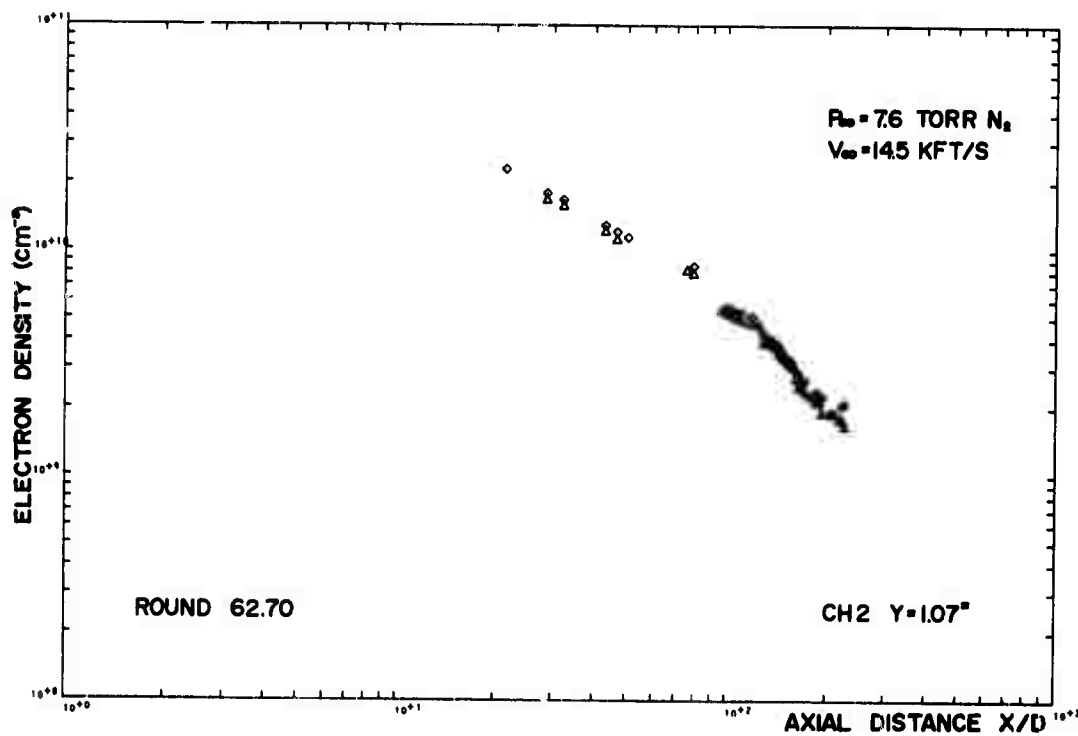


FIGURE F-1(b)

UNCLASSIFIED

177

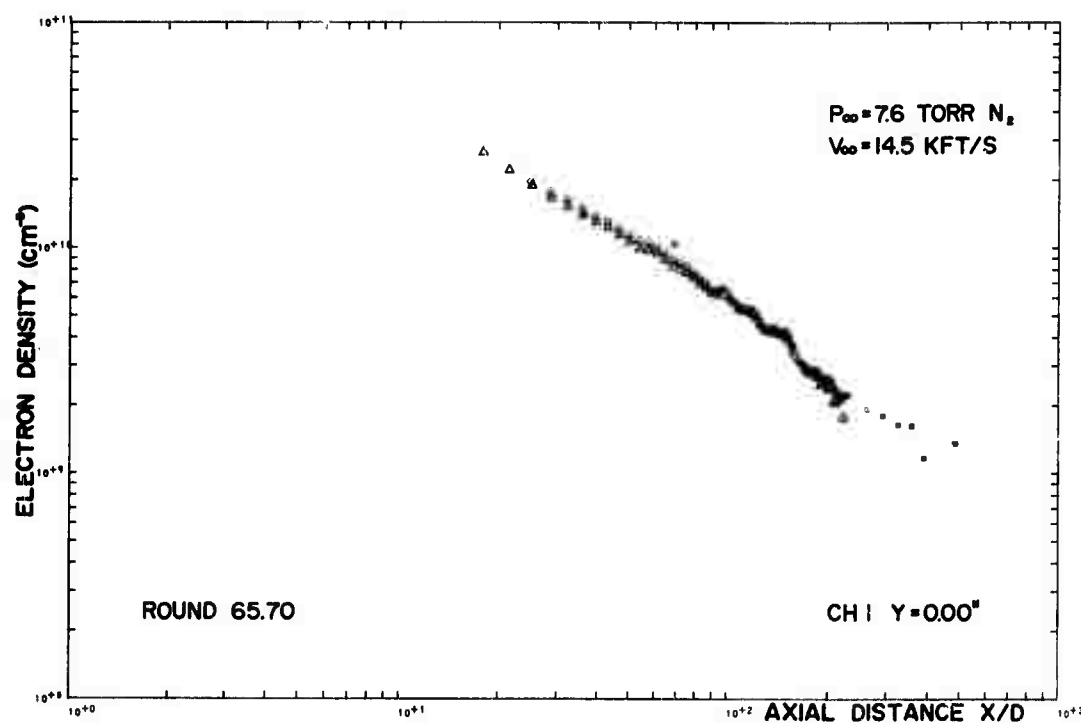


FIGURE F-2(a)

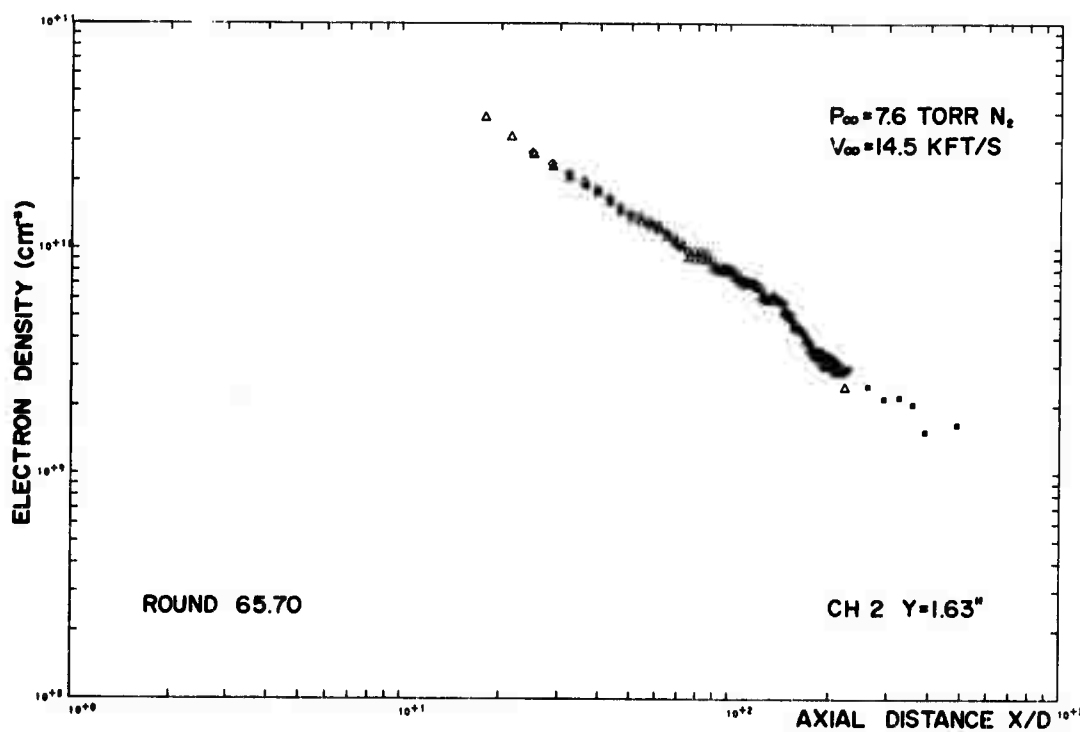


FIGURE F-2(b)

UNCLASSIFIED

178

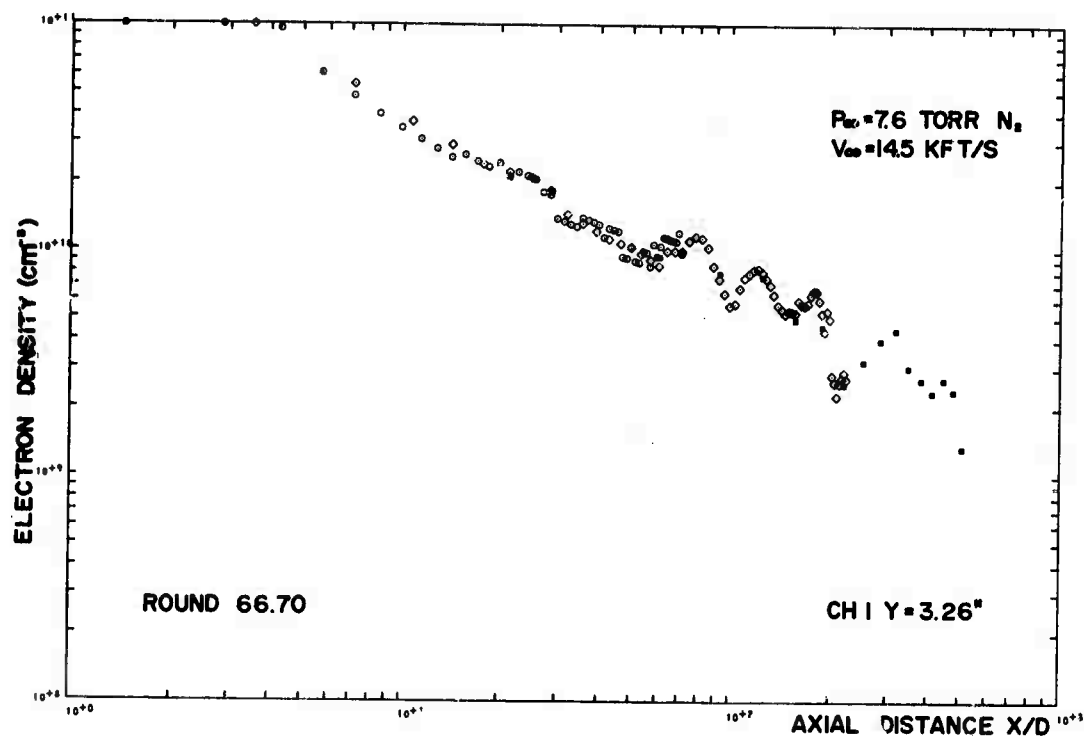


FIGURE F-3(a)

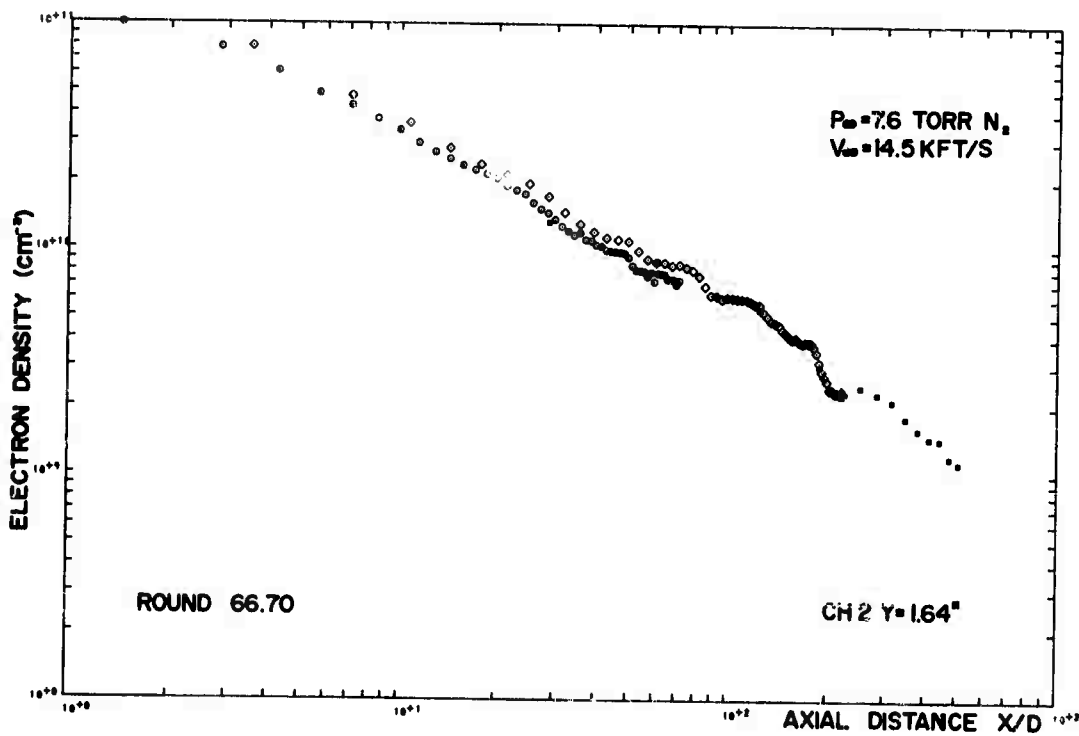


FIGURE F-3(b)

UNCLASSIFIED
179

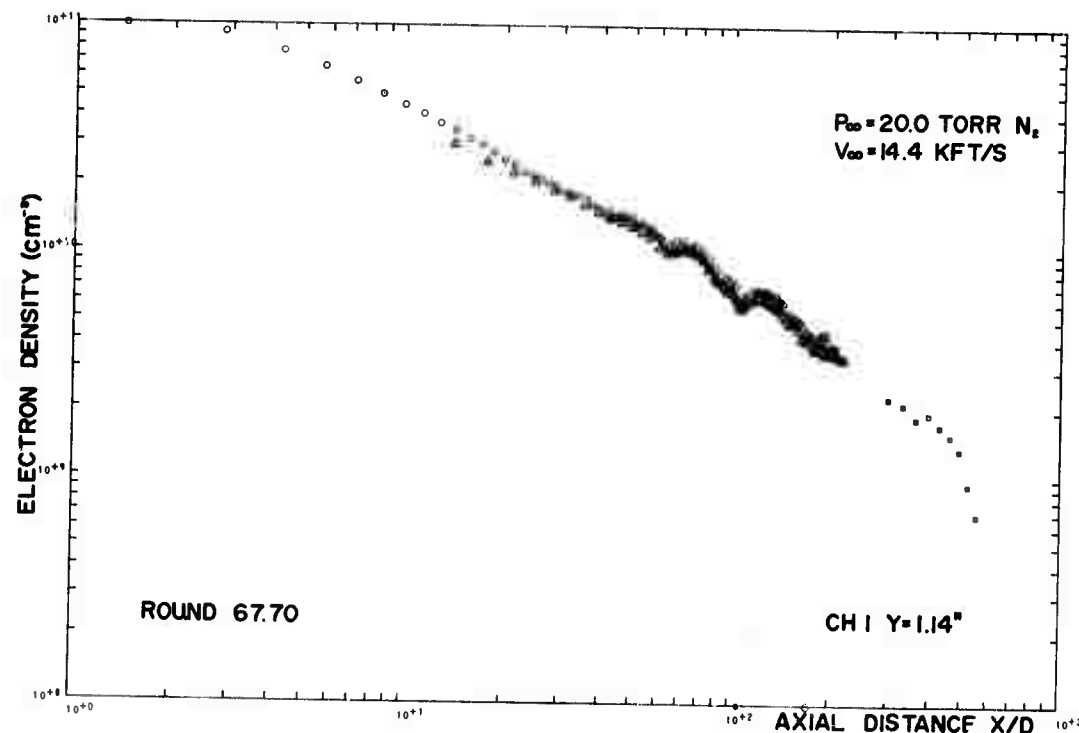


FIGURE F-4(a)

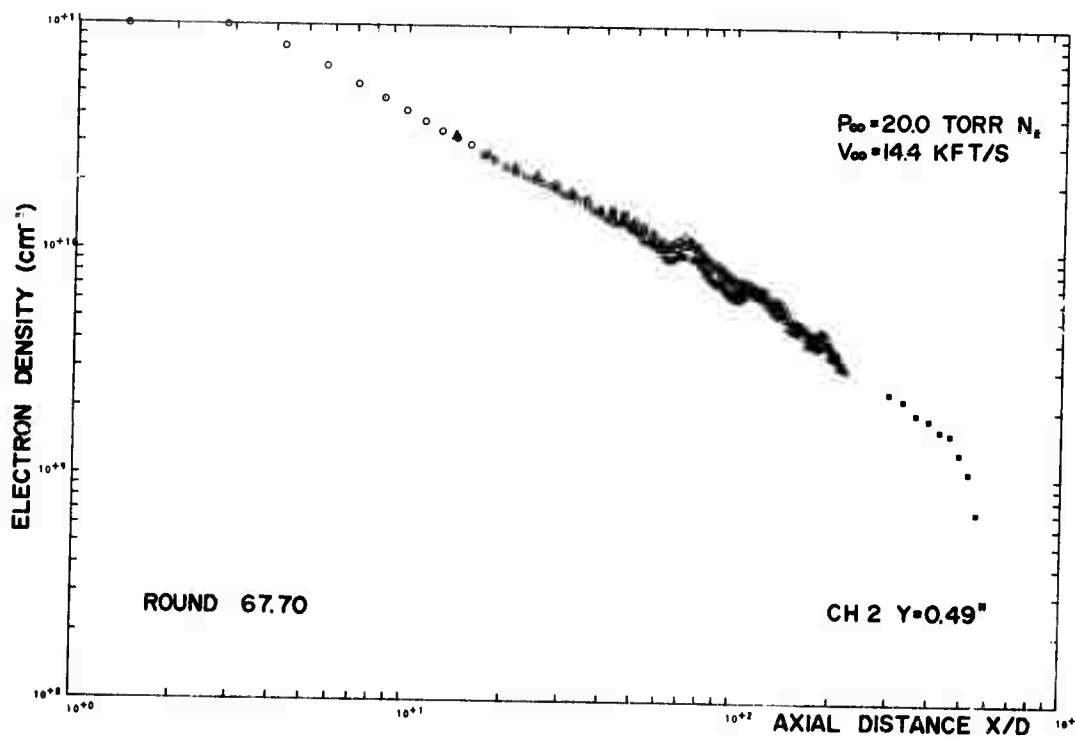


FIGURE F-4(b)

UNCLASSIFIED

180

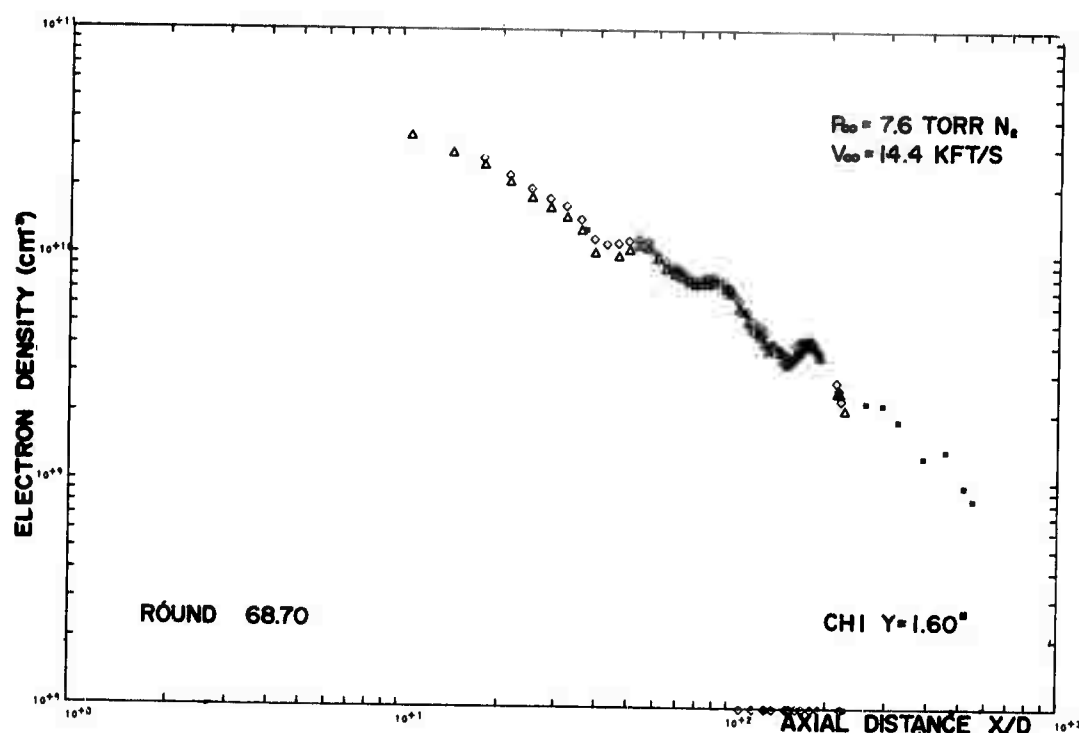


FIGURE F-5(a)

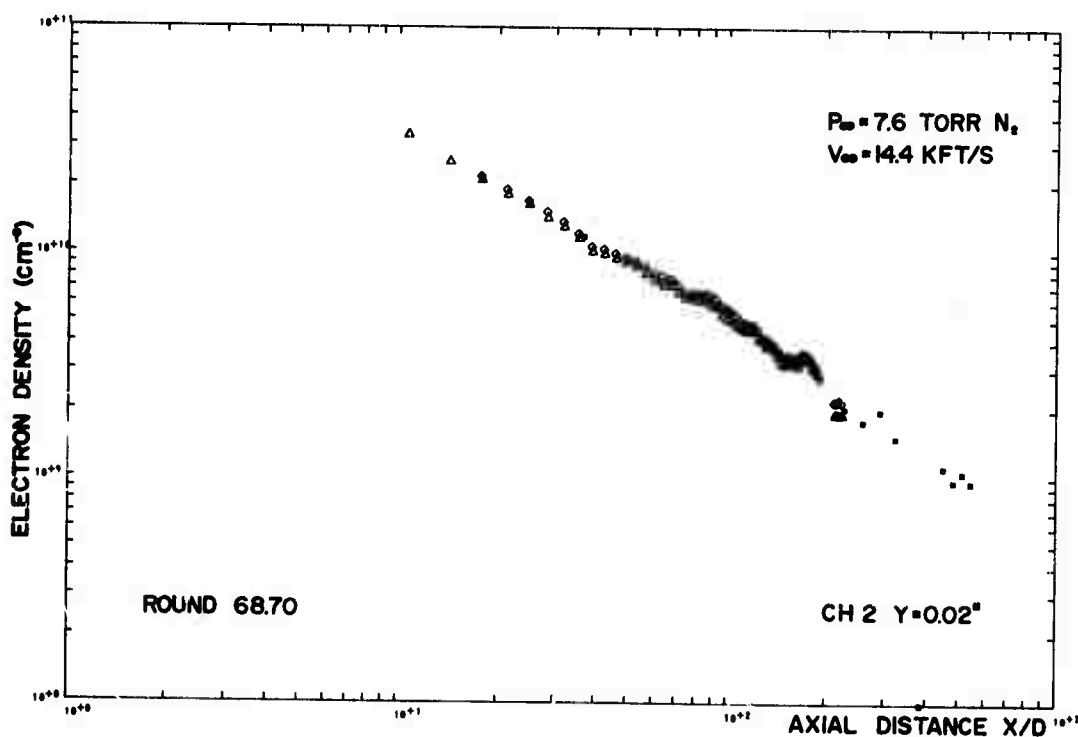


FIGURE F-5(b)

UNCLASSIFIED
181

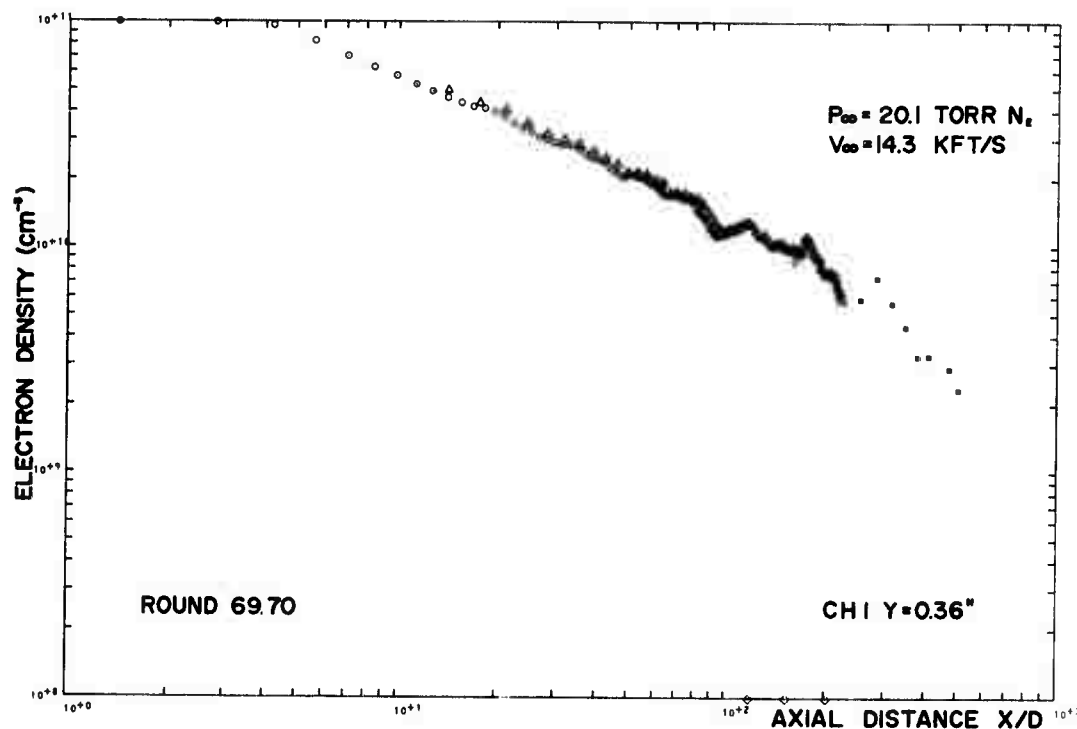


FIGURE F-6(a)

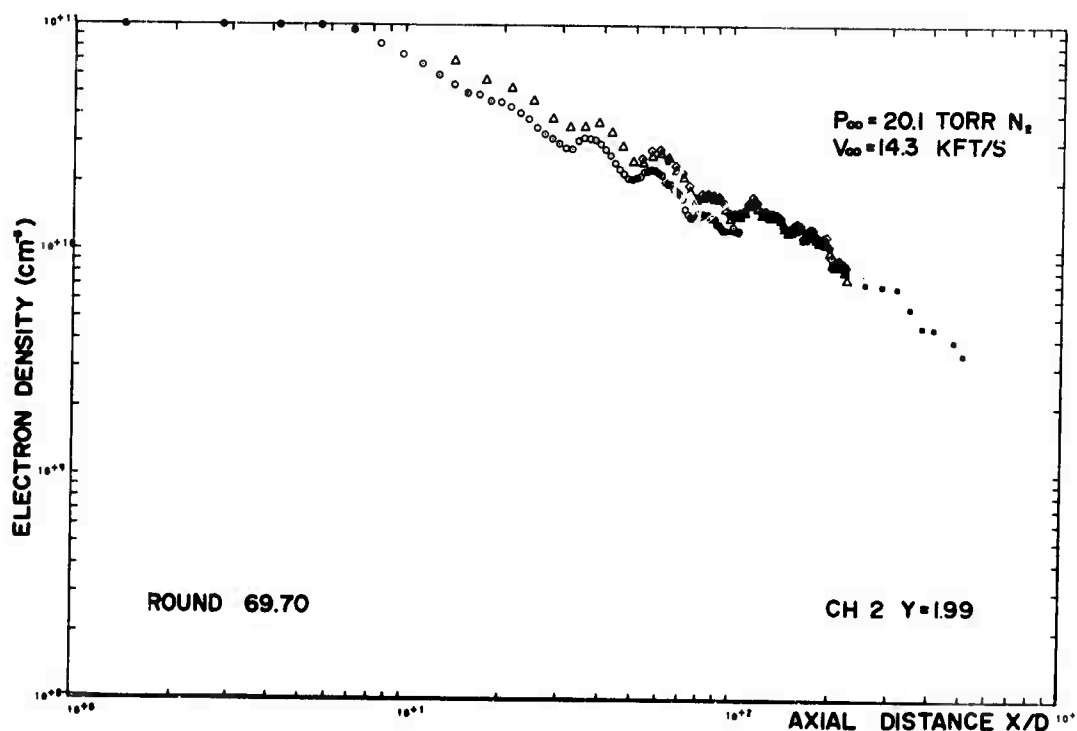


FIGURE F-6(b)

UNCLASSIFIED

182

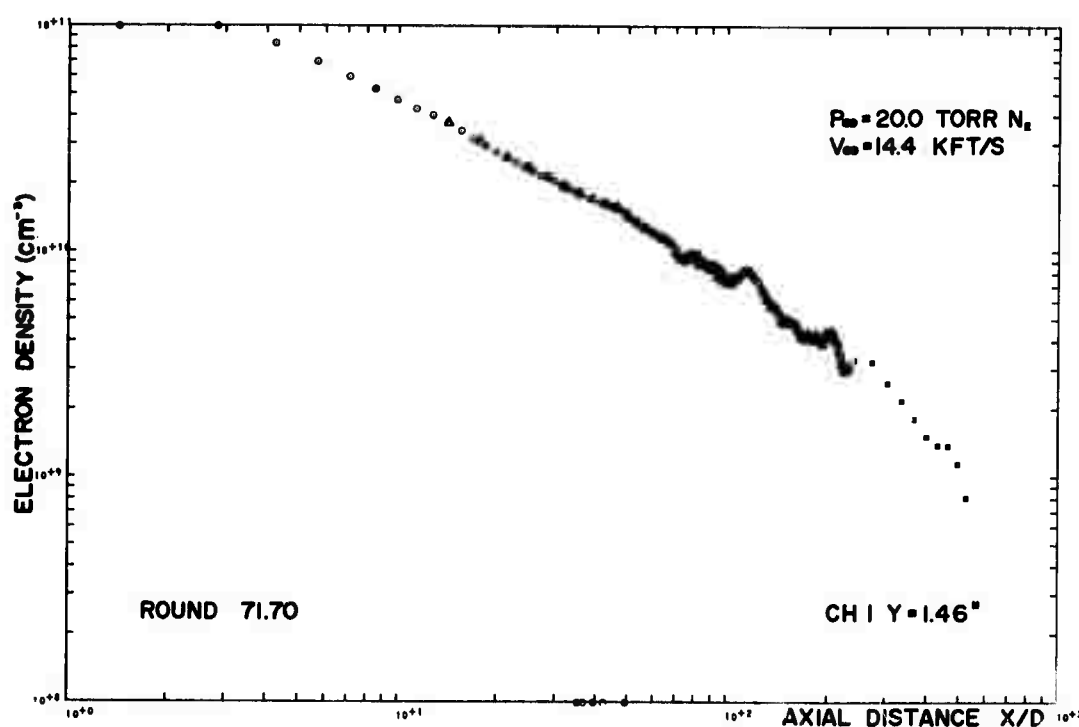


FIGURE F-7(a)

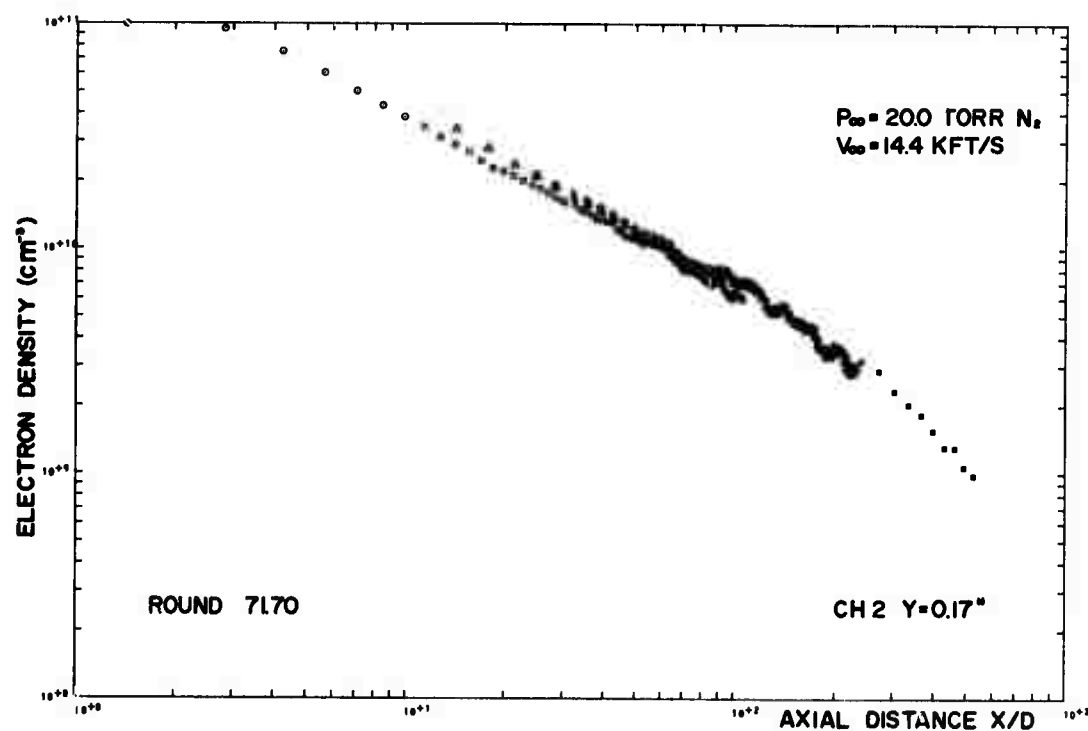


FIGURE F-7(b)

UNCLASSIFIED

183

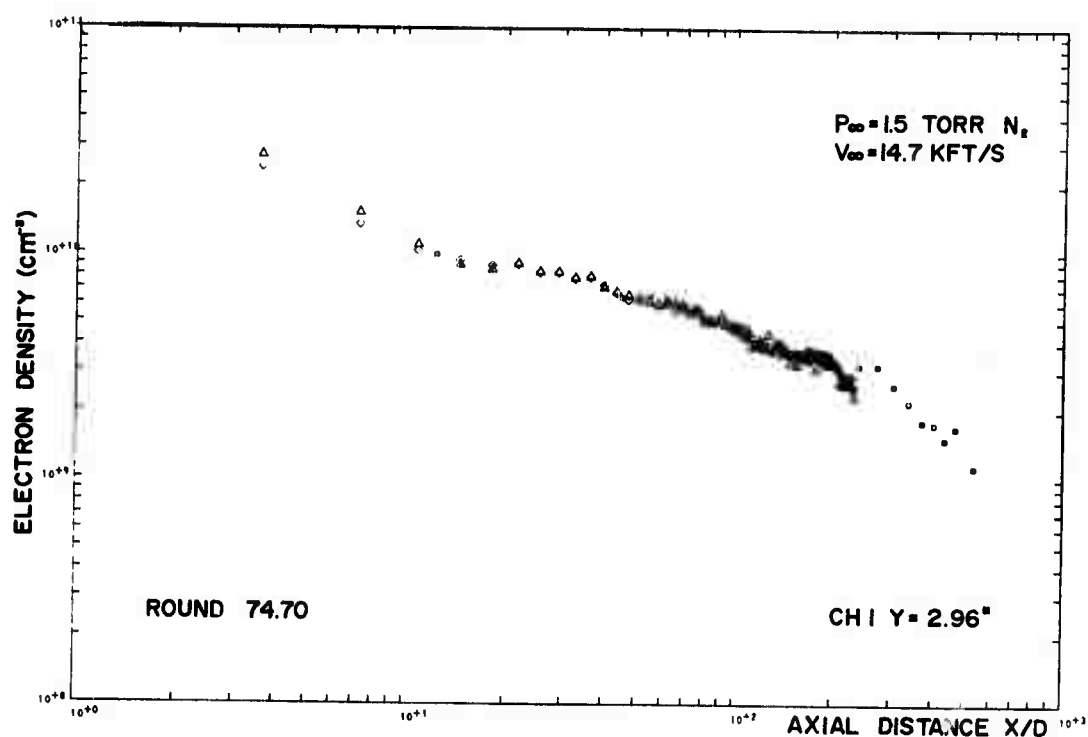


FIGURE F-8(a)

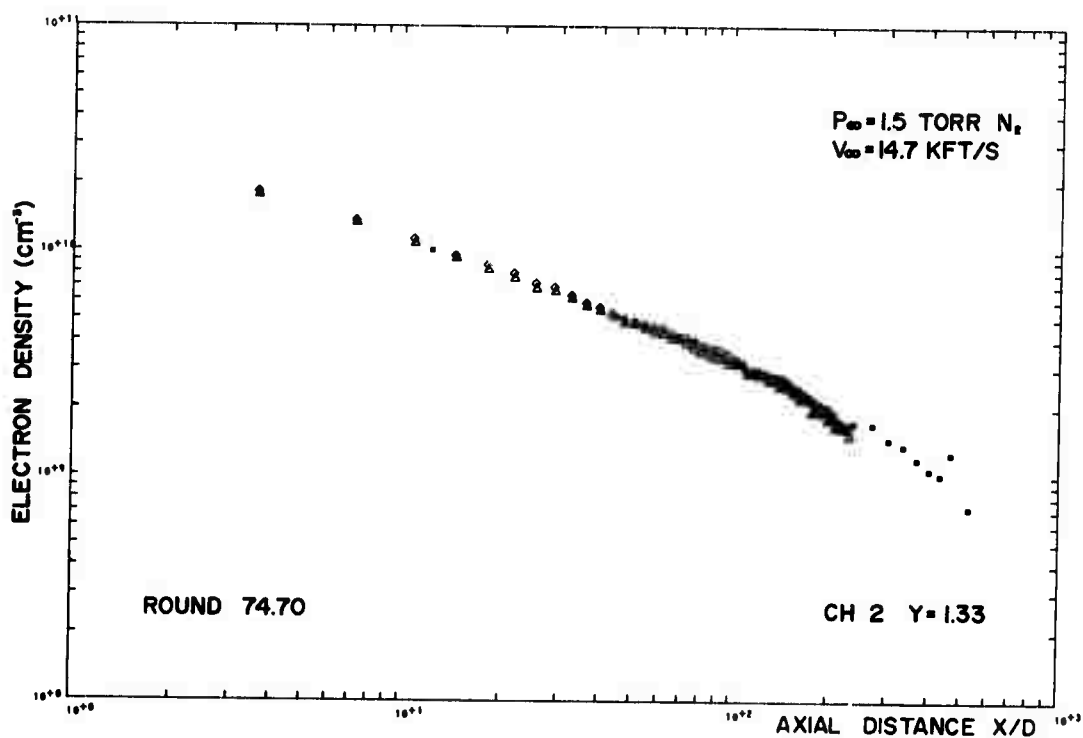


FIGURE F-8(b)

UNCLASSIFIED
184

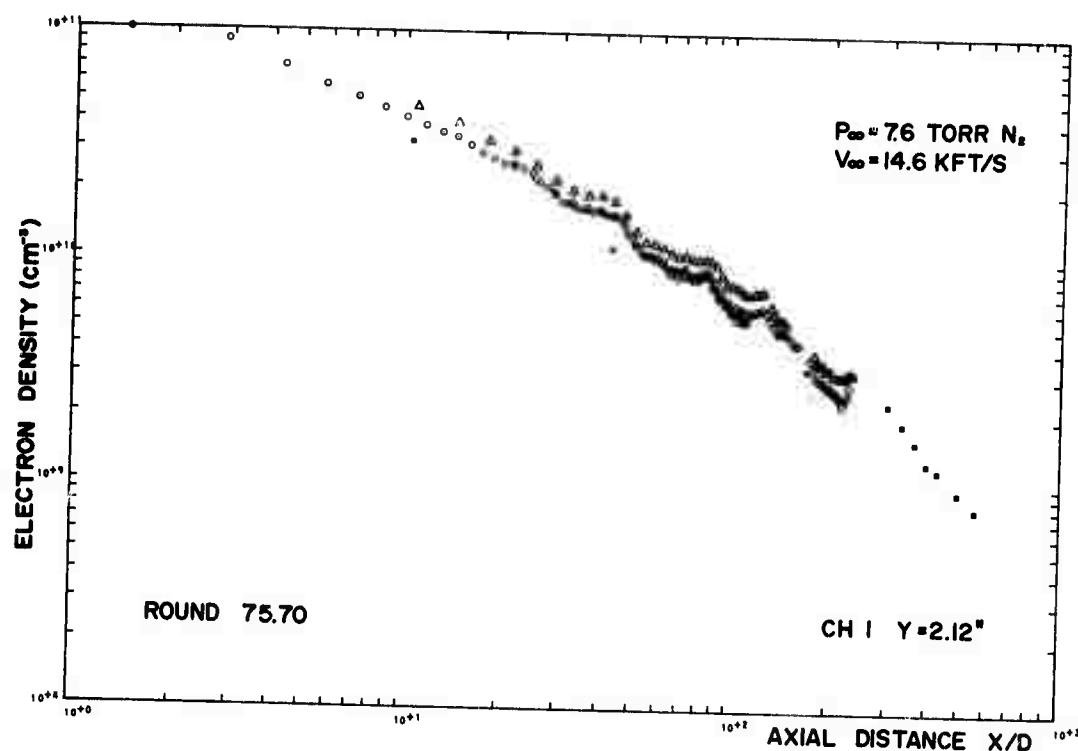


FIGURE F-9(a)

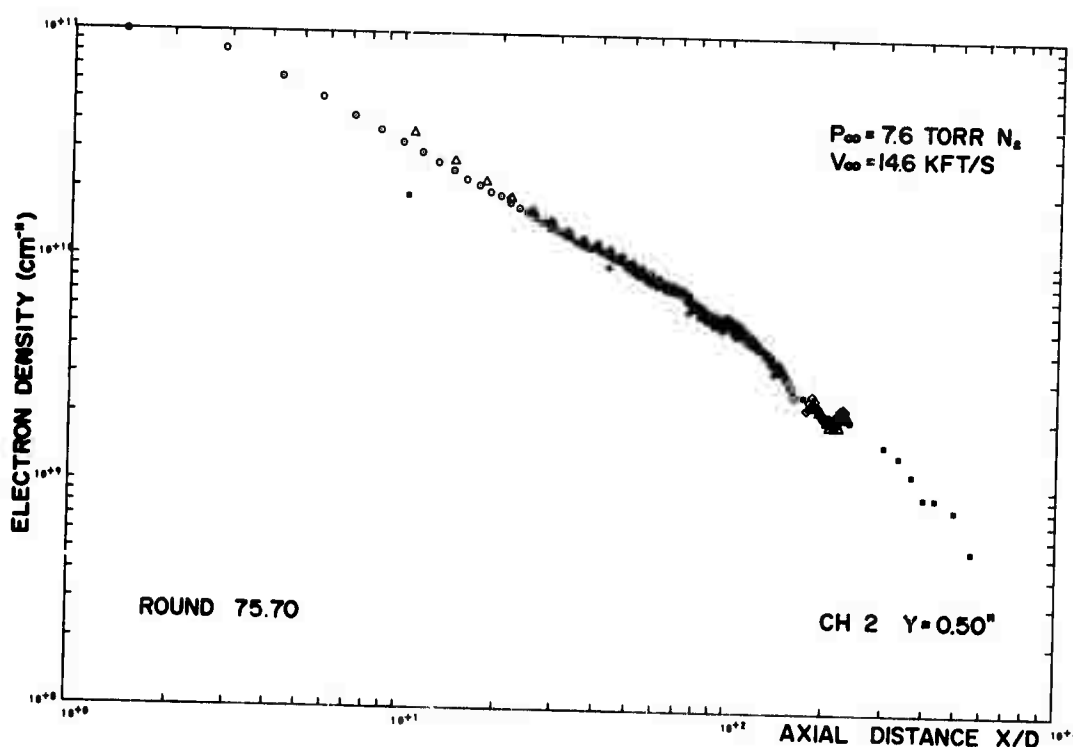


FIGURE F-9(b)